



HAL
open science

LES of two-phase reacting flows : stationary and transient operating conditions

Alexandre Eyssartier

► **To cite this version:**

Alexandre Eyssartier. LES of two-phase reacting flows : stationary and transient operating conditions. Fluid Dynamics [physics.flu-dyn]. Institut National Polytechnique de Toulouse - INPT, 2012. English. NNT : 2012INPT0011 . tel-04225375

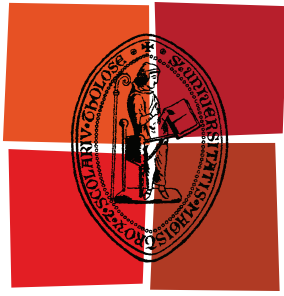
HAL Id: tel-04225375

<https://theses.hal.science/tel-04225375>

Submitted on 2 Oct 2023

HAL is a multi-disciplinary open access archive for the deposit and dissemination of scientific research documents, whether they are published or not. The documents may come from teaching and research institutions in France or abroad, or from public or private research centers.

L'archive ouverte pluridisciplinaire **HAL**, est destinée au dépôt et à la diffusion de documents scientifiques de niveau recherche, publiés ou non, émanant des établissements d'enseignement et de recherche français ou étrangers, des laboratoires publics ou privés.



Université
de Toulouse

THÈSE

En vue de l'obtention du
DOCTORAT DE L'UNIVERSITÉ DE TOULOUSE

Délivré par :
Institut National Polytechnique de Toulouse (INP Toulouse)

Discipline ou spécialité :
Dynamique des Fluides

Présentée et soutenue par :
Alexandre EYSSARTIER

le : vendredi 5 octobre 2012

Titre :

LES of two-phase reacting flows: stationary and transient operating conditions

Ecole doctorale :
Mécanique, Energétique, Génie civil et Procédés (MEGeP)

Unité de recherche :
CERFACS

Directeur(s) de Thèse :
Dr. Laurent Gicquel
Co: Dr. Gabriel Staffelbach

Rapporteurs :
Pascale Domingo, Directrice de recherche au CNRS-CORIA
Amsini Sadiki, Prof. Dr. Darmstadt University of Tech.

Membre(s) du jury :
Gérard Lavergne, Prof. ISAE Sup-Aéro
Ivan Fedoun, Maître de conf. Polytech Orléans, ICARE
Thierry Poinsot, Directeur de recherche à l'IMFT
Sébastien Roux, Dr. Ing. de recherche à SNECMA

Résumé

L'allumage et le réallumage de haute altitude présentent de grandes difficultés dans le cadre des chambres de combustion aéronautiques. Le succès d'un allumage dépend de multiples facteurs, des caractéristiques de l'allumeur à la taille des gouttes du spray en passant par le niveau de turbulence au point d'allumage. Déterminer la position optimale de l'allumeur ou le potentiel d'allumage d'une source d'énergie donnée à une position donnée sont ainsi des paramètres essentiels lors du design de chambre de combustion.

Le but de ces travaux de thèse est d'étudier l'allumage forcé des chambres de combustion aéronautiques. Pour cela, des Simulation numériques aux Grandes Echelles (SGE) d'écoulements diphasiques réactifs sont utilisées et analysées. Afin de les valider, des données expérimentales issues du banc MERCATO installé à l'ONERA Fauga-Mauzac sont utilisées. Cela permet dans un premier temps de valider la méthodologie ainsi que les modèles utilisés pour les SGE diphasiques évaporantes avant leur utilisation dans d'autres conditions d'écoulement. Le cas diphasique réactif statistiquement stationnaire est ensuite comparé aux données disponibles pour évaluer les modèles en condition réactives. Ce cas est étudié plus en détail à travers l'analyse de caractéristiques de la flamme. Celle-ci semble être le théâtre de régimes de combustion très différents. On note aussi que la détermination de la méthode numérique la plus appropriée pour le calcul d'écoulements diphasiques n'est pas évidente. De plus, deux méthodes numériques différentes peuvent donner des résultats en bon accord avec l'expérience et pourtant avoir des modes de combustion différents.

Les capacités de la SGE à correctement calculer un écoulement diphasique réactif étant validé, des SGE du phénomène transitoire d'allumage sont effectuées. La sensibilité observée expérimentalement de l'allumage aux conditions initiales, i.e. à l'instant de claquage, est retrouvé par les SGE. L'analyse met en évidence le rôle prépondérant de la dispersion du spray dans le développement initial du noyau de flamme. L'utilisation des SGE pour calculer les séquences d'allumage fournit de nombreuses informations sur le phénomène d'allumage, cependant d'un point de vue industriel, cela ne donne pas de résultat optimal, à moins de ne tester toutes les positions, ce qui rendrait le coût CPU déraisonnable. Des alternatives sont donc nécessaires et font l'objet de la dernière partie de ces travaux. On propose de dériver un critère local d'allumage, donnant la probabilité d'allumage à partir d'un écoulement diphasique (air et carburant) non réactif instationnaire. Ce modèle est basé sur des critères liés aux différentes phases menant à un allumage réussi, de la formation d'un premier noyau à la propagation de la flamme vers l'injecteur. Enfin, des comparaisons avec des données expérimentales sur des chambres aéronautiques sont présentées et sont en bon accord, indiquant que le critère d'allumage proposé, couplé avec une SGE d'écoulement diphasique non réactif, peut être utilisé pour optimiser la puissance et la position du système d'allumage.

Mots clés: Probabilités d'allumage, Allumage forcé, Simulation aux Grandes Echelles, Ecoulement diphasique, Combustion turbulente.

Abstract

Ignition and altitude reignition are critical issues for aeronautical combustion chambers. The success of ignition depends on multiple factors, from the characteristics of the ignitor to the spray droplet size or the level of turbulence at the ignition site. Finding the optimal location of the ignitor or the potential of ignition success of a given energy source at a given location are therefore parameters of primary importance in the design of combustion chambers.

The purpose of this thesis is to study forced ignition of aeronautical combustion chambers. To do so, Large Eddy Simulations (LES) of two-phase reacting flows are performed and analysed. First, the equations of the Eulerian formalism used to describe the dispersed phase are presented. To validate the successive LES, experimental data from the MERCATO bench installed at ONERA Fauga-Mauzac are used. It allows to validate the two-phase evaporating flow LES methodology and models prior to its use to other flow conditions. The statistically stationary two-phase flow reacting case is then compared to available data to evaluate the model in reacting conditions. This case is more deeply studied through the analysis of the characteristics of the flame. This last one appears to experience very different combustion regimes. It is also seen that the determination of the most appropriate methodology to compute two-phase flow flame is not obvious. Furthermore, two different methodologies may both agree with the data and still have different burning modes.

The ability of the LES to correctly compute burning two-phase flow being validated, LES of the transient ignition phenomena are performed. The experimentally observed sensitivity of ignition to initial conditions, i.e. to sparking time, is recovered with LES. The analysis highlights the major role played by the spray dispersion in the development of the initial flame kernel. The use of LES to compute ignition sequences provides a lot of information about the ignition phenomena, however from an industrial point of view, it does not give an optimal result, unless all locations are tested, which brings the CPU cost to unreasonable values. Alternatives are hence needed and are the objective of the last part of this work. It is proposed to derive a local ignition criterion, giving the probability of ignition from the knowledge of the unsteady non-reacting two-phase (air and fuel) flow. This model is based on criteria for the phases of a successful ignition process, from the first kernel formation to the flame propagation towards the injector. Then, comparisons with experimental data on aeronautical chambers are done and show good agreement, indicating that the proposed ignition criterion, coupled to a Large Eddy Simulation of the stationary evaporating two-phase non-reacting flow, can be used to optimize the ignitor location and power.

Key words: Ignition probabilities, Spark ignition, Large Eddy Simulation, Two-phase flow, Turbulent combustion.

Remerciements

Je tiens tout d'abord à remercier les rapporteurs, Pr. Pascale Domingo et Pr. Amsini Sadiki pour le temps passé à l'analyse du présent manuscrit ainsi que leurs commentaires éclairés. Je remercie plus largement l'ensemble des membres du jury qui m'ont fait l'honneur de juger ce travail.

Je remercie également la SNECMA (Groupe Safran) qui a financé ces travaux ainsi que mon tuteur Sébastien Roux qui m'a suivi tout au long de ces 3 années malgré mon éloignement à Toulouse.

Je remercie bien sûr l'ensemble de l'équipe CFD du CERFACS pour m'avoir accueilli et m'avoir fourni un environnement de travail idéal pour la réalisation de cette thèse. Je commencerais par l'aide apportée par les 2 secrétaires de l'équipe, Marie Labadens et Nicole Boutet, sans qui je me serais perdu dans la paperasse administrative et autres déplacements. Je remercie l'ensemble des séniors de l'équipe en commençant par mon directeur de thèse, Laurent Gicquel, merci pour ta patience lors de la rédaction de ce manuscrit mais aussi pour ta rigueur, ta confiance et ton soutien tout au long de ces 3 années qui n'ont pas toujours été un long fleuve tranquille mais ont su nous apporter son lot de satisfactions. Merci à Bénédicte Cuenot pour toutes ses discussions sur la théorie de la combustion, de la mécanique des fluides mais aussi de nos visions des mathématiques, qui a su porter et faire valoir l'utilité et la pertinence des travaux ayant menés au développement d'I-crit-LES.

Je souhaite remercier particulièrement Thierry Poinsot pour son aide et son influence sur mon parcours qui va bien au-delà de la thèse puisque cela a débuté dès mon stage de 2ème année au CERFACS, eh oui « on les prend au berceau maintenant ».

Parmi les « nouveaux séniors » j'ai une pensée particulière pour Antoine Dauplain qui m'a appris à me poser les bonnes questions lors de l'étude d'un signal acoustique et de son traitement notamment ; tu m'as sorti d'une mauvaise passe sur ce coup, merci.

Enfin je remercie les autres thésards et groupies du CERFACS qui sont pour beaucoup devenus de vrais amis et qui ont contribué à rendre ces années passées fort sympathiques. Je n'irai pas ici dans les détails, il y en a trop, et puis chacun sait ce que je lui dois. . .

Merci à tous !

Contents

Introduction

xvii

I	Equations and models for turbulent two-phase reacting flows	1
1	Description and models for the carrying gas phase	3
1.1	Transport equations for DNS	4
1.1.1	The perfect gas law	4
1.1.2	Diffusion velocities	5
1.1.3	The stress tensor	6
1.1.4	The energy flux	6
1.1.5	Definition of diffusion coefficients	6
1.1.6	The chemical source terms	7
1.2	Filtered equations for LES and closure models	8
1.2.1	The LES concept	8
1.2.2	LES filtering of the Navier-Stokes equations	9
1.2.3	Expressions and approximations of the resolved diffusive terms	10
1.2.4	Expression and closure of the SGS terms	11
1.2.5	Models for the turbulent viscosity	12
1.3	The thickened flame model for LES	13
1.3.1	The standard thickened flame model (TFLES)	14
1.3.2	The dynamic thickened flame model (DTFLES)	14
1.4	Remarks	16
2	Description and models for the dispersed phase	17
2.1	Liquid phase formalism: Eulerian VS Lagrangian frameworks	18
2.1.1	The Lagrangian approach	18
2.1.2	The Eulerian approach	19
2.2	Closure models for the dispersed equations	22
2.2.1	Drag source terms	23
2.2.2	Evaporation source terms	24
2.2.3	Closure of the uncorrelated motion	29
2.3	LES equations and closure for the dispersed phase	30
2.3.1	Filtering the conservative equations	30

2.3.2	Filtering of the non-linear terms	30
2.3.3	SGS fluxes	31
2.3.4	Resolved uncorrelated energy source term	32
2.3.5	Resolved coupling source terms	32
2.3.6	The LES equations for the dispersed phase	34
2.3.7	Closure of the coupling source terms in the gas equations	35
2.4	Additional remarks	35

II LES of two-phase reacting flow 37

3 LES of stationary two-phase reacting flow 39

3.1	Presentation of the MERCATO bench and available data	40
3.2	Numerical strategies	42
3.3	Numerical parameters	43
3.3.1	Geometry	43
3.3.2	Mesh	44
3.3.3	Boundary conditions	45
3.3.4	Characteristic time scales of the MERCATO target operating point . . .	47
3.3.5	Initial condition	49
3.4	Stationary non reacting LES	49
3.4.1	The gas phase	50
3.4.2	The liquid phase	52
3.4.3	Comparison with measurements	56
3.5	Stationary reacting LES	62
3.5.1	Global combustion regimes	63
3.5.2	Flame analysis and regimes	68
3.6	Conclusions	74

4 Transient LES spray ignition sequence 75

4.1	Computational setup and meshes	76
4.2	Sensitivity of the ignition process to the initial condition	79
4.3	Analysis of successful/failed ignitions	81
4.3.1	The failed ignition: $t_0 = 460ms$	83
4.3.2	The successful ignition: $t_0 = 463ms$	85
4.3.3	Quantitative comparisons of the two LES sequences	89
4.4	Conclusion of part II	92

III Methodology for ignition prediction of two-phase flows 95

5 The I-crit-LES approach 97

5.1	The notions of ignition probability	98
5.2	Identification of the relevant phenomena	98

5.2.1	The ignition scenario used in I-crit-LES	99
5.2.2	Criteria description	101
5.2.3	Ignition probability	110
5.2.4	Validation of the ignition scenario for I-crit-LES neglecting interaction with turbulence(phase 1 to 3)	112
5.2.5	The evolution of the I-crit-LES methodology	114
5.3	Conclusion	115
6	I-crit-LES: results	117
6.1	The KIAI configuration	118
6.1.1	Description of the burner	118
6.1.2	Validation of the cold LES against measurements (Results from D. Barré).118	
6.1.3	Application of I-crit-LES and confrontations	121
6.2	The Cambridge burner configuration	122
6.2.1	Description of the burner	122
6.2.2	Validation of the cold LES against measurements	125
6.2.3	Application and results of I-crit-LES V1	125
6.2.4	Evolutions of the results with I-crit-LES V2	127
6.3	The MERCATO configuration	128
6.3.1	Application and results of I-crit-LES V1	128
6.3.2	Evolutions of the results with I-crit-LES V2	132
6.4	Applications of I-crit-LES to realistic geometries	135
6.5	Conclusion of part III	135
	Conclusion and perspectives	137
	Appendix	143
A	Acoustic analysis of two swirlers using LES	143
A.1	Experimental setup	144
A.2	LES of the selected swirlers	146
A.2.1	Geometry and LES meshes	146
A.2.2	Numerical parameters	147
A.2.3	Flow topology and validation against measurements	147
A.2.4	Acoustics spectrum from LES	148
A.3	Identification of the eigenmodes	150
A.4	Detailed comparison of the LES and experimental spectrum	153
A.5	Influence of the boundary conditions	154
B	The principles of the FIM-UR methodology	159
C	Analytical developments of I-crit-LES criterion 2	163

List of Figures

1.1	Representation of the RANS (a) and LES (b) methods applied to a HIT spectrum.	9
2.1	Mesoscopic quantities and uncorrelated motion variable.	20
2.2	Evolution of the fuel mass fraction and of the liquid temperature for an isolated droplet.	24
2.3	Heat fluxes around a droplet	27
3.1	The experimental MERCATO bench at ONERA (picture from ONERA)	43
3.2	Description of the different elements of the MERCATO configuration	44
3.3	The LES domain of the MERCATO bench (half cut)	44
3.4	Axial cut of the mesh	45
3.5	Zoom on the modified liquid injection geometry (to use FIM-UR)	46
3.6	Mean gas velocity fields obtained with TTGC (left) and LW (right) [m/s]. Cut along the injection axis.	51
3.7	Transverse cut ($x = 40mm$) of the axial gas velocity fields obtained with TTGC (left) and LW (right) [m/s]	52
3.8	Picture of the bottom chamber (R. Lecourt) after tests. The painting has been diluted in the corners by kerosene droplets caught in the recirculation zones (light color).	52
3.9	RMS axial gas velocity fields obtained with TTGC (left) and LW (right) [m/s]. Cut along the injection axis.	53
3.10	Carburation of the gas phase obtained with TTGC (left) and LW (right). Cut along the injection axis.	53
3.11	Mean liquid velocity fields obtained with TTGC (left) and PSI (right) [m/s]. Cut along the injection axis.	54
3.12	RMS axial liquid velocity fields obtained with TTGC (left) and PSI (right) [m/s]. Cut along the injection axis.	55
3.13	Carburation of the liquid phase obtained with TTGC (left) and PSI (right). Cut along the injection axis.	56
3.14	Representation of the spray dispersion by the PVC. Isosurfaces of pressure $P = 100800Pa$ (green) and liquid volume fraction $\alpha_l = 5.10^{-4}$ (blue).	57
3.15	Axial velocity component. \circ represent data from $WR = 0.426 +$ correlations, \bullet represent data from $WR = 0.6$ directly.	58

3.16	Orthoradial velocity component. \circ represent data from $WR = 0.426$ + correlations, \bullet represent data from $WR = 0.6$ directly.	60
3.17	Radial velocity component. \circ represent data from $WR = 0.426$ + correlations, \bullet represent data from $WR = 0.6$ directly.	61
3.18	Flame topology from the experiments (courtesy of ONERA, R.Lecourt), chamber entrance on the left.	62
3.19	Mean fuel reaction rate in the mean axial plane. The black isoline represents $U_{g,ax} = 0$ and black vertical lines the positions of the measurements.	63
3.20	Axial velocity component	64
3.21	Instantaneous carburation fields for TTGC scheme. Black isoline denotes $HR = 10^8 W/m^3$	65
3.22	Instantaneous temperature fields for TTGC scheme. Black isoline denotes $HR = 10^8 W/m^3$	66
3.23	Instantaneous carburation fields for PSI scheme. Black isoline denotes $HR = 10^8 W/m^3$	67
3.24	Instantaneous temperature fields for PSI scheme. Black isoline denotes $HR = 10^8 W/m^3$	67
3.25	Mean gaseous temperature field with heat release isolines (white: $HR = 10^7 W/m^3$, grey: $HR = 10^8 W/m^3$). The numbers denotes the limits of the zones described next.	68
3.26	Heat release (integrated over the volume) function of the mixture fraction, and different zones contributions. Note that the mixture fraction being non dimensionned, the heat release "per mixture fraction" keeps [W] as unit.	69
3.27	Scatterplots of gaseous temperature according to the zone splitting	70
3.28	Scatterplots of fuel mass fraction according to the zone splitting	71
3.29	Scatterplots of heat release according to the zone splitting	72
3.30	Scatterplots of liquid volume fraction according to the zone splitting	73
4.1	Field cuts of mean variables in the axial plan $x = 0$: (a) Axial velocity (white line denotes $U = 0$ and (b) Liquid mass fraction (white line denotes $U_l = 0$	77
4.2	Initial energy deposit phase	78
4.3	Mesh refinements for energy deposition tests	80
4.4	Ignition tests: time evolution of the total fuel consumption rate ($\int \dot{\omega} dV$) in the whole combustor.	81
4.5	Snapshots of the 11 ignition sequences 1ms after the beginning of the deposit denoted by t_0 . The light gray isosurface denotes the $T_{gas} = 1500K$ surface. The slice is the axial median plane colored by the velocity magnitude. The following superscripts denote sequences that yield $\bar{\quad}$: a failed ignition ; *: a late ignition ; **: a successful ignition ; ***: a sharp ignition.	82
4.6	Initial solution fields. (a) Gaseous equivalence ratio (only evaporated fuel) at $t = 460ms$, (b) Liquid mass fraction at $t = 460ms$, (c) Gaseous equivalence ratio (only evaporated fuel) at $t = 463ms$, (d) Liquid mass fraction at $t = 463ms$	83

4.7	Failed ignition ($t_0 = 460ms$): field cuts of the gaseous temperature in the axial plan $x = 0$	85
4.8	Failed ignition ($t_0 = 460ms$): field cuts of the Kerosene mass fraction (gaseous) in the axial plan $x = 0$	86
4.9	Failed ignition ($t_0 = 460ms$): field cuts of the liquid volume fraction in the axial plan $x = 0$	87
4.10	Succeed ignition ($t_0 = 463ms$): field cuts of the gaseous temperature in the axial plan $x = 0$	88
4.11	Succeed ignition ($t_0 = 463ms$): field cuts of the intantaneous gaseous temperature at a later instant and prior to the full ignition of the burner	89
4.12	Succeed ignition ($t_0 = 463ms$): field cuts of the Kerosene mass fraction (gaseous) in the axial plan $x = 0$	90
4.13	Succeed ignition ($t_0 = 463ms$): field cuts of the liquid volume fraction in the axial plan $x = 0$	91
4.14	Temporal evolution of interesting variables	94
5.1	The 6 phase ignition scenario (dark zones correspond to ignited regions).	100
5.2	Sketch of the topology considered with the representation of the temperature profile at the end of the energy deposition.	103
5.3	Typical evolutions of the temperatures when ignition occurs (thermal runaway after t_{cc}).	104
5.4	Expansion of the initial laminar kernel.	106
5.5	Layers description of criterion 4	107
5.6	Isosurfaces of limits of validity of ignition criteria and the full index function of the liquid volume fraction, the droplet diameter and the energy deposit (White = success, i.e. = 1 / dark = failure, i.e. = 0).	109
5.7	Isosurfaces of limits of validity of ignition criteria and the global index as functions of the pressure, the initial gas temperature and the droplets size (White = success, i.e. = 1 / dark = failure, i.e. = 0). The spark energy is 50 mJ and the initial fuel volume fraction is $\alpha_l = 3.10^{-4}$	111
5.8	Ignition of a homogeneous droplet cloud ($E_{dep} = 4.3mJ$).	113
5.9	Comparison of the temporal evolution of maximum gas temperature between successful (1) and failed (2) ignition.	113
5.10	Minimal energy as a function of droplet diameter d_l for a stoichiometric mixture. 1 and 2 refer to Fig. 5.9.	114
6.1	Geometry of the KIAI burner.	119
6.2	Mean axial velocity field in the $x = 0$ plane (black line denotes 0 m/s)	119
6.3	Axial velocity profiles of the cold flow	120
6.4	Tangential velocity profiles of the cold flow	121
6.5	Comparison of experimental results with ignition criteria for the ignition operating point on KIAI.	123
6.6	Pictures of the burner (courtesy of Cambridge University, Pr. Mastorakos).	124

6.7	Geometry and mesh of the LES	125
6.8	Velocity profiles of the cold flow. Lines represent the LES. Lines + symbols represent the experiments.	126
6.9	Ignition probability maps	127
6.10	Comparison of the carburations XP vs LES	127
6.11	Comparison of ignition probability maps	128
6.12	Relevant criteria maps on the Cambridge configuration	129
6.13	I-CRIT-LES applied to single snapshots for the same times as in section 4.2. White: I-CRIT-LES=1 (ignition) ; Black: I-CRIT-LES=0 (no ignition). Reminder of Fig. 4.5: circle denotes spark location. The following superscripts denote sequences that yield $\bar{\cdot}$: failed ignition ; \ast :late ignition ; $\ast\ast$: successful ignition ; $\ast\ast\ast$: sharp ignition.	130
6.14	Criteria in the $x = 0$ plane (criteria 2 and 3 being valid in the whole combustor are not presented). Black cross: spark location for ignition sequences simulations. $E_{dep} = 100 mJ$	131
6.15	Global ignition index in the $x = 0$ plane given by I-crit-LES (V1) for $E_{dep} = 100 mJ$. Dark zones correspond to low ignition probability (white isoline for $P_{ign} = 0.33$). Arrows report experimental tests (white means ignitions have been observed, black means no ignition observed)	132
6.16	Criteria in the $x = 0$ plane. Black cross: spark location for ignition sequences simulations. $E_{dep} = 100 mJ$	133
6.17	Global ignition index in the $x = 0$ plane given by I-crit-LES (V2) for $E_{dep} = 100 mJ$. Dark zones correspond to low ignition probability (white isoline for $P_{ign} = 0.33$). Arrows report experimental tests (white means ignitions have been observed, black means no ignition observed)	134
6.18	Limiting criterion in the $x = 0$ plane. Black cross: spark location for ignition sequences simulations. $E_{dep} = 100 mJ$	134
A.1	Views of the experimental device	145
A.2	View of the LDA system.	145
A.3	Geometry of the LES domain	146
A.4	Comparative view of the simulated swirlers	147
A.5	LES mesh. Axial cut	148
A.6	Axial velocity fields, axial cut	149
A.7	LDA and LES mean axial velocity profiles.	150
A.8	Experimental measurement of the CRZ length.	150
A.9	Amplitude of the FFT of the LES signals (linear scale).	151
A.10	DSP amplitude fields from LES. Axial cut	152
A.11	Geometry and boundary conditions used for the acoustic computations.	152
A.12	Identification of the acoustic eigenmodes on the LES and experimental spectrums. Log scale.	153
A.13	Amplitude fields of the main acoustic eigenmodes (from acoustic solver AVSP). Axial cut.	154

A.14	Configuration A: LES and experimental spectrums. Log scale.	155
A.15	Configuration I: LES and experimental spectrums. Log scale.	155
A.16	Comparison of the acoustic spectrum LES and experimental for the two configurations. Log scale.	156
A.17	View of the modified boundary conditions for the reflecting test case.	156
A.18	Comparison of the acoustic spectrum for the configuration A.	157
B.1	Definition of parameters and sketch of the methodology FIM-UR	160
B.2	Liquid variable profiles in the discharge orifice plane $x = x_0$	161
B.3	Liquid variable profiles on the injection plane $x = x_i$	162

List of Tables

3.1	MERCATO operating points	41
3.2	Comments about MERCATO operating points	41
3.3	Characteristics of the mesh	45
3.4	Boundary conditions for the gas phase	46
3.5	Boundary conditions for the liquid phase	47
3.6	Artificial viscosity levels	49
4.1	Characteristics of the mesh used for ignition sequences	79
5.1	User input values for the model I-crit-LES	108
A.1	Recording protocole	146

Introduction

When dealing with turbo-reactor performance, the most thermodynamically efficient component still remains today the combustion chamber and improvements obtained on the most recent engines come from increased efficiencies of compressors and turbines. However, and because of the drastic changes of the legislation concerning pollutant emissions, the classical operating mode of the combustion chambers has to be reconsidered. Indeed, as legacy, the fuel/air mixture usually burns at an equivalence ratio close to stoichiometry or even rich, while reducing pollutant emissions ¹ requires to burn lean [1, 2]. This new burning regime presents several known drawbacks such as combustion instabilities [3, 4] or difficulties to ignite. Previous studies highlight that ignition system performance will be lowered when departing from stoichiometric fuel/air conditions [5]. and the ignition phase of the new systems is becoming even more critical.

Nowadays, ignition systems for aeronautics fall in two main categories, the spark ignitors and the torch ignitors:

- Gas turbine spark ignitors consist in two electrodes separated by semi-conductor material, a specific electrical device producing a high voltage between these two electrodes. The high voltage then induces breakdown which ionizes the surrounded mixture, i.e. plasma phase, and generates an electrical arc. The associated energy is transferred to the mixture through the subsequent plasma phase and is typically of the order of one Joule. However, because of losses by conduction, radiation and shock waves, only a few part of the spark energy is actually transferred to the mixture. The electrical discharge is usually repeated several times per second to increase the success rate of ignition of the combustor but it also reduce the lifespan of the electrodes.
- A torch ignitor system, a spark ignitor is associated to a starter pressurized nozzle (which has easier ignition conditions). This starter once ignited then produces a continuous pilot-flame which will ignite the main injector. Compared to the standard spark ignitor, such a device requires a smaller spark plug but may experience coke formation at the starter nozzle. To avoid such formations, the nozzle fuel injection is cut after ignition and bled continuously with air.

The dependency on the specificities of the ignition systems, although potentially of importance for the subsequent ignition sequence, is however out of the scope of the present document.

The purpose of this thesis is to study the ignition in the new aeronautical context presented above: i.e. premixed combustors and the physics at play during their ignition phase. The study of ignition started decades ago and the level of comprehension of the involved phenomena have led to more and more advanced techniques. Historically the part devoted to experimental measurements was larger than the one to computational studies. However, due to progress in computer power and numerical models the part of the numerical studies in the development of recent engines is quickly increasing. Furthermore, under some extreme conditions such as high pressure combustion (rocket engines combustion) [6] or highly transient phenomena (ignition)

¹mainly nitrogen oxides, NOx

[7], the access to measured data in the experiments can be very challenging [8] and the numerical simulations, within its own modeling and numerics limitations, can bring a bright insight. The numerical tools themselves cover a wide range of applications depending on the level of accuracy/predictivity required, from the potential flows to the so-called Direct Numerical Simulations (DNS), where the Navier-Stokes equations are directly computed. In the case of transient conditions of ignition, i.e. unsteady flows, the tools reduce to three categories:

1. URANS: Unsteady Reynolds-Averaged Navier-Stokes
2. LES: Large-Eddy Simulations
3. DNS: Direct Numerical Simulations

The URANS is cost effective but since the turbulence scales are fully modeled, the complex interaction between combustion and turbulent mixing would not be computed accurately. On the other hand, the DNS resolves the whole turbulence spectrum making the coupling with combustion easier but is very costly and remains confined to academic configurations [9, 10]. The use of LES appears as a good compromise between accuracy and CPU efficiency for the study of ignition in an industrial context. Furthermore, LES is becoming a standard tool for gaseous reacting flows [11, 12, 13, 14, 15]. The application of LES to non-reacting two-phase² flows [16, 17, 18] or to reacting two-phase flows [19, 20, 21, 22, 23] is at an earlier stage because of the multiple challenges associated with the description of fuel spray atomization, of interaction of droplets with flames or walls and the lack of experimental results which can be used to validate these CFD results.

Dense liquid phenomena like atomization [24, 25, 26, 27, 28] are out of the scope of this document and only diluted sprays are addressed. To study the spray dynamic, the two main formalisms available to the CFD community are the so-called Lagrangian [29, 30, 31] and Eulerian formalisms [32, 33, 34]. In the Lagrangian approach, the dispersed phase can be considered as a set of small discrete particles following point mechanic equations. In the Eulerian approach, the spray is described as a continuous phase like the gas phase with the properties of the mean local set of particles. The Eulerian solver used in this work has been developed and validated from the PhD work of Kaufmann (2004) [35] while the Lagrangian solver stems from the work of García (2005) [36]. The two formalisms are briefly described in Chapter 2.

In the context of ignition, recent measurement campaigns on the MERCATO bench from ONERA (see Tab. 3.1) provide data sets for both non-reacting and reacting two-phase flows which can be compared to stationary and transient LES. Such stationary monodisperse EE LES two-phase flow predictions are presented in Chapter 3. Based on these encouraging findings and although room for improvement is clear, the Euler-Euler turbulent reacting LES approach is then applied to the study of the fully transient phenomena issued by an energy deposit as encountered in an ignition sequence (cf. Chapter 4). Results from such simulations offer access to fully transient phenomena that could not be addressed numerically with other CFD models

²Since in aeronautic, the fuel used (Kerosene) is liquid at operating conditions, at least at the injection; two-phase flow modeling have to be taken into account.

(other than Direct Numerical Simulations, DNS). In particular, the fully transient phase that results from a sparking ignition phase can be simulated with LES which thus provides a dynamic description of the spatial and temporal evolution as well as the propagation of the flame front until full ignition or extinction of the burner. Findings confirm the potential of the approach in describing qualitatively the leading order mechanisms and also prove the importance of the initial flow field state in the neighborhood of the ignitor at sparking time. In his review on ignition [37], Pr. Mastorakos underlines the stochastic behavior of the ignition process which requires the introduction of an ignition probability to be quantifiable. Hence, performing LES of ignition sequences to study ignition requires numerous runs to determine ignition probabilities, bringing CPU cost to unreasonable value. Another way to provide ignition probabilities needs clearly to be developed. This is the objective of the Part III.

It may be assumed that the statistics of turbulent flow at the spark location determine the probability of igniting a kernel. This concept was first put forward by Birch *et al.* [38, 39] who introduced the term *flammability factor*, F . From this starting point, several studies [5, 40, 41, 42, 43] extended the concept and showed that the probability of igniting a kernel is the result of many factors and is not necessarily equal to F . In the specific context of aeronautical burners, the propagation of the turbulent flame to the fuel injection system and its stabilization is not certain although they are clear pre-requests for the ignition success of the engine. The probability of igniting the whole chamber is thus even lower than the one of igniting a flame kernel. This one burner ignition process is not fully local and for the moment has not been evaluated analytically [44, 45]. Building the ground for a simple analytical model predicting the ignition probability of a single burner is the actual objective of this thesis (cf. Chapter 5). Called I-crit-LES, this methodology based on analytical criteria uses a set of non reacting LES snapshots. The final set of criteria used to model the full ignition of a sector burner, are:

C1: The fuel distribution must guarantee a flammable mixture.

C2: The discharge energy must be sufficient to create a first hot gas kernel.

C3: The local conditions (vaporization time versus diffusion time) must allow the kernel to increase.

C4: The flame must not be quenched near walls.

C5: The flame speed must be larger than the local flow speed to allow the flame to propagate upwards.

C6: The local stress experienced by the kernel must be low enough to avoid aerodynamic quenching.

Finally, in Chapter 6, I-crit-LES is validated and illustrated through several configurations. The purpose is to cover a large range of conditions to test the limits of the model.

Part I

Equations and models for turbulent two-phase reacting flows

Chapter 1

Description and models for the carrying gas phase

In this first chapter, the conservative compressible Navier-Stokes equations [46, 47, 48, 49] are described. First, the unfiltered equations (used in Direct Numerical Simulations, DNS) are detailed with the different source terms needed for two phase reacting simulations. These sources terms include species fluxes due to multi-species formulation, heat release and species production/destruction due to chemical reaction. Other terms come from the exchange with the liquid phase (see chapter 2) like the evaporation rate, the drag force or the heat exchange between phases. Finally, the energy deposit used in Chapter 4 to perform ignition is also introduced in the following equations.

In the subsequent section, these equations are filtered to yield the Large Eddy Simulations (LES) set of governing equations and the associated closures needed to perform the simulations are detailed in chapters 3 and 4. Finally, the concept of the flame thickening for LES is briefly described as it is used to model the turbulent / combustion closure problems.

1.1 Transport equations for DNS

In the case of DNS, for the gas phase and neglecting the volume forces, the conservative compressible Navier-Stokes equations read:

$$\frac{\partial \rho}{\partial t} + \frac{\partial}{\partial x_j}(\rho u_j) = \Gamma \quad (1.1)$$

$$\frac{\partial \rho Y_k}{\partial t} + \frac{\partial}{\partial x_j}(\rho u_j Y_k) = \dot{\omega}_k - \frac{\partial J_{j,k}}{\partial x_j} + \Gamma \delta_{k,F} \quad (1.2)$$

$$\frac{\partial}{\partial t} \rho u_i + \frac{\partial}{\partial x_j}(\rho u_i u_j) = -\frac{\partial p}{\partial x_j} + \frac{\partial \tau_{ij}}{\partial x_j} + \Gamma \check{u}_{l,i} - F_{d,i} \quad (1.3)$$

$$\frac{\partial \rho E}{\partial t} + \frac{\partial}{\partial x_j}(\rho E u_j) = \dot{\omega}_T + \dot{Q} - \frac{\partial q_j}{\partial x_j} - \frac{\partial}{\partial x_j}[u_i(p\delta_{ij} - \tau_{ij})] + \Pi_g + \Gamma \frac{1}{2} \check{u}_{l,j}^2 - \check{u}_{l,j} F_{d,j} \quad (1.4)$$

Equations (1.1) - (1.4) respectively represent the conservation of mass ρ , species mass fraction Y_k , momentum u and total energy E . Naturally, for a mixture of N species, $\sum Y_k = 1$. Here, and for the rest of the document, \dot{Q} will be the heat source term of the ignition device and the index k indicates the k -th species.

The liquid source terms are introduced with Π_g standing for the heat transfert from the liquid to the gas, Γ the evaporation rate and F_d the drag force. However, they will be detailed and modeled only in the section dealing with the dispersed phase equations, and will be removed for the rest of this section.

1.1.1 The perfect gas law

The gaseous phase is considered as a perfect gas mixture. If we note N the total number of species in the mixture, we have:

$$p = \rho r T \quad (1.5)$$

where $r = \frac{R}{W}$ is the mean gas mixture constant. W the mixture mean molar mass is defined by:

$$\frac{1}{W} = \sum_{k=1}^N \frac{Y_k}{W_k} \quad (1.6)$$

In the same way, the mixture heat capacities C_p and C_v are defined from each gas heat capacity by:

$$C_p = \sum_{k=1}^N Y_k C_{p,k} \quad (1.7)$$

$$C_v = \sum_{k=1}^N Y_k C_{v,k} \quad (1.8)$$

1.1.2 Diffusion velocities

In a multi-species flow, mass conservation implies:

$$\sum_{k=1}^N Y_k V_{k,i} = 0 \quad (1.9)$$

where $V_{k,i}$ are the diffusion velocity components of the k -th species. The approximation of Hirschfelder-Curtis [50] defines these velocities as functions of the species gradients:

$$X_k V_{k,i} = -D_k \frac{\partial X_k}{\partial x_i} \quad (1.10)$$

where X_k is the molar fraction of the species k : $X_k = Y_k W / W_k$ and D_k is the diffusivity of the species k . Equation (1.10) can be rewritten as:

$$Y_k V_{k,i} = -D_k \frac{W_k}{W} \frac{\partial X_k}{\partial x_i} \quad (1.11)$$

However, summing the N species of Eq. (1.11) leads to a violation of the mass conservation written in Eq. (1.9). Hence, if using the approximation of Hirschfelder-Curtis and to enforce global mass conservation, a correction velocity has to be added [15]:

$$V_i^c = \sum_{k=1}^N D_k \frac{W_k}{W} \frac{\partial X_k}{\partial x_i} \quad (1.12)$$

Finally, the species diffusion flux $J_{i,k}$ is:

$$J_{i,k} = \rho V_{k,i} Y_k = -\rho \left(D_k \frac{W_k}{W} \frac{\partial X_k}{\partial x_i} - Y_k V_i^c \right) \quad (1.13)$$

and Eq. (1.2) is rewritten as:

$$\frac{\partial \rho Y_k}{\partial t} + \frac{\partial}{\partial x_j} (\rho u_j Y_k) = \dot{\omega}_k + \frac{\partial}{\partial x_j} \left[\rho \left(D_k \frac{W_k}{W} \frac{\partial X_k}{\partial x_j} - Y_k V_j^c \right) \right] \quad (1.14)$$

1.1.3 The stress tensor

The stress tensor τ_{ij} appearing in the momentum equation, Eq (1.3), is defined by the relations:

$$\tau_{ij} = 2\mu(S_{ij} - \frac{1}{3}\delta_{ij}S_{ll}) \quad (1.15)$$

and

$$S_{ij} = \frac{1}{2} \left(\frac{\partial u_j}{\partial x_i} + \frac{\partial u_i}{\partial x_j} \right) \quad (1.16)$$

where μ is the dynamic viscosity.

1.1.4 The energy flux

For a multi-species mixture, the energy flux q_i , Eq (1.4), is composed of two parts. The first one is a heat diffusion expressed by Fourier's Law and the second one from the species diffusion. q_i is written as:

$$q_i = \underbrace{-\lambda \frac{\partial T}{\partial x_i}}_{\text{Heat diffusion}} - \underbrace{\rho \sum_{k=1}^N \left(D_k \frac{W_k}{W} \frac{\partial X_k}{\partial x_i} - Y_k V_i^c \right) h_{s,k}}_{\text{Species diffusion}} \quad (1.17)$$

where λ is the thermal conductivity and $h_{s,k}$ is the sensible enthalpy of the species k . Soret (molecular species diffusion due to temperature gradients) and Dufour (heat flux due to species mass fraction gradients) effects are here neglected [51, 52].

1.1.5 Definition of diffusion coefficients

In most CFD codes for multi-species flows, the dynamic viscosity μ is often supposed independent of the mixture composition and close to air. In AVBP, two formula are available based on this hypothesis (plus the constant viscosity), Sutherland's Law [53] and the power law. They both depend on temperature. In this document, all the simulations are done with the power law:

$$\mu = \mu_{ref} \left(\frac{T}{T_{ref}} \right)^b \quad (1.18)$$

where b has a typical value of 0.76 for air. The thermal conductivity of the mixture is defined by:

$$\lambda = \frac{\mu C_p}{Pr} \quad (1.19)$$

where Pr is the Prandtl number (supposed constant).

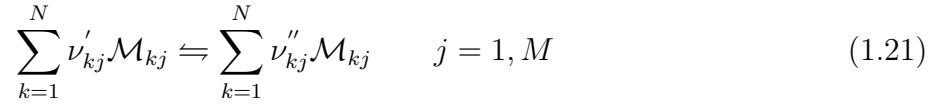
In the same way, instead of computing the thermal diffusivity coefficients of each species from the binary coefficients, a simplified definition is used:

$$D_k = \frac{\mu}{\rho S c_k} \quad (1.20)$$

where $S c_k$ is the Schmidt number of the species k , supposed constant in space and time. The values of the Schmidt and Prandtl numbers used in the simulations come from detailed computations with the COSILAB software [54].

1.1.6 The chemical source terms

The chemical source terms are $\dot{\omega}_k$ in Eq. (1.2) and $\dot{\omega}_T$ in Eq. (1.4). The chemical kinetic is described in this work by the Arrhenius' Law. First, we define a chemical mechanism of N species and M reactions:



The total reaction rate of the species k is the sum of the reaction rate of the species k for each reaction:

$$\dot{\omega}_k = \sum_{j=1}^M \dot{\omega}_{kj} = W_k \sum_{j=1}^M \nu_{kj} \mathcal{Q}_j \quad (1.22)$$

where $\nu_{kj} = \nu''_{kj} - \nu'_{kj}$ and \mathcal{Q}_j is the progress rate of the j -th reaction written as:

$$\mathcal{Q}_j = K_{f,j} \prod_{k=1}^N \left(\frac{\rho Y_k}{W_k} \right)^{\nu'_{kj}} - K_{r,j} \prod_{k=1}^N \left(\frac{\rho Y_k}{W_k} \right)^{\nu''_{kj}} \quad (1.23)$$

$K_{f,j}$ and $K_{r,j}$ are respectively the reaction rates of the forward and reverse reaction j :

$$K_{f,j} = A_{f,j} \exp\left(-\frac{E_{a,j}}{RT}\right) \quad (1.24)$$

where $A_{f,j}$ is the preexponential constant and $E_{a,j}$ is the activation energy. The reverse rates $K_{r,j}$ are computed from the forward rates through the equilibrium constants:

$$K_{r,j} = \frac{K_{f,j}}{K_{eq}} = \frac{K_{f,j}}{\left(\frac{p_a}{RT}\right)^{\sum_{k=1}^N \nu_{kj}} \exp\left(\frac{\Delta S_j^0}{R} - \frac{\Delta H_j^0}{RT}\right)} \quad (1.25)$$

where $p_a = 1\text{bar}$. ΔH_j^0 and ΔS_j^0 are the enthalpy (sensible + chemical) and the total entropy of the reaction j :

$$\Delta H_j^0 = h_j(T) - h_j(0) = \sum_{k=1}^N \nu_{kj} W_k (h_{s,k}(T) + \Delta h_{f,k}^0) \quad (1.26)$$

$$\Delta S_j^0 = \sum_{k=1}^N \nu_{kj} W_k s_k(T) \quad (1.27)$$

where $\Delta h_{f,k}^0$ is the mass enthalpy of formation of species k at the reference temperature $T_0 = 0\text{K}$.

Finally, the heat release due to combustion is defined by:

$$\dot{\omega}_T = - \sum_{k=1}^N \dot{\omega}_k \Delta h_{f,k}^0 \quad (1.28)$$

1.2 Filtered equations for LES and closure models

1.2.1 The LES concept

Large Eddy Simulations (LES) are now recognized as an alternative to the more classical Reynolds Averaged Navier-Stokes simulations (RANS). Both of these methodologies aim at describing the characteristics of turbulent flows, but with different levels of modeling. The development of the new equations is obtained applying operators on the Navier-Stokes equations. This step introduces new terms that have to be closed with models to solve the problems. The main difference between RANS and LES is the mathematical operator used to recast the original set of equations.

- In RANS, the operator consists in a mean of an ensemble of the flow realisations [55, 47, 56, 57, 58]. Assuming ergodicity of the flow, the operator is replaced by a temporal mean. The unclosed terms represent the physical phenomena over the whole frequency domain.
- In LES, the operator is a local filter of characteristic size Δ , independent of the time, which differentiates large scales (larger than the filter size) to small scales [59, 60, 61, 62, 63, 64, 65]. The unclosed terms are here representative only of the small scales (i.e. high frequencies) phenomena of the flow. Figure 1.1 illustrates the differences between RANS and LES when applied on a Homogeneous Isotropic Turbulent field (HIT).

The separation between scales introduced by the LES filter allows a dynamic representation of the large scales which are of primary importance in complex geometry. According to this, LES predictions of turbulent flows are more accurate than RANS since the large scales or large eddies and acoustic waves are resolved by the filtered Navier-Stokes equations [15]. Hence, LES

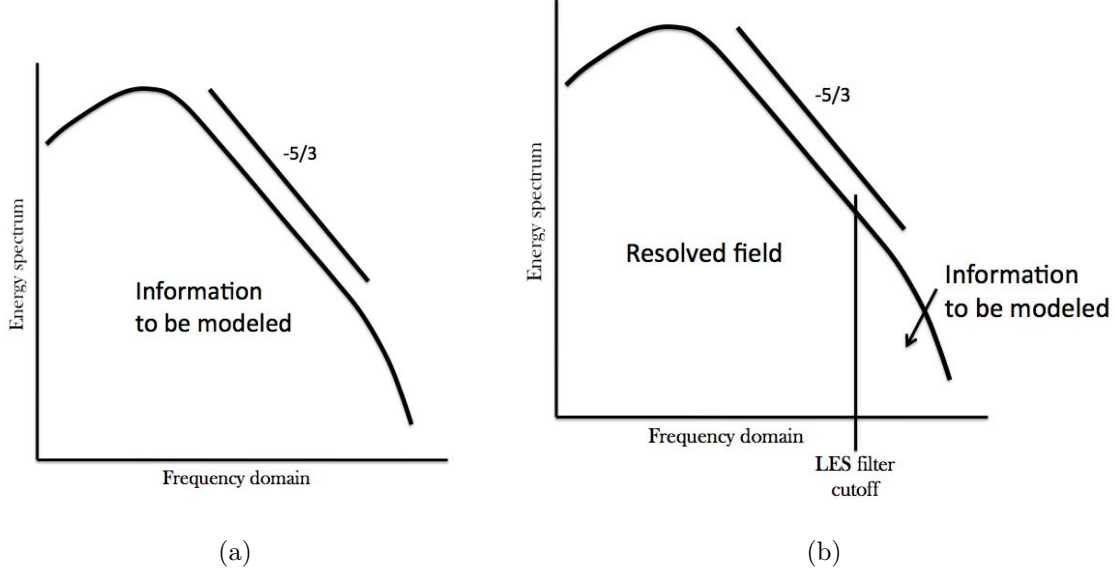


Figure 1.1: Representation of the RANS (a) and LES (b) methods applied to a HIT spectrum.

presents great advantages to compute turbulent flows of industrial applications. However, these possibilities may be reduced by the assumptions introduced in the closure models needed for LES. In the following, the equations resolved in AVBP for reacting LES are described.

1.2.2 LES filtering of the Navier-Stokes equations

The filtered variable \bar{f} is defined as the convolution product of the instantaneous variable f and a filter G_Δ of characteristic size Δ :

$$\bar{f}(x) = \int f(x')G_\Delta(x' - x)dx' \quad (1.29)$$

\bar{f} is the resolved part accessible to the numerical simulations while the Sub-Grid Scales (SGS) $f' = f - \bar{f}$ is modeled¹. For variable density flows, a density, ρ , weighted filtering, or Favre mean [55], is introduced:

$$\bar{\rho}\tilde{f} = \overline{\rho f} \quad (1.30)$$

Applying this filtering to the conservative equations without coupling with the liquid phase written in Section 1.1, we have:

$$\frac{\partial \bar{\rho}}{\partial t} + \frac{\partial}{\partial x_j}(\bar{\rho}\tilde{u}_j) = 0 \quad (1.31)$$

¹In AVBP, there is no explicit filter. Filtering comes from the resolution of the equations on a discretized domain, the implicit filter being the mesh size.

$$\frac{\partial \bar{\rho} \tilde{Y}_k}{\partial t} + \frac{\partial}{\partial x_j} (\bar{\rho} \tilde{u}_j \tilde{Y}_k) = \bar{\omega}_k - \frac{\partial}{\partial x_j} (\overline{J_{j,k}} + \overline{J_{j,k}^t}) \quad (1.32)$$

$$\frac{\partial}{\partial t} \bar{\rho} \tilde{u}_i + \frac{\partial}{\partial x_j} (\bar{\rho} \tilde{u}_i \tilde{u}_j) = -\frac{\partial \bar{p}}{\partial x_j} + \frac{\partial}{\partial x_j} (\overline{\tau_{ij}} + \overline{\tau_{ij}^t}) \quad (1.33)$$

$$\frac{\partial \bar{\rho} \tilde{E}}{\partial t} + \frac{\partial}{\partial x_j} (\bar{\rho} \tilde{E} \tilde{u}_j) = \bar{\omega}_T + \bar{Q} - \frac{\partial}{\partial x_j} (\overline{q_j} + \overline{q_j^t}) - \frac{\partial}{\partial x_j} [\overline{u_i (p \delta_{ij} - \tau_{ij})}] \quad (1.34)$$

where the superscript t indicates the turbulent SGS contributions which are unclosed and needed to ensure proper estimates and evolution of the mean filtered quantities.

1.2.3 Expressions and approximations of the resolved diffusive terms

The filtered diffusive terms are (see [15] for details):

- The laminar viscous tensor $\overline{\tau_{ij}}$ defined as:

$$\overline{\tau_{ij}} = \overline{2\mu(S_{ij} - \frac{1}{3}\delta_{ij}S_{ll})} \approx 2\bar{\mu}(\widetilde{S}_{ij} - \frac{1}{3}\delta_{ij}\widetilde{S}_{ll}) \quad (1.35)$$

with

$$\widetilde{S}_{ij} = \frac{1}{2} \left(\frac{\partial \tilde{u}_j}{\partial x_i} + \frac{\partial \tilde{u}_i}{\partial x_j} \right) \quad (1.36)$$

- The laminar species diffusion flux $\overline{J_{i,k}}$. High order correlations between variables are supposed negligible:

$$\begin{aligned} \overline{J_{i,k}} &= -\overline{\rho \left(D_k \frac{W_k}{W} \frac{\partial X_k}{\partial x_i} - Y_k V_i^c \right)} \\ &\approx -\bar{\rho} \left(\overline{D_k} \frac{W_k}{W} \frac{\partial \widetilde{X}_k}{\partial x_i} - \widetilde{Y}_k \widetilde{V}_i^c \right) \end{aligned} \quad (1.37)$$

with

$$\widetilde{V}_i^c = \sum_{k=1}^N \overline{D_k} \frac{W_k}{W} \frac{\partial \widetilde{X}_k}{\partial x_i} \quad (1.38)$$

$$\overline{D_k} \approx \frac{\bar{\mu}}{\bar{\rho} S c_k} \quad (1.39)$$

- The laminar energy flux \overline{q}_i :

$$\begin{aligned}\overline{q}_i &= -\lambda \frac{\partial \overline{T}}{\partial x_i} + \sum_{k=1}^N \overline{J_{i,k} h_{s,k}} \\ &\approx -\overline{\lambda} \frac{\partial \widetilde{T}}{\partial x_i} + \sum_{k=1}^N \overline{J_{i,k} \widetilde{h_{s,k}}}\end{aligned}\tag{1.40}$$

with

$$\overline{\lambda} = \frac{\overline{\mu} \overline{C_p}(\widetilde{T})}{Pr}\tag{1.41}$$

All of these equations suppose that spatial variations of the species diffusive fluxes are negligible and can be modeled as simple gradients.

1.2.4 Expression and closure of the SGS terms

The filtering process has produced additional unclosed terms called SGS terms. To close the set of Navier-Stokes equations, the SGS terms will be modeled:

- The SGS velocity tensor, or Reynolds tensor $\overline{\tau_{ij}}^t$:

$$\overline{\tau_{ij}}^t = -\overline{\rho}(\widetilde{u_i u_j} - \widetilde{u_i} \widetilde{u_j})\tag{1.42}$$

and is modeled as:

$$\overline{\tau_{ij}}^t = 2\overline{\rho} \nu_t (\widetilde{S_{ij}} - \frac{1}{3} \delta_{ij} \widetilde{S_{ll}})\tag{1.43}$$

where ν_t is the turbulent viscosity.

- The SGS species flux $\overline{J_{i,k}}^t$:

$$\overline{J_{i,k}}^t = \overline{\rho}(\widetilde{u_i \widetilde{Y}_k} - \widetilde{u_i} \widetilde{Y}_k)\tag{1.44}$$

and is modeled as:

$$\overline{J_{i,k}}^t = -\overline{\rho} \left(D_k^t \frac{W_k}{W} \frac{\partial \widetilde{X}_k}{\partial x_i} - \widetilde{Y}_k \widetilde{V}_i^{c,t} \right)\tag{1.45}$$

with:

$$\widetilde{V}_i^{c,t} = \sum_{k=1}^N D_k^t \frac{W_k}{W} \frac{\partial \widetilde{X}_k}{\partial x_i} \quad (1.46)$$

$$D_k^t = \frac{\nu^t}{Sc_k^t} \quad (1.47)$$

The turbulent Schmidt number is fixed in the simulations at $Sc_k^t = 0.6$ for all species.

- The SGS energy flux \overline{q}_i^t :

$$\overline{q}_i^t = \bar{\rho}(\widetilde{u}_i \widetilde{E} - \widetilde{u}_i \widetilde{E}) \quad (1.48)$$

and is modeled as:

$$\overline{q}_i^t = -\lambda_t \frac{\partial \widetilde{T}}{\partial x_i} + \sum_{k=1}^N \overline{J_{i,k}^t} \widetilde{h_{s,k}} \quad (1.49)$$

with

$$\lambda_t = \frac{\bar{\rho} \nu_t \overline{C_p}}{Pr^t} \quad (1.50)$$

To enforce a turbulent Lewis number of one in the simulations performed here, the turbulent Prandtl number is fixed at $Pr^t = 0.6$.

1.2.5 Models for the turbulent viscosity

The filtered Navier-Stokes equations have produced SGS terms describing the interaction between resolved and unresolved scales. The influence of the SGS on the resolved flow is modeled through the gradient assumption coupled to a turbulent viscosity ν_t , Eq. (1.43). This supposes that SGS effects on resolved energetic structures are purely dissipative. This assumption is valid in the theory of the turbulent energy cascade introduced by Kolmogorov [66]. In this section, two models commonly used are presented.

Smagorinsky model

The Smagorinsky model [67] has been developed in the sixties and tested in various configurations:

$$\nu_t = (C_S \Delta)^2 \sqrt{2 \widetilde{S}_{ij} \widetilde{S}_{ij}} \quad (1.51)$$

where Δ is the filter size (linked to the cell volume V_e by: $\Delta = (V_e)^{1/3}$) and C_S the model constant. The C_S value can go from 0.1 to 0.18, depending on the flow [68]. This closure generates the proper kinetic energy dissipation in homogeneous isotropic turbulence (HIT). In real geometry, it is generally too dissipative [69, 70]. However, because of its simplicity it is widely used. The estimation of the turbulent viscosity being based on the tensor S_{ij} , it becomes too high in strong mean gradient zones like shear layers or close to walls, producing potential artificial relaminarization of the flow.

WALE model (Wall Adaptative Local Eddy-viscosity)

This model developed by Nicoud & Ducros [71] adjusts the turbulent viscosity to meet the asymptotic behaviour of ν_t in the turbulent boundary layers. The turbulent viscosity is defined by:

$$\nu_t = (C_w \Delta)^2 \frac{(s_{ij}^d s_{ij}^d)^{3/2}}{(\widetilde{S_{ij} S_{ij}})^{5/2} + (s_{ij}^d s_{ij}^d)^{5/4}} \quad (1.52)$$

$$s_{ij}^d = \frac{1}{2}(\tilde{g}_{ij}^2 + \tilde{g}_{ji}^2) - \frac{1}{3}\tilde{g}_{kk}^2 \delta_{ij} \quad (1.53)$$

where Δ is filter size, $C_w = 0.4929$ is the model constant and \tilde{g}_{ij} is the resolved velocity gradient.

Other models

The two main SGS models have been presented here, but numerous models exist. A model based on the equation of k has been implemented by Moureau [72]. Resolving the transport of the turbulent kinetic energy, the turbulent viscosity can be recovered. The majority of the models evaluating ν_t come from theories based on turbulence in incompressible flows. However, it exists models taking into account the SGS dilation effects [73, 74, 75].

1.3 The thickened flame model for LES

When performing reacting simulations, usually the laminar flame thickness δ_L^0 is smaller than the mesh size h . To allow the use of "large" mesh size (in LES but also DNS) and to resolve the flame front on the available mesh the thickened flame model has been developed. For laminar flows, the thickening is obtained by artificially increasing diffusion while simply decreasing proportionately the reaction rates to guaranty the proper flame speed of the non thickened laminar premixed flame. In turbulent flows, the interaction between turbulence and chemistry may be modified by thickening which expresses itself in a modified Damkohler number [76]. Indeed, the scales smaller than $\mathcal{F}\delta_L^0$ (where \mathcal{F} is the thickening factor) do not act on the flame anymore. Likewise if the thickening procedure is directly extended to LES, flame wrinkling by vortices is further reduced. Since the flame surface is reduced artificially, the net reaction rate is underestimated. To correct this effect, an efficiency function \mathcal{E} , based on DNS results,

has been added by Colin [76]. The evaluation of the efficiency function is not detailed in the present document, the interested reader can report to the original article [76] for more details. The impact of the model on the filtered equations detailed in section 1.2.2 is described in the following.

1.3.1 The standard thickened flame model (TFLES)

The filtered mass equation (1.31) and momentum equation (1.33) are not affected by the thickening. For the species equation (1.32) and energy equation (1.34), the different fluxes and source terms involved are:

- The species diffusion flux $\overline{J_{i,k}}$:

$$\overline{J_{i,k}} = -\mathcal{E}\mathcal{F}\bar{\rho} \left(\overline{D_k} \frac{W_k}{W} \frac{\partial \widetilde{X}_k}{\partial x_i} - \widetilde{Y}_k \widetilde{V}_i^c \right) \quad (1.54)$$

- The energy flux $\overline{q_i}$:

$$\overline{q_i} = -\mathcal{E}\mathcal{F} \left(\bar{\lambda} \frac{\partial \widetilde{T}}{\partial x_i} + \sum_{k=1}^N \bar{\rho} \left(\overline{D_k} \frac{W_k}{W} \frac{\partial \widetilde{X}_k}{\partial x_i} - \widetilde{Y}_k \widetilde{V}_i^c \right) \widetilde{h_{s,k}} \right) \quad (1.55)$$

- The reaction rate $\overline{\dot{\omega}_k}$ of the species k :

$$\overline{\dot{\omega}_k}(\widetilde{Y}_k, \widetilde{T}) \rightarrow \frac{\mathcal{E}\overline{\dot{\omega}_k}(\widetilde{Y}_k, \widetilde{T})}{\mathcal{F}} \quad (1.56)$$

- The heat released by combustion $\overline{\dot{\omega}_T}$:

$$\overline{\dot{\omega}_T}(\widetilde{Y}_k, \widetilde{T}) \rightarrow \frac{\mathcal{E}\overline{\dot{\omega}_T}(\widetilde{Y}_k, \widetilde{T})}{\mathcal{F}} \quad (1.57)$$

1.3.2 The dynamic thickened flame model (DTFLES)

The TFLES model is adequate only for perfectly premixed flames. For partially premixed, it has to be modified for the following reasons:

- In non reactive zones with only mixing, the thermal and molecular diffusions are over-estimated by a factor \mathcal{F} . Furthermore, the SGS contributions of the energy and species fluxes should be taken into account (in the TFLES philosophy, as soon as the thickening is activated, the energy and species fluxes are resolved and hence SGS are removed).
- In the flame, due to thickening, the diffusion and source terms are resolved. Hence, SGS turbulent mixing terms can be removed.

In other words, the TFLES model has to remain unchanged in the flame but has to be adapted outside. The DTFLES model (Dynamic Thickening) has been developed to remove these issues [77]. The thickening factor is not constant anymore and varies from 1 to \mathcal{F}_{max} (from non reactive to reactive zones), following:

$$\mathcal{F} = 1 + (\mathcal{F}_{max} - 1)\mathcal{S} \quad (1.58)$$

where \mathcal{S} is a sensor depending on local temperature and mass fractions and written as:

$$\mathcal{S} = \tanh\left(\beta' \frac{\Omega}{\Omega_0}\right) \quad (1.59)$$

where Ω is a function used to detect the flame front. Ω is built based on parameters of the chemical kinetic scheme:

$$\Omega = Y_F^{\nu'_F} Y_O^{\nu'_O} \exp(-\Gamma_T \frac{E_a}{RT}) \quad (1.60)$$

The constant Γ_T is used to activate the thickening just before the reaction zone and has a typical value of 0.5 . The factor β' has a value of 500 in AVBP. Then, note that \mathcal{S} goes from 0 (non reactive zones) to 1 (in the flame).

Finally, the filtered equations detailed in section 1.2.2 become:

$$\frac{\partial \bar{\rho}}{\partial t} + \frac{\partial}{\partial x_j} (\bar{\rho} \tilde{u}_j) = 0 \quad (1.61)$$

$$\begin{aligned} \frac{\partial \bar{\rho} \tilde{Y}_k}{\partial t} + \frac{\partial}{\partial x_j} (\bar{\rho} \tilde{u}_j \tilde{Y}_k) = & \frac{\partial}{\partial x_j} \left[\bar{\rho} \left([\mathcal{E} \mathcal{F} \overline{D}_k + (1 - \mathcal{S}) D_t] \left[\frac{W_k}{W} \frac{\partial \tilde{X}_k}{\partial x_j} - \tilde{Y}_k \sum_{l=1}^N \frac{W_k}{W} \frac{\partial \tilde{X}_k}{\partial x_j} \right] \right) \right] \\ & + \frac{\mathcal{E} \overline{\dot{\omega}_k}}{\mathcal{F}} \end{aligned} \quad (1.62)$$

$$\frac{\partial}{\partial t} \bar{\rho} \tilde{u}_i + \frac{\partial}{\partial x_j} (\bar{\rho} \tilde{u}_i \tilde{u}_j) = -\frac{\partial \bar{p}}{\partial x_j} + \frac{\partial}{\partial x_j} \left[2(\bar{\mu} + \mu_t) (\tilde{S}_{ij} - 1/3 \tilde{S}_{ll} \delta_{ij}) \right] \quad (1.63)$$

$$\begin{aligned} \frac{\partial \bar{\rho} \tilde{E}}{\partial t} + \frac{\partial}{\partial x_j} (\bar{\rho} \tilde{E} \tilde{u}_j) = & -\frac{\partial}{\partial x_j} \left[u_i \left(\bar{p} \delta_{ij} - 2\bar{\mu} (\tilde{S}_{ij} - 1/3 \tilde{S}_{ll} \delta_{ij}) \right) \right] \\ & + \frac{\partial}{\partial x_j} \left[(\mathcal{E} \mathcal{F} \bar{\lambda} + (1 - \mathcal{S}) \lambda_t) \frac{\partial \tilde{T}}{\partial x_i} \right] \\ & + \frac{\partial}{\partial x_j} \left[\sum_{k=1}^N \bar{\rho} \left([\mathcal{E} \mathcal{F} \overline{D}_k + (1 - \mathcal{S}) D_t] \left[\frac{W_k}{W} \frac{\partial \tilde{X}_k}{\partial x_j} - \tilde{Y}_k \sum_{l=1}^N \frac{W_k}{W} \frac{\partial \tilde{X}_k}{\partial x_j} \right] \right) \tilde{h}_{s,k} \right] \\ & + \frac{\mathcal{E} \overline{\dot{\omega}_T}}{\mathcal{F}} + \overline{\dot{Q}} \end{aligned} \quad (1.64)$$

1.4 Remarks

In this chapter, the equations for the gas phase have been detailed. They include the different closures and models which will be used in the LES of this work (except the coupling source terms with the liquid phase). The source terms that depend on the liquid variables will be described in the next chapter. This will close the problem for two-phase flow reacting LES.

Chapter 2

Description and models for the dispersed phase

2.1 Formalism of the liquid phase: Eulerian versus Lagrangian frameworks

In this section, the modelisation of a dispersed phase issued by a spray for example is described. Dense liquid phenomena like atomisation [24, 25, 26, 27, 28] are out of the scope of this document and only diluted sprays are addressed. To study the spray dynamic, the two main formalisms available to the CFD community are the so-called Lagrangian [29, 30, 31] and Eulerian formalisms [32, 33, 34]. In the Lagrangian approach, the dispersed phase can be considered as a set of small discrete particles following point mechanic equations. In the Eulerian approach, the spray is described as a continuous phase like the gas phase with the properties of the mean local set of particles. In AVBP, the Eulerian solver has been developed from the PhD work of Kaufmann (2004) [35] and the Lagrangian solver from the work of García (2005) [36]. The two formalisms are briefly described with more details for the Eulerian approach.

2.1.1 The Lagrangian approach

The deterministic description of the Euler-Lagrange (EL) approach for spray consists in tracking the Lagrangian trajectory of each droplet, coupled to the conservation law for momentum, mass and energy of the gas phase described in an Eulerian formalism. At each time, for each droplet k , the following system is solved:

$$\frac{dX_{p,i}^{(k)}}{dt} = V_{p,i}^{(k)} \quad (2.1)$$

$$\frac{d}{dt} \left(m_p^{(k)} V_{p,i}^{(k)} \right) = F_{p,i}^{(k)} \quad (2.2)$$

$$\frac{dm_p^{(k)}}{dt} = \dot{m}_p^{(k)} \quad (2.3)$$

$$\frac{d}{dt} \left(m_p^{(k)} C_p^{(k)} T_p^{(k)} \right) = \dot{Q}_p^{(k)} \quad (2.4)$$

where $X_{p,i}^{(k)}$ are the droplet k coordinates, $V_{p,i}^{(k)}$ its velocity components, $m_p^{(k)}$ its mass, $C_p^{(k)}$ its heat capacity at constant pressure, $T_p^{(k)}$ its temperature, $F_{p,i}^{(k)}$ the external forces, $\dot{m}_p^{(k)}$ the evaporation rate and $\dot{Q}_p^{(k)}$ the heat flux exchanges with the gas phase.

The main advantage of the EL method is the intrinsic treatment of polydispersion and trajectory crossings [27, 78, 79]. However, due to the coupling and influence of the gas phase, the turbulence demands an evaluation of the forces acting on the particle and vice versa. This approach is commonly used in DNS solvers [80, 81, 82], which solve the whole range of turbulent scales, and its potential in LES has been underlined [83, 84, 85, 29]. The Lagrangian approach is also used for RANS simulations of industrial configurations, modeling the effect of turbulence on particle dispersion [86, 87, 88, 89]. Note that in AVBP, the Lagrangian approach does not

use any model to reconstruct the SGS effect of the gas phase on the forces and fluxes acting on the droplets.

From a numerical point of view, the localisation of the particles in the Eulerian mesh needs precise algorithms [90, 91, 92]. In parallel computing with domain partitioning, the particle exchanges between processors may be difficult [93]. Once particles are located, interpolations have to be done to exchange the coupling terms from the Eulerian mesh to the particles and vice versa. To avoid too high numerical diffusion during interpolation, high order schemes are required increasing CPU costs [94].

From a hardware point of view, tracking millions of particles at each time step requires huge CPU and memory resources. This problem is usually overcome gathering real, initially close, particles into numerical particles (also called parcels)[95]. Hence, the number of particles to track can be seriously reduced, but an additional modelisation is necessary [96]. Furthermore, to ensure statistical convergence and to avoid strong discontinuities in coupling source terms, a minimum number of parcels is required [97].

An additional difficulty introduced by these approaches is its capacity to perform efficient parallel LES. Performing parallel LES, the domain partitioning is the most efficient method using large number of processors. However, mesh partitioning for the gas solver is not optimised for the Lagrangian solver. Indeed, the particle distribution in the domain may be very different to the Eulerian cell distribution and changes in time. A very large number of Lagrangian trajectories is thus computed potentially on only few processors, which lowers the parallel efficiency. This potential imbalance in workload distribution leads to a decrease of the parallel performance [98]. To keep efficient parallelism on thousand processors, the domain partitioning has to be adapted dynamically during the computation [99, 19].

2.1.2 The Eulerian approach

In this approach, the idea is to represent the dispersed phase properties by Eulerian fields. We do not focus on individual particles anymore. The spray is seen as a continuous phase. Various methods have been developed in the literature like the *fast Eulerian method* [100] and the *two fluids method* [101]. The Eulerian approach of the spray used in this document is based on the works of Février and Simonin [102, 103, 104]. This one is based on a statistical approach of the *two fluids method*, called *mesoscopic EE approach*. The main idea of this description is to discriminate the variables describing a volume of particles from particle characteristics. The statistically averaged Euler-Euler (EE) equations come from the kinetic theory of gases [105]. The main steps of the equation derivation are summarized in the following, for more details please report to [106, 107].

1. A *pdf* of the particles $f_p(\mathbf{c}_p, \xi_p, \mu_p, \mathbf{x}, t | \mathcal{H}_f)$ is conditioned by a flow realisation of the carrying phase \mathcal{H}_f . In the particle realisations space, each particle is identified by its position \mathbf{x} at the time t , its mass μ_p , its velocity \mathbf{c}_p and its temperature ξ_p .

2. The Boltzmann type transport equation describing the evolution of the *pdf* is written.
3. Using the *pdf*, a local statistical mean of the spray properties is defined. The mesoscopic quantities are defined from the spatial mean mass of the particle quantity Ψ :

$$\check{\Psi} = \langle \Psi \rangle_l = \frac{1}{\rho_l \check{\alpha}_l} \int \mu_p \Psi(\mathbf{c}_p, \xi_p, \mu_p) f_p(\mathbf{c}_p, \xi_p, \mu_p, \mathbf{x}, t | \mathcal{H}_f) d\mathbf{c}_p d\xi_p d\mu_p \quad (2.5)$$

The deviation from the mesoscopic mean $\check{\Psi}$ is noted $\Psi'' = \Psi - \check{\Psi}$. Mesoscopic quantities and uncorrelated motion are represented on Fig. 2.1.

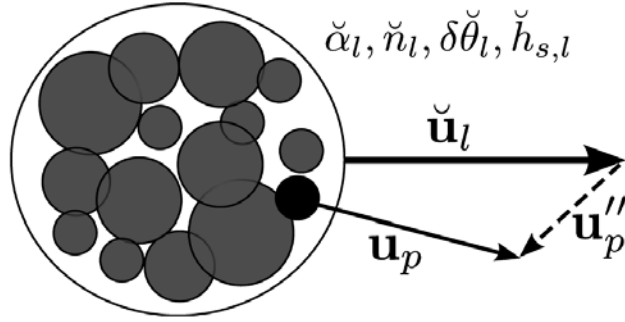


Figure 2.1: Mesoscopic quantities and uncorrelated motion variable.

4. The *pdf* transport equation is multiplied by a spray variable Ψ , then the mean operator defined in Eq. (2.5) is applied and leads to the generalized Enskog equation.
5. Replacing Ψ by appropriate quantities, we defined the mesoscopic conservation equation set. In AVBP, the transported quantities are: \check{n}_l the number of particles per unit volume, $\check{\alpha}_l$ the liquid volume fraction, $\check{\mathbf{u}}_l$ the mesoscopic velocity, $\delta\check{\theta}_l = \langle \frac{1}{2} u_{p,i}'' u_{p,i}'' \rangle_l$ the Random Uncorrelated Energy (RUE) and $\check{h}_{s,l}$ the sensible mesoscopic enthalpy. The second and third order tensors of the uncorrelated motion are defined as:

$$\delta\check{R}_{l,ij} = \langle u_{p,i}'' u_{p,j}'' \rangle_l \quad (2.6)$$

$$\delta\check{S}_{l,ijk} = \langle u_{p,i}'' u_{p,j}'' u_{p,k}'' \rangle_l \quad (2.7)$$

The set of transport equations for the mesoscopic variables is given below, where Γ is the liquid mass exchange to the gas phase due to evaporation, Φ_l is the enthalpy exchange rate to the liquid, \mathbf{F}_d is the drag force generated by the gas phase to the liquid and W_θ is the uncorrelated energy exchange rate due to drag force:

$$\frac{\partial}{\partial t} \check{n}_l + \frac{\partial}{\partial x_j} \check{n}_l \check{u}_{l,j} = - \frac{\partial}{\partial x_j} \check{n}_l \{ \delta \check{u}_{l,j} \}_l \quad (2.8)$$

$$\frac{\partial}{\partial t} \rho_l \check{\alpha}_l + \frac{\partial}{\partial x_j} \rho_l \check{\alpha}_l \check{u}_{l,j} = - \Gamma \quad (2.9)$$

$$\frac{\partial}{\partial t} \rho_l \check{\alpha}_l \check{u}_{l,i} + \frac{\partial}{\partial x_j} \rho_l \check{\alpha}_l \check{u}_{l,i} \check{u}_{l,j} = - \frac{\partial}{\partial x_j} \rho_l \check{\alpha}_l \delta \check{R}_{l,ij} - \Gamma \check{u}_{l,i} + F_{d,i} \quad (2.10)$$

$$\frac{\partial}{\partial t} \rho_l \check{\alpha}_l \delta \check{\theta}_l + \frac{\partial}{\partial x_j} \rho_l \check{\alpha}_l \delta \check{\theta}_l \check{u}_{l,j} = - \frac{\partial}{\partial x_j} \rho_l \check{\alpha}_l \delta \check{S}_{l,ij} - \rho_l \check{\alpha}_l \delta \check{R}_{l,ij} \frac{\partial}{\partial x_j} \check{u}_{l,i} - \Gamma \delta \check{\theta}_l + W_\theta \quad (2.11)$$

$$\underbrace{\frac{\partial}{\partial t} \rho_l \check{\alpha}_l \check{h}_{s,l}}_1 + \underbrace{\frac{\partial}{\partial x_j} \rho_l \check{\alpha}_l \check{h}_{s,l} \check{u}_{l,j}}_2 = \underbrace{\hspace{10em}}_3 \underbrace{\hspace{10em}}_4 \underbrace{-\Gamma \check{h}_{s,l}}_5 \underbrace{\hspace{10em}}_6 + \underbrace{\Phi_l}_7 \quad (2.12)$$

In the above equations, the first terms noted 1 correspond to temporal variations, 2 terms correspond to convection due to mesoscopic motion, 3 convection due to uncorrelated motion (except in Eq. (2.8) where it is an additional convection term due to mesoscopic motion), 4 anisotropic effects of the mesoscopic stress tensor, 5 evaporation source terms, 6 drag source terms and 7 thermal conduction source terms. In this thesis, only monodisperse flows are studied. There is thus only one diameter per cell. Hence the second term ($\frac{\partial}{\partial x_j} \check{n}_l \{ \delta u_{l,j} \}_l$) in Eq. (2.8) is cancelled.

6. Closures of the mesoscopic motion equations are given in the next section in the context of non evaporating flows. Two terms have to be modeled:

- (a) the effect of the unresolved motion or uncorrelated motion which represent the deviation from mesoscopic motion (terms 3 and 4).
- (b) the coupling terms with the gas phase: drag force, mass and heat exchange between the phases (terms 5, 6 and 7).

As the equations obtained with the EE approach are close to those of the gas phase, efficient parallel algorithms used for gas solver can be used for the liquid solver. Furthermore, since the mesh used for the liquid phase is the same as the one of the gas phase, load balance of the processors is identical for both phases. Actually, the two-phase flow solver EE is an extension of the gas solver with an additional set of variables and closure models. Hence, the CPU cost is not linked to the number of particles but to the number of Eulerian equations and the complexity of the closure models. Usually, it takes twice the time of the equivalent purely gaseous computation.

One major drawback of the above retained set of equations comes from the highly compressible properties of the governing equations which with the EE method leads to stability issues of the numerical schemes. The numerical schemes used to compute the liquid phase will be presented in section 3.2. The absence of diffusive terms and pressure like terms produces sharp gradients of the mesoscopic variables. These physical phenomena lead to numerical issues that slow the application of the EE method in an industrial context (see P. Sierra and N. Lamarque [108] PhD thesis for detailed investigations).

Another limitation of this EE method arises with droplet trajectories. Indeed, by definition, for each point of the mesh there is only one mesoscopic velocity, i.e. *mono-cinétique* method as described by De Chaisemartin [109]. Corrections relying on the *DQMOM* method (Direct Quadrature Method of Moments) [110] specifically address such issues and thus are able to predict trajectory crossing with the Eulerian formalism.

2.2 Closure models for the dispersed equations

Here are presented the assumptions made to introduce modeling for the evaporation and drag terms present in EE and EL models. For our application only the EE terms are given although they could be expressed in a purely Lagrangian formalism. The assumptions **H1-H7** are equivalent to those used in the Lagrangian approach to write particle tracking equations. The assumption **H8** allows to simply link the particle density \check{n}_l and diameter d to the liquid volume fraction $\check{\alpha}_l$:

$$\check{\alpha}_l = \check{n}_l \frac{\pi d^3}{6} \quad (2.13)$$

- H1** The particles are spherical non-deformable droplets.
- H2** The density ratio between the liquid and the gas allows to limit the interacting forces to drag.
- H3** The temperature (and so the sensible enthalpy) is uniform inside the droplets.
- H4** Gravity is negligible.
- H5** The dispersed phase is diluted (the liquid volume fraction $\check{\alpha}_l < 0.01$) and the gaseous volume fraction is $1 - \check{\alpha}_l \approx 1$
- H6** Droplet-droplet interactions are negligible.
- H7** The low impact of the diluted liquid phase on the carrying phase allows to condition the statistics on only one realisation of the carrying phase.
- H8** The spray is locally monodisperse.
- H9** Droplets have locally the same temperature (mono-temperature spray).

2.2.1 Drag source terms

1. The term \mathbf{F}_d in Eq. (2.10) is derived from the force \mathbf{F}_p exerted on an individual isolated droplet:

$$F_{d,i} = \rho_l \check{\alpha}_l \left\langle \frac{F_{p,i}}{m_p} \right\rangle_l \quad (2.14)$$

The drag force exerted by the gas on an individual droplet is modeled by a Stokes Law extended by a correlation from Schiller and Naumann valid for particle Reynolds number Re_p lower than 1000 [111]:

$$\mathbf{F}_p = \frac{1}{2} C_D \rho \pi \frac{d^2}{4} |\mathbf{u} - \mathbf{c}_p| (\mathbf{u} - \mathbf{c}_p) \quad (2.15)$$

$$\text{with } C_D = \frac{24}{Re_p} (1 + 0.15 Re_p^{0.687})$$

$$\text{and } Re_p = \frac{\rho |\mathbf{u} - \check{\mathbf{u}}_l|}{\mu} \quad (2.16)$$

Following the averaging of Eq. (2.14), the drag term is expressed as a function of the mesoscopic velocity:

$$\mathbf{F}_d = \frac{\rho_l \check{\alpha}_l}{\tau_p} (\mathbf{u} - \check{\mathbf{u}}_l) \quad (2.17)$$

where τ_p is the relaxation time of the particle expressed as:

$$\frac{1}{\tau_p} = \frac{1 + 0.15 Re_p^{0.687}}{\tau'_p} \quad \text{where } \tau'_p = \frac{\rho_l d^2}{18\mu}$$

2. The drag term W_θ in the uncorrelated energy equation, Eq. (2.11) is written from the drag force exerted on an individual droplet, Eq. (2.15) and reads:

$$W_\theta = \rho_l \check{\alpha}_l \left\langle \mathbf{u}_p'' \cdot \frac{\mathbf{F}_p}{m_p} \right\rangle_l = - \frac{2\rho_l \check{\alpha}_l}{\tau_p} \delta \check{\theta}_l \quad (2.18)$$

Note that drag is thus a destruction term of the uncorrelated energy. It tends to impose to the set of particles the same velocity, close to the gaseous velocity and to minimize velocity deviations.

2.2.2 Evaporation source terms

In this section, variables at the droplet surface (see Fig. 2.2) are noted with the subscript ξ , and those at infinite use the subscript ∞ (in practice, this reports to the next cell or node). The fuel species will use the subscript F .

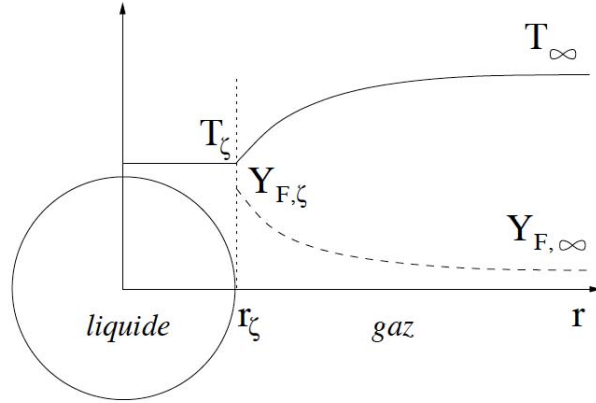


Figure 2.2: Evolution of the fuel mass fraction and of the liquid temperature for an isolated droplet.

1. The evaporation rate Γ .

The mass transfert term Γ from liquid to gas is expressed as the average of the droplet mass variations, Eq. (2.19). This mass variation is determined solving the problem of an evaporating isolated droplet without combustion inside a gaseous flow. Hence,

$$\Gamma = -\rho_l \check{\alpha}_l \left\langle \frac{1}{m_p} \frac{dm_p}{dt} \right\rangle_l = -\check{n}_l \left\{ \frac{dm_p}{dt} \right\}_l \quad (2.19)$$

The evaporation model used assumes thermodynamic equilibrium at the interface and infinite thermal conductivity of the liquid. Hence, using Clausius-Clapeyron Law, the uniform droplet temperature $T_p = T_\xi$ can be linked to the gaseous fuel mass fraction at the interface. For the resolution of an isolated evaporating droplet, readers are pointed to the books of Kuo [56] and Sirignano [101].

The variation of thermodynamic and transport properties of the gas surrounding the isolated droplet is taken into account evaluating these properties at a reference temperature T_{ref} and at a composition $Y_{k,ref}$ defined by the "1/3-2/3" law, Eqs. (2.20) - (2.22). The law assumes that the gas layer surrounding the droplet, and hence its thermodynamic and transport properties, follow a quasi-steady evolution. This assumption has been validated by Hubbard *et al.* [112].

$$T_{ref} = \frac{1}{3}T_\infty + \frac{2}{3}T_\xi \quad (2.20)$$

$$Y_{F,ref} = \frac{1}{3}Y_{F,\infty} + \frac{2}{3}Y_{F,\xi} \quad (2.21)$$

$$Y_{k,ref} = Y_{k,\infty} \frac{1 - Y_{F,ref}}{1 - Y_{F,\infty}} \quad \text{for } k \neq F \quad (2.22)$$

The product $[\rho D_F]$ being constant, it is evaluated at the droplet surface. Its value depends on the model used to compute the transport coefficients. The coefficient $[\rho D_F]$ is written:

$$[\rho D_F] = \frac{\mu(T_{ref})}{Sc_F} \quad (2.23)$$

The difference of fuel mass fraction between the interface and the reference point at the infinity is evaluated by Spalding mass number, B_M :

$$B_M = \frac{Y_{F,\xi} - Y_{F,\infty}}{1 - Y_{F,\xi}} \quad (2.24)$$

$Y_{F,\xi}$ may be expressed as a function of the molar fraction $X_{F,\xi}$ as in Eq.(2.25) where $W_{nF,\xi}$ is the mean molar weight of the mixture of all species except fuel.

$$Y_{F,\xi} = \frac{X_{F,\xi} W_F}{X_{F,\xi} W_F + (1 - X_{F,\xi}) W_{nF,\xi}} \quad (2.25)$$

Assuming that the mixture composition does not change between ξ and ∞ , $W_{nF,\xi}$ only depends on known variables of the far-field namely $Y_{F,\infty}$ and W , the molar weight of the mixture of all species in the gas phase:

$$W_{nF,\xi} = W_{nF,\infty} = \frac{1 - Y_{F,\infty}}{1 - Y_{F,\infty} \frac{W}{W_F}} W \quad (2.26)$$

$X_{F,\infty}$ is given by the Raoult Law for an ideal mixture of perfect gas:

$$X_{F,\infty} = \frac{P_{F,\infty}}{P} \quad (2.27)$$

where $P_{F,\infty}$ is the partial pressure of gaseous fuel at the interface given by the Clausius-Clapeyron Law:

$$P_{F,\infty} = P_{cc} \exp \left(\frac{W_F L_v(T_l^{ref})}{R} \left(\frac{1}{T_{cc}} - \frac{1}{T_\xi} \right) \right) \quad (2.28)$$

The couple (P_{cc}, T_{cc}) corresponds to an arbitrary reference point on the saturation curve, R is the universal gas constant and $L_v(T_l^{ref})$ the latent heat at T_l^{ref} . The latent heat L_v at a given temperature T is defined as:

$$L_v(T) = h_{s,F}(T) - h_{s,l}(T) \quad (2.29)$$

Applying the average operator to Eq. (2.19), we get Eq. (2.30), with B_M given by Eq. (2.24), $[\rho D_F]$ by Eq. (2.23) and the droplet diameter, d , extracted from Eq. (2.13).

$$\Gamma = \pi \check{n}_l d S h [\rho D_F] \ln(1 + B_M) \quad (2.30)$$

2. The Π_g term in the equation of the total energy of the gas phase and the Φ_l term in the equation of the liquid enthalpy.

The heat transfert from the liquid to the gas Π_g is expressed as an average of the enthalpy tranfert of the droplets, Eq. (2.31). The heat transfert resulting from the evaporation of an isolated droplet without combustion inside a gaseous flow has two contributions given in Eq. (2.32): the heat flux by conduction ϕ_g^c and the enthalpy flux due to evaporation ϕ_g^{ev} . The heat transfert term Π_l from gas to liquid is the opposite of the heat transfert from liquid to gas Π_g .

$$\Pi_g = \rho_l \check{\alpha}_l \left\langle \frac{\phi_g^t}{m_p} \right\rangle_l = \check{n}_l \{ \phi_g^t \}_l \quad (2.31)$$

$$\phi_g^t = \phi_g^c + \phi_g^{ev} \quad (2.32)$$

$$\Pi_g = \Phi_g + \Lambda_g \quad \text{with} \quad \Phi_g = \check{n}_l \{ \phi_g^c \}_l \quad \text{and} \quad \Lambda_g = \check{n}_l \{ \phi_g^{ev} \}_l \quad (2.33)$$

$$\Pi_l = -\Pi_g \quad (2.34)$$

A recast of the thermal fluxes at the interface of the evaporating droplet gives:

$$\phi_g^t + \phi_l^t = \phi_g^c + \phi_g^{ev} + \phi_l^c + \phi_l^{ev} = 0 \quad (2.35)$$

highlighting the total heat flux of the droplet ϕ_l^t which has also two contributions: the conductive flux ϕ_g^c and the enthalpy flux due to evaporation ϕ_l^{ev} . These different contributions are presented in Fig. 2.3. The enthalpy fluxes by phase changes of the droplet and surrounding gas are exclusively linked to the mass variation of the droplet:

$$\phi_g^{ev} = -\frac{dm_p}{dt} h_{s,F}(T_\xi) \quad (2.36)$$

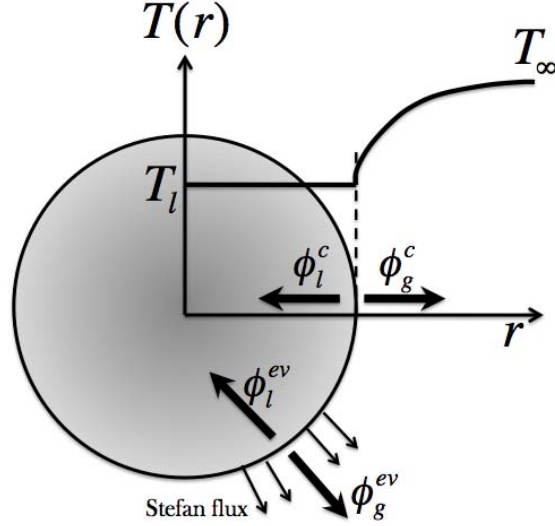


Figure 2.3: Heat fluxes around a droplet

$$\phi_l^{ev} = \frac{dm_p}{dt} h_{s,l}(T_\xi) \quad (2.37)$$

Hence, the sum of the enthalpy fluxes by phase change of an isolated droplet and surrounding gas is simply function of the latent heat L_v at the interface temperature T_ξ and of the mass transfert:

$$\phi_g^{ev} + \phi_l^{ev} = -\frac{dm_p}{dt} L_v(T_\xi) \quad (2.38)$$

Integrating the enthalpy conservation equation from the interface to infinity, we have:

$$\frac{dm_p}{dt} = -\pi d Nu \frac{\lambda}{C_p} \ln(1 + B_T) \quad (2.39)$$

$$B_T = \frac{C_p(T_\infty - T_\xi)}{L_{eff}} \quad \text{with} \quad L_{eff} = L_v(T_\xi) + \frac{\phi_l^c}{-\frac{dm_p}{dt}} \quad (2.40)$$

where B_T is the temperature Spalding number and L_{eff} is the effective latent heat of vaporisation [101]. C_p and λ are evaluated at the reference temperature T_{ref} and with the composition $Y_{k,ref}$ as defined in Eqs. (2.20)-(2.22) and supposed constant between the interface and infinity. As for $[\rho D_F]$, the evaluation of the thermal conductivity λ at the

reference point depends on the models used to compute the transport coefficients. We have:

$$C_p = \sum_{k=1}^N Y_{k,ref} C_{p,k}(T_{ref}) \quad (2.41)$$

$$\lambda = \frac{C_p \mu(T_{ref})}{Pr} \quad (2.42)$$

From the Eqs. (2.19), (2.30) and (2.39), we find a relation between B_M and B_T that reads:

$$B_T = (1 + B_M)^\beta \quad \text{with} \quad \beta = \frac{Sh}{Nu Le_F} \quad (2.43)$$

where Le_F is the Lewis number of the fuel in the mixture considered.

Finally, merging Eqs. (2.35) and (2.38)-(2.40), the conductive flux in the gas phase becomes:

$$\phi_g^c = -\pi d Nu \lambda (T_\infty - T_\xi) \frac{\ln(1 + B_T)}{B_T} \quad (2.44)$$

Through the assumption **H9**, neglecting uncorrelated enthalpy, Φ_g and Λ_g , Eq. (2.33) can be written as:

$$\Phi_g = -\check{n}_l \pi d Nu \lambda (T_\infty - \check{T}_l) \frac{\ln(1 + B_T)}{B_T} \quad (2.45)$$

$$\Lambda_g = \Gamma h_{s,F}(\check{T}_l) \quad (2.46)$$

Writting $\Lambda_l = \check{n}_l \{\phi_l^{ev}\}_l$ the transfert of liquid mesoscopic enthalpy by phase change, and applying the average operator to Eq. (2.38) along with a neglect of uncorrelated enthalpy, we obtain:

$$\Lambda_l = -\Gamma h_{s,l}(\check{T}_l) = -\Gamma C_{p,l}(\check{T}_l - T_l^{ref}) \quad (2.47)$$

Then the mesoscopic conductive flux Φ_l can be defined, as $\Pi_l = \Lambda_l + \Phi_l$. Because of the infinite liquid thermal conductivity assumption, Φ_l should lead to an instantaneous evolution of the liquid temperature \check{T}_l .

$$\Phi_l = -\Pi_g + \Gamma h_{s,l} \quad (2.48)$$

To take into account the increase in evaporation rate of a droplet mist due to potential convection effects, the Nusselt and Sherwood numbers seen in the expressions Eqs. (2.30) to (2.45) rely on the correlations of Frossling (1938).

$$Nu = 2 + 0.552Re_p^{1/2}Pr^{1/3} \quad (2.49)$$

$$Sh = 2 + 0.552Re_p^{1/2}Sc_F^{1/3} \quad (2.50)$$

2.2.3 Closure of the uncorrelated motion

Several modelisations of the uncorrelated motion have been proposed [102, 113, 114]. In AVBP, for the second order tensor $\delta\check{R}_{l,ij}$ a viscosity model is used and for the third order tensor $\delta\check{S}_{l,ijk}$ a diffusivity model [107] is introduced.

Effect of the uncorrelated motion by the mesoscopic motion

The term $-\rho_l\check{\alpha}_l\delta\check{R}_{l,ij}\frac{\partial}{\partial x_j}\check{u}_{l,i}$ in Eq. (2.11) is a production/destruction term of uncorrelated energy by the mesoscopic motion. Assuming local equilibrium and weak anisotropy, the deviatoric part of the second order tensor of the uncorrelated velocities $\delta\check{R}_{l,ij}^* = \delta\check{R}_{l,ij} - \frac{2}{3}\delta\check{\theta}_l\delta_{ij}$ can be closed applying a Boussinesq model leading to a viscous type model [113]:

$$\delta\check{R}_{l,ij}^* = -\nu_{RUM} \left(\frac{\partial\check{u}_{l,i}}{\partial x_j} + \frac{\partial\check{u}_{l,j}}{\partial x_i} - \frac{2}{3}\frac{\partial\check{u}_{l,k}}{\partial x_k}\delta_{ij} \right) \quad \text{with :} \quad \nu_{RUM} = \frac{1}{3}\tau_p\delta\check{\theta}_l \quad (2.51)$$

This source term is then only function of the mesoscopic velocity gradients and of the uncorrelated energy:

$$-\rho_l\check{\alpha}_l\delta\check{R}_{l,ij}\frac{\partial}{\partial x_j}\check{u}_{l,i} = -\rho_l\check{\alpha}_l\delta\check{R}_{l,ij}^*\frac{\partial\check{u}_{l,i}}{\partial x_j} - \frac{2}{3}\rho_l\check{\alpha}_l\delta\check{\theta}_l\frac{\partial\check{u}_{l,j}}{\partial x_j} \quad (2.52)$$

Effect of uncorrelated energy by the uncorrelated motion

The term $-\frac{\partial}{\partial x_j}\rho_l\check{\alpha}_l\delta\check{S}_{l,ijk}$ in Eq. (2.11) corresponds to the convection of the uncorrelated energy by the uncorrelated motion. This flux is expressed as a third order tensor of the uncorrelated velocities $\delta\check{S}_{l,ijk}$. As the Fourier Law for the temperature, a diffusive model is applied [114] :

$$\delta\check{S}_{l,ijk} = -\kappa_{RUM} \quad \text{with :} \quad \kappa_{RUM} = \frac{10}{27}\tau_p\delta\check{\theta}_l \quad (2.53)$$

To tackle the difficulty to represent more precisely these uncorrelated variables, complex closures have been studied by Masi [115] and Sierra in her PhD (2012).

2.3 LES equations and closure for the dispersed phase

The equations and closures developed in the previous section are for the DNS formalism. Hence, as for the carrying phase (Chapter 1), the equations of the dispersed phase will be filtered in the following for the LES formalism.

2.3.1 Filtering the conservative equations

The LES filtering of the dispersed phase is similar to the one of the gas phase. The mean Favre of a mesoscopic function \check{f}_l of the dispersed phase is similar to the one of a function f for the gas phase and is obtained replacing the density ρ by the liquid volume fraction $\check{\alpha}_l$:

$$\bar{\alpha}_l \widehat{f}_l = \overline{\check{\alpha}_l \check{f}_l} \quad (2.54)$$

where $\bar{\alpha}_l$ is the filtered liquid volume fraction. To simplify the notations, the $\check{\cdot}$ is omitted since the LES filtering is only applied on mesoscopic variables of the dispersed phase.

In order to have equivalence between the filtered Favre mean based on the volume fraction and the density, we assume that the flow is monodisperse at the filter scale. It means that SGS variance of the diameter is neglected : $\bar{d} \approx d$. Thus we have:

$$\overline{\check{n}_l \check{f}_l} = \frac{6\bar{\alpha}_l}{\pi d^3} \overline{\check{f}_l} = \frac{6}{\pi d^3} \bar{\alpha}_l \widehat{f}_l = \bar{n}_l \widehat{f}_l \quad (2.55)$$

where \bar{n}_l is the filtered droplet density.

Applying this procedure to the Eulerian conservative equations for the dispersed phase, we obtain the LES conservative equations for the spray:

$$\frac{\partial \bar{\mathbf{w}}_l}{\partial t} + \nabla \cdot \bar{\mathbf{F}}_l = \bar{\mathbf{S}}_l \quad (2.56)$$

where $\bar{\mathbf{w}}_l = (\bar{n}_l, \rho_l \bar{\alpha}_l, \rho_l \bar{\alpha}_l \hat{u}_l, \rho_l \bar{\alpha}_l \hat{v}_l, \rho_l \bar{\alpha}_l \hat{w}_l, \rho_l \bar{\alpha}_l \hat{\delta}\theta_l, \rho_l \bar{\alpha}_l \hat{h}_{s,l})^T$ is the vector of the mesoscopic conservative variables of the liquid phase. $\bar{\mathbf{S}}_l$ is the filtered source term and $\bar{\mathbf{F}}_l$ is the filtered fluxes tensor.

2.3.2 Filtering of the non-linear terms

For the filtered second order $\widehat{\delta R}_l$ and third order $\widehat{\delta S}_l$ tensors of the uncorrelated motion, the decomposition and closure presented in section 2.2.3 are used:

$$\widehat{\delta R}_{l,ij} = \widehat{\delta R}_{l,ij}^* + \frac{2}{3} \widehat{\delta\theta}_l \delta_{ij} \quad (2.57)$$

$$\widehat{\delta R}_{l,ij}^* = -\hat{v}_{RUM} \widehat{S}_{l,ij}^* \quad (2.58)$$

$$\widehat{\delta S}_{l,ij} = -\hat{\kappa}_{RUM} \frac{\partial \widehat{\delta \theta}_l}{\partial x_j} \quad (2.59)$$

where $\widehat{S}_{l,ij}^*$ is the deviatoric part of the resolved stress tensor of the dispersed phase:

$$\widehat{S}_{l,ij}^* = \frac{\partial \hat{u}_{l,i}}{\partial x_j} + \frac{\partial \hat{u}_{l,j}}{\partial x_i} - \frac{2}{3} \frac{\partial \hat{u}_{l,k}}{\partial x_k} \delta_{ij} \quad (2.60)$$

$$\hat{\nu}_{RUM} = \frac{1}{3} \bar{\tau}_p \widehat{\delta \theta}_l \quad (2.61)$$

$$\hat{\kappa}_{RUM} = \frac{10}{27} \bar{\tau}_p \widehat{\delta \theta}_l \quad (2.62)$$

and where the filtered relaxation time $\bar{\tau}_p$ is obtained with the approximation:

$$\frac{1}{\bar{\tau}_p} \approx (1 + 0.15 \overline{Re_p}^{0.687}) \frac{18 \bar{\mu}}{\rho_l d^2} \quad (2.63)$$

$$\text{with: } \overline{Re_p} \approx \frac{\bar{\rho} |\tilde{\mathbf{u}} - \hat{\mathbf{u}}| d}{\bar{\mu}} \quad (2.64)$$

2.3.3 SGS fluxes

The SGS stress tensor for the dispersed phase $\bar{\tau}_{l,ij}^t$

Moreau [116] has shown that the modelisation of the SGS mesoscopic motion of the dispersed phase has to take into account the compressibility effects when modeling both the deviatoric and diagonal part of the tensor. Different SGS models have been studied in [117]. The model implemented in AVBP [107] is a Smagorinsky model for the deviatoric part and a Yoshizawa model [118] for the diagonal part linked to the compressibility effects.

$$\bar{\tau}_{l,ij}^t = -\rho_l \bar{\alpha}_l (\widehat{u_{l,i} u_{l,j}} - \widehat{u_{l,i}} \widehat{u_{l,j}}) \quad (2.65)$$

$$\text{model: } \bar{\tau}_{l,ij}^t = \rho_l \bar{\alpha}_l \nu_{l,t}^d \widehat{S}_{l,ij}^* - \frac{2}{3} \rho_l \bar{\alpha}_l \nu_{l,t}^s \left| \widehat{S}_l^* \right| \delta_{ij} \quad (2.66)$$

This modelisation introduces two SGS viscosities, $\nu_{l,t}^d$ and $\nu_{l,t}^s$:

$$\nu_{l,t}^d = C'_S{}^2 \Delta^2 \left| \widehat{S}_l^* \right| \quad \text{with: } C'_S = 0.12 \quad (2.67)$$

$$\nu_{l,t}^s = C'_Y{}^2 \Delta^2 \left| \widehat{S}_l^* \right| \quad \text{with: } C'_Y = 0.025 \quad (2.68)$$

SGS uncorrelated energy diffusion flux $\bar{q}_{\theta,i}^t$

Similarly to the modelisation of the SGS thermal flux, a turbulent Prandtl number for the dispersed phase Pr_l^t is introduced :

$$\bar{q}_{\theta,i}^t = \rho_l \bar{\alpha}_l (\widehat{u_{l,i} \delta \theta_l} - \widehat{u_{l,i}} \widehat{\delta \theta_l}) \quad (2.69)$$

$$\text{model: } \bar{q}_{\theta,i}^t = 2 \rho_l \bar{\alpha}_l \frac{\nu_{l,t}^d}{Pr_l^t} \frac{\partial \widehat{\delta \theta_l}}{\partial x_i} \quad (2.70)$$

All the simulations presented in this document are performed with $Pr_l^t = 0.7$.

SGS sensible liquid enthalpy diffusion flux $\bar{q}_{h,i}^t$

The effects of this flux are supposed negligible. Hence:

$$\bar{q}_{h,i}^t = \rho_l \bar{\alpha}_l (\widehat{u_{l,i} h_{s,l}} - \widehat{u_{l,i}} \widehat{h_{s,l}}) \approx 0 \quad (2.71)$$

2.3.4 Resolved uncorrelated energy source term

The filtered uncorrelated energy production by the uncorrelated velocity tensor is written:

$$-\overline{\rho_l \check{\alpha}_l \delta \check{R}_{l,ij} \frac{\partial}{\partial x_j} \check{u}_{l,i}} = -\rho_l \bar{\alpha}_l \delta \widehat{R}_{l,ij} \frac{\partial \hat{u}_{l,i}}{\partial x_j} - \underbrace{\left[\rho_l \check{\alpha}_l \delta \check{R}_{l,ij} \frac{\partial \check{u}_{l,i}}{\partial x_j} - \rho_l \bar{\alpha}_l \delta \widehat{R}_{l,ij} \frac{\partial \hat{u}_{l,i}}{\partial x_j} \right]}_{\bar{\mathbb{U}}_\theta^t} \quad (2.72)$$

The term $\bar{\mathbb{U}}_\theta^t$ still has to be closed. It is a production term by the SGS motion. It acts like a dissipation in the SGS uncorrelated energy equation. From an equilibrium assumption of the SGS uncorrelated energy [107], $\bar{\mathbb{U}}_\theta^t$ is modeled as:

$$\bar{\mathbb{U}}_\theta^t = \bar{\tau}_{l,ij}^t \frac{\partial \hat{u}_{l,i}}{\partial x_j} \quad (2.73)$$

2.3.5 Resolved coupling source terms

Filtering of the drag source terms

1. The variation rate of the momentum due to drag force $\bar{\mathbf{F}}_d$ is evaluated from filtered quantities:

$$\bar{F}_{d,i} = \frac{\overline{\rho_l \bar{\alpha}_l}}{\tau_p} (u_i - \check{u}_{l,i}) \quad (2.74)$$

$$\overline{F}_{d,i} \approx \frac{\rho_l \overline{\alpha}_l}{\tau_p} (\tilde{u}_i - \hat{u}_{l,i}) \quad (2.75)$$

2. The variation rate of the uncorrelated energy due to drag force \overline{W}_θ :

$$\overline{W}_\theta = - \overline{\left(\frac{2\rho_l \overline{\alpha}_l}{\tau_p} \delta\check{\theta}_l \right)} \quad (2.76)$$

$$\overline{W}_\theta \approx - \frac{2\rho_l \overline{\alpha}_l}{\tau_p} \widehat{\delta\theta}_l \quad (2.77)$$

Filtering of the evaporation source terms

1. The evaporation rate $\overline{\Gamma}$:

The filtered evaporation rate is built from the resolved variables.

$$\overline{\Gamma} = \overline{\pi \check{n}_l d Sh [\rho D_F] \ln(1 + B_M)} \quad (2.78)$$

$$\overline{\Gamma} \approx \pi \overline{n}_l d \overline{Sh} \frac{\overline{\mu}}{Sc_F} \ln(1 + \overline{B}_M) \quad (2.79)$$

$$\text{with } \overline{Sh} \approx 2 + 0.55 \overline{Re}_p^{1/2} Sc_F^{1/3} \quad (2.80)$$

$$\overline{B}_M \approx \frac{Y_{F,\xi}(\widehat{T}_l) - \tilde{Y}_F}{1 - Y_{F,\xi}(\widehat{T}_l)} \quad (2.81)$$

The validation of the approximation of Eq. (2.79) has been checked by Boileau [106] on a particle laden HIT.

2. The filtered variation rates of the momentum, uncorrelated energy and enthalpy by evaporation are evaluated by:

$$\overline{\Gamma \check{u}_{l,i}} \approx \overline{\Gamma} \widehat{u}_{l,i} \quad (2.82)$$

$$\overline{\Gamma \delta\check{\theta}_l} \approx \overline{\Gamma} \widehat{\delta\theta}_l \quad (2.83)$$

$$\overline{\Gamma \check{h}_{s,l}} \approx \overline{\Gamma} \widehat{h}_{s,l} \quad (2.84)$$

3. The filtered conductive flux of enthalpy Φ_l is built from Eq. (2.48), resolved variables and the filtered evaporation rate from Eq. (2.79) :

$$\bar{\Phi}_l = -\bar{\Pi}_g + \overline{\Gamma h_{s,l}(\tilde{T}_l)} \approx -\bar{\Pi}_g + \bar{\Gamma} \widehat{h}_{s,l} \quad (2.85)$$

In the same way, the filtered heat transfert from liquid to gas $\bar{\Pi}_g$ is estimated by:

$$\begin{aligned} \bar{\Pi}_g &= \bar{\Lambda}_g + \bar{\Phi}_g \\ &= \overline{\Gamma h_{s,l}(\tilde{T}_l)} - \overline{\check{n}_l \pi d N u \lambda (T_\infty - \tilde{T}_l)} \frac{\ln(1 + B_T)}{B_T} \\ &\approx \bar{\Gamma} \widehat{h}_{s,l}(\widehat{T}_l) - \bar{n}_l \pi d \overline{N u \lambda} (\tilde{T}_\infty - \widehat{T}_l) \frac{\ln(1 + \bar{B}_T)}{\bar{B}_T} \end{aligned} \quad (2.86)$$

Finally, we have:

$$\bar{\Phi}_l \approx -\bar{\Gamma} L_v(\widehat{T}_l) + \bar{n}_l \pi d \overline{N u \lambda} (\tilde{T}_\infty - \widehat{T}_l) \frac{\ln(1 + \bar{B}_T)}{\bar{B}_T} \quad (2.87)$$

$$\text{with: } \overline{N u} \approx 2 + 0.55 \overline{Re}_p^{1/2} Pr^{1/3} \quad (2.88)$$

$$\bar{B}_T \approx (1 + \bar{B}_M)^\beta \quad \text{with: } \beta = \frac{\overline{Sh}}{\overline{Nu Le}_F} \quad (2.89)$$

2.3.6 The LES equations for the dispersed phase

Gathering all the filtered variables, the equations of section 2.1.2 become:

$$\frac{\partial}{\partial t} \bar{n}_l + \frac{\partial}{\partial x_j} \bar{n}_l \widehat{u}_{l,j} = 0 \quad (2.90)$$

$$\frac{\partial}{\partial t} \rho_l \bar{\alpha}_l + \frac{\partial}{\partial x_j} \rho_l \bar{\alpha}_l \widehat{u}_{l,j} = -\bar{\Gamma} \quad (2.91)$$

$$\begin{aligned} \frac{\partial}{\partial t} \rho_l \bar{\alpha}_l \widehat{u}_{l,i} + \frac{\partial}{\partial x_j} \rho_l \bar{\alpha}_l \widehat{u}_{l,i} \widehat{u}_{l,j} &= -\frac{\partial}{\partial x_j} \rho_l \bar{\alpha}_l \widehat{\delta R}_{l,ij} + \frac{\partial}{\partial x_j} \bar{\tau}_{l,ij}^t \\ &\quad - \bar{\Gamma} \widehat{u}_{l,i} + \bar{F}_{d,i} \end{aligned} \quad (2.92)$$

$$\begin{aligned}
\frac{\partial}{\partial t} \rho_l \bar{\alpha}_l \widehat{\delta\theta}_l + \frac{\partial}{\partial x_j} \rho_l \bar{\alpha}_l \widehat{\delta\theta}_l \widehat{u}_{l,j} &= - \frac{\partial}{\partial x_j} \rho_l \bar{\alpha}_l \widehat{\delta S}_{l,ij} - \frac{\partial}{\partial x_j} \bar{q}_{\theta,j}^t \\
&\quad - \rho_l \bar{\alpha}_l \widehat{\delta R}_{l,ij} \frac{\partial \widehat{u}_{l,i}}{\partial x_j} - \bar{\tau}_{l,ij}^t \frac{\partial \widehat{u}_{l,i}}{\partial x_j} \\
&\quad - \bar{\Gamma} \widehat{\delta\theta}_l + \bar{W}_\theta
\end{aligned} \tag{2.93}$$

$$\frac{\partial}{\partial t} \rho_l \bar{\alpha}_l \widehat{h}_{s,l} + \frac{\partial}{\partial x_j} \rho_l \bar{\alpha}_l \widehat{h}_{s,l} \widehat{u}_{l,j} = - \frac{\partial}{\partial x_j} \bar{q}_{h,j}^t - \bar{\Gamma} \widehat{h}_{s,l} + \bar{\Phi}_l \tag{2.94}$$

2.3.7 Closure of the coupling source terms in the gas equations

Applying the spatial filter Δ to the coupling terms of Eqs. (1.1)-(1.4), and using the approximations used for the dispersed phase, we have:

$$\left(\begin{array}{c} \bar{\Gamma} \\ \bar{\Gamma} \delta_{k,F} \\ \bar{\Gamma} \widehat{u}_{l,i} - \bar{F}_{d,i} \\ \bar{\Pi}_g + \bar{\Gamma} \frac{1}{2} \overline{\check{u}_{l,i}^2} - \overline{\check{u}_{l,i} F_{d,i}} \end{array} \right) \tag{2.95}$$

The term $\overline{\check{u}_{l,i}^2}$ is function of the SGS tensor. The SGS kinetic energy transfert term is neglected.

$$\overline{\check{u}_{l,i}^2} = \frac{-\bar{\tau}_{l,ii}^t}{\rho_l \bar{\alpha}_l} + \widehat{u}_{l,i}^2 \approx \widehat{u}_{l,i}^2 \tag{2.96}$$

The term $\overline{\check{u}_{l,i} F_{d,i}}$ is computed as the product between the resolved mesoscopic velocity and the resolved drag force, hence once closed the coupling source terms of the gas equations are:

$$\left(\begin{array}{c} \bar{\Gamma} \\ \bar{\Gamma} \delta_{k,F} \\ \bar{\Gamma} \widehat{u}_{l,i} - \bar{F}_{d,i} \\ \bar{\Pi}_g + \bar{\Gamma} \frac{1}{2} \widehat{u}_{l,i}^2 - \widehat{u}_{l,i} \bar{F}_{d,i} \end{array} \right) \tag{2.97}$$

2.4 Additional remarks

In this chapter, models and closures of the filtered equations for the liquid phase have been presented. The closures and models are still under developments (cf. work of P. Sierra and E. Masi). For AVBP, most of the efforts are focused on the evaporation rate Γ and on the closure of the second order tensor of the uncorrelated velocities $\delta \widehat{R}_{l,ij}$, Eq. (2.72). There are widely detailed in the thesis of P. Sierra (2012).

It is also important to note that there is no direct combustion of liquid fuel possible (like pyrolysis [119]). The liquid fuel first evaporates and then burns in the gas phase. In addition,

there is no modification of the liquid equations due to the thickening flame model. Hence, in the case of large droplets able to reach the reaction zone, i.e. the thickened zone, the evaporation rate may not be adequate with the reaction rate adjusted by the efficiency function. Kaufmann in [35] has performed some tests, applying the thickening factor to evaporation (through the thermal conductivity). However, it is not obvious that the link between wrinkling and evaporation rate is the same as between wrinkling and reaction rate. To conclude, the solution is theoretically consistent only for homogeneous combustion regime.

Hence, in the following simulations, the droplet combustion regimes [8] are not directly addressed and the aim is primarily to provide an indirect status on the modeling strategy in the context of turbulent two phase flows. This is obtained by comparing LES results with experimental data.

Part II

LES of two-phase reacting flow

Chapter 3

LES of stationary two-phase reacting flow of the MERCATO bench

Large-Eddy Simulation (LES) is becoming a standard tool for gaseous reacting flows [11, 12, 13, 14, 15]. The application of LES to non-reacting two-phase flows [16, 17, 18] or to reacting two-phase flows [19, 20, 21, 22, 23] is at an earlier stage because of the multiple challenges associated with the description of fuel spray atomization, of interaction of droplets with flames or walls and the difficulty to compare with experimental results to validate CFD simulations. Recent measurement campaigns on the MERCATO bench from ONERA (see Tab. 3.1) provide data sets for both non-reacting and reacting two-phase flows which can be compared to LES. On this bench, LES of the non-reacting two-phase flows were previously performed and validated against measurement [120]. Comparison between a monodisperse Eulerian model as well as monodisperse and polydisperse Lagrangian models have been applied to the dispersed phase and gave similar results for the mean flow [121]. In this document, and apart from the previous studies of reacting two-phase flows [19, 20, 21], the operating point studied has been defined to specifically address the transient phenomenon of ignition. However, prior to study ignition, the different assumptions made through the models used have to be assessed. In this chapter, to evaluate precisely the accuracy and limitations of these models, LES are performed in a statistically stationary context.

First, the LES non-reacting predictions are validated against measurements to illustrate and assess the effect of the numerical setup in two-phase flow. Second, the reacting LES is compared to the measurements and then, a more precise study of the characteristics of the swirler two-phase flow flame is performed and underlines the large variety of combustion regimes present in this simulation.

3.1 Presentation of the MERCATO bench and available data

The MERCATO bench presented in this section has been previously studied in several PhD theses, both experimental (García-Rosa, 2008 and Linassier, 2011) and numerical (Lamarque, 2007; Sanjosé, 2009 and Sénoner, 2009) and has been involved in several project like TIMECOP-AE ¹ (part of the 7th European Commission project) or CALAS ² (consortium project associated with the Aquitaine region, France). This bench aims at studying reacting two-phase flows for both stationary and transient combustion. A picture of the MERCATO bench, located at ONERA Fauga-Mauzac, is presented in Fig. 3.1. A lot of data has been produced by R. Lecourt and PhD students over the past years and are available to the community [7, 120, 122].

Even if the chamber geometry is quite simple (simple rectangular box with optical accesses), the injection system corresponds to a modified pilot injector of the Makila DLN, designed by Turbomeca. At the end of the injector a Delavan atomizer for the liquid kerosene issues a hollow cone spray. The injection system is composed of a radial swirler with twelve vanes ending on a straight cylindrical diffuser 3 cm large connected to the combustion chamber. The combustion chamber has a cross section of 13 × 13 cm² and is 50 cm in length. The flow inside this chamber is representative of typical aeronautical chambers. Injected through the

¹Towards Innovative Methods for Combustion Prediction in Aero-Engines

²Conditions d'Allumage de chambres aéronautique par LASER

inlet channel in the plenum, the main air stream enters tangentially the vanes of the swirler and takes high orthoradial velocity according to the axis of the chamber. The outgoing injector air goes through a diffuser of 10 *mm* long and 30 *mm* in diameter. The sudden change of section at the chamber entrance, Fig. 3.2, generates Corner Recirculation Zones (CRZ). The swirled air flow tends to expand radially but is limited by these CRZ, leading to a cone shape flow. Due to the swirl motion, a central toroidal recirculation zone (CTRZ) appears along the chamber axis. This kind of flow is very useful in aeronautical chamber since when burning, the hot gases recirculate close to the injection of both air and fuel. This helps to have a compact stable flame over a wide range of operating points.

Table 3.1: MERCATO operating points

Test case	WR	\dot{m}_{air} (g/s)	$\dot{m}_{kerosene}$ (g/s)	P_{air} (bar)	T_{air} (K)	U_{bulk} (m/s)
1	0.6	35.5	2.26	1	293	46.9
2	0.142	6.6	0.9	1	463	14
3	0.284	13.15	1.2	1	463	27.85
4	0.426	19.8	2	1	463	41.85
5	0.6	19.8	undefined	1	233	41.85

Table 3.2: Comments about MERCATO operating points

Test case	comments
1	Reference case for burning mesurements, studied in this thesis.
2	Equivalent to WR=0.2 in high altitude conditions
3	Equivalent to WR=0.4 in high altitude conditions
4	Equivalent to WR=0.6 in high altitude conditions
5	High altitude conditions

The operating points tested experimentally at ONERA in the context of the ignition study are summarized in Tab. 3.1 and 3.2. Test cases 2, 3 and 4 have been previously simulated by Sanjosé [123] and Sénoner [121] in their PhD. In this thesis, we focus only on the operating point 1. Based on mass flow and temperature at atmospheric pressure, it is supposed equivalent to high altitude cold condition as evidenced by its reduced mass flow rates, Tables 3.1-3.2, W_R defined by:

$$W_R = \frac{\dot{m}_{air} \sqrt{T_g}}{P} \quad \text{in } kg/\sqrt{K}/s/bar \quad (3.1)$$

where \dot{m}_{air} is the air mass flow, T_g the gas temperature and P the pressure going through the burner.

3.2 Numerical strategies

Because of the highly compressible characteristic of the Eulerian equations of the dispersed phase (see Part 1), the simulations EE may experience very strong local gradients of the liquid mass field. The difficulty to both meet accuracy requirements and robustness for the dispersed phase leads to various numerical strategies. This section presents briefly the strategies used for the simulations performed with the LES solver AVBP. For more details about numerical methods implemented in AVBP, readers can report to the theses of N. Lamarque [108] and A. Roux [124].

Several convection schemes are implemented in AVBP for the two phase flow equations. The computations presented in this thesis try to evaluate two of these:

- Centered scheme (TTGC) and artificial viscosity
- Uncentered scheme (PSI)

These two schemes correspond to two different strategies: either use a high order scheme with artificial viscosity or use a more diffusive scheme.

The TTGC scheme is a finite-element centered scheme, it has a third order precision in space and time [125]. The temporal integration is done in two steps by a prediction-correction method. This scheme has been developed for AVBP and has good precision on unstructured meshes, for any type of element (tetraedra, hexaedra, pyramides, prisma...) and for a reasonable CPU cost compared to other schemes with the same precision [125]. To evaluate upwind schemes on the resolution of the dispersed phase, the PSI scheme [108, 124] has been used. This scheme is used with the Lax-Wendroff (LW) scheme for the gas phase. Both of these schemes make the temporal integration in one step. The LW scheme is a second order (in space and time) centered scheme, while PSI scheme is a first order (in space and time) upwind scheme.

The convection scheme TTGC has very low dissipation, however it generates high frequency oscillations (wiggles) in high gradient zones. For the transport of gaseous variables, the diffusive operator may not be sufficient to suppress them completely. For the transport of the liquid phase, there is no diffusion term³. The use of artificial viscosity allows to dissipate the wiggles generated by the dispersive behaviour of the centered schemes. According to the idea of Jameson *et al.* [126], a linear combinaison of viscosity (second order) and hyperviscosity (fourth order) is added to the residuals to help solving the gradients through smoothing. The key point is then to determine a sensor to apply this viscosity, i.e. a function going from 0 to 1, which is able to recognize numerical oscillations efficiently and stay local to avoid precision degradation of the numerical scheme in the whole domain. In this thesis, for all simulations, the CMS (CMS-lite when solving *RUM*) sensor of artificial viscosity is used for the liquid phase (see the thesis of Sanjose for more details [123]). This artificial viscosity sensor is specifically constructed to help solving EE numerical problems since particularly difficult to handle.

³Except for SGS closures and uncorrelated motion closure in the momentum equation.

The PSI scheme has been implemented in AVBP by Lamarque [108] and Roux [124]. It is a backward residual distributed scheme. It means that the residuals are distributed, function of the flow direction, on the nodes downstream of the cells, so dispersion phenomena are limited. Furthermore, PSI has positivity and linear preservation properties of the solution. The PSI scheme presents excellent robustness. Unfortunately, it introduces large levels of dissipation in the flow direction, limiting its precision to first order both in space and time [108]. To summarize, the two sets of numerical schemes which will be evaluated are (gas phase / liquid phase):

1. TTGC / TTGC ; for the high order scheme + artificial viscosity strategy.
2. LW / PSI ; for the lower order, more robust strategy.

This confrontation is a first step to identify which couple of numerical schemes is more adapted to perform ignition simulation of two-phase flows. However, a demonstration of the capacities of the two strategies through the whole range of potential LES is out of the scope of this work. Note that to perform LES, many alternative families of numerical schemes exist presenting high potential. Among these are the FCT schemes (Flux Corrected Transport) [127, 128] or VMM schemes (Variational Multiscale Method) [129, 130, 131]. Even being promising, they still need more assessments on complex geometries.

3.3 Numerical parameters

3.3.1 Geometry

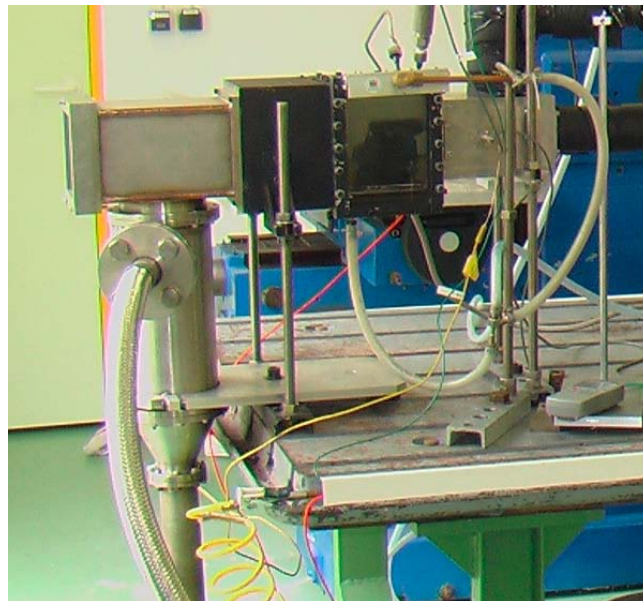


Figure 3.1: The experimental MERCATO bench at ONERA (picture from ONERA)

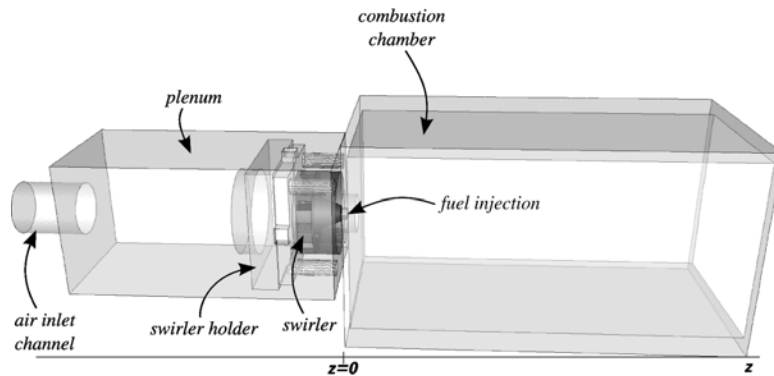


Figure 3.2: Description of the different elements of the MERCATO configuration

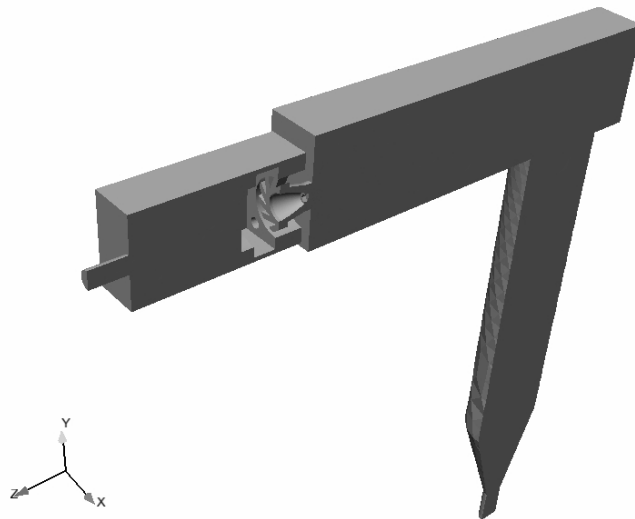


Figure 3.3: The LES domain of the MERCATO bench (half cut)

For this case, the computational domain includes all the geometric elements that may influence the aerodynamics and acoustics of the chamber. The flow exit which goes through an exhaust pipe, which is added after the combustion chamber (Fig. 3.1 and 3.3). Inside the exhaust pipe is a coflow which allows to work under low pressure conditions, using the Venturi effect. In the present case, the bench is operated at ambient conditions and for both the experiments and LES, the coflow within the exhaust pipe is not activated. Note however that the flow deviation experienced between the chamber and the exhaust pipe helps to close the recirculation zone, and hence, avoids recirculation issues at the outlet boundary condition.

3.3.2 Mesh

The mesh is fully tetradric, allowing an easier resolution of the actual geometry and easier mesh refinement/coarsening. The mesh, Fig. 3.4, is very fine close to the liquid injector with a

typical cell size of 0.3 mm (a zoom of the mesh around the swirler is displayed on Fig. 3.4 b)) yielding about 26 cells to discretize the hollow cone of the liquid spray (especially the liquid volume fraction α_l , Fig. 3.5).

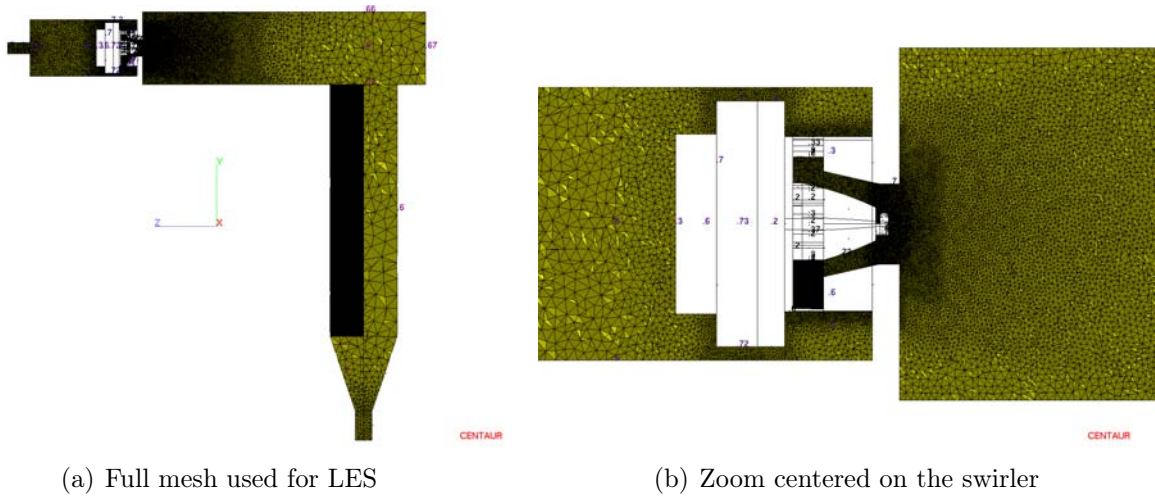


Figure 3.4: Axial cut of the mesh

The resulting mesh has about 1.2 million nodes and 6.8 million cells. The mesh characteristics are presented in Table 3.3.

Table 3.3: Characteristics of the mesh

Cell number	6 798 047
Node number	1 237 854
Mesh volume	0.31 m^3
Smallest element volume	$3.2 \cdot 10^{-12} \text{ m}^3$

3.3.3 Boundary conditions

The boundary conditions for the gas phase are summarized in Table 3.4 and those for the liquid phase in Table 3.5. The fuel used is kerosene, modeled by the surrogate KERO_LUCHE defined by Luche in [132]. The liquid injection profiles being unknown at the injection plan, they have to be recovered from the measurements, performed downstream at 6 mm from the injector. An evaluation is thus needed for a reconstruction of the profile at the liquid inflow location. A methodology, called FIM-UR, using the principle of upstream reconstruction has been developed by M.Sanjosé [123]. It uses injector characteristics and correlations from Lefebvre [133] and Cossali [134] to recover liquid and gas injection profiles from downstream to upstream location. Note that to apply the liquid injection profiles built with the FIM-UR

methodology, the liquid injection surface has been enlarged from $r = 0.25 \text{ mm}$ to $r = 4 \text{ mm}$ to result into the geometry shown on Fig. 3.5. Because of the Eulerian formalism used for the liquid phase, and as explained in chapter 2, the liquid variables must be defined everywhere, even at the pure air inlet. To avoid significant interaction of this injection with the gas phase, at the air inlet, the liquid phase is injected at a low diameter ($d_l = 5 \mu\text{m}$) and with a low liquid volume fraction ($\alpha_l = 10^{-8}$) which limits the reverse impact of the drag force. The mass transfert is cancelled by clipping the evaporation source term for d_l under $5 \mu\text{m}$. Note that this clipping value has to be set with care. Indeed if the clipping diameter is too small, in strong evaporative regions, the droplet diameter could drop under zero, leading to numerical issues. On the other hand, if it is set too high, the resolved evaporation rate is strongly affected. Although the study of the influence of the clipping diameter is out of the scope of this work, tests confirm the suitability of the chosen parameters for the operating conditions targeted.

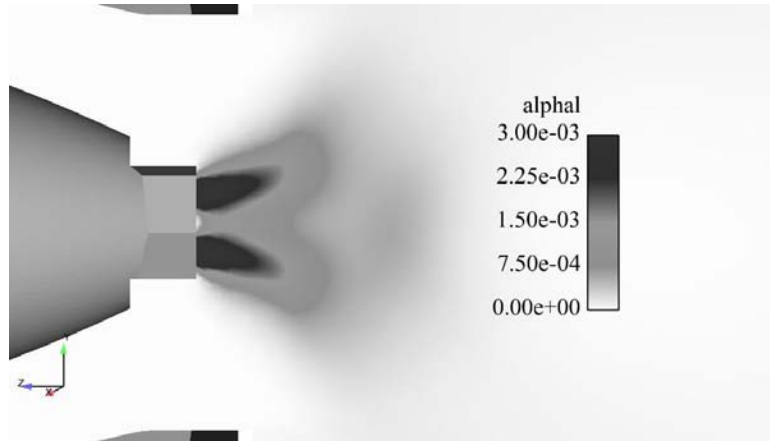


Figure 3.5: Zoom on the modified liquid injection geometry (to use FIM-UR)

Table 3.4: Boundary conditions for the gas phase

Name	Type	Physical parameter	Value
Air injection	NSCBC	Temperature	$T_g = 285K$
		Mass flow	$\dot{m}_{air} = 35.5g/s$
		Species mass fraction	$Y_{N_2} = 0.67$ $Y_{O_2} = 0.23$
Liquid injection	NSCBC	Temperature	$T_g = 285K$
		Bulk velocity	U_{bulk} from FIM-UR
		Species mass fraction	$Y_{N_2} = 0.67$ $Y_{O_2} = 0.23$
Outlet	NSCBC	Pressure	101250
Walls	walls	No-slip adiabatic	

The injection parameters for the liquid injector come from the experiments, the mean diameter used is equal to the Sauter mean diameter measured at 6 mm from the chamber entrance wall and based on characterisation of the liquid injection system [120].

Table 3.5: Boundary conditions for the liquid phase

Name	Type	Physical parameter	Value
Air injection	Dirichlet	Temperature	$T_l = 285K$
		Volume fraction	$\alpha_l = 10^{-8}$
		Droplet diameter	$d_l = 5\mu m$
		Bulk velocity	$U_{bulk} = 0m/s$
Liquid injection	Dirichlet	Temperature	$T_l = 285K$
		Mass flow	$\dot{m}_l = 2.26g/s$
		Droplet diameter	$d_l = 60\mu m$
Outlet	Dirichlet		
Walls upstream liquid injection	walls	No-slip	
Walls downstream liquid injection	walls	Slip	

3.3.4 Characteristic time scales of the MERCATO target operating point

Prior to any computation, it is of interest to characterize a configuration through the different time scales linked to the different physical phenomena. Here we can define:

The convective time τ_{conv} corresponds to the time taken by the gas to go from the chamber entrance to the end of the chamber. First we define the bulk velocity in the chamber:

$$\dot{m}_{air} = \rho U_{bulk} S_{chamber} \quad (3.2)$$

where $S_{chamber}$ is the transverse surface of the chamber. For the operating point $W_R = 0.6$, we have $U_{bulk} = 1.8 m/s$. According to the chamber length $L_C = 50 cm$, we have:

$$\tau_{conv} = \frac{L_C}{U_{bulk}} \approx 278 ms \quad (3.3)$$

The swirl time τ_{swirl} corresponds to the time for a complete revolution of the flow around the injection axis. Because of the phenomena of vortex breakdown [135] that we will see in section 3.4, two different swirl times are defined: one for the upstream part of the central toroidal recirculation zone (CTRZ) $\tau_{swirl,up}$ and another one for the downstream part $\tau_{swirl,dw}$. They are evaluated *a posteriori* from LES mean flow quantities at an axial position $x = 25 mm$ and a radial position $r = 14.75 mm$ for $\tau_{swirl,up}$ (this correspond to

an edge of the CTRZ before the vortex breakup axial position $x = 80 \text{ mm}$). The second point being at $x = 85 \text{ mm}$, $r = 60 \text{ mm}$ for $\tau_{swirl,dw}$ (position after the vortex breakup). The two time scales hence read:

$$\tau_{swirl,up} = \frac{2\pi}{\omega} = 0.74 \text{ ms} \quad (3.4)$$

$$\tau_{swirl,dw} = 12 \text{ ms} \quad (3.5)$$

where $\omega = \frac{U_\theta(r)}{r}$ is the rotating frequency and U_θ the orthoradial velocity. It is interesting to note that these two swirl characteristic times differ by more than an order of magnitude, highlighting a sudden change in the flow behaviour. This will be described in more detail in this chapter.

The droplet relaxation time τ_p corresponds to the time of relaxation of the droplet velocity to the carrying gas velocity (by the drag force). It is written:

$$\tau_p = \frac{\rho_l d_l^2}{18\mu} \quad (3.6)$$

where ρ_l is the liquid density and μ the viscosity of the gas. For the droplet diameters, d_l , involved in the simulations and ranging from $60\mu\text{m}$ (injection diameter) to $5\mu\text{m}$ (clipping diameter), we have $0.06\text{ms} < \tau_p < 8.7\text{ms}$.

From these times, Stokes numbers are defined ($St = \tau_p \frac{|U_\theta(r)|}{r}$). Looking at how the droplets will be affected by the swirl we evaluate the Stokes number at the two positions defined for the swirl times above. For large droplets close to the injection we have $St_{swirl,up} = 11.8$ meaning they have almost ballistic trajectories. For small droplets in the downstream part of the CTRZ, we have $St_{swirl,dw} = 0.005$, meaning that they are almost tracers and follow the gas phase.

The vaporization time τ_{vap} is determined from the evaporation mass transfer as expressed from Spalding's theory [136]:

$$\tau_{vap} = \frac{\rho_l d_l^2}{6\Phi Sh \rho D \ln(1 + B_M)} \quad (3.7)$$

where B_M is the mass Spalding number. At the injection conditions, Table 3.5, $\tau_{vap} \approx 110 \text{ ms}$.

These characteristic times will be used to analyse the results of section 3.4.

3.3.5 Initial condition

Since this is the first time this operating point is computed, the initial condition was made from scratch. As an initial guess, the computed domain is filled with *air* at $T_g = 285\text{ K}$ and $P = 101250\text{ Pa}$ without liquid. The velocity components are set to zero. Then, when the gas phase is statistically converged, the liquid phase is added with a liquid volume fraction $\alpha_l = 10^{-8}$ at $T_l = 285\text{ K}$ and with a diameter $d_l = 5\mu\text{m}$. The velocity of the liquid phase is initially set equal to the gas phase.

3.4 Stationary non reacting LES

In this section, the flow topology obtained from LES is addressed. As presented in section 3.2, to deal with the liquid phase in the Euler/Euler (EE) formalism, two couples of numerical schemes (gas/liquid) available in AVBP are tested: LW/PSI and TTGC/TTGC. The artificial viscosity levels necessary for such EE simulation are presented in Table 3.6.

		LW/PSI	TTGC/TTGC
Gas phase	2 nd order	0.05	0.1
	4 th order	0.01	0.01
Liquid phase	2 nd order	0.04	0.6
	4 th order	0.004	0.03

Table 3.6: Artificial viscosity levels

For the liquid phase, transported variables take the form $\rho_l \alpha_l X$. Because this phase is described here as a continuous medium, the variable α_l has to be defined at each point of the computational domain as seen in Fig. 3.5 and due to the nature of the governing equations may experience large variations over a very short distance. Hence, non diffusive schemes like TTGC may have difficulties to handle such high gradients (not present in the gaseous phase) while satisfying physical constraints. This is why, this scheme is used with artificial viscosity to smooth gradients and avoid negative values of α_l . On the other hand, the PSI scheme has been designed to deal with such gradients, and hence does not need high artificial viscosity. The outcome is however a more diffusive and a lower order scheme which may be not recommandable with LES.

For the gaseous phase, even if the TTGC scheme is more precise than the LW scheme, their differences are assumed negligible compared to those of the liquid phase, i.e. TTGC vs PSI. It is thus assumed that the differences that may be observed in the gaseous fields, between the two approaches, come from the resolution of the liquid phase. According to these remarks, it is not clear which numerical strategy will produce the best results at least with the grid resolution retained in this work. The evaluation of these two strategies is one of the objective of the present section.

3.4.1 The gas phase

Swirled flows in combustion chambers have been widely studied in the literature [137, 135]. These flows are very useful to anchor the flame thanks to the large recirculation zones generated by the swirl motion quantified by the non dimensioned Swirl number defined as:

$$S = \frac{\int_0^R \rho u_x u_\theta r^2 dr}{R \int_0^R \rho u_z^2 r dr} \quad (3.8)$$

For values of S below 0.6, the flow exiting the vanes behaves like a classic jet without recirculation along the axis. Above 0.6, the jet enlarges suddenly radially and generates along the axis a zone where the flow propagates upstream. This is known as the Central Toroidal Recirculation Zone (CTRZ).

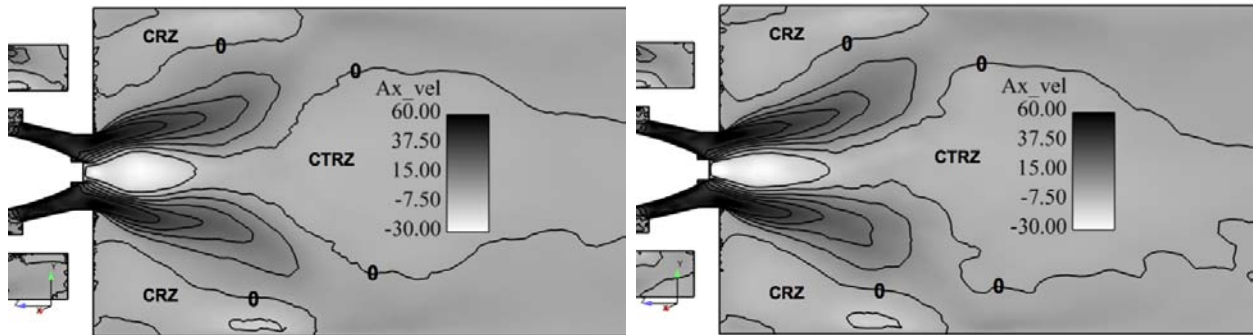
The recirculation zones present in MERCATO are identified in Fig. 3.6 a) and b) by the isolines of zero axial velocity. For the gas phase the two numerical strategies used here provide the same results.

In the MERCATO chamber, the swirl number is high enough ($S=0.77$) to generate along the injection axis a CTRZ. Its formation is due to an adverse pressure gradient, as described in [137]. The sudden expansion of the section when the flow enters the chamber produces a radial pressure gradient. This radial gradient generates Corner Recirculation Zones (CRZ). While the CTRZ has a symmetry of revolution, close to the chamber entrance wall the CRZ does not (see Fig. 3.7). This is due to the square section of the chamber. This cross structure is also present in the experiment as seen in Fig. 3.8.

Figure 3.6 c) and d) display the orthoradial component of the gas velocity. According to Fig. 3.6 a) b), when the orthoradial velocity drops, the radial pressure gradient decreases suddenly and the flow expands radially. This leads to the sudden radial expansion of the CTRZ around $x = 80mm$, it also coincides with the closure of the CRZ. This expansion is also visible through the conversion of the orthoradial momentum to the radial momentum on Fig. 3.6 e) and f). This kind of phenomenon is observed and described in [135], according to the authors the narrow shape of the CTRZ may be due to the presence of a Precessing Vortex Core (PVC).

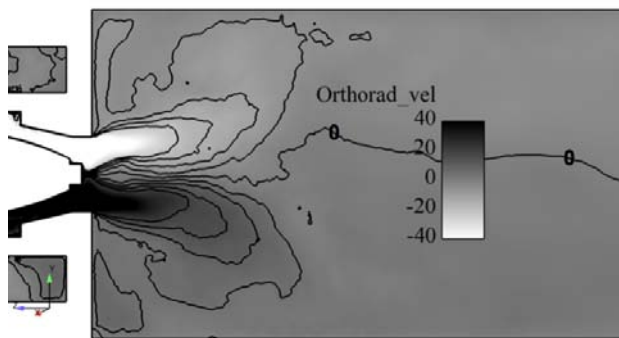
Figure 3.9 displays the RMS of the axial velocity. These fluctuations are very strong close to the injection and can reach up to 50% of the mean axial velocity, underlining that the flow is highly turbulent. The other RMS components present the same spatial evolution and are not shown here.

Figure 3.10 presents the carburation of the chamber. Since there is no combustion, the oxydiser O_2 is not consumed, the kerosene mass fraction Y_{kero} fields or equivalence ratio fields are similar. Because of the relatively low temperature ($T_g = T_l = 285K$), the gaseous kerosene mass fraction remains very low (saturation being reached). Indeed, the source term comes from evaporation of the liquid phase and is very slow. This very low evaporation rate explains that the gaseous kerosene is concentrated within the recirculation zones. Furthermore, and because of the low temperature, even with a very high residence time in the CTRZ (roughly $2\tau_{conv}$)

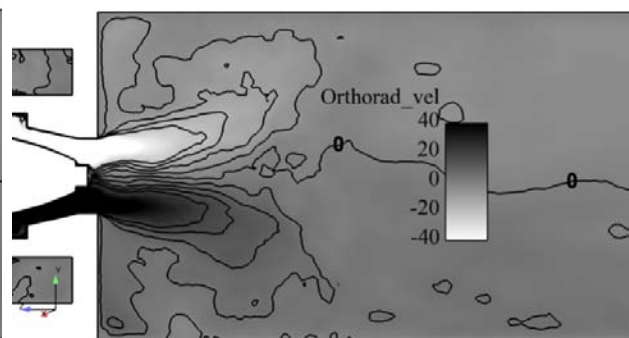


(a) Axial velocity (TTGC)

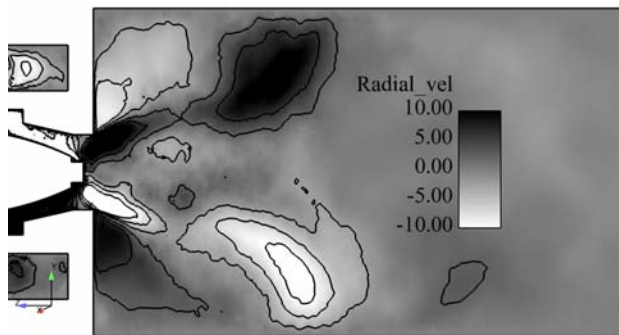
(b) Axial velocity (LW)



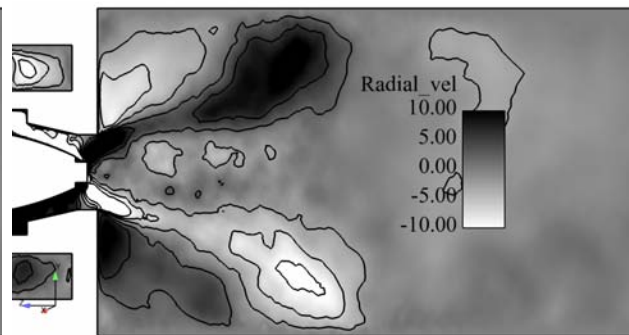
(c) Orthoradial velocity (TTGC)



(d) Orthoradial velocity (LW)



(e) Radial velocity (TTGC)



(f) Radial velocity (LW)

Figure 3.6: Mean gas velocity fields obtained with TTGC (left) and LW (right) [m/s]. Cut along the injection axis.

the saturation pressure of the kerosene is low and limits the gaseous equivalence ratio to about 0.3.

From this analysis, it is seen that the choice made (between TTGC or PSI) for the resolution of the liquid phase does not significantly impact the dynamic and the dispersion of the fuel in the gaseous phase. To go further in the analysis, a direct comparison of the resolved liquid phase is addressed below.

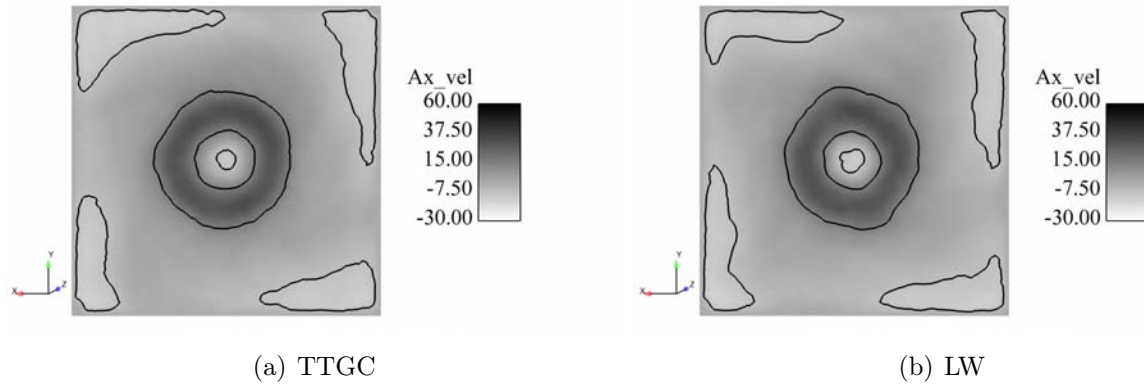


Figure 3.7: Transverse cut ($x = 40mm$) of the axial gas velocity fields obtained with TTGC (left) and LW (right) [m/s]



Figure 3.8: Picture of the bottom chamber (R. Lecourt) after tests. The painting has been diluted in the corners by kerosene droplets caught in the recirculation zones (light color).

3.4.2 The liquid phase

The velocity fields of the liquid phase (Fig. 3.11) are similar to the gas phase except close to the injection. This is to be related to the Stokes number evaluated in section 3.3.4. Close to the injection, the spray is dense and large size droplets can enter the CTRZ axially (positive velocity in Fig. 3.11a) and b) close to the liquid injector). The radial expansion of the spray is more progressive (Fig. 3.11 e) and f)) than for the gas phase because of the liquid relaxation time.

Contrarily to the gas phase, discrepancies appear in the liquid axial velocity obtained between the two numerical approaches. With TTGC, the CTRZ exhibited by the liquid phase is splitted in two parts around $x = 80mm$, which is not the case with PSI. The axial liquid velocity inside the upstream part of the CTRZ does not reach $-30m/s$ values like with PSI. This high reverse

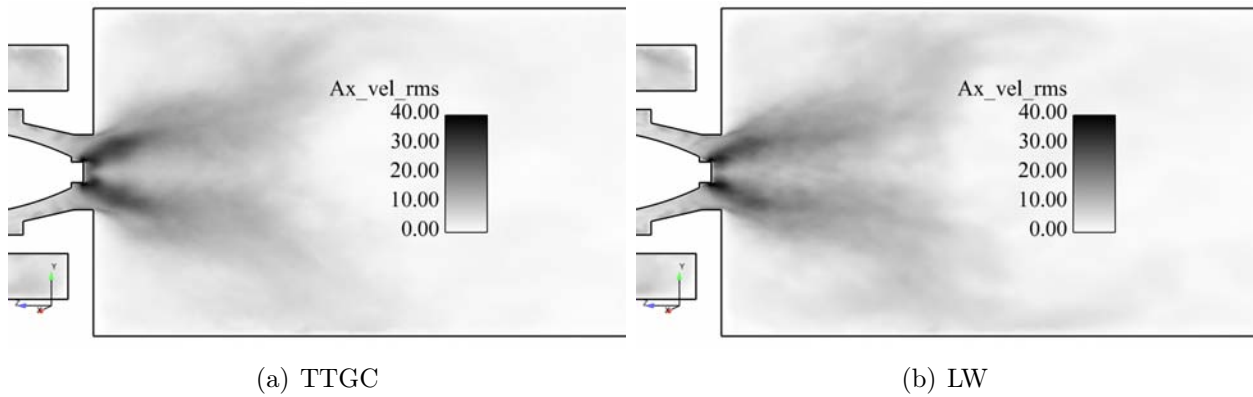


Figure 3.9: RMS axial gas velocity fields obtained with TTGC (left) and LW (right) [m/s]. Cut along the injection axis.

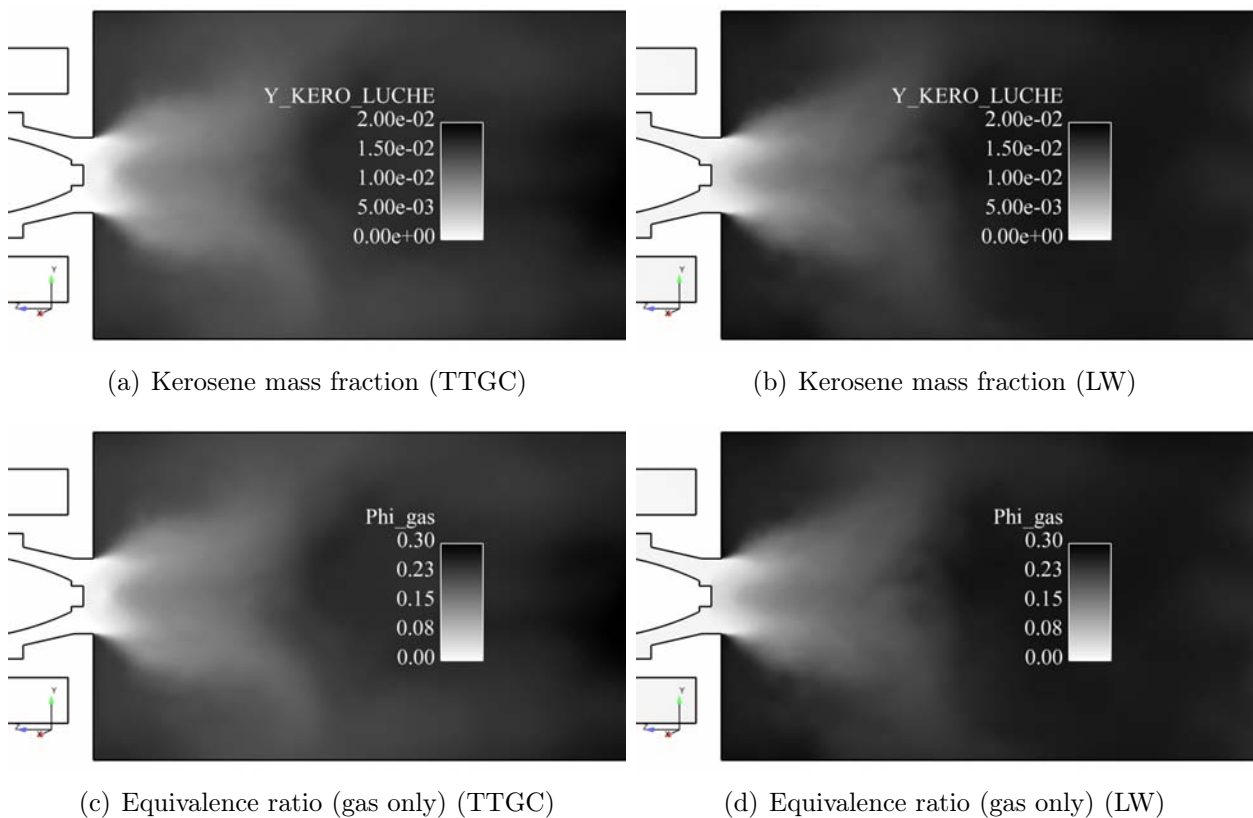


Figure 3.10: Carburation of the gas phase obtained with TTGC (left) and LW (right). Cut along the injection axis.

velocity present with PSI brings the stagnation point closer to the liquid injector if compared to TTGC. All parameters being identical between the two simulations, the modification of the stagnation point is *a priori* due to the scheme used.

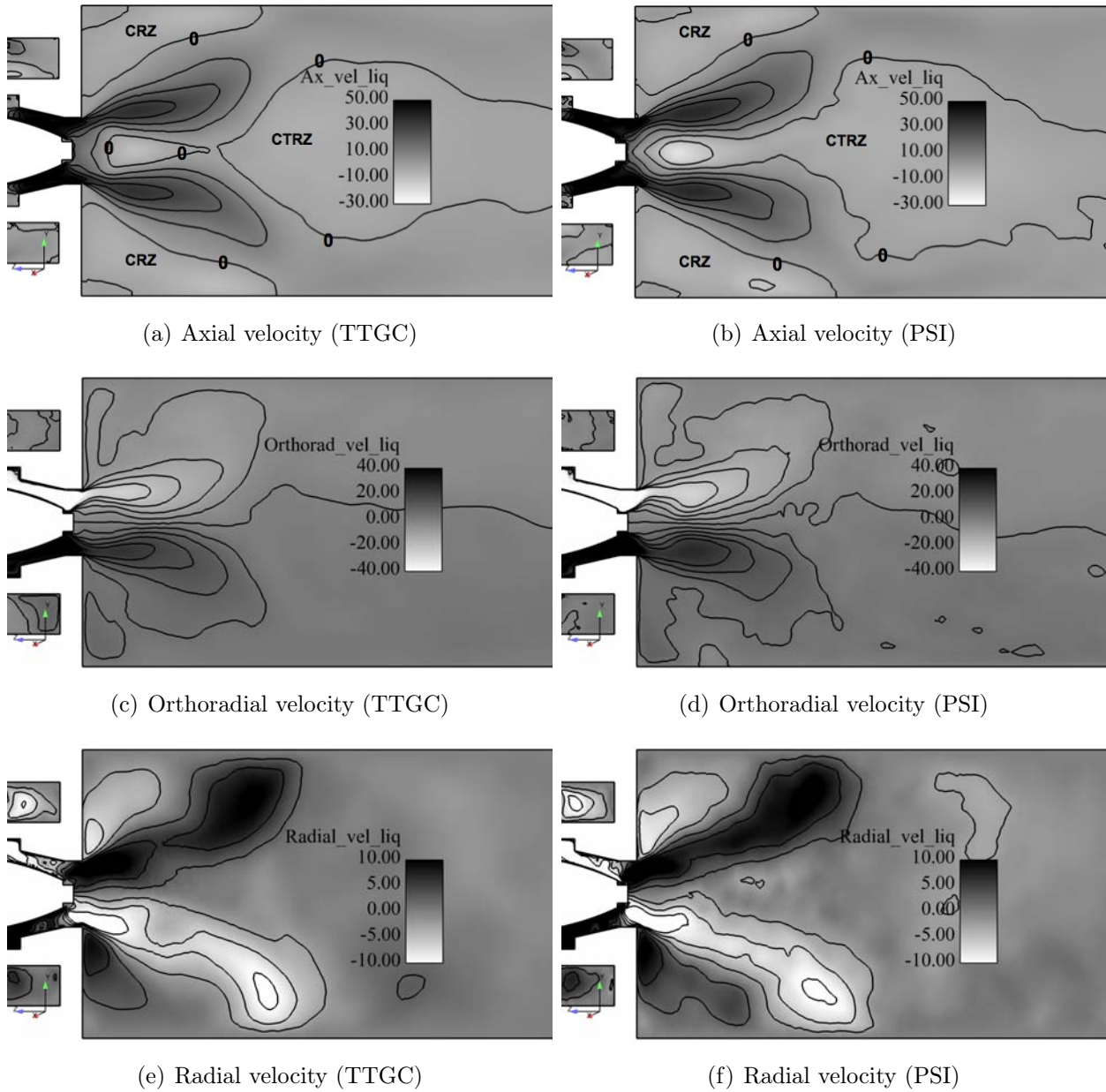


Figure 3.11: Mean liquid velocity fields obtained with TTGC (left) and PSI (right) [m/s]. Cut along the injection axis.

Figure 3.12 displays the RMS values of the liquid axial velocity. Like for the gas phase, the higher levels are located close to the injection where the mean velocity is the highest. However, they are lower than the gaseous RMS, due to the inertia of the large droplets at the injection. As for the mean axial velocity, there is some discrepancies between TTGC and PSI. Even if both schemes present similar shapes, RMS levels from PSI are slightly higher than TTGC. This may be due to the large amount of artificial viscosity applied with TTGC for the liquid phase

or too low resolution for such a centered scheme.

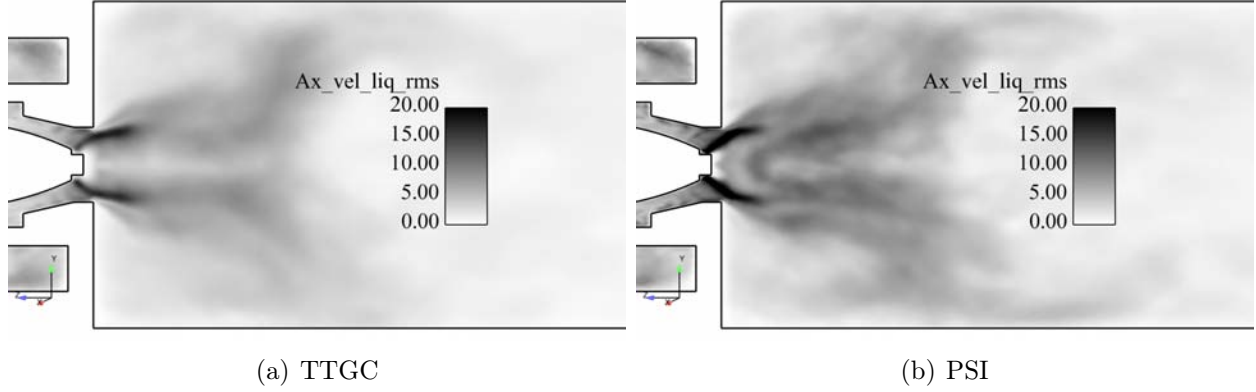


Figure 3.12: RMS axial liquid velocity fields obtained with TTGC (left) and PSI (right) [m/s]. Cut along the injection axis.

If we now look at the carburation of the chamber by the liquid phase, it seems that even if the evaporated fuel presents similar results for both numerical approaches, the liquid charge represented by α_l in Fig. 3.13 a) and b) are locally very different. The liquid charge in the CRZ and close to the walls are pretty similar between TTGC and PSI, however in the CTRZ, α_l level obtained with PSI is about four times lower than with TTGC. The liquid phase in the PSI computation does not seem to enter the CTRZ as much as with TTGC.

One major outcome of such different dynamics is illustrated through, the dispersion of the spray which is different between the two computations. Close to the liquid injector, in Fig. 3.13 a) and in agreement with Fig. 3.11, the position of the stagnation point further downstream with TTGC than with PSI allows the spray to expand further downstream. With PSI, the spray seems more affected by the gaseous phase and expands earlier in the radial direction. The liquid is thus rapidly evacuated through the exhaust pipe.

Similarly to Fig. 3.9 which illustrates the axial velocity RMS, Fig. 3.12 locates maximum of liquid RMS around the liquid injection hollow cone. One origine of these peaks relates to the presence of a Precessing Vortex Core (PVC) which affects the spray dispersion in the near injection region, Fig. 3.14. Figure 3.14 illustrates how the spray is affected by the PVC. The spray is rolled up around the PVC, and then blown by the high velocity of the air going out of the swirler. Consequently, the more the spray is affected by the PVC, the larger the radial dispersion will be.

Finally, the difference in terms of liquid charge seen in Fig. 3.13 a) and b) is also visible in the liquid equivalence ratio (Fig. 3.13 c) and d)) and in the global equivalence ratio (liquid + gas) (Fig. 3.13 e) and f)).

To conclude, even if the gaseous fields from the two numerical strategies are similar, the discrepancies observed in the liquid axial velocity fields close to the nozzle have a strong influence on the carburation of the CTRZ. Computing correctly the liquid injection seems therefore of primary importance and numerics as well as modeling (cf. P.Sierra PhD (2012)) play a crucial role in that region. In order to quantify more precisely these predictions, confrontation of the

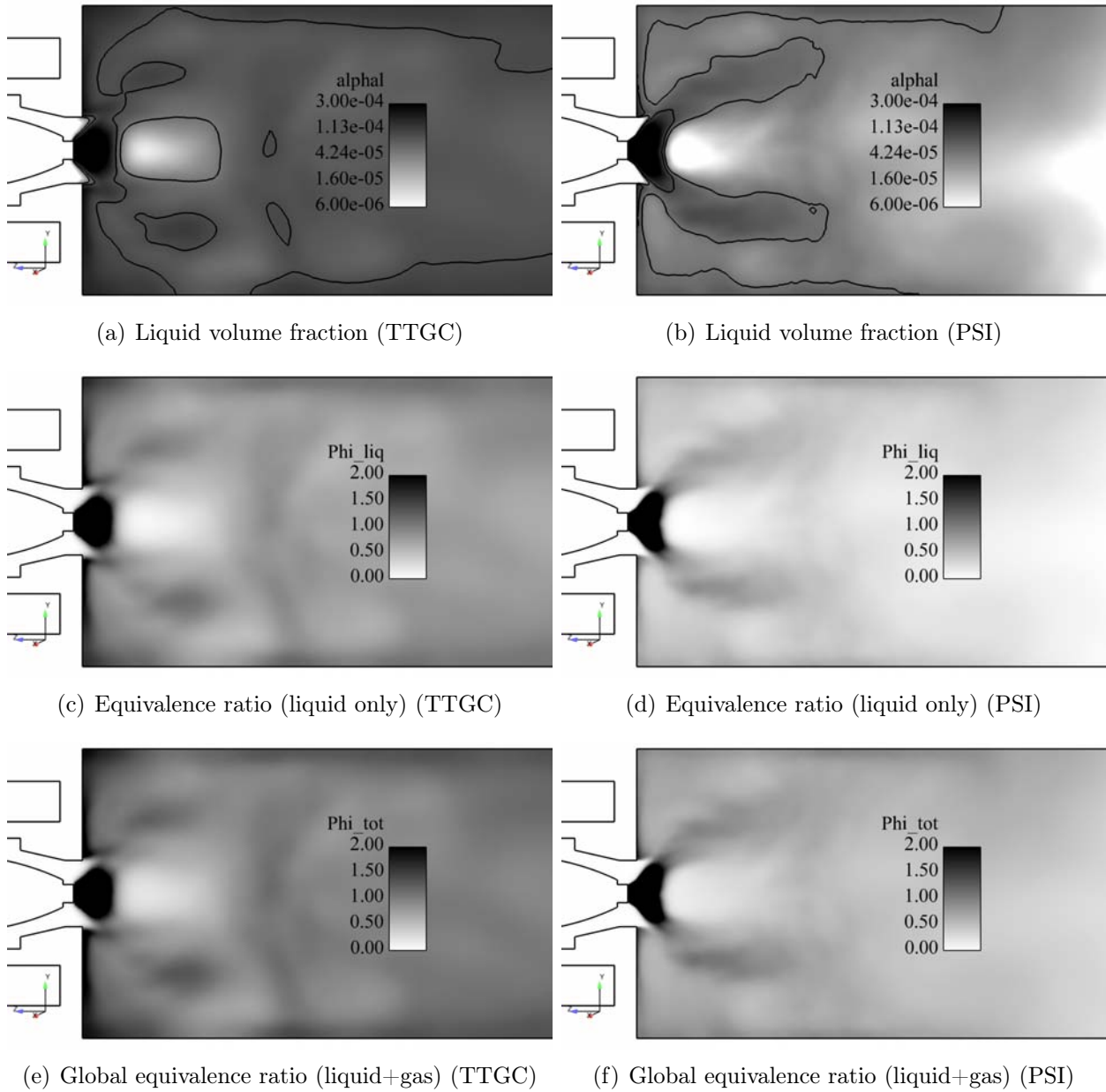


Figure 3.13: Carburation of the liquid phase obtained with TTGC (left) and PSI (right). Cut along the injection axis.

cold LES with experimental measurements are addressed thereafter.

3.4.3 Comparison with measurements

Prior to the study of the stable flame regimes issued by the two-phase flow combustion in the MERCATO bench, the aerodynamics of the cold flow has to be validated against measurements.

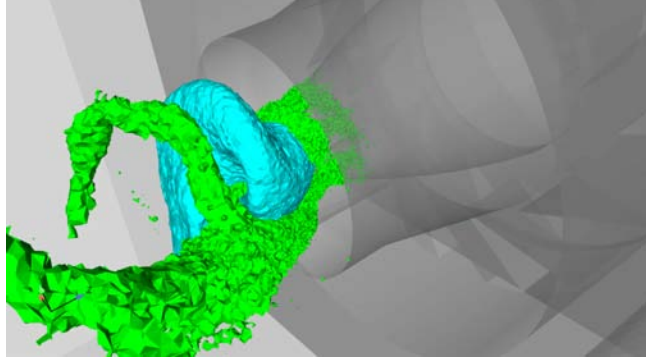


Figure 3.14: Representation of the spray dispersion by the PVC. Isosurfaces of pressure $P = 100800 Pa$ (green) and liquid volume fraction $\alpha_l = 5.10^{-4}$ (blue).

For this part, the experimental measurements (from ONERA) of the simulated operating point ($WR = 0.6$) are not available at each axial position. However, possibilities of data reduction have been underlined by R.Lecourt in [122]. For the gaseous phase, LDA measurements provide the three velocity components which are proven proportional to WR . For PDA measurements of the liquid phase, more complex correlations have been defined. The data of the axial liquid velocity $U_{l,ax}$ is approximated by the following expression:

$$U_{l,ax}/(WR^{1.45} \dot{m}_{kerosene}^{-0.42}) = (-2.271.10^{-6}r^6 + 0.004r^4 + 0.4r^2 + 20)e^{-(\frac{r}{15})^3} \quad (3.9)$$

where r is the distance to the axis in millimeters and $\dot{m}_{kerosene}$ is the kerosene mass flow. The orthoradial component $U_{l,\theta}$ is evaluated from the axial one through the correlation of the angle $\theta = \arctan(U_{l,\theta}/U_{l,ax})$:

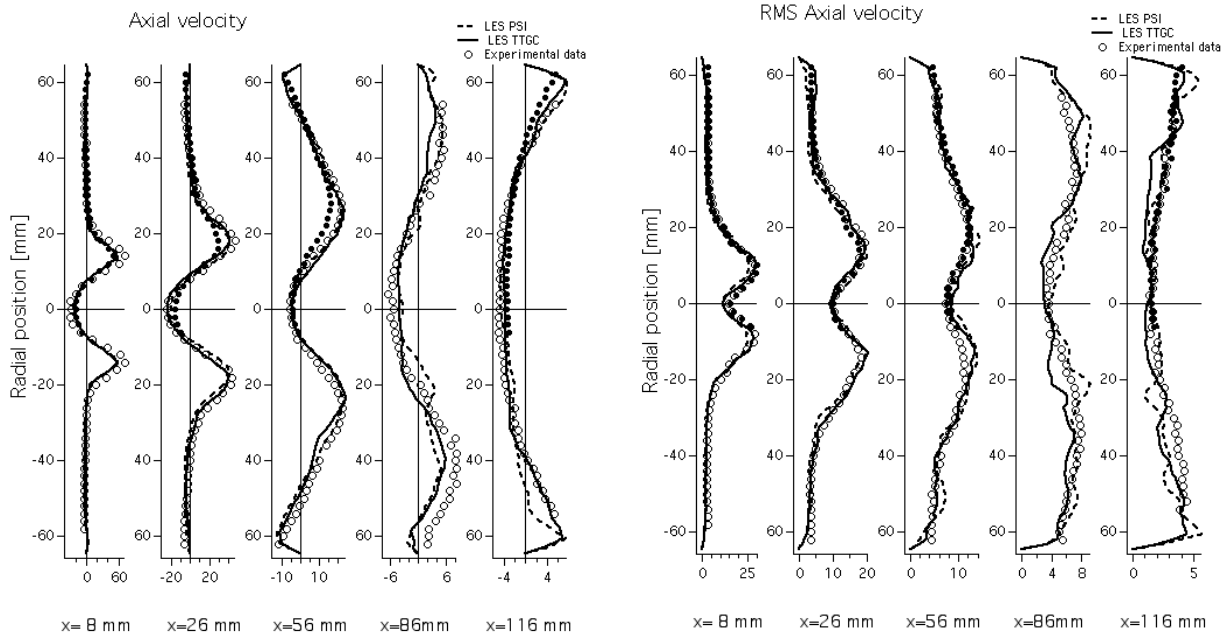
$$\theta = -0.000072r^5 + 0.006430r^4 - 0.220669r^3 + 3.426499r^2 - 21.857364r \quad (3.10)$$

The radial component profile $U_{l,r}$ is independent of the kerosene flow rate and proportional to WR , it reads:

$$U_{l,r}/WR = 0.0008r^4 - 0.0475r^3 + 0.6967r^2 + 0.3679r \quad (3.11)$$

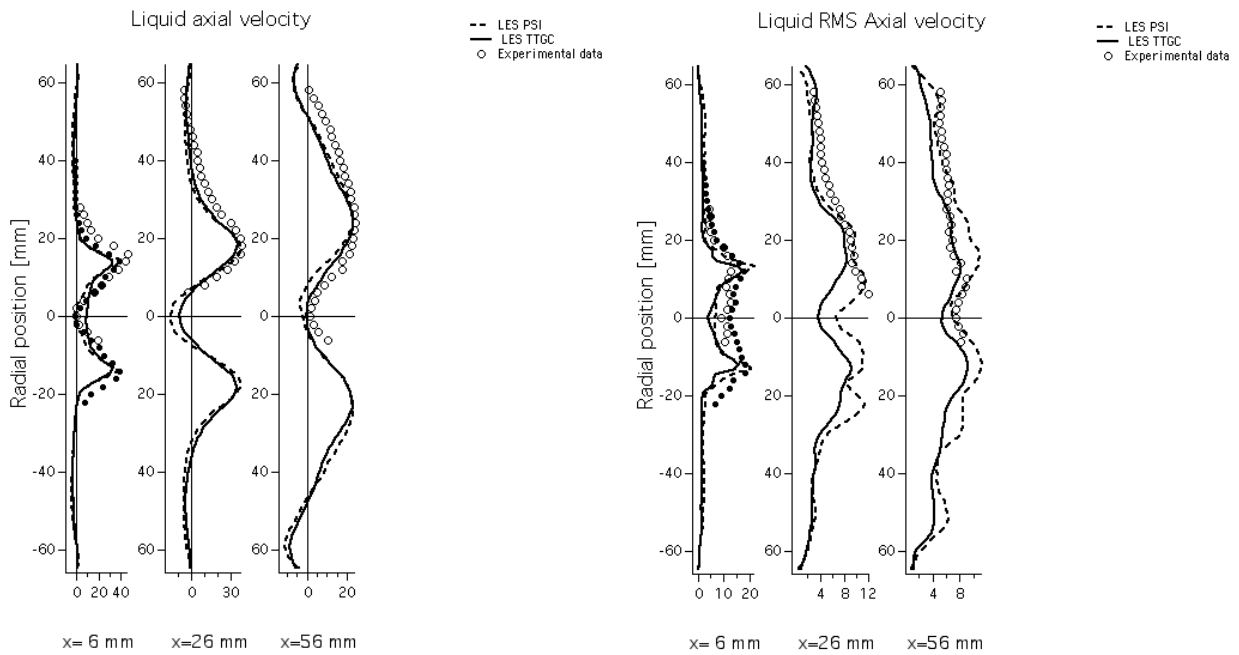
In the following plots, all experimental data are displayed whenever available. Filled circles represent actual measurements obtained for the operating point $WR = 0.6$ and simulated by LES, while the empty circles correspond to data of the operating point $WR = 0.426$ rescaled using the above correlations. These are compared with LES profiles computed with the numerical schemes TTGC/TTGC and LW/PSI. Note that in all subsequent figures and to simplify the notations, the couple TTGC/TTGC will be identified as TTGC and the couple LW/PSI as PSI.

All axial velocity component profiles collapse onto the same line, for all positions and for both phases, Fig. 3.15. From these more quantitative comparisons, the expansion of the jet is well recovered as well as the RMS levels. Note the slight lack of convergence of the gaseous



(a) Gaseous mean

(b) Gaseous RMS



(c) Liquid mean

(d) Liquid RMS

Figure 3.15: Axial velocity component. \circ represent data from $WR = 0.426 +$ correlations, \bullet represent data from $WR = 0.6$ directly.

LES profiles at $x = 86 \text{ mm}$ especially compared to the one at 116 mm , Fig. 3.15a) and b). The vortex breakdown of the CTRZ oscillating at a low frequency around the axial position $x = 80$

mm increases of the characteristic time and larger fluctuations is expected when compared to profiles at 116 mm . As seen previously in the velocity fields, a small difference between the two LES is visible on the liquid phase at $x = 6\text{ mm}$, Fig. 3.15c). The upstream limit of the CTRZ is correctly predicted by the PSI scheme at $x = 6\text{ mm}$ while the axial velocity value obtained with TTGC still has positive value (i.e. larger penetration length of the liquid jet).

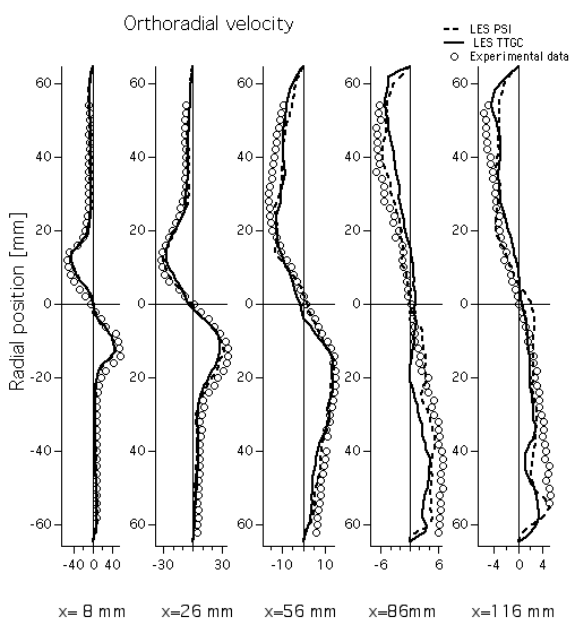
The correct predictions of the orthoradial component of the gaseous phase, Fig. 3.16a) and b), underline a correct evaluation of the swirl which is essential for the size of the recirculation zones. The predictions for the liquid phase seem less accurate close to injection, Fig. 3.16c) and d). However the two experimental profiles present quite large differences, and LES results are closer to the measurement of the actual operating condition.

For the radial component, LES give very good results for both numerical schemes and for the gaseous phase, Fig. 3.17a) and b), for all positions. However, the prediction of the liquid phase, Fig. 3.17c) and d), seems more challenging. From the early axial position $x = 6\text{ mm}$, the maximum of the radial component is underpredicted, and seems to increase with the axial position. The radial position of the maximum of the liquid radial velocity from LES is also closer to the axis than the experimental one. However, for the first profile $x = 6\text{ mm}$, the LES are not that far from the actual measurement. Even if additional measurements at the operating point $WR = 0.6$ would be of interest to conclude clearly, some improvements in the modelisation of the liquid phase are still needed to better compare with the measurements.

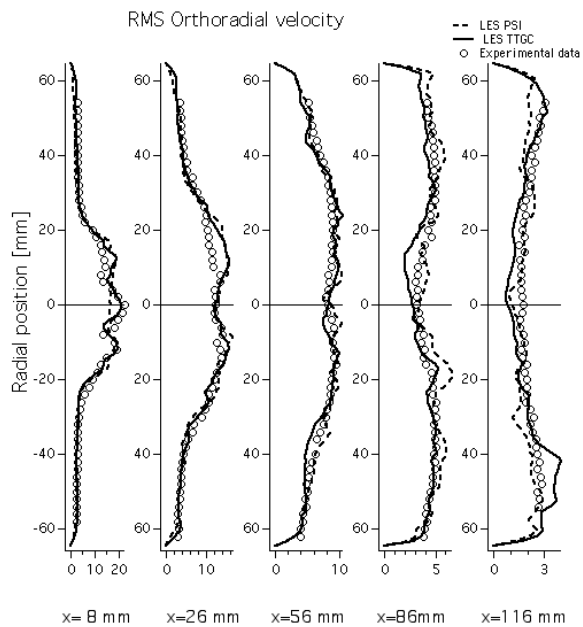
To conclude about this study of stationary non reacting LES, despite obvious limitations introduced by the formalism used, i.e. Euler/Euler monodispersed, the aerodynamics of the cold flow has been validated against measurements with fair agreement. As expected, the choice of the liquid numerical scheme (between TTGC and PSI) does not impact significantly the resolution of the gaseous phase. In addition, accuracy of the LES prediction is very good compared to the measurements.

On the other hand, conclusions about the liquid phase is not clear for several reasons. First, the assumption of locally monodisperse droplets may highly affect the spray dispersion. More advanced models constructed to adress local polydispersion could be used to tackle this issue [138, 139]. Second, the lack of data due to the difficulties to measure liquid phase velocity at the operating point $WR = 0.6$ are filled by the extrapolation of the measurements done at $WR = 0.426$ with the correlations Eq. 3.9, Eq. 3.10 and Eq. 3.11. Comparisons between the two resulting measurements underline the limits of this procedure. Then, about the numerical strategies, even if some discrepancies in terms of liquid carburation have been observed in section 3.4, the two LES are both able to match the aerodynamics of the experimental measurements of this non-reacting two-phase flow ⁴. Although obtained for a fixed grid resolution, current studies point to the potential need for high order schemes to properly address two-phase flows. Despite these limitations, the questions of the influence of these choices and the accuracy of LES on the reacting case is adresssed in the next section.

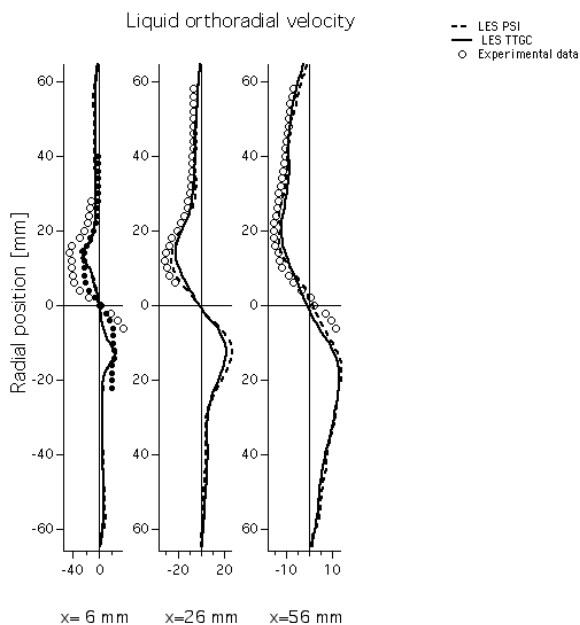
⁴Note that even if the results obtained with PSI seem more physical, this may be due to the preferential diffusion of the residuals along the streamlines. Further quantitative comparisons has to be done to conclude.



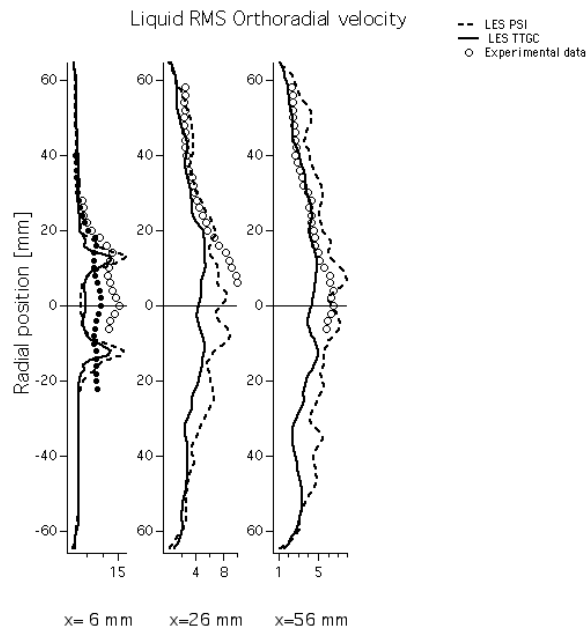
(a) Gaseous mean



(b) Gaseous RMS

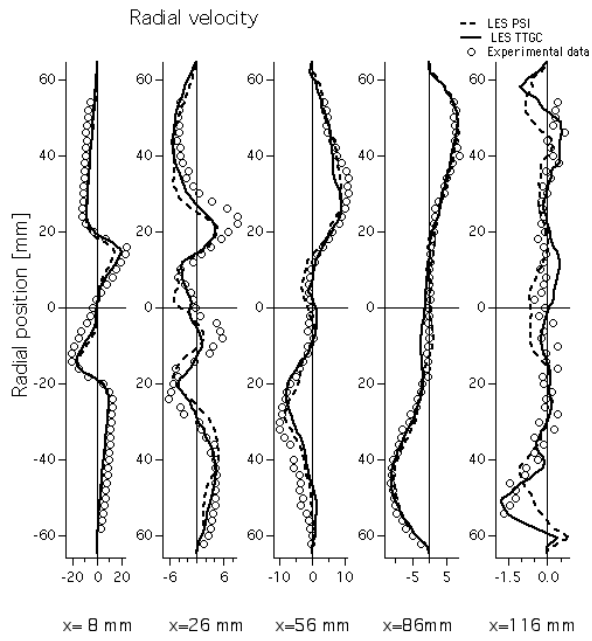


(c) Liquid mean

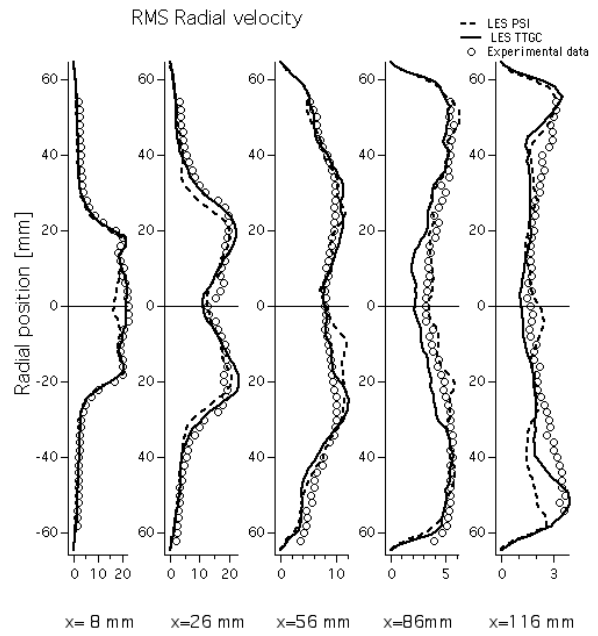


(d) Liquid RMS

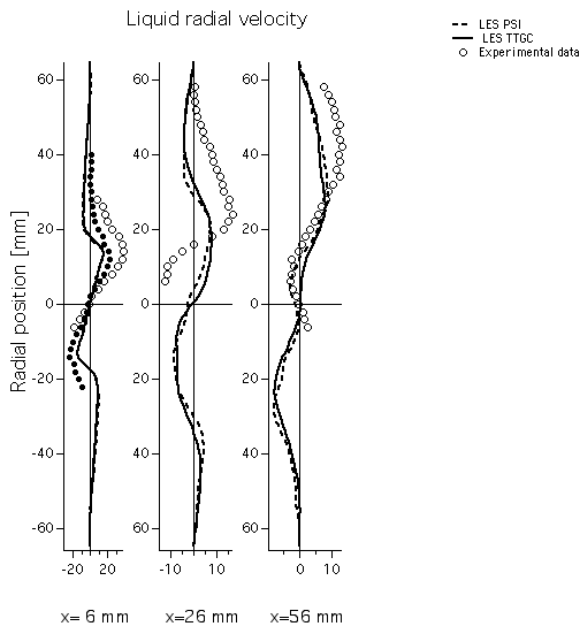
Figure 3.16: Orthoradial velocity component. \circ represent data from $WR = 0.426 +$ correlations, \bullet represent data from $WR = 0.6$ directly.



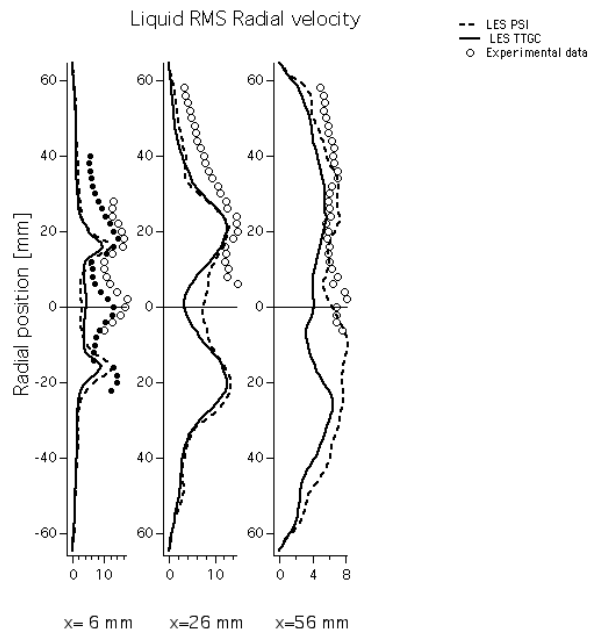
(a) Gaseous mean



(b) Gaseous RMS



(c) Liquid mean



(d) Liquid RMS

Figure 3.17: Radial velocity component. \circ represent data from $WR = 0.426 +$ correlations, \bullet represent data from $WR = 0.6$ directly.

3.5 Stationary reacting LES

In this section, the stationary two-phase flame is studied. The operating point is the same as the one used in the non-reacting case ($WR = 0.6$). The main characteristics of the flow are hence similar to those of the cold case and are not detailed here. However analysis of the flame topology will be detailed based on instantaneous solutions in section 3.5.1. The numerical setup is also the same as for all the non-reacting LES (mesh, boundary conditions, SGS model...). To describe the chemistry, the simplified 2-step chemical kinetic scheme BFER [140] is used associated with a thickened flame model [76, 77]. The dynamic thickening is used and adapts to the cell size of the mesh in order to have five points within the flame front. An image of the actual flame as seen in the experiment is shown in Fig. 3.18. This flame has the classical compact M-shape of swirl burner flames [141]. It is shorten by the recirculation zone and is anchored close to the chamber wall entrance around the swirler exit.

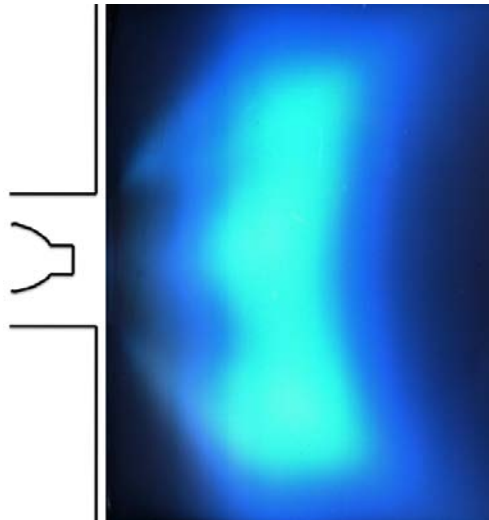


Figure 3.18: Flame topology from the experiments (courtesy of ONERA, R.Lecourt), chamber entrance on the left.

As for the non reacting case (section 3.4), for the gaseous phase, LDA measurements provide the three velocity components. For the liquid phase the velocity components are measured using PDA method. The axial positions of measurements for the reacting case are displayed in Fig. 3.19. Note that they are different than in the non reacting case. In the following, all mean fields or profiles obtained from LES and presented have been averaged over 60 *ms*. If we look at the mean reaction rate of the fuel oxidation reaction (Fig. 3.19) computed by LES, the same shape than in experiments is recovered. The flame is mainly anchored at the combustor end-wall and has a static position over few millimeters; the velocity fluctuations are very low in this zone. On the contrary, the upstream limit of the central recirculation zone (delimited by the black line on Fig. 3.19) is submitted to quite large velocity (and equivalence ratio) fluctuations which lead to a more diffused mean flame brush.

Mean velocity profiles obtained numerically and measured for the steady reacting case are presented on Fig. 3.20. LES match measurements, the main differences appearing for gaseous

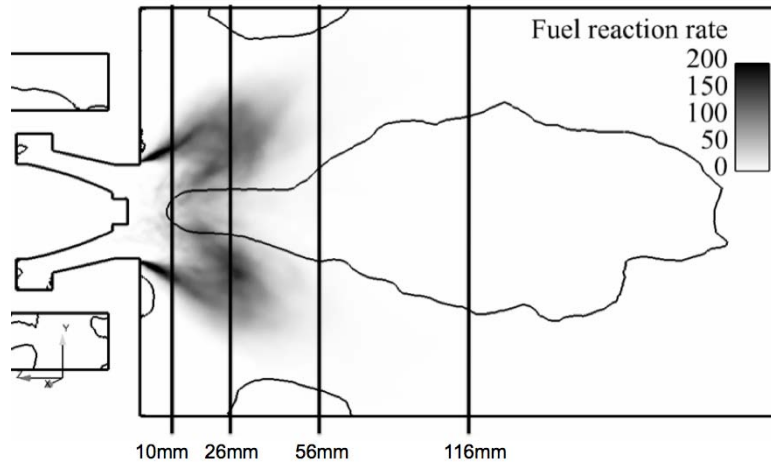


Figure 3.19: Mean fuel reaction rate in the mean axial plane. The black isoline represents $U_{g,ax} = 0$ and black vertical lines the positions of the measurements.

velocity profiles close to the fuel injection. According to the profiles at $x = 10 \text{ mm}$ and 26 mm , it seems that the central recirculation zone is slightly upstream in the LES if compared to experiments. Despite the limitations of the Eulerian monodisperse approach used for the liquid phase ⁵, good agreement is observed for the mean liquid phase profiles confirming the potential of this approach for reacting flows. Note that the lack of data at 116 mm in Fig. 3.20c) is due to the very low concentration of liquid that is almost evaporated at this position and hence not captured experimentally.

Now if comparing the two set schemes, the results are globally similar, however three discrepancies has to be underlined. First, the RMS levels from LW/PSI are higher than with TTGC/TTGC which means larger fluctuations of the flame, especially at $x = 116 \text{ mm}$. This may be due to different combustion regimes in the two computed flames. Another point is the intensity of the CTRZ at $x = 10 \text{ mm}$; with PSI scheme, the liquid still experiences reverse flow while it is almost quiescent with TTGC, i.e. stagnation point. The location of this point being of primary importance for the carburation of the chamber, it can also affect the combustion regimes of the flame as suspected above. Then, for both phases, the mean axial velocities at $x = 56 \text{ mm}$ are slightly higher with PSI along the whole profile. We cannot conclude on this precisely yet, but since the mass flow has to be conserved, it can be assumed that the thermal expansion due to burning is different in the two computations.

To investigate in more details these effects, the flame topology and typical flame diagnostics are studied for both schemes in the following paragraph, based on instantaneous fields.

3.5.1 Global combustion regimes

In the previous section (section 3.4), differences in terms of carburation and around the stagnation point have been observed depending on which numerical scheme is used. In order to find

⁵this has been detailed in the previous section about non reacting LES.

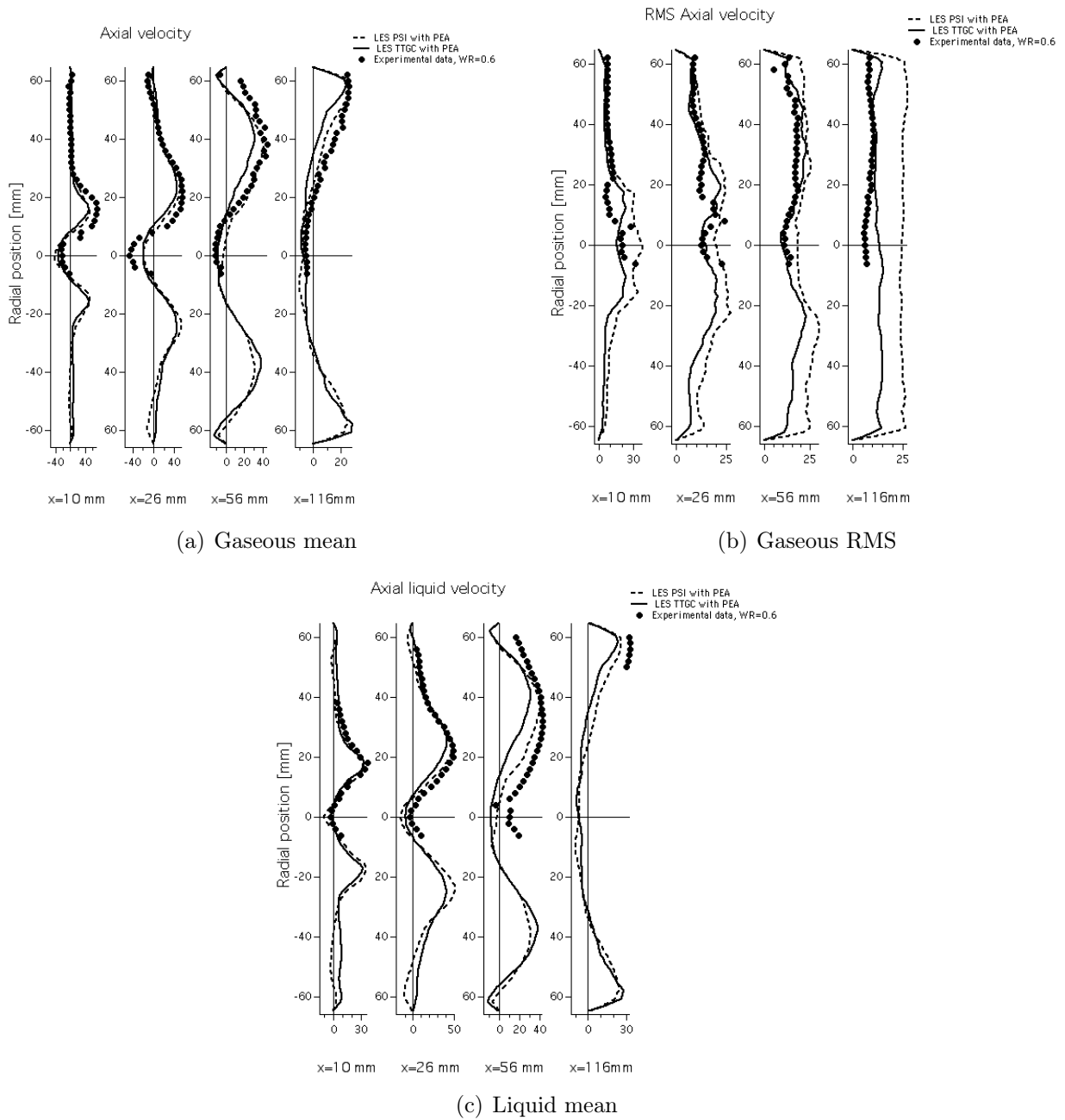


Figure 3.20: Axial velocity component

out if there is a more appropriate numerical scheme or methodology to compute the stationary flame of MERCATO, the carburation (Kerosene and O_2 mass fraction, equivalence ratio and liquid volume fraction) and temperatures fields, for the two numerical schemes, are gauged in the following. As reference, note that for these operating conditions (Pressure of 1 atmosphere and fresh gases temperature of 285 K), the adiabatic flame temperature T_{adia} at the stoichiometry is 2278.3 K. For the liquid phase, the saturation temperature is 445.1 K. To investigate

the combustion behaviour in MERCATO, snapshots are first presented.

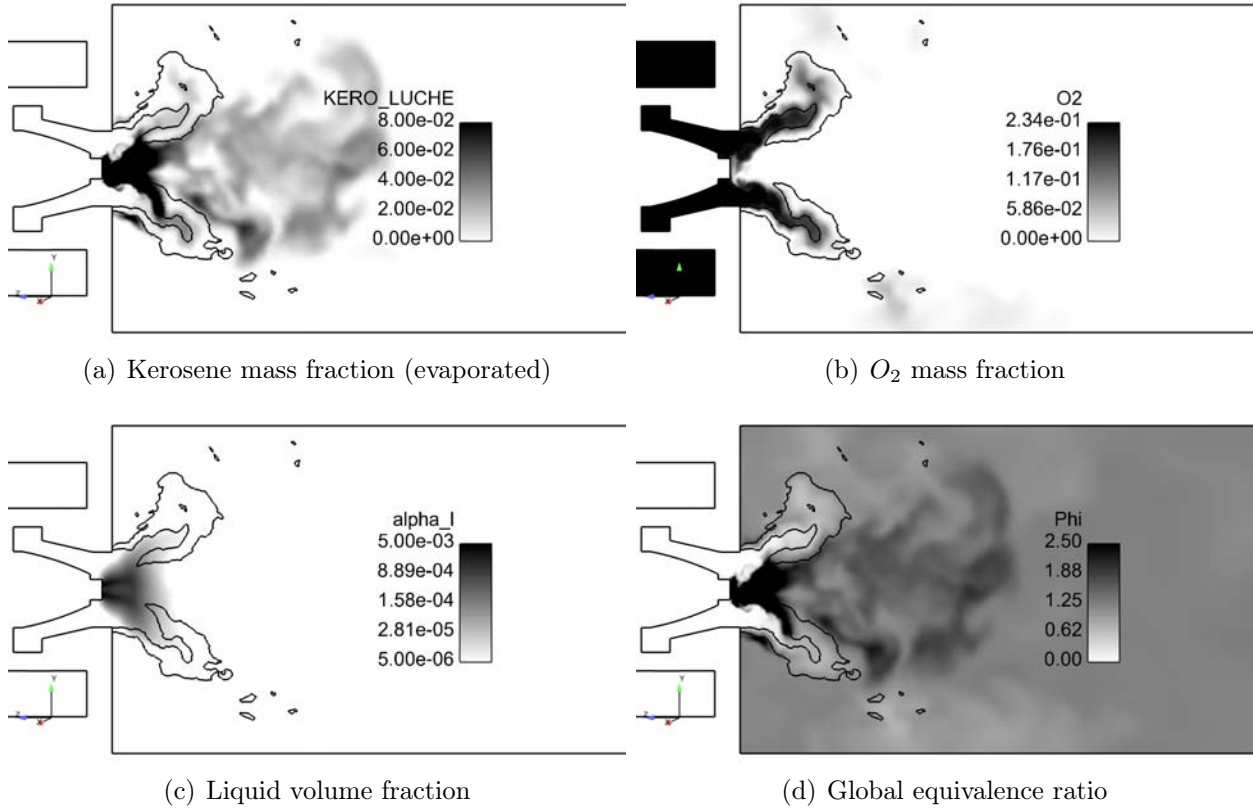


Figure 3.21: Instantaneous carburation fields for TTGC scheme. Black isoline denotes $HR = 10^8 W/m^3$.

TTGC flame: Figure 3.21a) presents the evaporated kerosene, i.e. gaseous field. It has a very high concentration in the upstream part of the CTRZ and is almost absent from the CRZ. The other reactant, O_2 , is present only upstream the flame front (Fig. 3.21b)). The CRZ is thus filled only by burnt gases while the CTRZ contains both burnt gases and evaporated kerosene. This implies a richer mixture within the CTRZ than in the CRZ (Fig. 3.21d)). The high concentration of gaseous kerosene in the CTRZ is due to the proximity of the liquid injection. The liquid kerosene⁶ is able to go through a part of the flame front and reaches the inner part of the CTRZ (Fig. 3.21c)) where it evaporates quickly because of the high temperature of the burnt gases.

However, because of evaporation (which acts as a sink for the enthalpy) and very rich mixture, the burnt gas temperature within the CTRZ is lower than the one in the CRZ (where the fuel is almost evaporated and the mixture close to stoichiometry) as seen in

⁶Note the apparent non sensitivity of the liquid phase to the turbulent mixing, the spray seems only subject to diffusion.

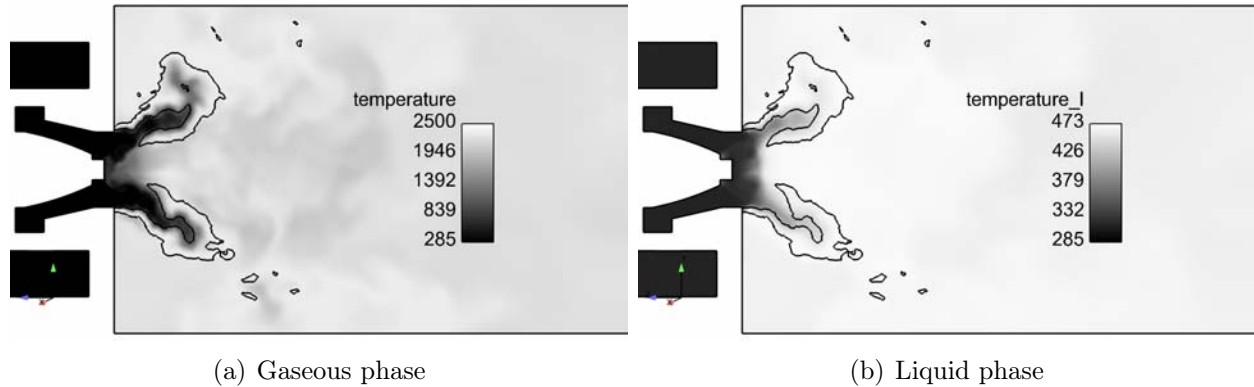


Figure 3.22: Instantaneous temperature fields for TTGC scheme. Black isoline denotes $HR = 10^8 W/m^3$.

Fig. 3.22a). The difficulty of the flame to heat up the liquid phase close to the nozzle is also visible in Fig. 3.22b).

PSI flame: The carburation fields obtained with the PSI scheme are displayed on Fig. 3.23. The main comments done for TTGC are still valid here. However the flame front is more wrinkled and the mixing of the evaporated kerosene seems more effective (Fig. 3.23a). The sensitivity of the liquid phase (Fig. 3.23c) to turbulent mixing seems indeed greater than with TTGC (Fig. 3.21c) : the oriented diffusion of the PSI scheme looks to be favorable and helps to deal with the interaction of dense spray with turbulence instead of spreading too much the liquid phase in the transverse direction. The liquid does not diffuse much towards the CTRZ and the hollow cone is wrinkled by the precessing vortex core (PVC) and dispatched inside the flow exiting from the swirler. A consequence is that kerosene evaporates mainly on the fresh gas side of the flame front (Fig. 3.23a) and mixes with O_2 which produces a mixture closer to stoichiometry in the CTRZ (Fig. 3.23d). The very rich mixture is only present here very close to the nozzle and remains outside the CTRZ.

Even if very rich mixtures are less present due to more progressive evaporation than in the computation with TTGC, the sensitivity of the liquid phase to turbulence generates pockets of liquid fuel which can evaporate and burn at different rates. These differences lead to larger local fluctuations seen through the fields of temperature for both gas and liquid phases as seen in Fig. 3.24.

As previously assumed through the analysis of the velocity profiles, the instantaneous fields display different turbulent flame structures. The PSI flame is more wrinkled, leading to larger fluctuations while the TTGC flame appears more quiet. Indeed, in TTGC computation, Fig. 3.21c), the spray is mainly dispersed by the diffusion from artificial viscosity, while with PSI, Fig. 3.23c), the dispersion is due to its interaction with the PVC and turbulence. Hence, the initial artificial diffusion of the liquid within the CTRZ tends to reduce its intensity

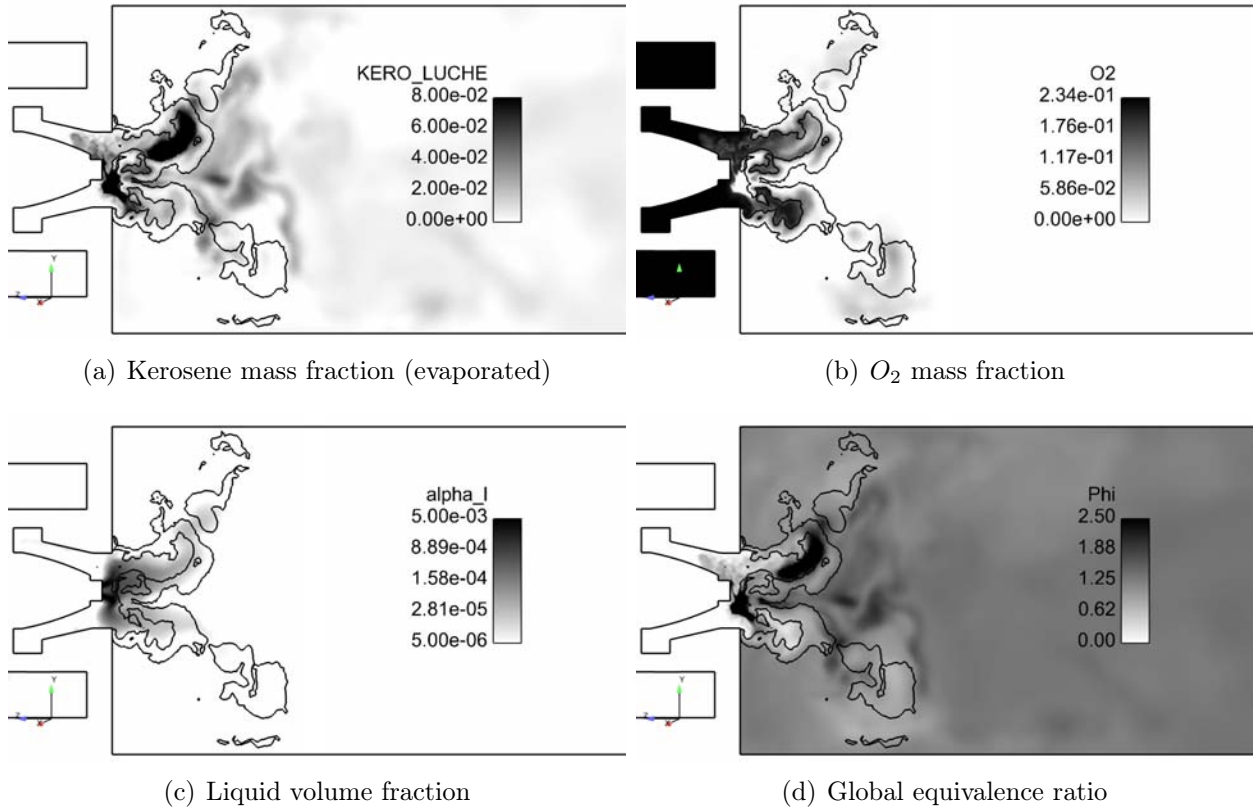


Figure 3.23: Instantaneous carburation fields for PSI scheme. Black isoline denotes $HR = 10^8 W/m^3$.

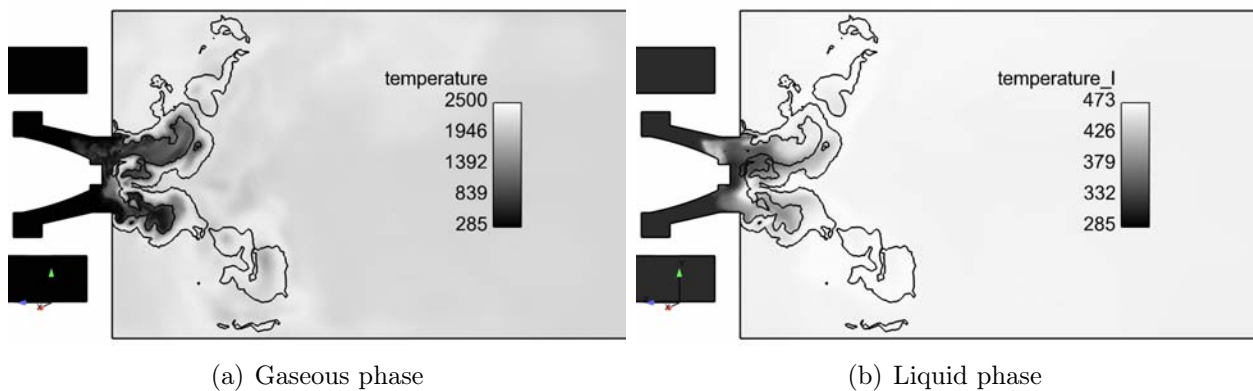


Figure 3.24: Instantaneous temperature fields for PSI scheme. Black isoline denotes $HR = 10^8 W/m^3$.

in the upstream part. Hence, due to the high quality mesh required by the TTGC scheme, in this study, the artificial viscosity added to stabilize the LES was still too strong to ensure the potential precision of the TTGC scheme. However, to conclude in a more general context, com-

plementary data or simulations are clearly needed to discriminate which strategy reproduces the proper dynamics.

Since the influence of the numerical scheme used for liquid phase increases as we get closer to the liquid injection, i.e. more dense spray, and according to the limited available data, the PSI scheme will be used to further study the stationary flame structure. Indeed, within their own clear modeling limits ⁷, a study of the combustion regimes occurring within the swirled two-phase flow flames could provide clues on major phenomena involved. More diagnostics on flame regimes are thus proposed in the following section.

3.5.2 Flame analysis and regimes

Based on the mean flame position as displayed in Fig. 3.25 and on the observations of the previous section, three zones of study are defined (Fig. 3.25). Zone 1 represents the most stable part of the flame with good evaporation and mixing, it is the main part of the CRZ. Zone 2 represents the most loaded (in liquid) part of the flame; expected to be the richest one is located within the CTRZ. Then, Zone 3 is located in the main air flow and experiences large velocity fluctuations.

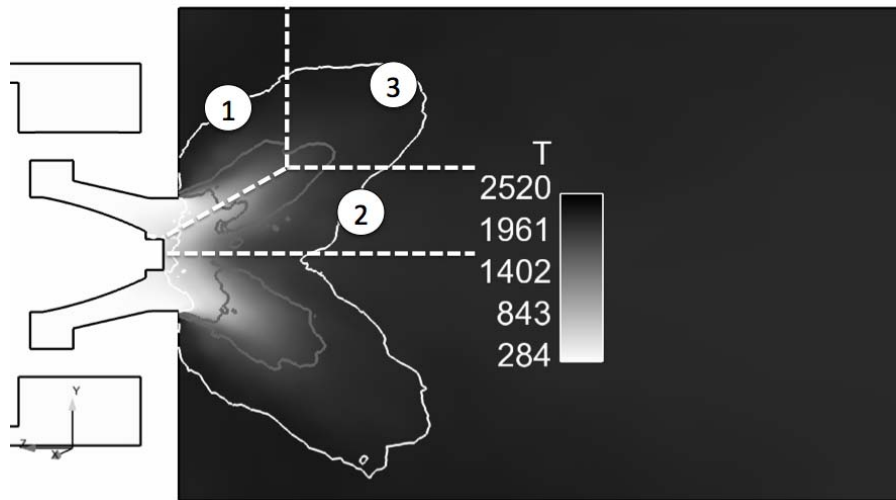


Figure 3.25: Mean gaseous temperature field with heat release isolines (white: $HR = 10^7 W/m^3$, grey: $HR = 10^8 W/m^3$). The numbers denotes the limits of the zones described next.

The different contributions of each zone to the total heat release are displayed in Fig. 3.26. From this result, the global heat release presents two peaks. The most energetic one is close to stoichiometry ($z=0.054$) and a secondary peak around a mixture fraction z of 0.065 ($\phi = 1.2$). Zone 1 and zone 2 contribute each one to about 50% of the main peak (around $z = 0.05$) while the second peak of total heat release receives contributions from the three zones. As expected from the previous section, the heat release from zone 1 is centered at the bulk equivalence ratio $\phi = 0.95$ and is highly energetic but it has also a tail on the rich side. The energy released by

⁷Major limits being: Eulerian formalism, locally monodisperse spray description, numerical schemes issues.

the rich part of zone 1 is much lower than the part due to stoichiometry combustion but is still more powerful than the contributions of the two other zones. These make the zone 1 the most powerful part of the flame.

Zone 2 has the smallest contribution to the total heat release. There is almost no lean combustion and it has two maxima at $z = 0.054$ (stoichiometry) and at $z = 0.065$. Because of the proximity of the fuel injection, zone 2 experiences poor mixing prior to combustion and hence burns rich as confirmed by these results.

Zone 3 has no common boundary with the fuel injection system. Gases entering this zone have thus potentially been subject to partially burning flames as evidenced by Fig. 3.25. These burnt gases (from zones 1 and 2) induce an excess in concentration of CO_2 compared to CO . The reverse reaction of the equilibrium CO/CO_2 thus dominates and leads to the negative contribution around $z = 0.06$. Note that in this specific region, the fluctuating releases of liquid pockets seen in the previous section also bring flammable mixture which contributes to the second part of the stoichiometry peak of the total heat release, HR , as evidenced by Fig. 3.26.

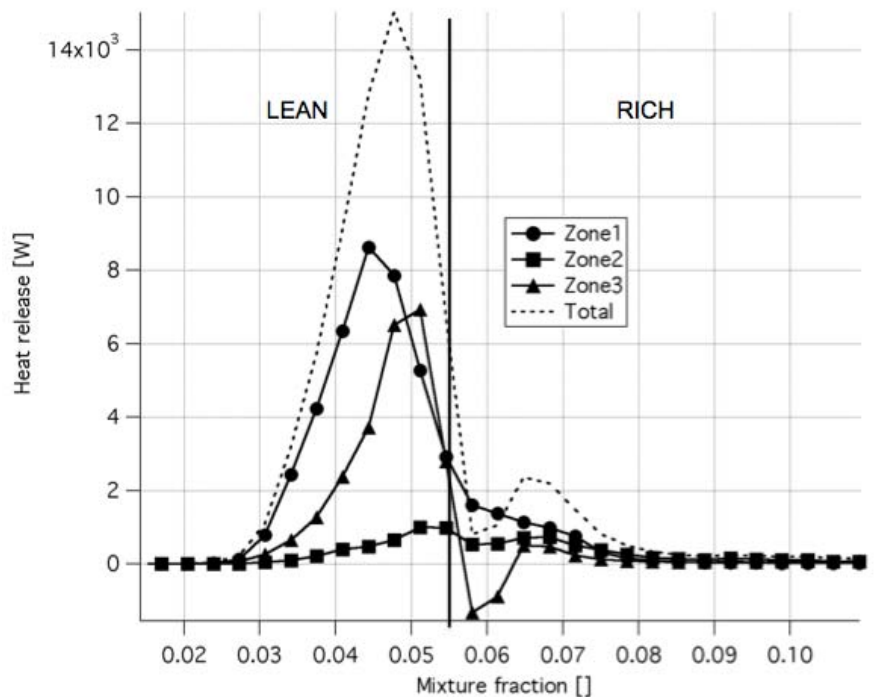


Figure 3.26: Heat release (integrated over the volume) function of the mixture fraction, and different zones contributions. Note that the mixture fraction being non dimensioned, the heat release "per mixture fraction" keeps [W] as unit.

To go further in details for the different combustion characteristics of each zone, variables of interest are drawn in scatterplot format in Figs. 3.27- 3.30.

Figure 3.28 displays sharply the mixing and burnt lines while in Fig. 3.27 the intermediate states are more visible. In zone 1, Fig. 3.27b), it appears that the mixture is essentially lean with various stages (purely mixing, burning and burnt). This is due to the long path that the

liquid injected fuel has to follow to reach this zone, it has time to evaporate and mix with air. In addition, according to the proximity of the air entrance, it is expected to mix leaner than the bulk equivalence ratio. In zone 2, Fig. 3.27c), the mixture starts from lean mixing up to rich burning, there is almost no point on the lean burnt gas line. Indeed, contrarily to the zone 1, the liquid fuel injection is in contact with zone 2 and the mixture burns rich as expected. Zone 3 has no proximity to any entrance (air or fuel), the mixture reaching this part has already experienced mixing and burning. Hence in Fig. 3.27d) the points are packed along the burnt gas lines (lean and rich).

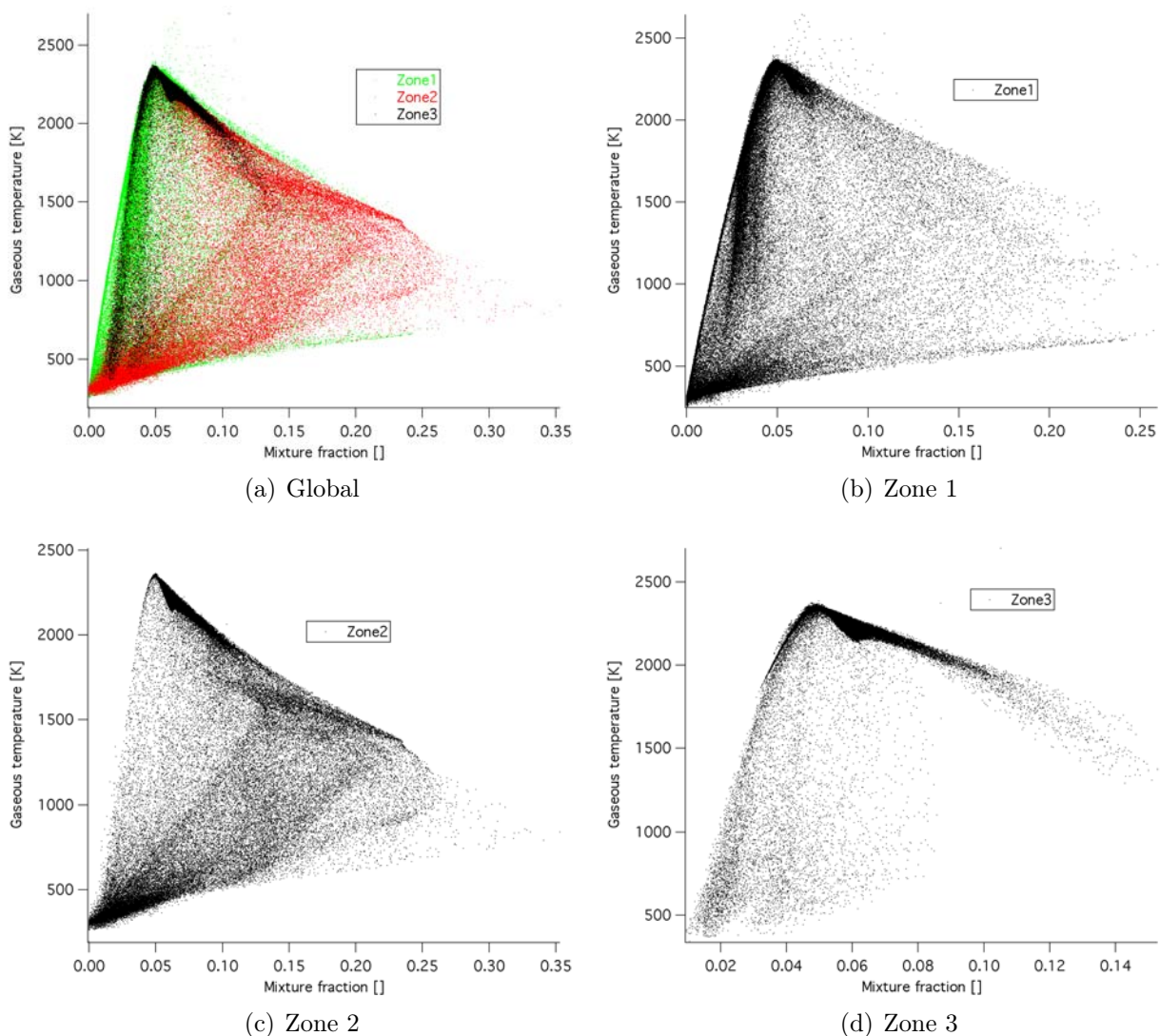


Figure 3.27: Scatterplots of gaseous temperature according to the zone splitting

Figure 3.28 confirms the previous observations: zone 1 mixes and burns mainly lean while zone 2 has no points on the lean burnt gas line. In zone 3, Fig. 3.28d), the mixture is mainly

rich burnt gases. However, the burning points (between the mixing line and the burnt gas line) are on the lean side

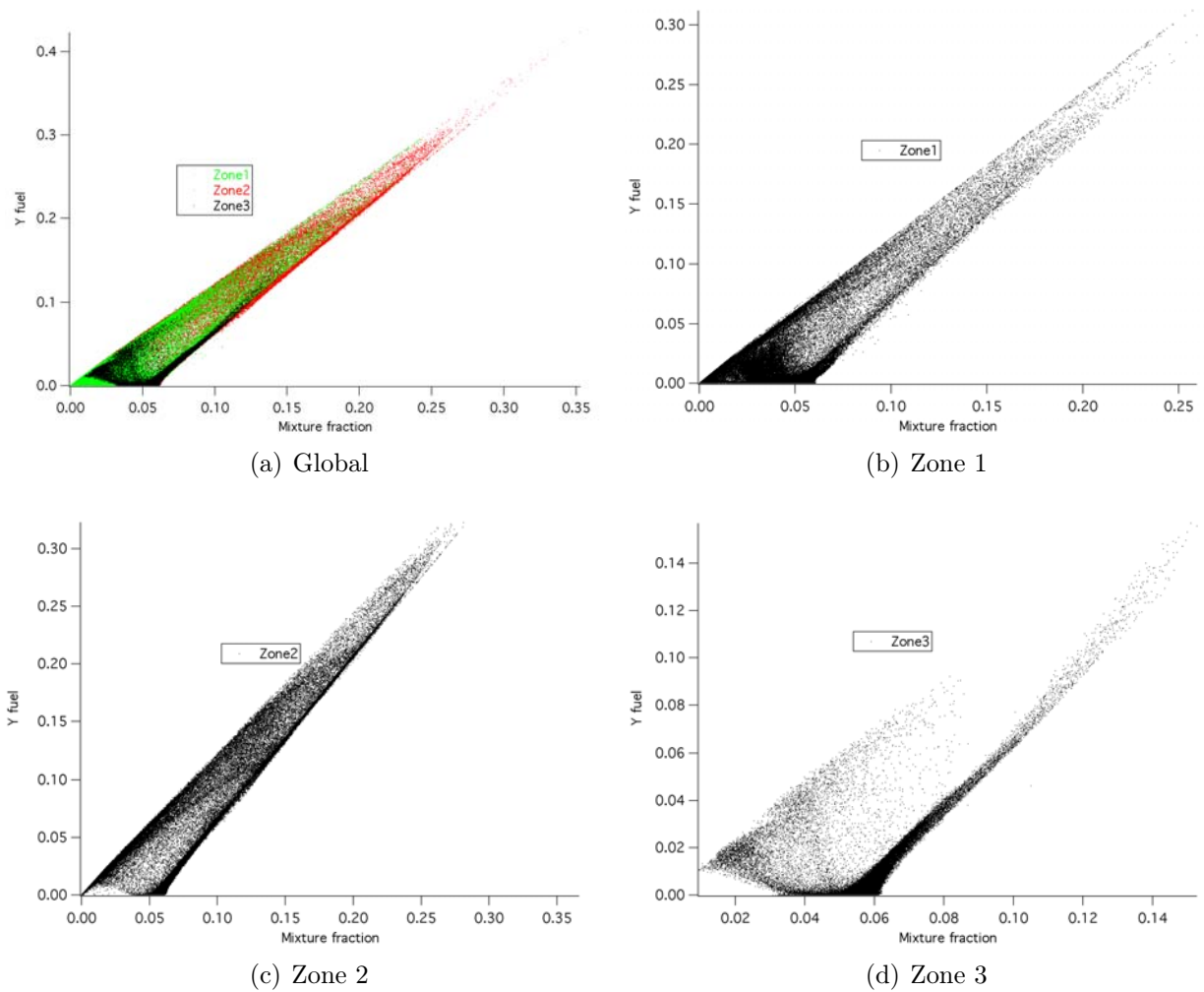


Figure 3.28: Scatterplots of fuel mass fraction according to the zone splitting

According to Fig. 3.26, Fig. 3.29 underlines the small contribution of the rich combustion occurring in zone 2. Indeed, in spite of the small number of burning points in zone 3 (i.e. small burning volume), the combustion close to stoichiometry is more effective.

The fuel being injected as a liquid, it may be interesting to follow the evolution of the liquid volume fraction in these different zones and the eventual influence on the combustion in MERCATO. At the liquid injection, according to the FIM-UR methodology, the maximum liquid volume fraction α_l is about 10^{-2} . Because of the clipping on the minimum diameter ($5\mu m$), α_l can not be smaller than 10^{-7} , hence points next to this value (Fig. 3.30) behave like passive scalars⁸. This explain the accumulation of points close to $\alpha_l = 10^{-7}$ and the bulk equivalence

⁸because of the clipping, they do not evaporate anymore, and because of their small diameter and low load,

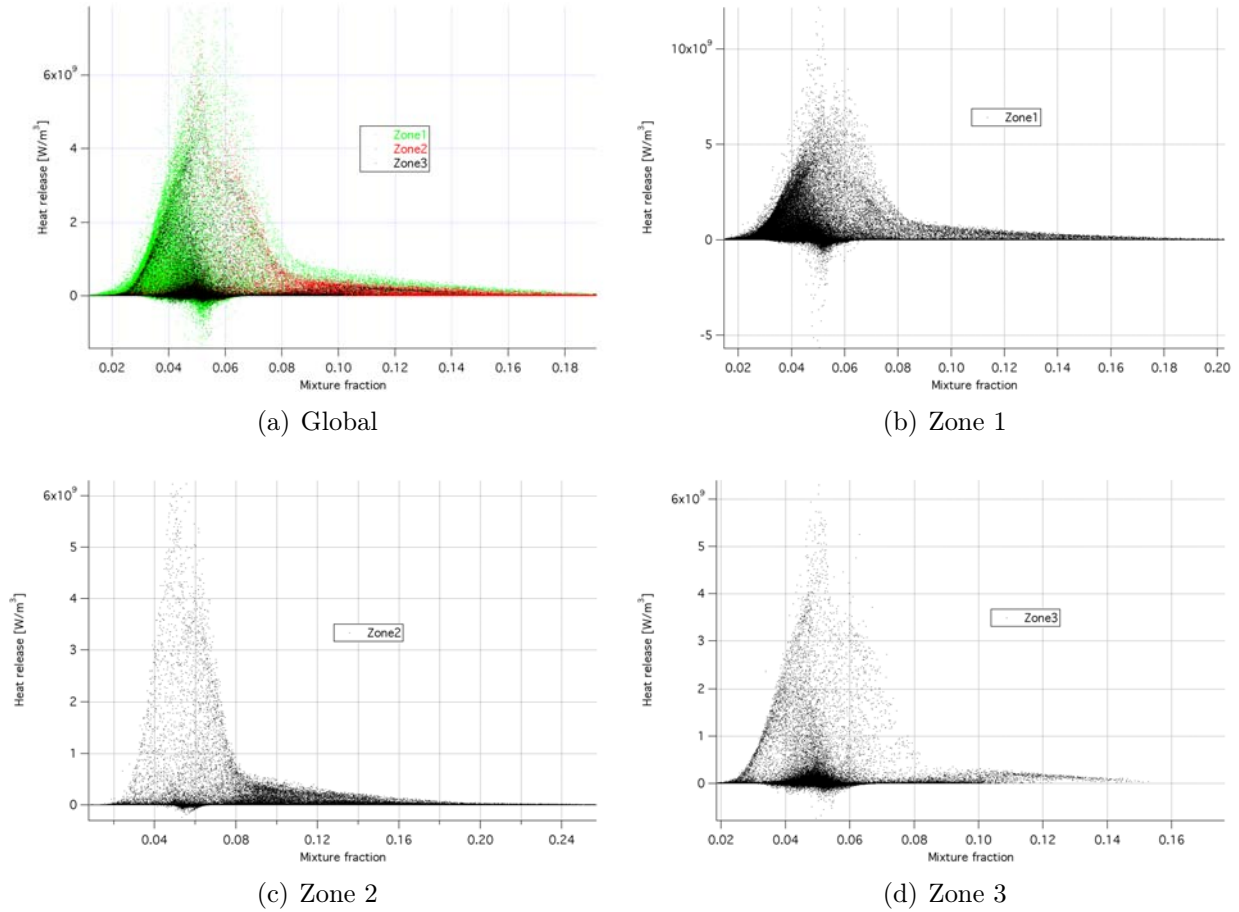


Figure 3.29: Scatterplots of heat release according to the zone splitting

ratio $\phi = 0.95$ ($z = 0.051$).

In zone 2 (Fig. 3.30c), the closest to the liquid injection, a large number of points are highly loaded (more than 10^{-4}). When evaporating, they produce rich mixture. After evaporation, they begin to mix and the mixture fraction decreases.

In zone 1 (Fig. 3.30b), the kerosene is already partially evaporated which lowers the average α_l . The sudden contact between the pure air from the swirler and the liquid just next to the nozzle is identified by the numbering points close to $z = 0$. The progressive evaporation, mixing and burning bring these points to pack next to the stoichiometry and at the clipping liquid volume fraction.

When the fuel reaches the zone 3 (Fig. 3.30d), it is almost evaporated and mixed. Hence, all the points are packed next to the stoichiometry and at the clipping α_l .

This first attempt to describe the potential combustion regimes of a swirled two-phase flow flame highlights complex and multiple interactions leading to various local conditions. Indeed,

they do not affect the gaseous phase.

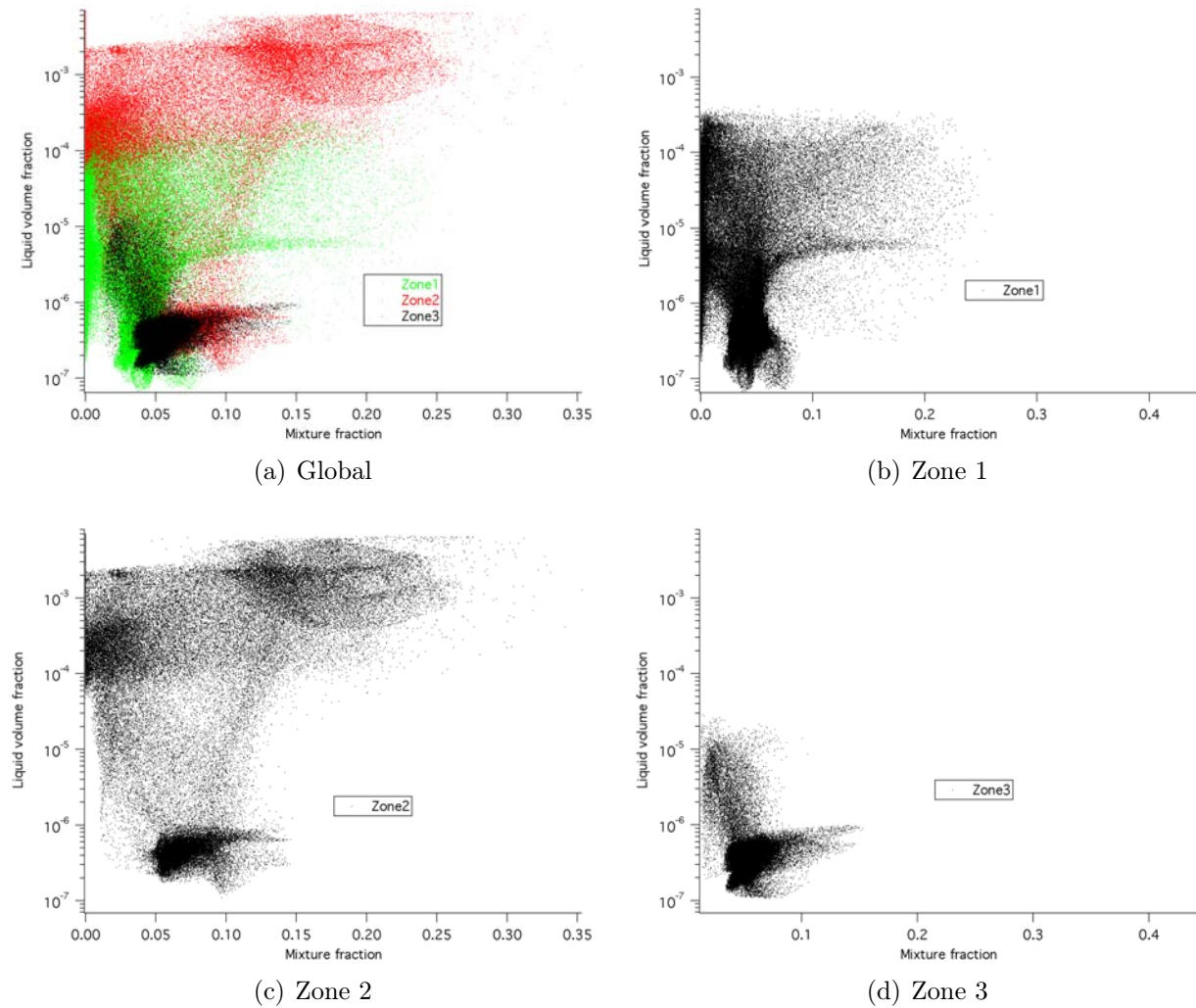


Figure 3.30: Scatterplots of liquid volume fraction according to the zone splitting

despite the strong approximation of locally monodisperse droplet diameter and the numerical issues coming from the Eulerian formalism, a wide range of combustion regimes is observed from lean to rich combustion, premixed to diffusion flame as well as fuel droplets within the burnt gases. All of these imply specific design of the combustion model and chemistry. Indeed, burning from lean to rich implies a wide validation of the chemical kinetic scheme to get the right reaction rates, the right flame velocity and adiabatic temperature. Second, dealing with diffusion flame while using a thickened flame model may be inappropriate since there is no flame thickness clearly defined like for the premixed ones. Finally, having fuel remaining in the liquid phase within the burnt gases may lead to heterogeneous combustion or even pyrolysis. Hence, in addition to the limitations highlighted from the non reacting study (section 3.4), to rigorously compute such complex flame a lot of phenomena have to be taken into account for modeling.

3.6 Conclusions

LES of stationary two-phase flows have been performed. The results obtained in the non-reacting case have been validated against measurements with extensive comparisons of the velocities profiles. After a validation of the reacting case with the available data, a deeper analysis the combustion observed in this configuration is done. It underlines the difficulty to properly integrate the liquid phase. Indeed, the carburation of the chamber and hence the forecoming evaporation is closely linked to the dispersion of the spray right after the injection. This carburation will influence the combustion regimes (premixed/diffusion) and the unsteady behaviour of the flame. Local analysis of the flame indicates that in this kind of configuration the flame burns both as a premixed and diffusion flame. If classified in terms of the distance to the fuel injection nozzle, premixed lean flame burns far from the nozzle and rich one around the CTRZ. It also appears that the most powerfull part is the outer premixed flame.

Since the ability of the LES to correctly predict two-phase flow combustion has been partly established in stationary conditions and based on the available data, the natural capacity of the LES to describe fully transient phenomena is applied to test its capacity for ignition phenomena. In the next chapter, the stochastic behaviour of ignition and its linked difficulties like predictibility are adressed. Then, several fully transient ignition phase of a carbured chamber are presented using LES. Each ignition sequence using as initial condition a statistically converged non-reacting solution from this chapter. This will aim at understanding the ignition process to propose then an analytical model for industrial type predictions.

Chapter 4

Transient LES spray ignition sequence in the MERCATO bench

The ignition phase of a jet engine cycle is by definition a critical phase and is part of the certification of the jet engines which needs for security reasons to ignite or re-ignite in specific conditions. To fulfil such requirements, fundamental ignition study receives great interest from industry. However this fully transient phase is a complex phenomenon, not yet fully understood and controlled. Experiments show that ignition may be successful or fail in the same operating conditions, even in simple geometry lab-scale configurations [142, 143, 144]. As a consequence, ignition is usually described in terms of probability of success [37]. This probability is the result of the space and time fluctuations of the fluid state at the igniter location, and is therefore conditioned by local phenomena. To understand the process of ignition, previous numerical studies have been devoted to gaseous ignition [145, 146] and in particular demonstrate the concept of minimum energy for successful ignition [40, 147]. More recently, Garcia-Rosa [148] used zero and one-dimensional sub-models to describe the very first moments of ignition. Less work has been devoted to the ignition of a two-phase mixture, mainly because the simulation of two-phase flows still presents multiple challenges associated with the dispersed phase description (cf. Chapter 3). Note however that LES of two-phase reacting flows offer access to fully transient phenomena that could not be addressed numerically with other CFD models (other than DNS). In particular, the fully transient phase that results from a sparking ignition phase can be simulated with LES which thus provide a dynamic description of the spatial and temporal evolution as well as the propagation of the flame front until full ignition or extinction of the burner.

In the following, LES is used to reproduce the details of ignition sequences and burning of the two-phase mixture on the MERCATO bench. The objective is to validate ignition scenario and understand the probabilistic character of ignition within the limits of the LES model. In particular the main factors influencing the failure or success of ignition are identified and implications for ignition systems optimization are derived. The operating condition retained for the LES study of an ignition phase has already been computed for statistically stationary regimes: (I) gaseous non-reacting flow with evaporating droplets 3.4.3 and (II) reacting flow with droplets 3.5. Comparisons against experimental data proved the proposed strategy to be of great interest for the resolution of such complex flows. Based upon these encouraging findings and although room for improvement is clear, this chapter extends the Euler-Euler turbulent reacting LES approach to the ignition phase of the MERCATO burner.

4.1 Computational setup and meshes

The computational domain used in this chapter is the same as the one used for the stationary regime (subsection 3.3.1). All simulations use zero velocity at walls for the gas velocity. In the simulation the liquid phase follows a slip condition at walls. One of the main factors controlling the dispersion of the droplets is the description of the injection pattern. As in the stationary case there is no computation of primary atomization at the injector outlet and the EE approach relies on measurements and empirical correlations to adjust the injection condition at the atomizer outlet plane (FIM-UR methodology [123]). According to the results obtained

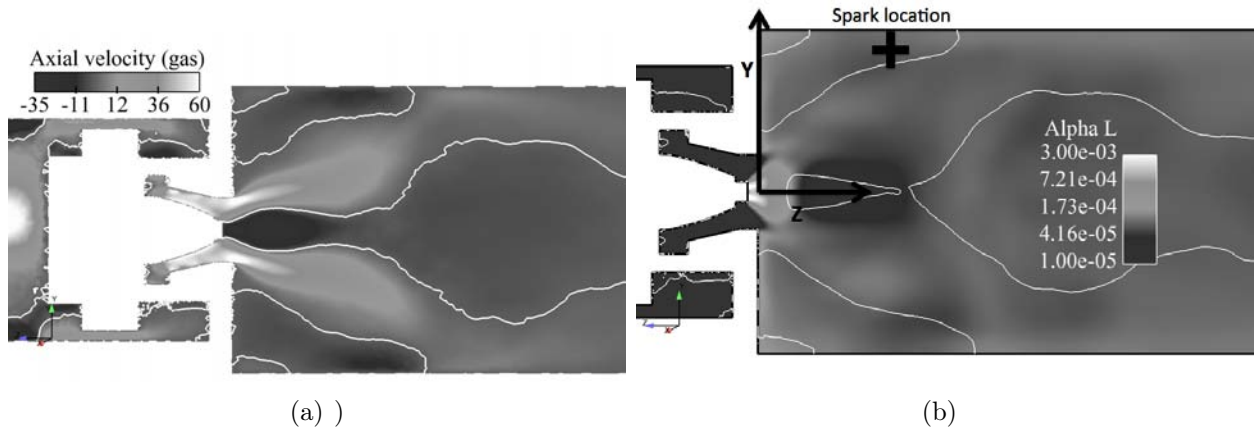


Figure 4.1: Field cuts of mean variables in the axial plan $x = 0$: (a) Axial velocity (white line denotes $U = 0$ and (b) Liquid mass fraction (white line denotes $U_l = 0$).

from stationary computations, there is no clear discrimination between TTGC and PSI. Hence, known the theoretical better precision of the TTGC scheme (vs PSI), the following ignition sequences will follow this numerical strategy.

As a reminder, Fig. 4.1 shows the flow topology issued by the cold evaporating Euler/Euler LES simulation. The spark location (dark cross on Fig.4.1b)) is in the near wall region where the swirling jet impacts the lateral walls of the combustor. This region is characterized by large temporal variations of the particle number density, flow velocities (liquid and gas velocities) and fuel concentrations. These variations are of clear importance and will impact the early stage of the initial flame kernel formation following the sparking sequence as discussed in the presentation of the transient LES. Note that this first sparking point coincides with the experimental position for which statistical analysis of the ignition probability of the whole burner is obtained with MERCATO [7].

At the earliest stages of the energy deposit modeling is required. Indeed, in reality and at sparking time, a plasma-like phase is issued by the igniter yielding non-equilibrium phenomena [149, 150]. These interactions and physics are not well understood and cannot be taken into account by the LES solver. Following this gas ionization early stage, a return to equilibrium occurs yielding an equivalent gas composition and temperature in a volume whose shape is usually affected by the flow behavior during the plasma-like phase and expansion rate. Although not known in shape and composition, this specific phase can be approximated by depositing in the LES simulation, a spherical energy source modulated in time by a Gaussian like transient phase to mimic sparking Eq. (4.1) (Energy Deposit model (ED) [151]). All of the model parameters are in this case obtained *a priori* based on the power input needed for the spark plug device. Note that no dependencies of the prediction to these model parameters are provided

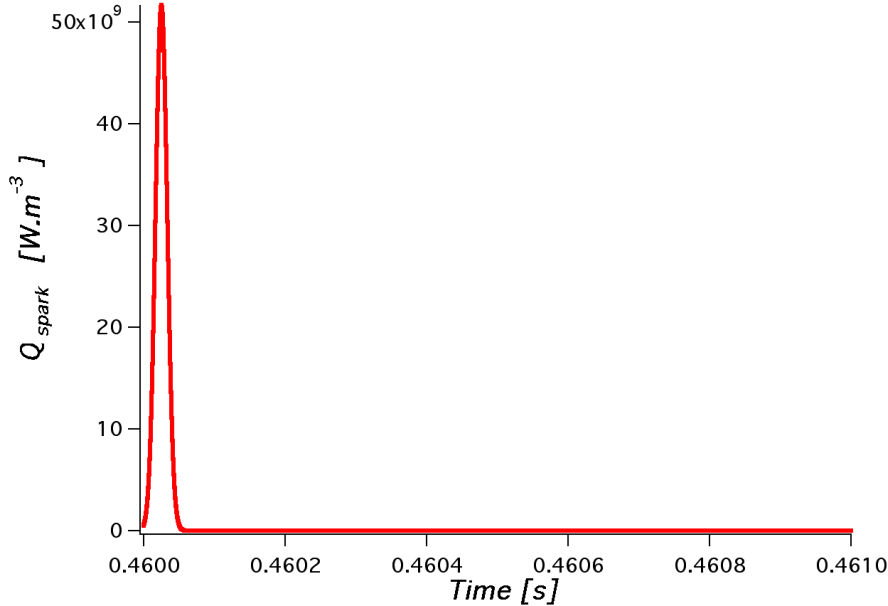


Figure 4.2: Initial energy deposit phase

in this work (although they are known to be of importance).

$$\dot{e}_{dep}(x, t) = \frac{E_{dep}}{(\sqrt{2\pi})^2 \sigma_x \sigma_t} e^{-\frac{1}{2} \left(\frac{x-x_0}{\sigma_x} \right)^2} e^{-\frac{1}{2} \left(\frac{t-t_0}{\sigma_t} \right)^2} \quad (4.1)$$

In Eq. (4.1) $E_{dep} = \int \dot{e}_{dep} dt dV = \int e_{dep} dV$ is the total amount of energy transferred by the spark to the gas, σ_x and σ_t are parameters that control the size and duration of the source term, x_0 and t_0 are the space and time coordinates of the deposit. For the simulations discussed afterwards, the spark characteristics are: $\sigma_x = 1.8 \text{ mm}$, $\sigma_t = 8.2 \text{ } \mu\text{s}$ and $E_{dep} = 50 \text{ mJ}$ (see Fig. 4.2).

In order to ease the establishment of the initial flame kernel following the energy deposit model, great care is needed in the numerical integration of the earliest instants. Theoretically the initial kernel formation is dictated by fully laminar phenomena and no artificial LES turbulent sub-model should interfere in this early stage [152]. To do so, local mesh refinement is mandatory to avoid artificial thickening (in our case $3\Delta x < \delta_l^0$) and changes of the different time-scales during this stage. The resulting mesh has about 2.8 million nodes and 13.1 million cells. The mesh characteristics are presented in Tab. 4.1. A view of the local refinement enforced at the sparking locations is illustrated on Fig. 4.3. In this work only the upper location will be detailed ($z = 56 \text{ mm}$ and $y = 57 \text{ mm}$). This mesh is hence used in the first milliseconds of the LES run which covers the energy deposit phase of Fig. 4.2 and the establishment of a local laminar flame fronts. The initial refinement, specific for ignition, is designed large enough to avoid flame front quenching when the ignition solution will be interpolated back to the regular mesh, i.e. the diameter of the refined sphere must be larger than twice the thickened flame thickness. In this zone, for the regular mesh, the cell size is of about 1 mm and the thickening

spread the flame front through three cells. This brings the thickened flame thickness on the regular mesh to 3 *mm*. In our case, not to be too close to the critical limit, the diameter of the refined sphere is four times the local thickened flame thickness. The resulting refined sphere has thus a diameter of 12 *mm* with a typical cell size of $\Delta x = 0.2 \text{ mm}$ ($\delta_l^0 \approx 0.7 \text{ mm} > 3\Delta x$). Once this initial critical transient is obtained and the initial laminar flame kernel has reached the boundaries of the refined sphere, interpolation onto the original LES mesh (shown on Fig. 3.4) is obtained and the run is continued with all LES options being activated.

Table 4.1: Characteristics of the mesh used for ignition sequences

Cell number	13 114 728
Node number	2 786 634
Mesh volume	0.31 m^3
Smallest element volume	3.2 $10^{-12} m^3$

4.2 Sensitivity of the ignition process to the initial condition

Due to the non deterministic behaviour of a turbulent flow and other interacting phenomena (atomization, micro-mixing...), processes depending on the instantaneous local conditions such as ignition are usually considered as stochastic processes in [37]. Because of these random variability at the time of deposit and the succession of events that results into different temporal evolutions. This variability is naturally embedded in the purely unsteady prediction issued by LES and can be partly representative of the physics present within the experiments. Depending on the degree of variability of the flow at the point of energy deposit, Fig. 4.1, and the time at which sparking occurs, the actual and upcoming state of the flow appear to greatly impact the preliminary instant during which the initial flame kernel will evolve. This initial transient phase will determine the success or failure of the burner full ignition. To illustrate this contrast in activity at the time of sparking and its impact on the ignition success or failure, 11 different initial fields are used for the spark location, which is subject to large flow temporal variations. The temporal evolution of the total consumption rate is shown on Fig. 4.4 for all 11 tests. During the spark, up to $t_0 + 0.05 \text{ ms}$, the curves perfectly collapse, the energy deposition dominates all other phenomena. In a second phase, still in early instants and up to $t_0 + 0.4 \text{ ms}$, the consumption rates follow almost the same slope. At this stage, the energy given to the initial kernel is strong enough to cancel the impact of turbulence, the kernel remains laminar. Then the energy density of the kernel decreasing, it becomes sensitive to local structures from turbulence. Very different evolutions are thus observed: from fast ignition to immediate failure, with intermediate behaviors where ignition starts more or less slowly and leads to complete ignition or failure.

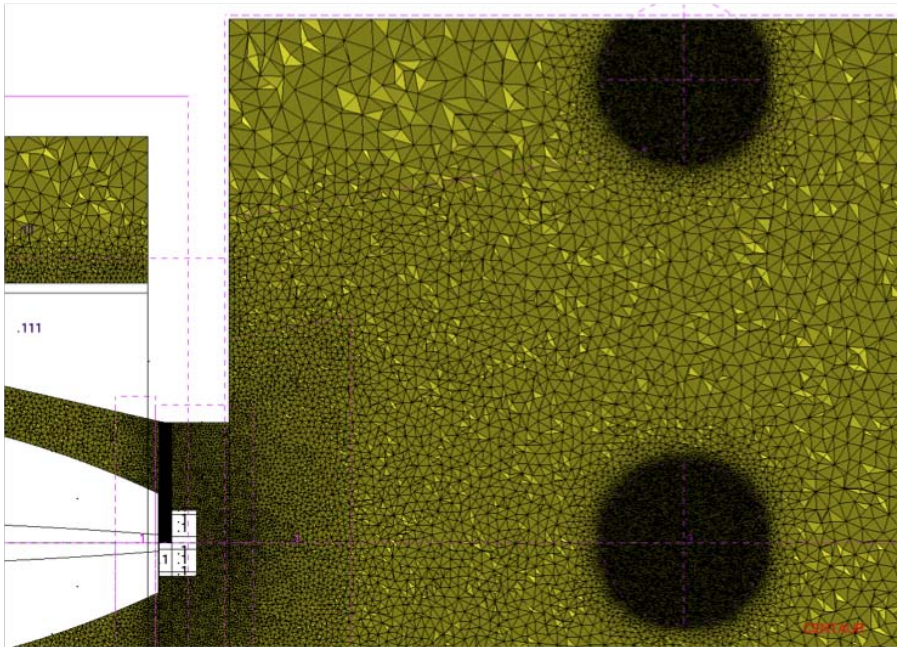


Figure 4.3: Mesh refinements for energy deposition tests

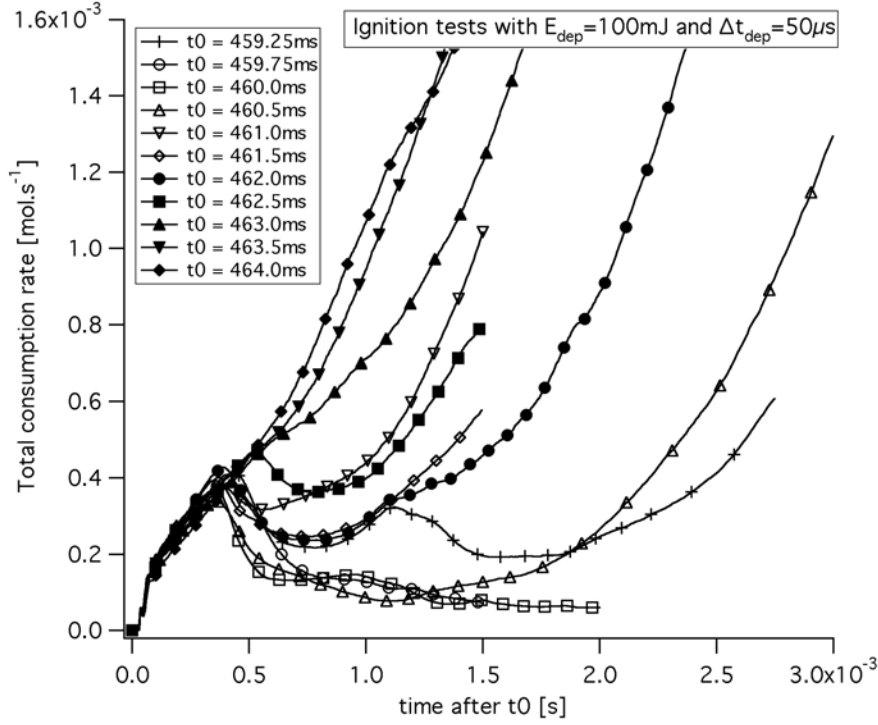


Figure 4.4: Ignition tests: time evolution of the total fuel consumption rate ($\int \dot{\omega} dV$) in the whole combustor.

The snapshots corresponding to the 11 different ignition times of Fig. 4.4, are shown on Fig. 4.5. The flame front is strongly influenced by the surrounding fluid as time proceeds toward full ignition or extinction of the burner. At given instant, some flame kernels have already begun to shrink (Fig. 4.5 b)c)) when other ones have widely spread (Fig. 4.5 i) j) k)). Figure 4.5 g) for example, has an intermediate behavior, and is potentially affected by turbulence (highly wrinkled). In the next section, two of those LES will be described in more details to identify phenomena involved in such extreme behaviours. Comparing with the experiment findings, here $P_{success} = \frac{9}{11} > P_{expe} = \frac{1}{3}$. This may be due to difficulties to get the correct reaction rate and flame speed in such conditions or more certainly the actual limits of the EE model evidences in chapter 3.

4.3 Analysis of successful/failed ignitions

This section presents the temporal evolution of two LES simulations produced out of the eleven: one successful ($t_0 = 463 \text{ ms}$) and one failing ($t_0 = 460 \text{ ms}$) ignition phase. Figure 4.6 provides a qualitative view of the two initial fields at sparking and yielding to the two extreme results. Instantaneous snapshots of the spatial evolution of the flame (through variables such as gaseous temperature, kerosene mass fraction and liquid volume fraction) within the two-phase flow fields are provided at representative instants of the fully transient phase as obtained numerically with

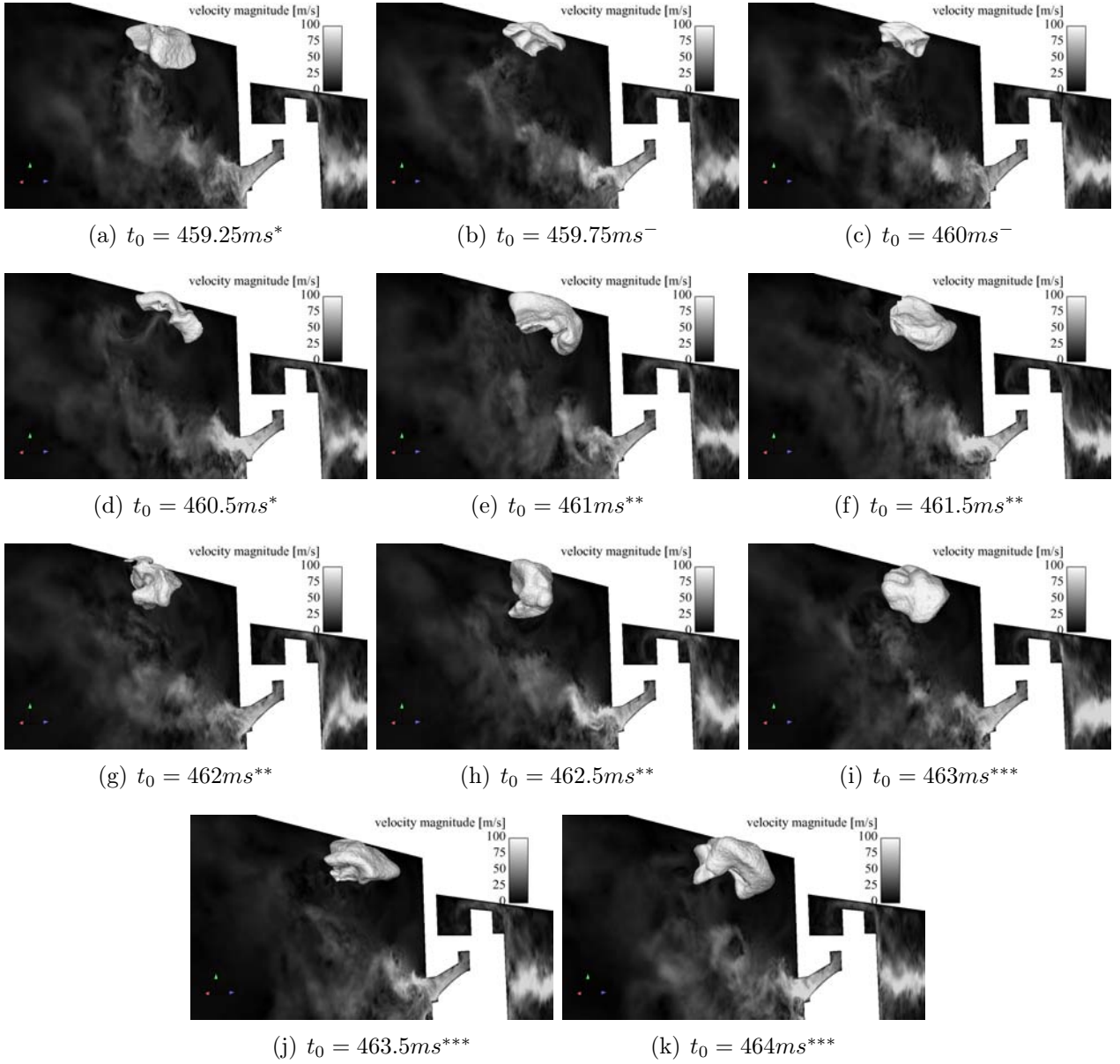


Figure 4.5: Snapshots of the 11 ignition sequences 1ms after the beginning of the deposit denoted by t_0 . The light gray isosurface denotes the $T_{gas} = 1500K$ surface. The slice is the axial median plane colored by the velocity magnitude. The following superscripts denote sequences that yield $-$: a failed ignition ; $*$: a late ignition ; $**$: a successful ignition ; $***$: a sharp ignition.

AVBP. The first intent of such diagnostics is to identify the macroscopic behaviour of the ignition phase as it proceeds from the sparking time and as obtained with the Euler/Euler reacting flow solver. Success or failure of the burner ignition is, in these cases, clearly illustrated and

in the case of a failed ignition identification, the limiting factors is underlined. At this occasion, the differences in instantaneous behaviours are highlighted prior to a more quantitative presentation of the prediction in the last paragraph (4.3.3).

Note that to ease visualization, only the longitudinal mid-plane of the computational domain is shown (although the real simulation predictions are fully 3D). The diagnostics are furthermore restrained to the primary region of the burner: i.e. the region located at the exit of the swirler outlet section.

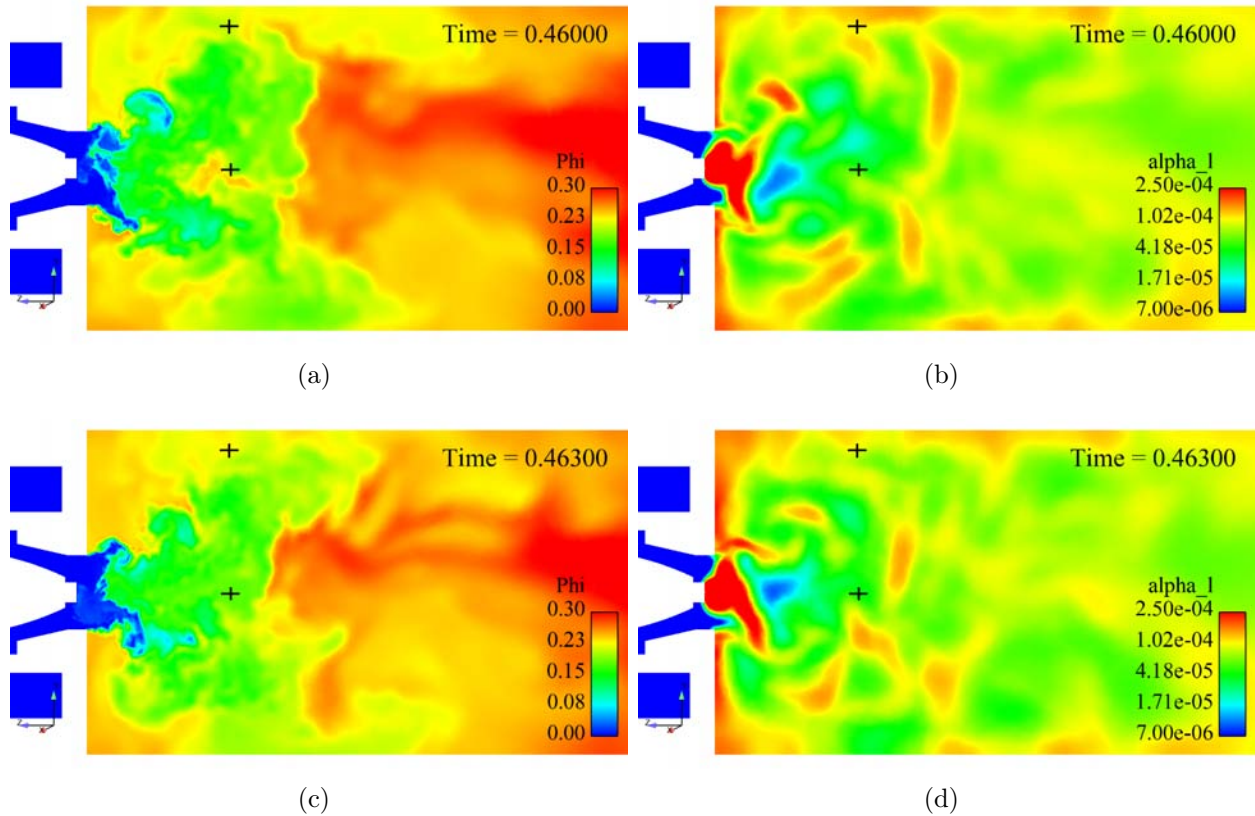


Figure 4.6: Initial solution fields. (a) Gaseous equivalence ratio (only evaporated fuel) at $t = 460ms$, (b) Liquid mass fraction at $t = 460ms$, (c) Gaseous equivalence ratio (only evaporated fuel) at $t = 463ms$, (d) Liquid mass fraction at $t = 463ms$.

4.3.1 The failed ignition: $t_0 = 460ms$

Preliminary illustrations of the LES predictions as time proceeds from the sparking time provide interesting information. In the very early phase, the energy deposit allows the establishment of a spherical flame in agreement with the intent of the spark model adopted for that part of the LES, Fig. 4.7a). The expansion of this initial kernel rapidly evolves and results from

the interaction of the hot spot issued by the model and the local evolution of the surrounding fluid, Fig. 4.7b). The first effects are the local diffusion of the heat deposited because of the colder surrounding air and liquid phase. The dominant mechanism is the heat transfer from the hot spot to evaporate the colder local liquid fuel to sustain a flame front. At the same time, the initially spherical kernel starts to be deformed by the evolving surrounding fluid and the proximity of the initial kernel with the wall. At latter times, Fig. 4.7 c) d), the kernel gets more and more deformed and loses energy (lower and lower peak temperature) due to the exchanges with the fluid. The imbalance of heat exchange combined with the local fuel liquid and gaseous mass fraction yield local quenching of the initial flame front which slowly decays until total extinction and a failed ignition LES sequence.

Views of the gaseous kerosene mass fraction at the same instants as for Fig. 4.7 are provided on Fig. 4.8. A first observation of these fields confirms the transfer of heat to the liquid phase and the production of gaseous kerosene in the vicinity of the initial spark location. This rich pocket of fuel stems from the energy deposited by the ignition model and then the combustion process that takes place around the initial kernel. Just like for the temperature field, the evolving flow field deforms the initially spherical fuel pocket. At the last instant, flame quenching has occurred, Fig. 4.8 e), and the fuel rich zone starts to diffuse because of turbulent mixing.

Figure 4.9 shows the evolution of the liquid volume fraction as the LES proceeds through the ignition phase. As underlined in the previous series of snapshots, the liquid is largely evaporated in the region of the initial spark producing a hot fuel rich kernel of gases. It is also noted on these views that at the very early instants, $t = 0.4603$ ms or Fig. 4.8b), a large valued liquid volume fraction region comes and interacts with the energy deposit kernel. It is suspected that this structures carries a lot of liquid fuel that cannot be fully evaporated by combustion or the energy provided in the early phase. Although the initial laminar flame is created, its energy is insufficient to evaporate all the liquid fuel presented by the surrounding flow field. As time goes on, the flame is quenched mainly because of the insufficient strength of the flame to counteract the heat loss to the liquid phase, Fig. 4.9e).

Many factors can explain the failure of the ignition phase as identified by LES. One potential reason already advanced in the previous discussion is the imbalance between the heat produced by the initial flame kernel and the energy needed to evaporate the liquid fuel. The local gaseous fuel rich condition is also a mechanism to take into account with the possible apparition of inflammable mixture conditions because of an excessive evaporation of the liquid fuel. Flow strain is a second source of quenching: the local turbulent flow field may induce large flow and velocity variations which strain the flame front to the point of extinction [153]. Further exploitations of these predictions are clearly needed and will be developed in section 4.3.3. However, LES of this initial transient phase is very promising especially in light of the second sparking event presented below.

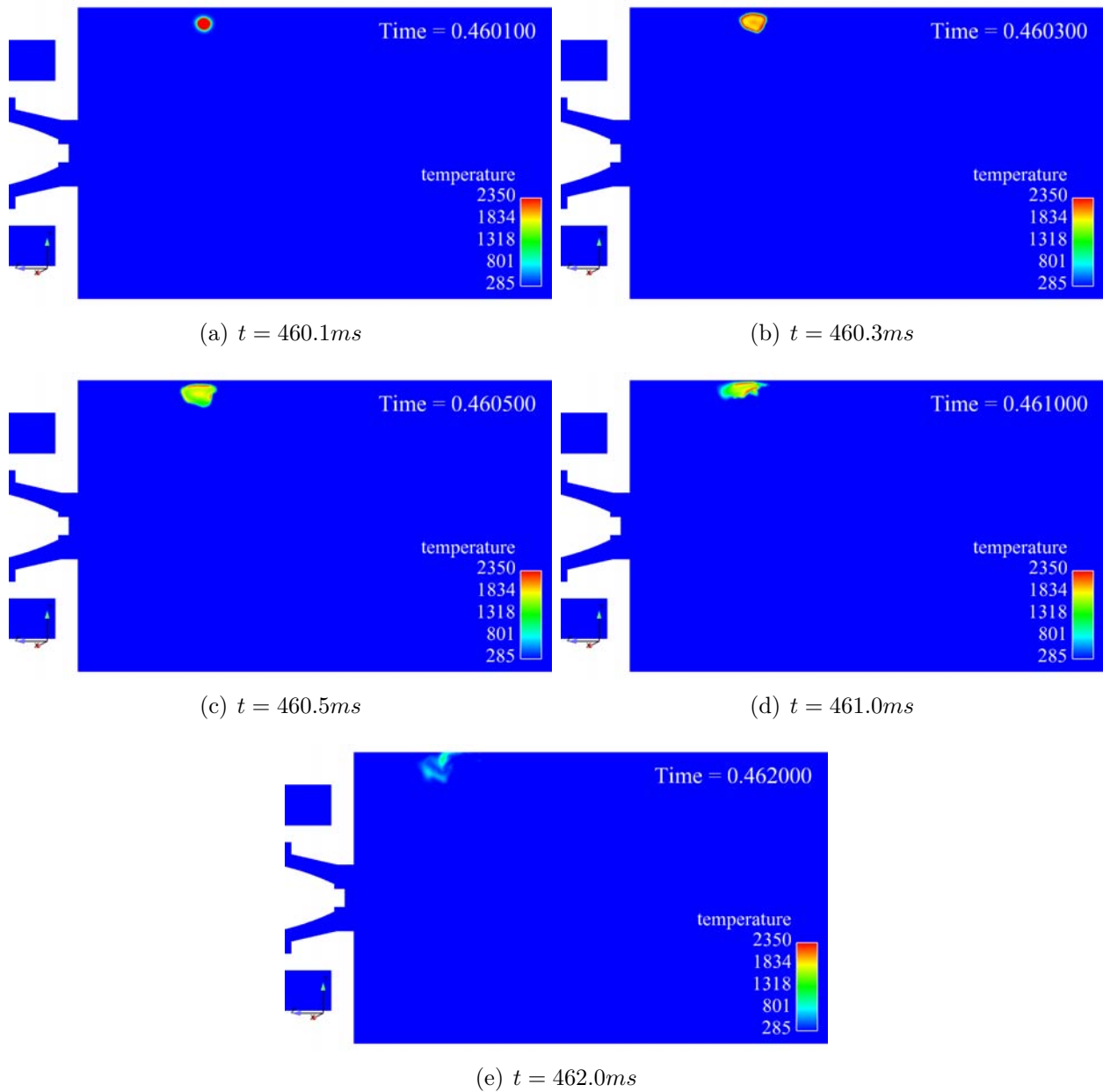


Figure 4.7: Failed ignition ($t_0 = 460ms$): field cuts of the gaseous temperature in the axial plan $x = 0$

4.3.2 The successful ignition: $t_0 = 463ms$

As already mentioned, ignition success or failure depends on the location and flow state at the time of sparking. If these local evolutions are not able to sustain adequate conditions for the creation of a propagating flame, it will result in a failure to ignite the chamber as observed in the previous case. A second attempt is here presented and discussed. The only difference between these two ignition sequences is the flow state at sparking time. As illustrated in the

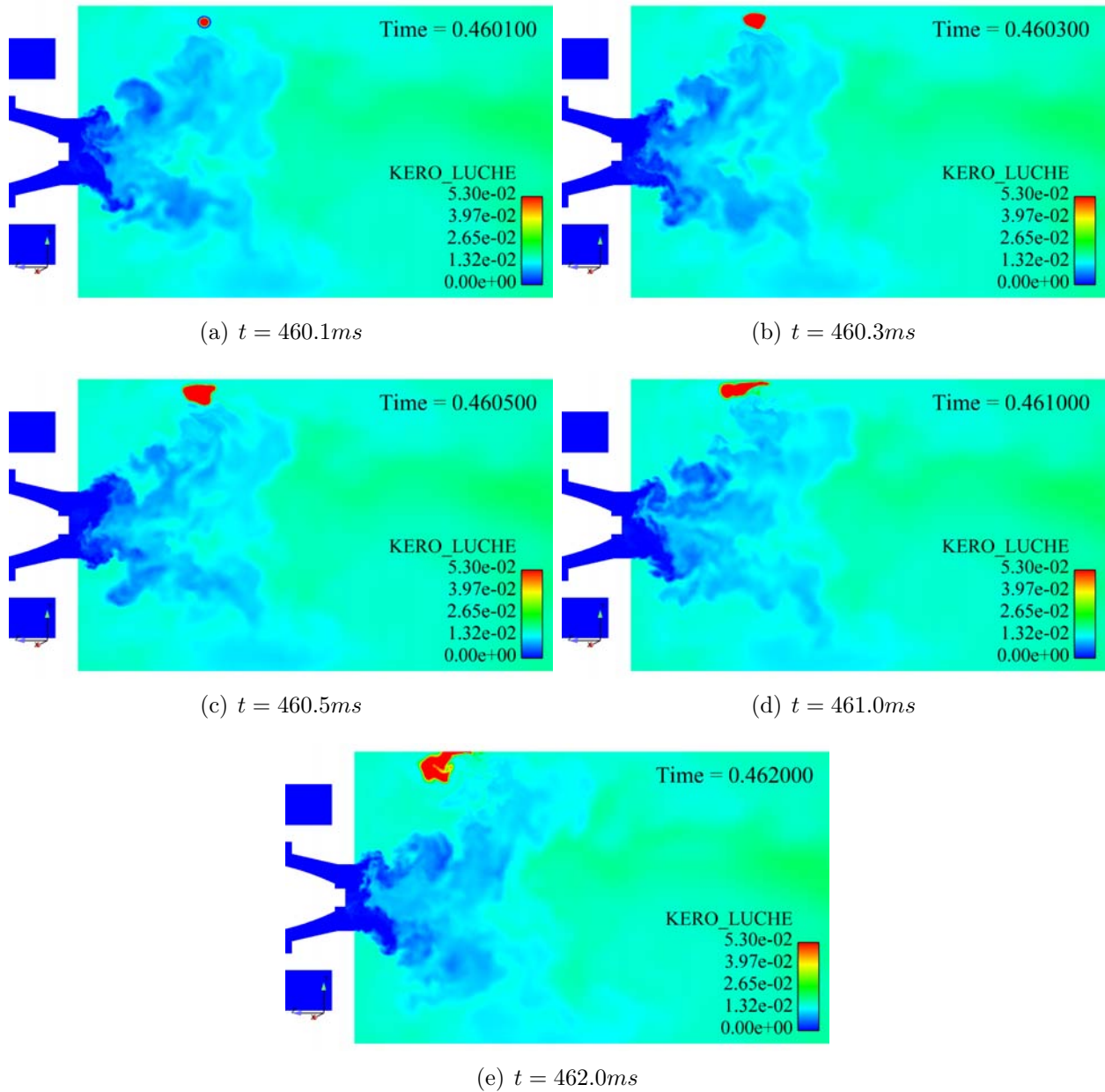


Figure 4.8: Failed ignition ($t_0 = 460ms$): field cuts of the Kerosene mass fraction (gaseous) in the axial plan $x = 0$

following predictions, the early evolution of the initial flame kernel greatly differs and yields a successful ignition of the burner.

Figure 4.10 shows the temporal evolution of the temperature field as time proceeds from the initial sparking time. Similarly to Fig. 4.7 a), the early initial time, Fig. 4.10 a), coincides with a local temperature field taking on a spherical shape as enforced by the sparking model

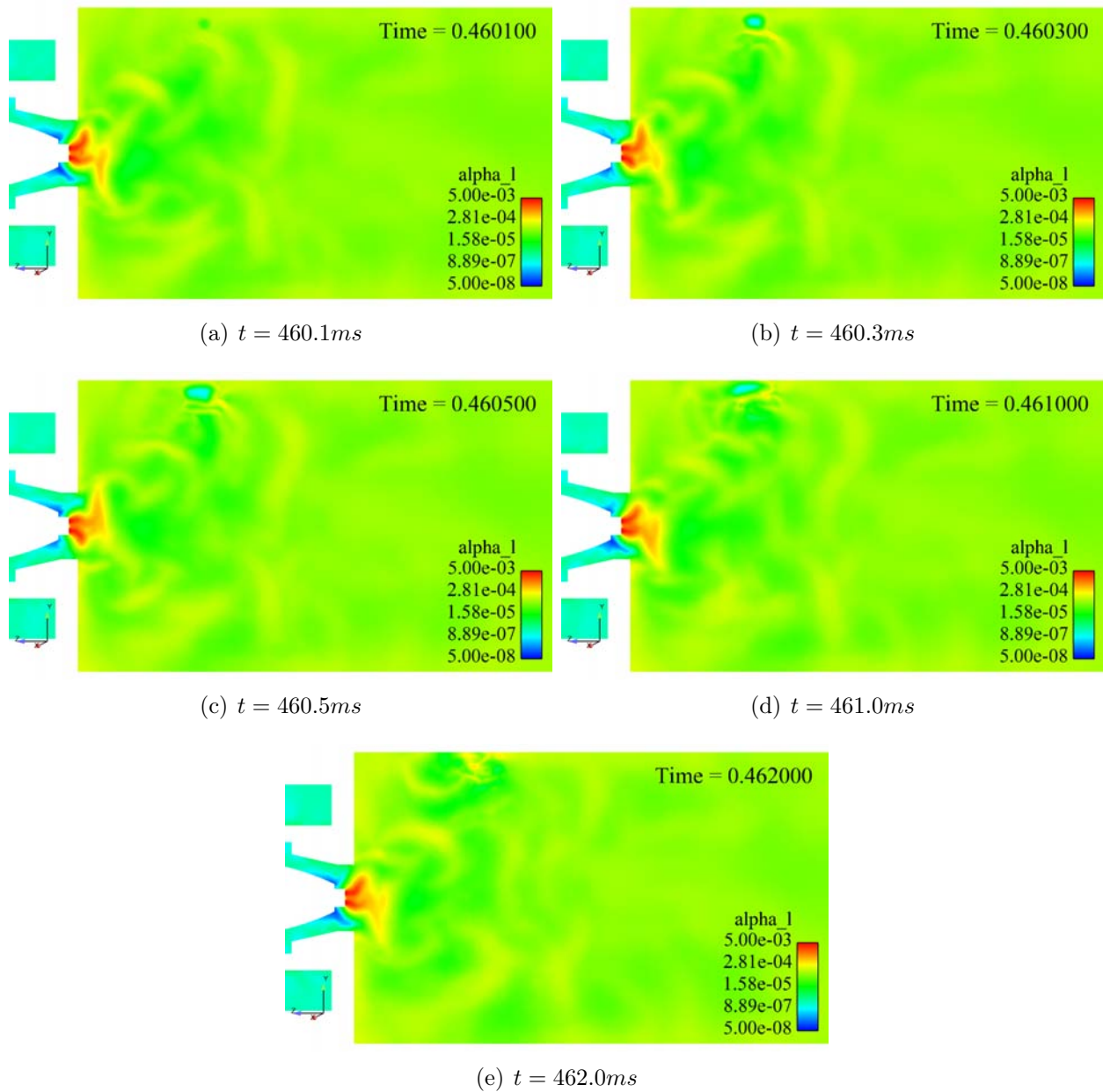


Figure 4.9: Failed ignition ($t_0 = 460ms$): field cuts of the liquid volume fraction in the axial plan $x = 0$

and little interaction with the surrounding fluid is observed. At the second time instant, the initial temperature field denotes a nearly spherical flame with colder products surrounded by a hot layer or flame front. Contrarily to the first numerical experiment, the kernel remains almost spherical if compared to the previous attempt. That observation is further emphasized by Figs. 4.10 c) and d). However and contrarily to the previous case, combustion seems to be able to sustain the local flow conditions and two distinct flame fronts are clearly visible

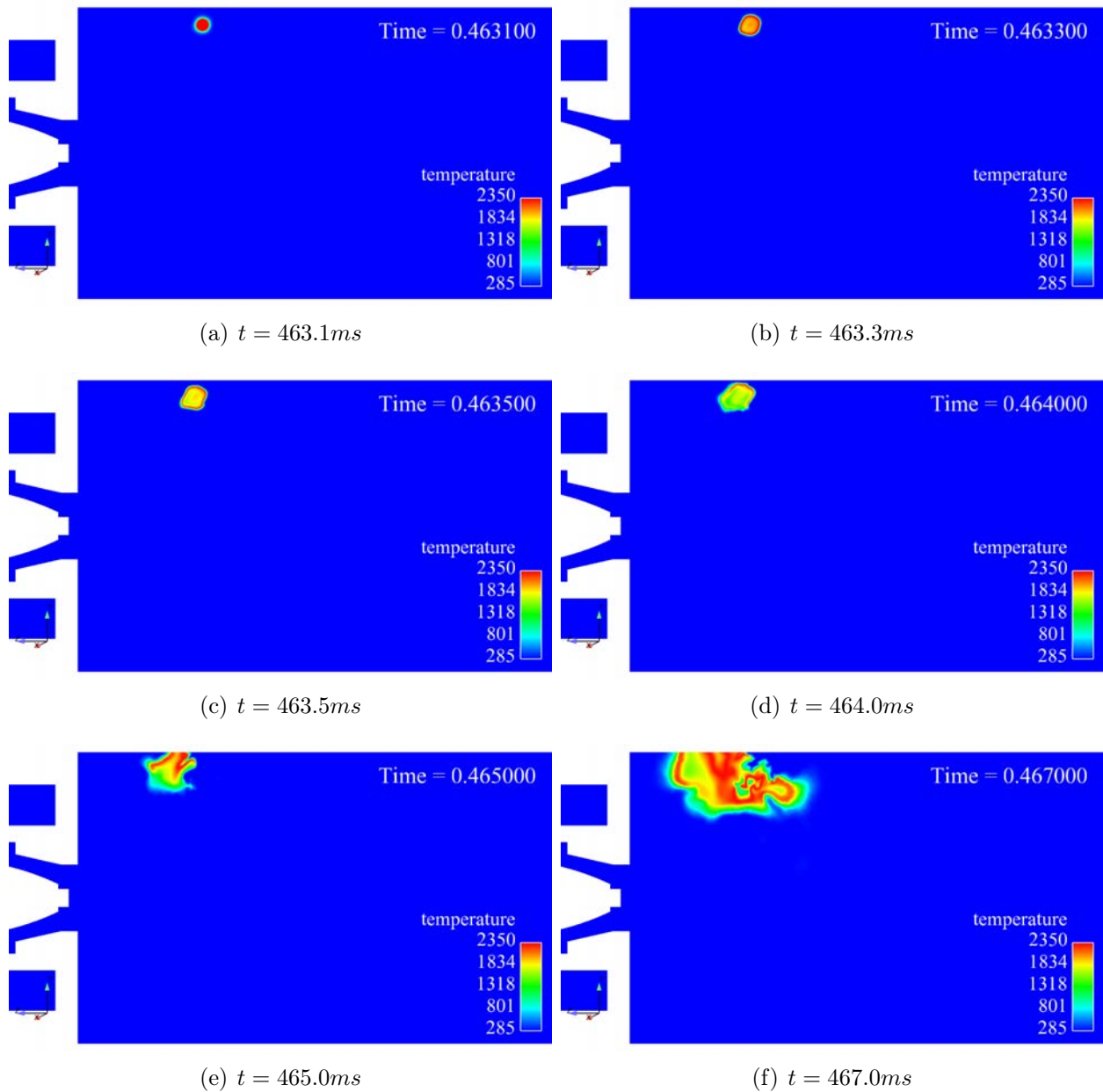


Figure 4.10: Succeed ignition ($t_0 = 463ms$): field cuts of the gaseous temperature in the axial plan $x = 0$

on Fig. 4.10 e). These two fronts keep growing, Fig. 4.10 f), producing a large region of hot products and a propagating flame which ultimately ignites the entire burner, Fig. 4.11.

Although the heat loss at $t = 0.04633$ ms results in a diminution of the peak temperature at the center of the initially spherical deposit, Figs. 4.12 and 4.13 a), the surrounding flame front seems to be more robust and much less deformed by the surrounding fluid. The main

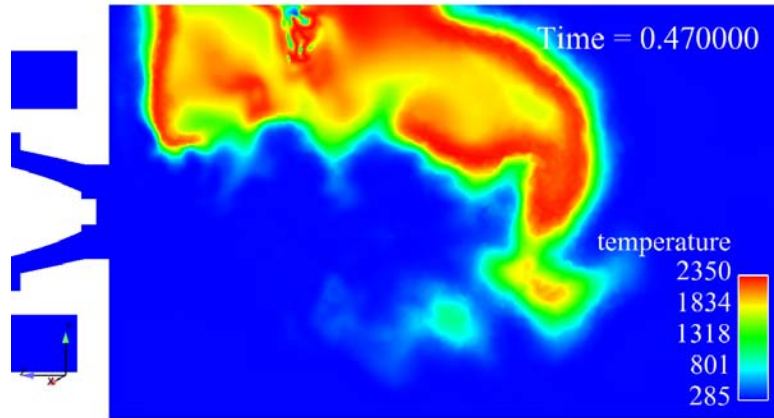


Figure 4.11: Succeed ignition ($t_0 = 463ms$): field cuts of the intantaneous gaseous temperature at a later instant and prior to the full ignition of the burner

difference between failed ignition and successful ignition is that at this specific instant the local fuel equivalence ratio (liquid plus gaseous) is much more favorable to combustion, Figs. 4.12, 4.13 a) & b). The local fluid velocities are also smaller and the initial kernel is much less constrained by the flow. At $t = 0.04635$ ms, Figs. 4.12 & 4.13 c), the differences between the two cases are clearly visible. Heat losses are still important, Figs. 4.12 & 4.13 c), d); however, the initial kernel size perdures in size and even keeps extending (contrarily to Fig.4.7 d). At $t = 0.0465$ ms, Figs. 4.12 & 4.13 e), combustion clearly proceeds and becomes powerful enough to evaporate the local liquid fuel and at the same time consumes the available mixture of gaseous fuel and air. From that time on, the flame fronts propagate respectively in the downstream direction, perpendicularly to the top lateral wall and upstream in the corner recirculation zone located between the top lateral wall and the end combustor wall.

4.3.3 Quantitative comparisons of the two LES sequences

A more quantitative analysis of the LES prediction are first obtained by directly comparing the temporal evolutions of the mean flow quantities, Fig. 4.14. In order to ease understanding only terms considered of importance are shown: i.e. the maximum gas and liquid temperatures as well as the mass transfer between the two phases (evaporation of liquid fuel into gaseous kerosene), the maximum gaseous kerosene mass fraction and the two mean reaction rates are plotted as functions of time. Note at this point that the LES modeling approach considers that combustion can only take place in the gaseous phase and no liquid combustion can occur in the predictions. Hence, at a given instant combustion is mainly controlled by evaporation and the gas fuel mass fraction as well as the two phase temperatures, which locally determine the evaporation rate which feeds combustion.

In the early instant of the two LES, Figs. 4.14 a) & b), the gas temperature and liquid

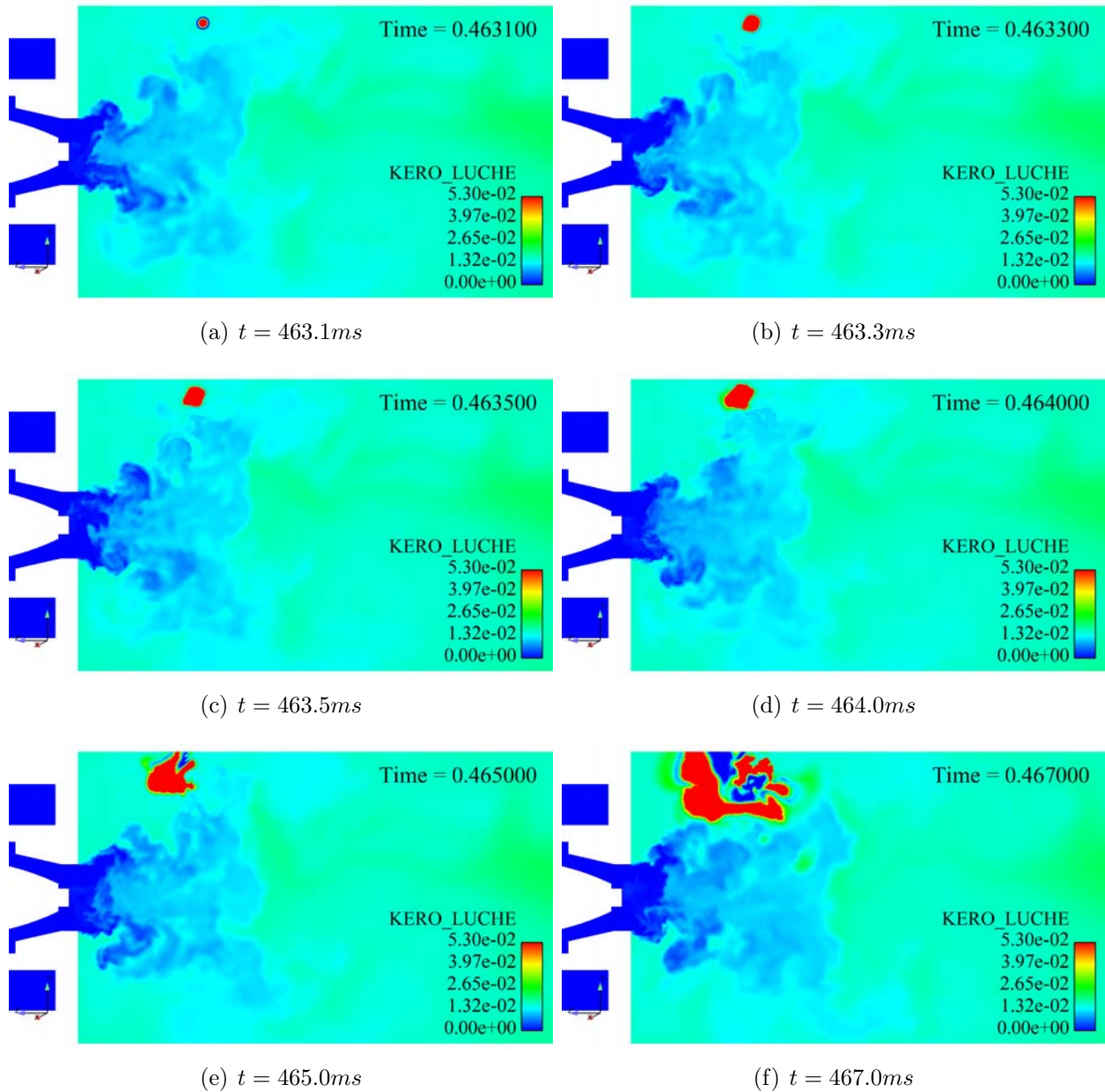


Figure 4.12: Succeed ignition ($t_0 = 463ms$): field cuts of the Kerosene mass fraction (gaseous) in the axial plan $x = 0$

temperature increase to reach the maximum peak temperature of the ED model for the gas and the saturation temperature for the liquid phase. The liquid phase temperature then remains at this level while the gas peak temperature decreases slowly towards the adiabatic flame temperature of a stoichiometric flame. It indicates that combustion has taken place and that heat loss also plays a role in the diffusion of the initial heat released by the ED model. Being very similar in behaviours, these two quantities indicate that most of the differences occur due to

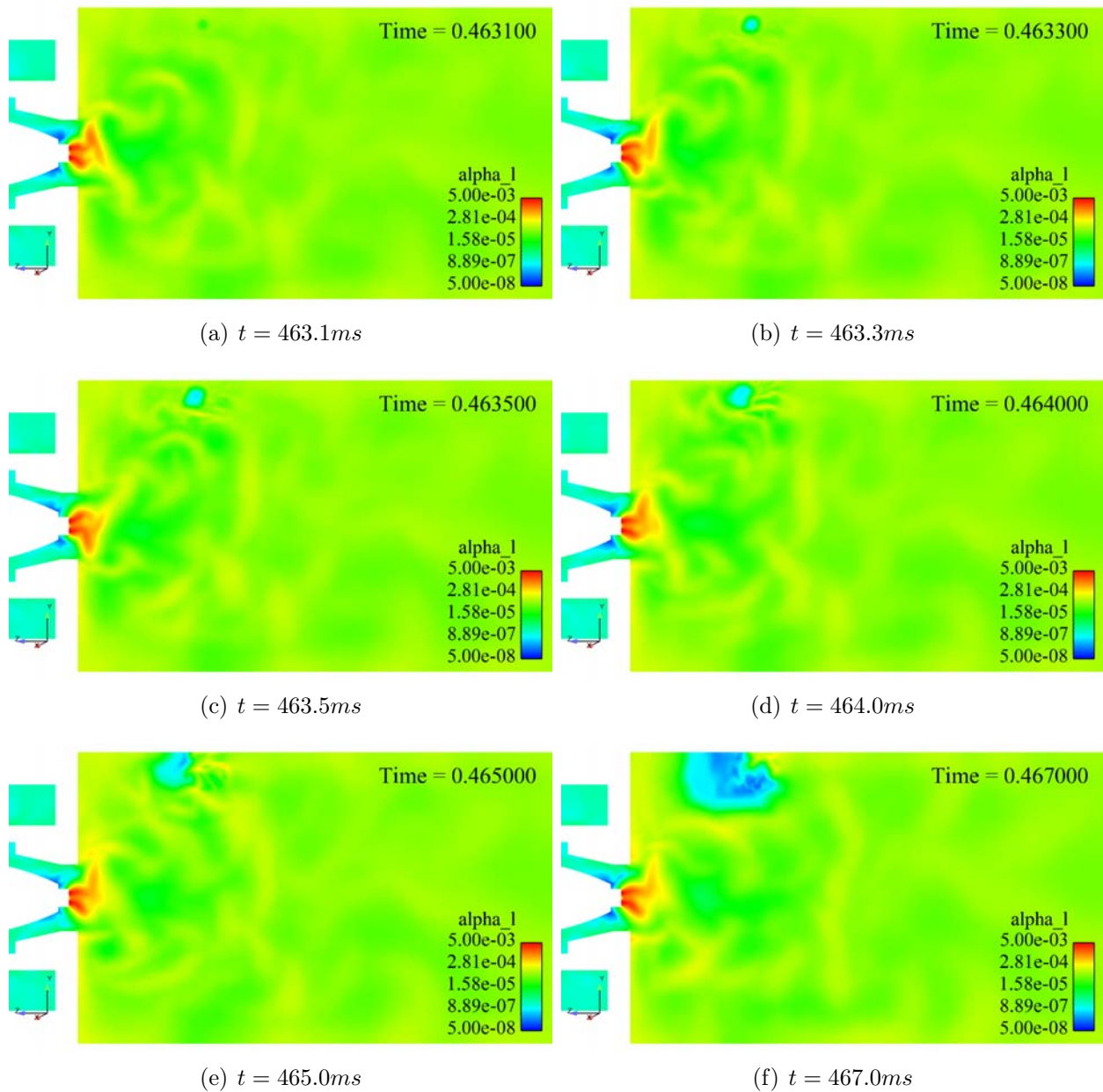


Figure 4.13: Succeed ignition ($t_0 = 463ms$): field cuts of the liquid volume fraction in the axial plan $x = 0$

the exchanges between the two phases which is partly illustrated by the evaporation rate of the liquid phase and the peak kerosene mass fraction available for combustion, Figs. 4.14 c) & d).

Two distinct temporal evolutions are identified from the evaporation rate of the liquid phase, Fig. 4.14 c) & d). At $t_0 + 0.2ms$, local conditions (saturation) and combustion, Figs. 4.14 e) & f), allow to reduce the evaporation rate with the apparition of a pseudo-equilibrium state

(constant kerosene max mass fraction for a given duration), Figs. 4.14 d). The two ignition phases then evolve in distinct manners. For the failed case, the pseudo-equilibrium is disturbed due to the local increase of the volume liquid fraction which brings cold liquid fuel to the flame front. That increase of available cold fuel yields an increase in heat loss from the flame to the liquid, which produces more gaseous fuel, Fig. 4.14 d). Combustion is thus locally reaching rich conditions and eventually goes above the flammability limit. Combustion consumption rates hence drop suddenly indicating a weakening flame up until total quenching and the failure of the ignition sequence. The successful case is much less perturbed and instead reaches equilibrium values and the steady increase of the combustion rates, Fig. 4.14 e) & f), indicate the success of the sequence.

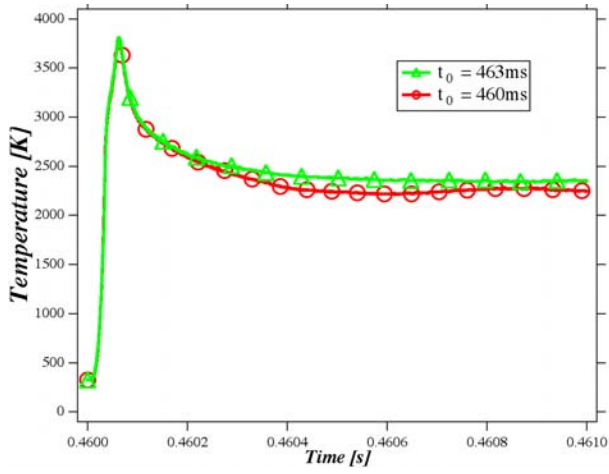
In our case, the interaction between the PVC and the spray affects the liquid phase dispersion and leads releases of these dense liquid pockets at the spark location. In the successful ignition case, $t_0 = 463 \text{ ms}$, during the initial kernel expansion, the local conditions remain stable and favorable. However in the failure ignition case, $t_0 = 460 \text{ ms}$, after 0.3 ms , a dense liquid pocket brings, through evaporation, the local equivalence ratio above the flammability limits. Hence, locally, the total equivalence ratio can vary from lean to rich which explains the different evolutions observed in LES. It is clear from these evolutions that LES can identify the impact of different interactions between the first flame kernel and the temporally and spatially evolving fluid state. However, the accuracy of the ignition predictions are first dependent on the quality of the prediction of the instantaneous fluid state from cold LES. Indeed, as previously highlighted (chapter 3), the limitations in terms of liquid dispersion of the Eulerian monodisperse description may influence the carburation of the chamber and thus the initial condition for spark ignition. In the future, more investigations are still needed for this approach to offer more detailed diagnostics. Modeling of ignition is a second issue and although the present predictions are very encouraging other approaches need to be tested to guarantee the observed solver response [145, 146, 151, 152]. Finally detailed experimental diagnostics are required to fully validate such simulations.

4.4 Conclusion of part II

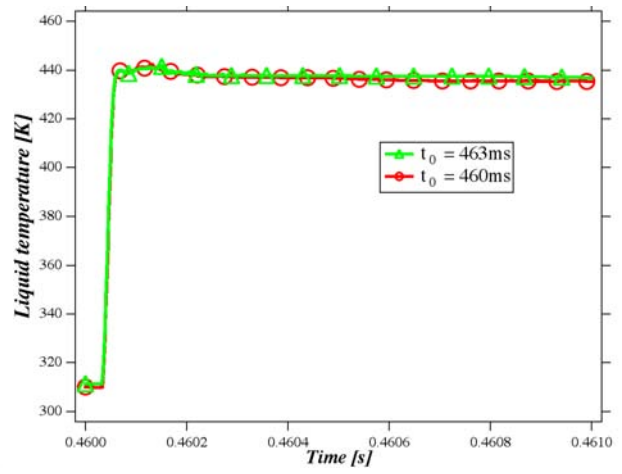
Predictions provide reasonable qualitative agreement with available data provided by ONERA [7] for both cold and reacting stationary conditions. Issues pertaining to the proper treatment of the two-phase inflow conditions are nonetheless highlighted and stress the potential importance of the primary and secondary atomization processes that cannot be properly addressed as of today. Despite this initial shortcoming of the proposed numerical strategy (local monodispersion, infinite droplet conductivity, thickened flame model,...), the stochastic nature and more precisely the importance of the initial state of the fluid in the region of the igniter is evidenced by the 11 LES of an ignition phase. These seem of primary importance to determine the success or failure of the ignition of the burner. Indeed, for identical operating conditions a very large variability has been observed, from failed ignition to quick growth of the initial flame kernel.

This variability underlines the difficulties to predict ignition even if the mean local conditions seem favorable. One single LES of an ignition sequence is clearly not enough to conclude on the behaviour of the flame during this transient phenomenon, and only statistics like ignition probability will really give applicable results.

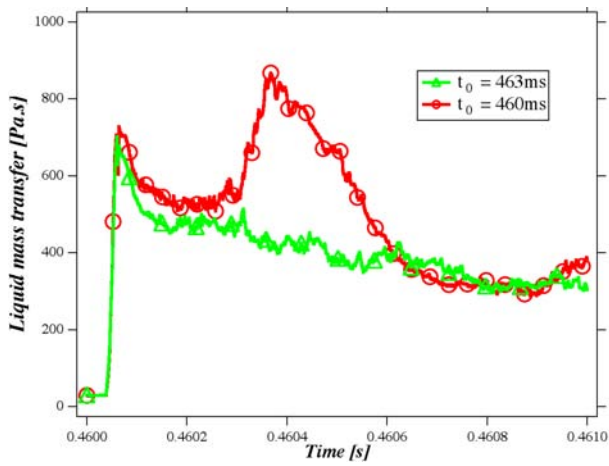
However, performing LES of ignition sequences to construct such probabilities is too expensive. To evaluate if the chamber will be ignited, at least 10 *ms* of physical time (based on previous simulations) have to be computed (and up to 70 *ms* in some cases). For MERCATO, which is an intermediate in terms of complexity between academic burner and real combustion chamber, it takes about 5000 CPU hours to compute 8 *ms* of an ignition sequence. To have statistically converged probability, at least 50 different initial fields have to be tested (to get the first statistical moment). Using a map of 10 by 10 positions (which gives poor resolution) brings the total CPU cost to 25 millions hours for just one operating conditions. Another way to provide ignition probabilities needs clearly to be developed. This is the objective of the part [III](#).



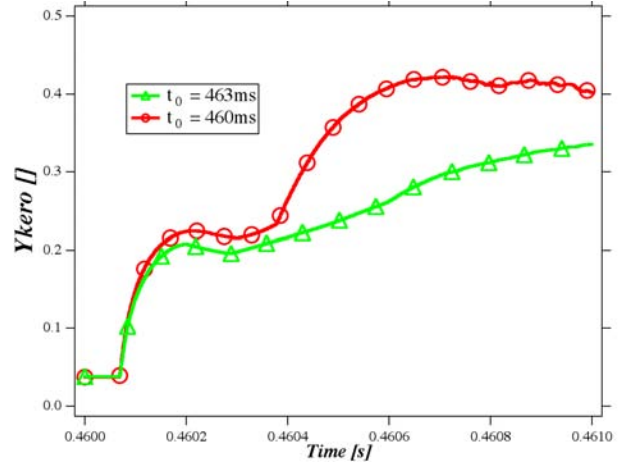
(a) Gaseous temperature



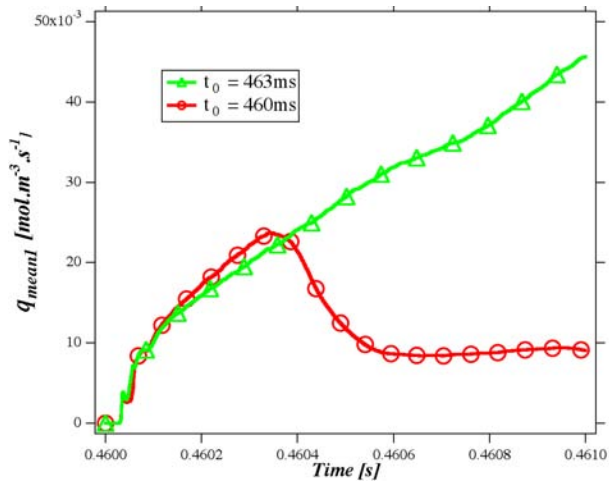
(b) Liquid temperature



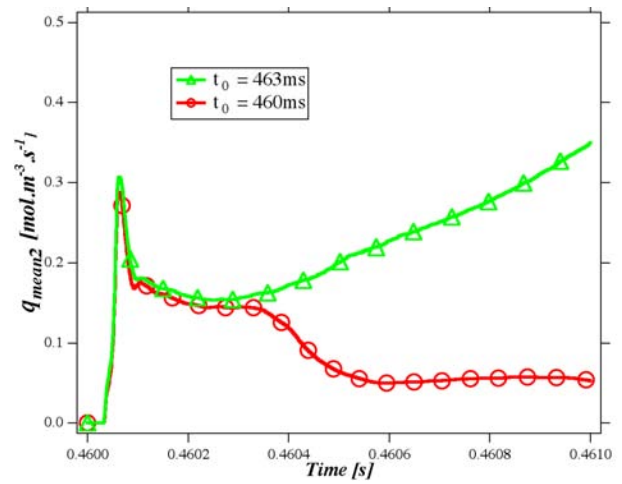
(c) Liquid mass transfer



(d) Evaporated kerosene mass fraction



(e) Reaction rate of the fuel oxydation reaction



(f) Reaction rate of the equilibrium CO/CO_2 reaction

Figure 4.14: Temporal evolution of interesting variables

Part III

Methodology for ignition prediction of two-phase flows

Chapter 5

The I-crit-LES approach

5.1 The notions of ignition probability

As seen in chapter 4 and underlined by Pr. Mastorakos in his review on ignition [37], the stochastic behaviour of the ignition process requires the introduction of an ignition probability to be quantifiable. Among the identified mechanisms impacting the success or failure of an ignition sequence, one can list :

1. It may be assumed that the statistics of turbulent mixture fraction fluctuations at the spark location determine the probability of whether the spark samples flammable mixture or not. Hence, it cannot be treated based only on the mean values. This concept was first put forward by Birch *et al.* [38, 39] who introduced the term *flammability factor*, F , for the integrated value of the mixture fraction pdf between Φ_{lean} and Φ_{rich} . F is the probability of finding nominally flammable fluid at a point and this probability, to a first approximation, can be used to discuss the statistics of spark success.
2. In reality, ignition success depends also on the size and the energy deposit leading to the definition of the Minimum Ignition Energy (MIE). This concept has been first introduced by Ballal and Lefebvre in [5] and then widely studied and extended [40, 41, 42, 43] from quiescent gaseous mixtures to heterogeneous fuel-air mixtures.
3. Finally, the possibility that the kernel can be quenched by high local strain cannot be discounted, since it is known that this may occur during forced ignition of turbulent mixtures [154, 155]. The probability of igniting a kernel is thus the result of many factors and is not necessarily equal to F .

In the specific context of aeronautical burners, the propagation of the turbulent flame to the fuel injection system and its stabilisation is not certain although they are clear pre-requisites for the ignition success of the engine. The probability of igniting the whole chamber is thus even lower than the one of igniting a flame kernel. This one burner ignition process is not local and for the moment has not been evaluated analytically [44, 45] although research is going on. Building the ground for a simple analytical model predicting the ignition probability of a single burner is clearly of interest and is the actual objective of this chapter.

5.2 Identification of the relevant phenomena

Building an analytical model to predict ignition probability based on cold flow data is the objective of the section.

For this model called I-crit-LES, a general ignition scenario is built, leading to a series of analytical criteria, which are all necessary for successful ignition. These criteria are exclusively based on the non-reacting flow (i.e. before ignition) local conditions, and may be applied to instantaneous realisations of the flow. They are introduced to model the controlling processes of

ignition and to identify the limiting phenomena in many situations. Applying these deterministic criteria to a set of instantaneous solutions (LES snapshots), used as a statistical sample of the flow, a probability of ignition may be calculated at each point in the combustion chamber. In the previous chapter 4, LES of full ignition sequences in a swirled kerosene/air flow were presented to illustrate the phenomena which the I-crit-LES model has to take into account. Taking one flow realisation, sections 5.2.1 and 5.2.2 establishes the ignition scenarios and criteria. Then section 5.2.3 shows how a set of instantaneous flow solutions can be used together with the criteria of section 5.2.2 to compute an ignition probability. The difficulties to ignite due to high local strain are taken into account through the addition of a specific criterion detailed in section 5.2.5. Since, this criterion is very difficult to evaluate (evaluation the extinction strain) and that it may be of primary importance for the prediction of ignition under purely gaseous conditions, results of the I-crit-LES methodology with and without this criterion will be compared. To finish, the model for ignition prediction will be applied to real combustion chambers and compared to experimental results in the next chapter 6.

5.2.1 The ignition scenario used in I-crit-LES

In most aeronautical applications, ignition is produced by a spark or a laser which deposits a certain amount of energy in a cold mixture of gas and droplets. The following ignition sequence is considered as complete and successful if a stabilised flame is installed at the end of the process. The main objective of the current analysis does not restrain to the local ignition of the first flame kernel (like in minimum ignition energy studies in premixed flames [147, 156]) but rather try to predict if the global stabilisation of the flame is obtained depending on the configuration and overall operating condition.

The process to evaluate hence starts with the creation of a small kernel just after the spark or laser discharge. The deposited energy must therefore be sufficient to sustain the first flame kernel until combustion takes over and produces sufficient heat to increase the initially sparked hot volume. After reaching a sufficient size, the kernel (which may have been convected to another location in the meantime) starts to interact with surrounding turbulent flow and may convert into a turbulent flame. Ignition is completed after this turbulent flame has propagated upwards to the fuel injection system and stabilizes there. In annular combustion chambers (typical of gas turbines), the last phase of clear industrial interest is the propagation of combustion from one burner to the other (or light around sequence). This last step is a large scale phenomenon and depends on the burner geometry and operating conditions is not analysed here. It can however be studied with full annular simulations as in Boileau et al. [23].

The full ignition of one sector can be recast into the following phenomenological steps (Fig. 5.1):

1. Droplet dispersion in the chamber (phase 1 in Fig. 5.1): the first step prior to igniting a burner is to inject fuel and mix it with air. In the proposed solution, this specific initial state is described by the LES of a cold (possibly evaporating) two-phase flow, which produces instantaneous distributions of liquid and gaseous fuel in the chamber. The local

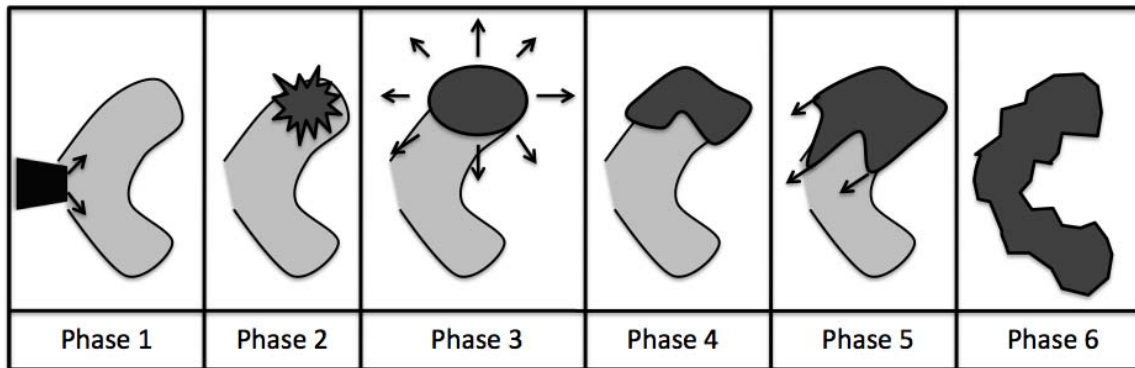


Figure 5.1: The 6 phase ignition scenario (dark zones correspond to ignited regions).

mixture fraction and velocity fields at the moment of ignition are crucial. Its statistical description is used as input of the I-CRIT-LES model to determine the local mixture flammability.

2. Spark or laser discharge and first hot gas kernel (phase 2 in Fig. 5.1): ignition is triggered by an energy deposition which leads to complex processes including non-equilibrium physics. If sufficient, the energy deposition leads to the creation of a small hot gas kernel. The size and temperature of this first kernel are critical for its later growth and need to be determined.
3. Growth and convection of the kernel (phase 3 in Fig. 5.1): if conditions are favorable, combustion starts around the hot gas. If the vaporisation time is small compared to the heat diffusion time, the hot gas kernel becomes a flame kernel and its size increases [43]. This transition results from the competition of different heat exchanges in and between the two phase flow.
4. Transition to a turbulent flame (phase 4 in Fig. 5.1): after reaching a size comparable to the smallest turbulent structures, the flame kernel starts to interact with turbulence, leading to wrinkling and stretching of the flame front. In most situations, this will accelerate flame propagation. If turbulence is too strong however, flame quenching may occur [155]. This last point is not considered in the present analysis as turbulent quenching is not expected to be a major mechanism (highly local phenomenon) in the target applications. However another quenching mechanism may occur in case of flame interaction with cold walls and is considered in the present analysis during Phase 4. According to the distance of the flame kernel to the wall and to its local speed, it may lose heat through the interaction with the wall. If this interaction lasts more than a characteristic time of

the interaction [157], the flame will quench.

5. Propagation of the turbulent flame towards the injection system (phase 5 in Fig. 5.1): usually the ignition system is located downstream of the injection system, and the turbulent flame kernel is created away from the stationary flame position of the ignited burner. In order to stabilize near the injector, the turbulent flame must propagate upstream, i.e. against the mean flow. This is possible only in low velocity zones, around or in recirculation zones, and requires a turbulent flame speed (evaluated from the local laminar flame speed and velocity fluctuations [158, 159]) larger than the local flow speed.
6. Stabilisation of the flame: this is the end of the ignition process of a single burner ignition phase. It is considered as automatically satisfied if all phases 1 to 5 are fulfilled.

For the full annular burner ignition a seventh step should be added, corresponding to the flame propagation from ignited burners to their neighbours [23]. This last step is not considered here.

In the following, steps 1 to 5 are associated to five conditions that must be fulfilled for the successful completion. In the modeling the sequence is viewed as a series of successive criteria to be satisfied prior the evaluation of the next one :

C1 (step 1): The fuel distribution must guarantee a flammable mixture.

C2 (step 2): The discharge energy must be sufficient to create a first hot gas kernel.

C3 (step 3): The local conditions (vaporisation time versus diffusion time) must allow the kernel to increase.

C4 (step 4): The flame must not be quenched near walls.

C5 (step 5): The flame speed must be larger than the local flow speed to allow the flame to propagate upwards.

These five conditions will now be expressed in terms of criteria which depend on the instantaneous flow fields and change from one flow realisation to another. Note that the turbulence levels are not directly addressed, only the instantaneous filtered variables are used. A way of introduction of a dependence on the SGS turbulence level may be the use of RMS or SGS of associated variables and would be an interesting study for a future work.

5.2.2 Criteria description

Criterion 1: Flammability

During a two-phase flow ignition, the available fuel is the fuel vapor (usually small) and the liquid fuel which will evaporate at the spark location. As a consequence, flammability of the mixture is evaluated by the total (gas + liquid) equivalence ratio, that must be in the

flammability limits of the considered fuel. Defining the equivalence ratio as:

$$\Phi = \Phi_{gas} + \Phi_{liq} = s \frac{Y_F}{Y_O} + s \frac{\rho_l \alpha_l}{\rho Y_O} \quad (5.1)$$

where s is the stoichiometric ratio, Y_F and Y_O respectively the fuel and the oxidizer mass fraction, ρ the gas phase density, ρ_l the liquid phase density and α_l the liquid mass fraction. Criterion 1 thus writes:

$$\Phi_{low} \leq \Phi \leq \Phi_{high} \quad (5.2)$$

where Φ_{low} and Φ_{high} are respectively the low and high flammability limits, known for usual fuels.

Criterion 2: Energy discharge and first kernel

Spark ignition issued by an electric system has been described in details by R.Maly and R.Vogel [160]. They recall that three phases (or discharge modes) can usually be distinguished. The first one is the breakdown phase. It lasts several nanoseconds (1-10 ns) and is the scene of very high voltage (about 10 kV) and currents (about 200 A). It implies the creation of a cylindrical plasmatic channel between the two electrodes, where temperature and pressure can respectively reach several tens of thousands degrees and 200 bars. The breakdown phase is very efficient as very few energy losses are observed. The following phases are the arc and glow discharges. Voltage, current and number of ionized particles are much lower but this phase is much longer (hundreds of microseconds to milliseconds) and heat losses due to conduction in the electrodes become very important.

Kono et al. [161] and later Kravchik and Sher [146] underlined that first, mass and energy transfers are controlled by the high pressure wave (blast wave) created by the breakdown. While expanding at high velocities, the shape of the kernel changes and quickly becomes spherical [146, 162]. At the same time, ionization takes place releasing energy and slowing down the cooling of the kernel [146, 162]. This fast expansion phase ends only after about one hundred microseconds, and is followed by a slower expansion controlled by heat conduction and mass diffusion. Although this plasma phase corresponds to the highest heat transfer and gas temperature, it is too short and strong to be a limiting process of ignition and is therefore not described here. In fact, the crucial parameter is the fluid state at the end of the plasma phase (when the gas has come back to equilibrium), resulting from the true amount of energy transferred to the gas at the end of the discharge. This amount has been evaluated and measured by several authors [160, 163] and is typically 10 to 30% of the spark energy.

For laser ignition, the energy deposit is simpler to evaluate since lasers directly transfer almost the whole energy to the gas, even if a part of this energy can produce a strong pressure wave through the dilatation of the ionized gas [150].

The previous observations were obtained for pure gaseous mixtures. In a spray, droplets evaporation is much slower than the energy transfer from the igniter to the gas: it is assumed here that droplets do not interact directly with the igniter and are heated only by their interaction with the hot gas (see Fig. 5.2). Furthermore, in practical devices, the spray is very diluted at

the spark location so that the energy absorbed by the liquid is very small.

Based on the above physical description of the energy deposit, the minimum energy required to install a first kernel is in the following determined by considering the heating, evaporation and ignition of a homogeneous mist of droplets in an initially fuel-vapor free gaseous environment (Fig. 5.2).

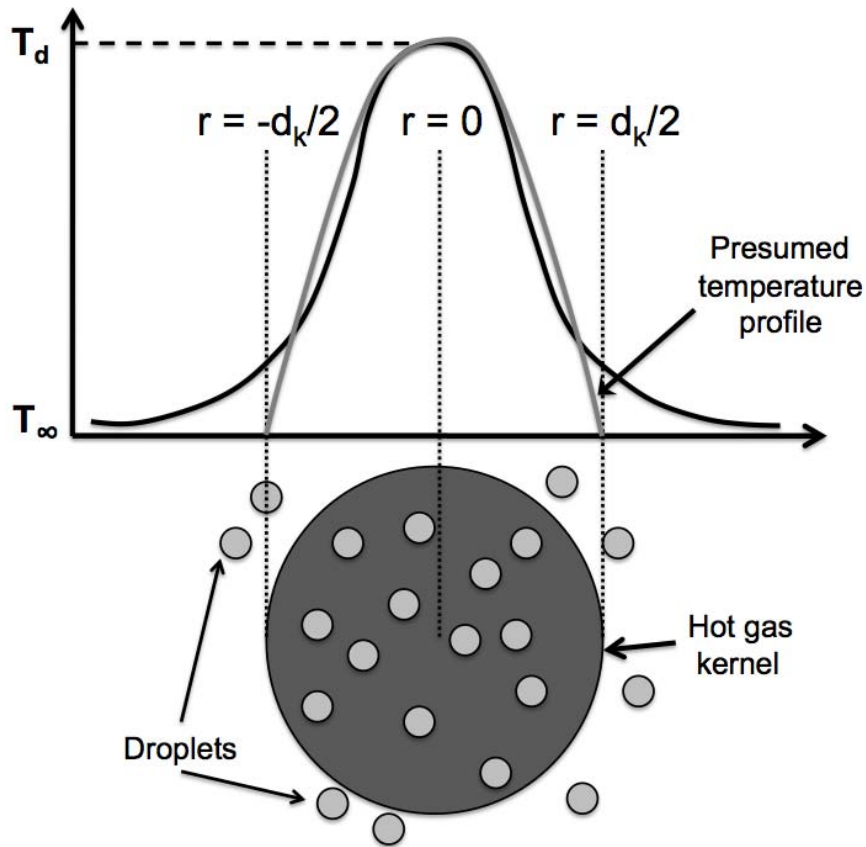


Figure 5.2: Sketch of the topology considered with the representation of the temperature profile at the end of the energy deposition.

For such a simplified configuration, numerical tests (see 5.2.4) show that if the liquid is too far from saturation conditions when combustion starts, evaporation is too slow to feed the flame. A criterion can be constructed by introducing an ignition temperature T_{ign} which is the temperature at which the chain-branching reaction balances the terminating reaction [164]. The criterion may be expressed in terms of a gas temperature, that must stay above the ignition temperature T_{ign} until the liquid has reached its saturation temperature T_{cc} . If t_{cc} is the time at which the liquid reaches saturation, criterion 2 is:

$$T(t_{cc}) \geq T_{ign} \quad (5.3)$$

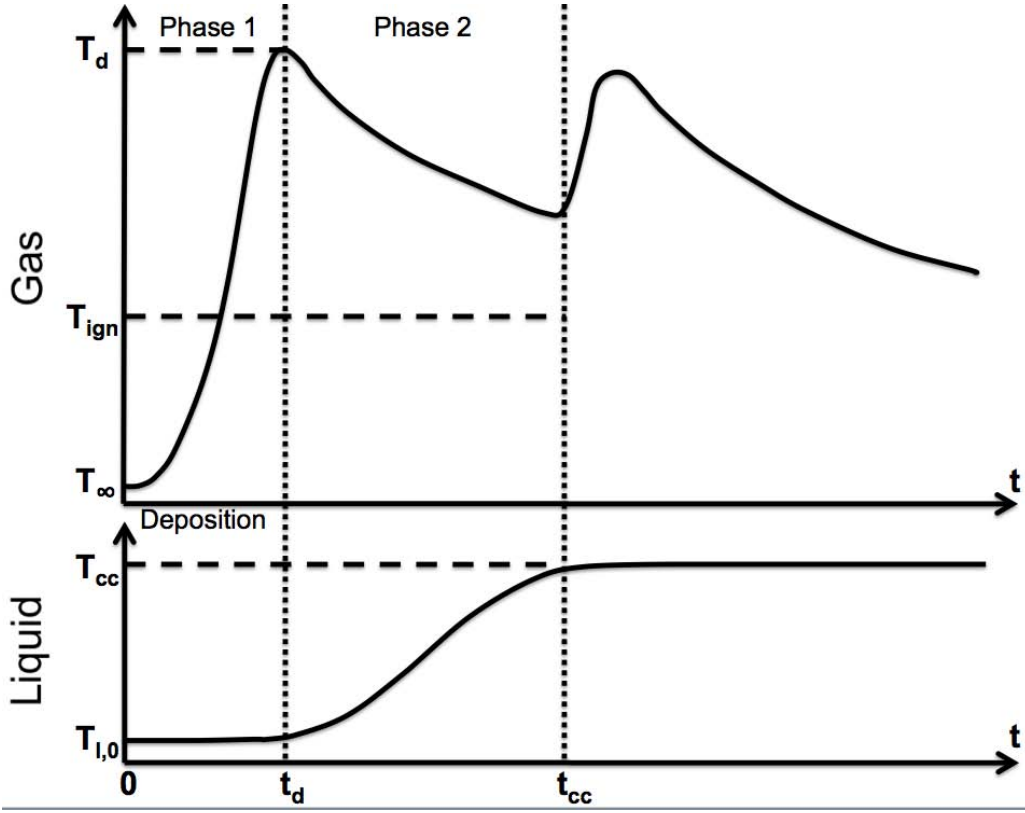


Figure 5.3: Typical evolutions of the temperatures when ignition occurs (thermal runaway after t_{cc}).

Hence, criterion 2 requires the knowledge of the gas temperature temporal evolution $T(t)$, which is obtained from the evolution equations for the gas (T) and liquid (T_l) temperatures at the spark location (typical evolutions are shown in Fig. 5.3). Its evaluation is obtained taking into account heat diffusion, heat transfer between the two phases and a source term (the spark energy during the deposition phase, $S = \dot{e}_{dep}$) in a simplified form (see appendix C for detailed developments):

$$\frac{\partial T}{\partial t} = \frac{T_\infty - T}{\tau_{diff}} + \frac{T_l - T}{\tau_{cond}} + \frac{S}{\rho C_p} \quad (5.4)$$

$$\frac{\partial T_l}{\partial t} = -A \frac{T_l - T}{\tau_{cond}} \quad (5.5)$$

These equations are written for the deposition phase (phase 1 in Fig. 5.3) and the heating phase of the droplets, before they reach T_{cc} , therefore with negligible evaporated fuel, i.e. negligible combustion. A unity Lewis number is assumed. The initial temperatures for the gas and liquid phases are respectively noted T_∞ and $T_{l,0}$. $T_d = T_\infty + e_{dep}/\rho C_p$ is the gas temperature at the end of the energy deposit phase, e_{dep} being the total volumic energy deposit. The parameter

$A = \rho C_p / \alpha_l \rho_l C_{p,l}$ is the liquid to gas ratio of heat capacities, with α_l the liquid volume fraction. The two characteristic times $\tau_{diff} = d_k^2 / 8n_{dim}D$ and $\tau_{cond} = d_l^2 / 6D\alpha_l Nu$ describe heat diffusion in the gas and heat transfer between the phases, n_{dim} being the number of dimensions. In these expressions, D is the heat diffusion, d_k is the initial kernel size (i.e. the deposit size), and d_l is the droplet diameter. Solving these two equations yields:

$$T(t_{cc}) = T_d - \frac{\tau_{cond}}{A\tau}(T_{cc} - T_{l,0}) \quad (5.6)$$

where $1/\tau = 1/\tau_{diff} + 1/\tau_{cond}$. Finally criterion 2 becomes:

$$\frac{e_{dep}}{\rho C_p} \geq (T_{ign} - T_\infty) + \frac{\tau_{cond}}{A\tau}(T_{cc} - T_{l,0}) \quad (5.7)$$

or

$$\frac{e_{dep}}{\rho C_p} \geq (T_{ign} - T_\infty) + \left(\alpha_l + \frac{4n_{dim}d_l^2}{3Nu d_k^2} \right) \frac{\rho_l C_{p,l}}{\rho C_p} (T_{cc} - T_{l,0}) \quad (5.8)$$

This criterion expresses that the energy deposit must be sufficient to heat the gas from T_∞ to at least T_{ign} and the liquid from $T_{l,0}$ to T_{cc} while the gas temperature does not cool down to a temperature lower than T_{ign} . Note that $d_l = 0$ (i.e. and $\alpha_l = 0$) provides the gaseous limit of the criterion.

Criterion 3: Kernel growth

The next step is to sustain the kernel and corresponds to phase 3 in Fig. 5.1. In the ongoing process, the initial flame kernel being issued by the spark discharge (criterion 2 satisfied), if combustion is not strong enough, the heat release is not sufficient to compensate for the cooling of the gas due to diffusion, i.e. the kernel quenches because of the evaporation of the surrounding liquid field.

This third criterion is derived following the methodology of Ballal and Lefebvre (1981)[43]. Considering a hot gas kernel surrounded by a flame, in a mixture of fresh gas and droplets (Fig. 5.4), characteristic times of evaporation τ_{vap} , diffusion τ_{diff} and combustion τ_{comb} are compared. Combustion is thus sustained if the droplets can evaporate and burn before heat diffuses away:

$$\tau_{vap} + \tau_{comb} \leq \tau_{diff} \quad (5.9)$$

As combustion is fast compared to diffusion and evaporation, $\tau_{comb} \approx 0$. The vaporization time is determined from the evaporation mass transfer as expressed in Spalding's theory [136]:

$$\tau_{vap} = \frac{\rho_l d_l^2}{6\Phi Sh \rho D \ln(1 + B_M)} \quad (5.10)$$

where B_M is the mass Spalding number. After rearrangement with Eq. (5.9), one finds criterion 3:

$$\frac{d_k}{d_l} \geq \sqrt{\frac{4n_{dim}\rho_l}{3\Phi Sh \rho \ln(1 + B_M)}} \quad (5.11)$$

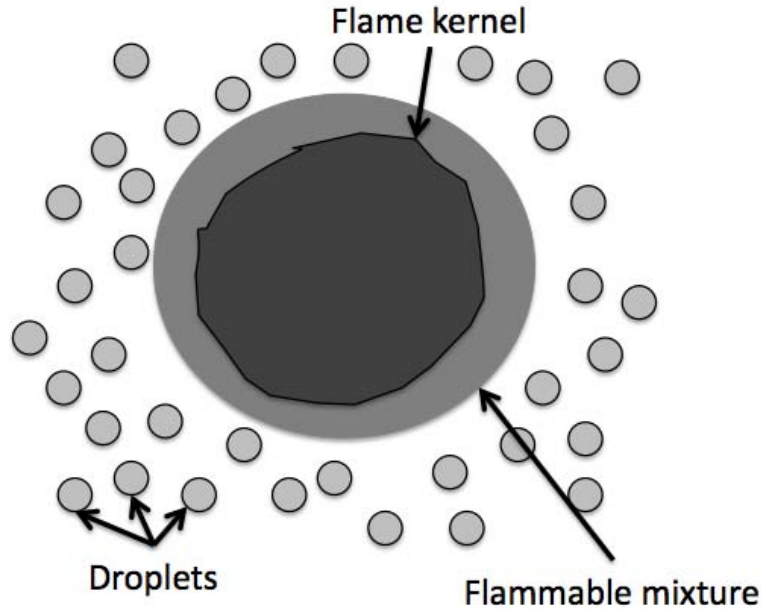


Figure 5.4: Expansion of the initial laminar kernel.

which compares the flame kernel size d_k to the droplet size d_l . Since, this phase compares variables after relaxation of the initial plasma, the flame kernel is compared after its relaxation towards the adiabatic flame temperature. The kernel size d_k is thus the equivalent hot gas sphere produced by the energy deposit. If the kernel size is too small compared to the droplet diameter, heat diffusion is too fast compared to evaporation and the flame can not survive.

Criterion 4: Wall quenching

Previous studies [165, 166, 157, 167] have shown that a flame can not exist at a distance to the wall smaller than a critical distance called the quenching distance δ_Q . Therefore a flame ignited too close to a wall will not be able to survive. The quenching distance has been evaluated for various laminar flames interacting with walls, and is usually expressed as a Peclet number $Pe_Q = \delta_Q/\delta_l^0$ where δ_l^0 is the local laminar flame thickness. This number is of the order of 3.0 for usual hydrocarbons (1.7 for H_2/O_2) when the flame propagates normally to the wall (head on quenching). A characteristic time of the interaction t_Q is also defined, which represents the time to quench the flame. This time is also given in a non-dimensional form $\tau_Q = t_Q/t_l^0$ where $t_l^0 = \delta_l^0/S_l^0$. For typical hydrocarbons $\tau_Q \approx 2.1$ [157, 167].

Knowing Pe_Q and τ_Q , criterion 4 is expressed differently depending on the flame front wall distance δ (Fig. 5.5):

- First, if the kernel is initiated within the quenching layer, i.e. if $\delta \leq \delta_Q$, it has to leave

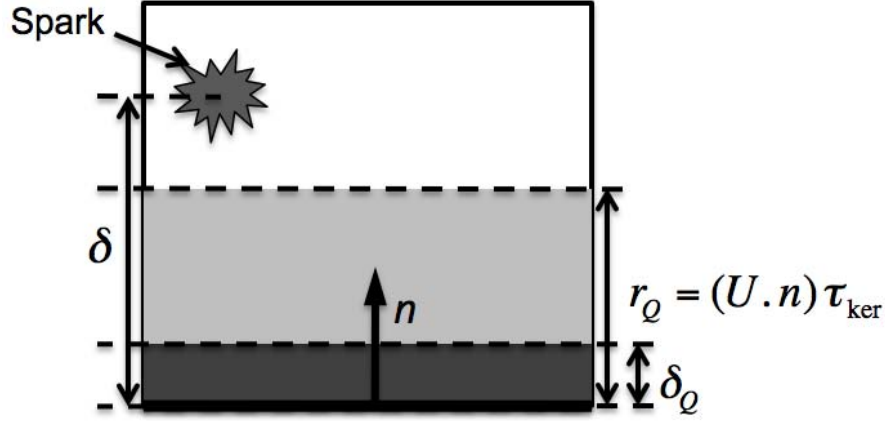


Figure 5.5: Layers description of criterion 4

this zone before $t = t_Q$, then:

$$\delta \leq \delta_Q \quad \& \quad \mathbf{U} \cdot \mathbf{n} > \frac{\delta_Q - \delta}{t_Q} > 0 \quad (5.12)$$

where \mathbf{U} is the local flow velocity vector and \mathbf{n} the wall normal.

- Second, even if $\delta > \delta_Q$, the flame may convect within the quenching layer. Hence, it has to be strong enough before entering this zone. To quantify this "strength", it is assumed that the flame is strong enough when it has developed during at least $\tau_{ker} = t_{cc} + \tau_{diff}$ which represents the time to reach equilibrium (i.e. non super adiabatic temperature). This leads to the definition of an "overlayer distance" $r_Q = (\mathbf{U} \cdot \mathbf{n}) \tau_{ker}$ and a second condition which reads:

$$r_Q \geq \delta > \delta_Q \quad \& \quad \mathbf{U} \cdot \mathbf{n} > 0 \quad (5.13)$$

- At last, if:

$$\delta > r_Q \quad (5.14)$$

Note that criterion 4 is validated independently of other criteria.

Criterion 5: Upstream flame propagation

The turbulent flame created in step 5 must propagate upstream and ignite the complete chamber. This last step is a complex issue probably requiring full LES of ignition sequences (something we do not want to perform to use the present model) or Lagrangian simulations of the kernel trajectory (see for ex [45]). To construct a criterion based only on instantaneous

snapshots, criterion 5 in I-crit-LES considers a simpler condition, stating that the flame velocity must allow the front to propagate upstream: the turbulent flame speed S_T must be larger than the local flow mean velocity \mathbf{U} vector along the burner axis \mathbf{n}_{inj} :

$$\mathbf{U} \cdot \mathbf{n}_{inj} - S_T \leq 0 \quad (5.15)$$

where $S_T \approx S_L^*(\Phi) + u'$ is the turbulent flame speed [158, 159], u' being the turbulent velocity fluctuation. The laminar flame speed $S_L^*(\phi)$ being applied to two-phase flow flames is corrected for lean combustion based on [43]:

$$S_L^*(\phi) = \left(\frac{\tau_{vap}}{D} + \frac{1}{(S_L^0)^2} \right)^{-1/2} \quad (5.16)$$

Global ignition index

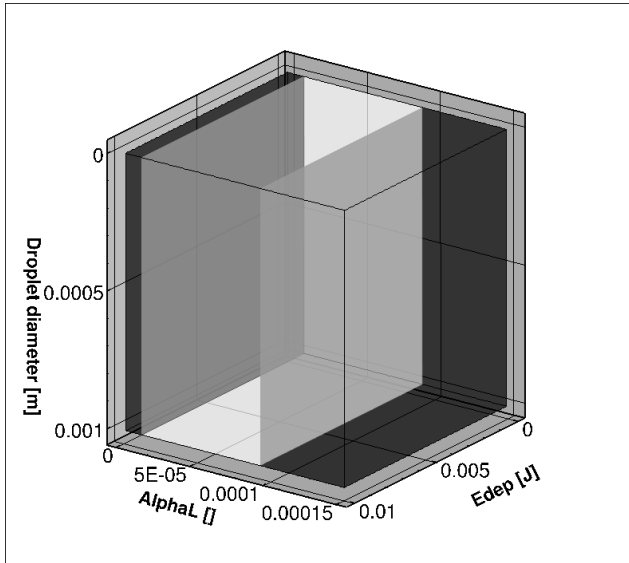
All five criteria are necessary for ignition and are combined in an ignition index $I_{ign} = C_1 \times C_2 \times C_3 \times C_4 \times C_5$, where C_i takes the value 1 if criterion i is verified and 0 otherwise. At this stage, the ignition index is applied to one flow snapshot and is a deterministic quantity which can take only 0 or 1 values. The input values of the model given by the user are summarized in Table 5.2.2, the other ones being directly extracted from the cold LES snapshot. Typical evolutions of the index I_{ign} are shown in Figs. 5.6 & 5.7.

Stoichiometric coefficient (used in C1)	s
Lean flammability limit (used in C1)	Φ_l
Rich flammability limit (used in C1)	Φ_r
Activation temperature (used in C2)	T_a
Spark energy deposit (used in C2)	E_{dep}
Spark diameter (used in C2/C3)	d_k
Adiabatic flame temperature (used in C2/C3)	T_{adia}
Laminar flame thickness (used in C4)	δ_L^0
Laminar flame speed (used in C5)	S_L^0
Mean flow orientation (used in C5)	\mathbf{n}_{inj}

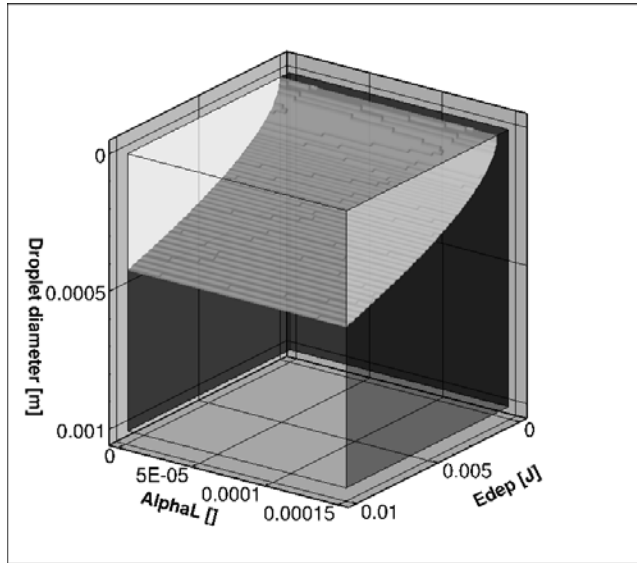
Table 5.1: User input values for the model I-crit-LES

Criterion 1 for example (flammability, Fig. 5.6a) does not depend on droplet diameter or the spark energy deposit. Criterion 2 (first kernel creation) depends on the droplet diameter and spark energy but the liquid volume fraction has almost no influence. The growth of the flame kernel (Criterion 3 Fig. 5.6c) is controlled essentially by the droplet diameter. Finally, the global index can take complex dependances (Fig. 5.6d) when it is plotted versus droplet diameter, spark energy and fuel liquid mass fraction.

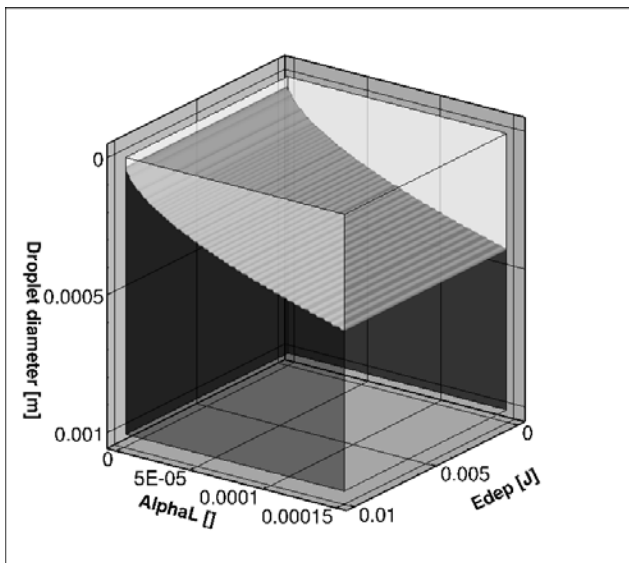
Sensitivity to pressure, initial gas temperature and droplet diameter



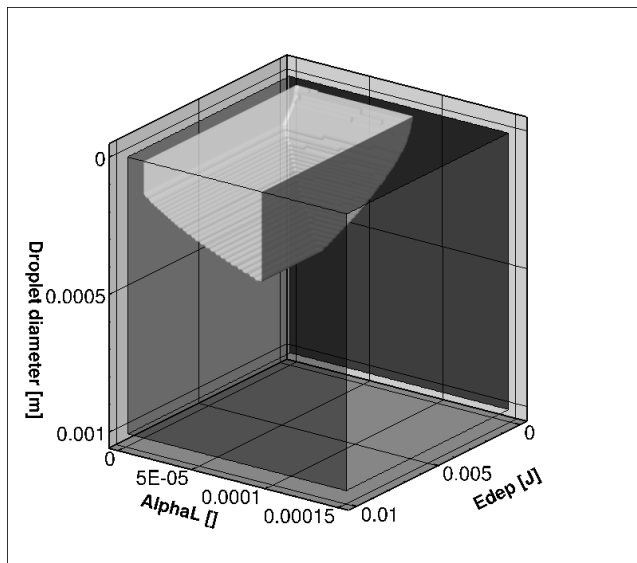
(a) Criterion 1: flammability limits



(b) Criterion 2: kernel ignition



(c) Criterion 3: kernel growth



(d) Ignition index I_{ign}

Figure 5.6: Isosurfaces of limits of validity of ignition criteria and the full index function of the liquid volume fraction, the droplet diameter and the energy deposit (White = success, i.e. = 1 / dark = failure, i.e. = 0).

The first three criteria, C_1 to C_3 are local and it is interesting to study their sensitivity to pressure P , initial gas temperature T_∞ and droplet diameter d_l spaces, or equivalently to the burner operating conditions prior to the ignition phase. For the exercise, the fuel used is the kerosene surrogate defined by Luche [168]. The energy deposit $E_{dep} = 50mJ$ and the liquid

volume fraction $\alpha_l = 3 \cdot 10^{-4}$ are fixed; P ranges from 10^4 to $5 \cdot 10^6$ Pa, T_∞ from 250 to 500 K and d_l from 10^{-6} to 10^{-4} m. To first order, Fig. 5.7 shows that ignition is more difficult at high pressure: almost all criteria become 0 when pressure is higher than 30 bars. The maximum pressure at which ignition becomes impossible will be called P_{il} and isosurfaces of P_{il} versus gas temperature and initial droplet diameter correspond to the transition of light to dark zones in Fig. 5.7. For criterion 1 (flammability limits), P_{il} varies mainly with temperature: higher initial temperatures lead to easier ignition and higher values of P_{il} . The second criterion (kernel ignition) is even more sensitive to temperature (Fig. 5.7b) but the third one (kernel propagation in Fig. 5.7c) leads to a limit pressure P_{il} depending mainly on the droplet diameter. Finally, the resulting surface for P_{il} obtained from the combination of criterion 1 to 3 leads to the complex shape of Fig. 5.7d.

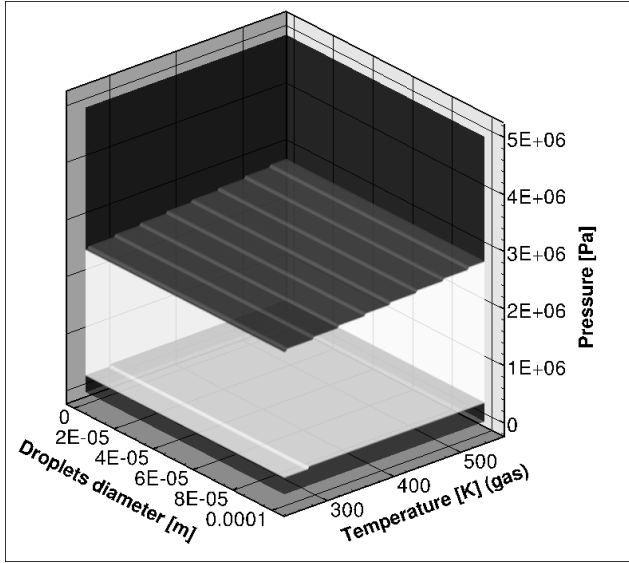
5.2.3 Ignition probability

The ignition scenario and criteria described above (sections 5.2.1 and 5.2.2) are developed in a fully deterministic framework: that is for one given flow solution, the model predicts if ignition will be successful or fail with a 0 or 1 ignition index. However exact conditions (temperature and composition of the liquid and gas phase) at the location and moment of ignition fluctuate due to turbulence which clearly affects the success of the ignition sequence.

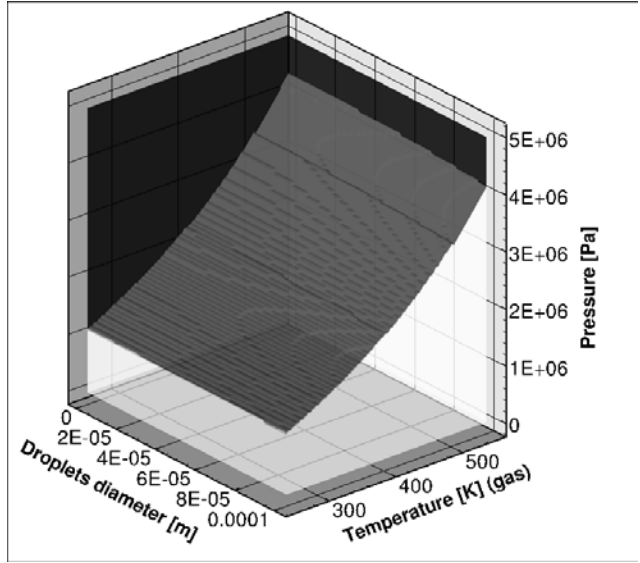
Figure 4.4 is obtained through expensive LES and justifies the development of the present model: it would be much too expensive to perform series of ignition sequences with LES at each igniter location to obtain ignition probabilities. As described by Mastorakos [37], a probabilistic model is a better suited and to meet this requirement the I-crit-LES needs to be applied to a series of instantaneous non-reacting LES snapshots (which is unique and much faster) to evaluate the ignition probability without actually simulating the time dependent ignition series of events. In this approach, each instantaneous LES solution is viewed as one flow realisation, the finite set of instantaneous fields being used as a statistical ensemble of samples representative of the turbulent field. This requires that the solutions be taken after statistical convergence of the LES unsteady flow. Applying criteria C_1 to C_5 to a series of N realisations (instantaneous solutions at $t = t_k$) allows to build a probability for the local ignition index:

$$p(I_{ign}) = \frac{1}{N} \sum_{k=1}^N I_{ign}(t_k) \quad (5.17)$$

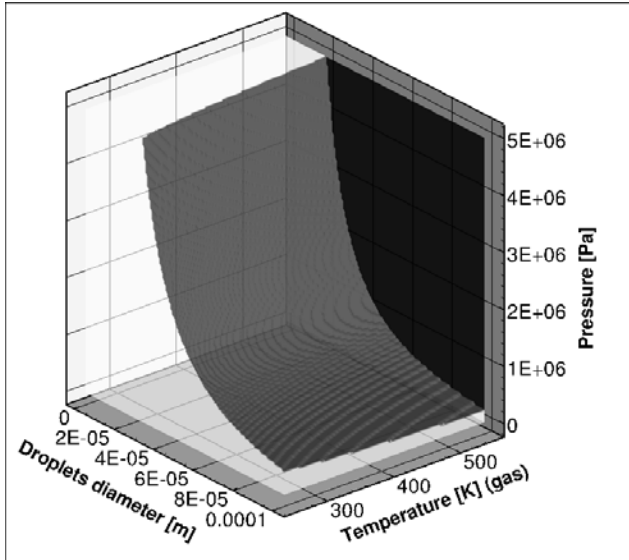
The N realisations used are chosen to provide a sample of the "signal" according to the signal processing theorem of Shannon. Hence, the discretization chosen will determine the smallest resolved structure and may be adapted according to the desired accuracy. This statistical estimate is a three-dimensional field giving the probability of completion of all ignition steps at each location in the burner, and varies from 0 to 1 (by construction). Using the same definition, one can also build an individual probability which is specific to one criterion replacing $I_{ign}(t_k)$ by $C_i(t_k)$, and showing how a potential step of the ignition will behave. If we suppose statistical independence of the criteria C_1 to C_5 one can write $p(I_{ign}) = \prod_{i=1}^5 p(C_i)$, where the



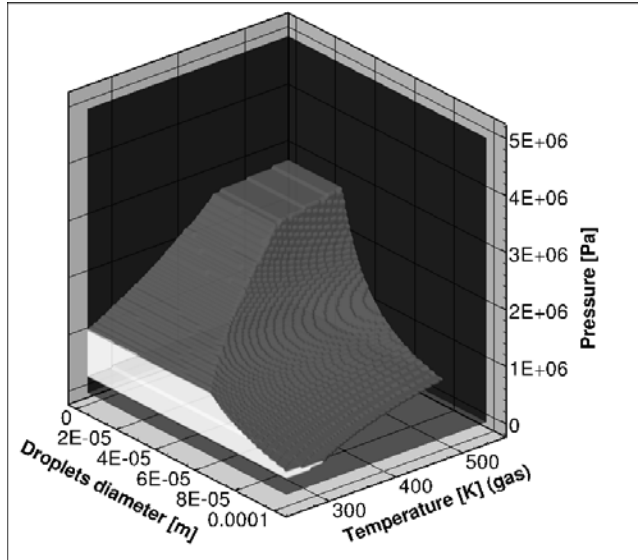
(a) Criterion 1: flammability limits



(b) Criterion 2: kernel ignition



(c) Criterion 3: kernel growth



(d) Ignition index

Figure 5.7: Isosurfaces of limits of validity of ignition criteria and the global index as functions of the pressure, the initial gas temperature and the droplets size (White = success, i.e. = 1 / dark = failure, i.e. = 0). The spark energy is 50 mJ and the initial fuel volume fraction is $\alpha_l = 3.10^{-4}$

probabilities $p(C_i)$ are individually built following Eq. (5.17). Tests (not presented here) show that these two definitions of $p(I_{ign})$ do not provide exactly the same results. Hence, criteria C_1 to C_5 are not statistically independent, especially C_2 and C_3 (the amount of the energy deposit

will directly influence the size of the kernel at the beginning of phase 3, Fig. 5.8) and the first definition of the probability is used, Eq. (5.17).

The present approach also allows to identify the potential causes of failure when the ignition probability, $p(I_{ign})$, is lower than 0.5, identifying the limiting criterion as the criterion with the lowest probability $p(C_i)$. The same analysis may be conducted on only one instantaneous solution, identifying the cause of failure by the first criterion for which $C_i = 0$ given the LES initial flow state. In this case the analysis is fully deterministic.

5.2.4 Validation of the ignition scenario for I-crit-LES neglecting interaction with turbulence(phase 1 to 3)

Prior to the application of the provided strategy to real geometry (chapter 6), one-dimensional simulations were performed to study the sensitivity of the evolution of the two-phase mixture (Fig. 5.8) to the input parameter E_{dep} and the associated criterion (Fig. 5.10). For this purpose, a simple 1D DNS where a two-phase mixture of air and kerosene (only liquid initially and monodisperse droplets) is ignited by a 1D spark for which the local energy deposited by unit volume is [151]:

$$\dot{e}_{dep}(x, t) = \frac{E_{dep}}{(\sqrt{2\pi})^2 \sigma_x \sigma_t} e^{-\frac{1}{2} \left(\frac{x-x_0}{\sigma_x}\right)^2} e^{-\frac{1}{2} \left(\frac{t-t_0}{\sigma_t}\right)^2} \quad (5.18)$$

In Eq. 5.18 $E_{dep} = \int \dot{e}_{dep} dt dV = \int e_{dep} dV$ is the total amount of energy transferred by the spark to the gas, σ_x and σ_t are parameters that control the size and duration of the source term, x_0 and t_0 are the space and time coordinates of the deposit. Initial conditions are $P = 1atm$ with a temperature of $300K$ for both phases. The liquid phase is described by a monodispersed Eulerian formalism and the evaporation model is based on the Spalding description (see details in Part I). The droplets size is $60\mu m$ and the liquid mass fraction 10^{-4} . The spark characteristics are: $\sigma_x = 0.5mm$ and $\sigma_t = 8.2\mu s$. The liquid fuel is kerosene (surrogate and chemical kinetic scheme from Franzelli and Riber (2010) [140]).

The temporal evolution of the droplet (dashed line) and gas (solid line) temperatures are shown in Fig. 5.8. In a first phase ($t \leq t_d$), the gas temperature increases sharply, under the effect of the energy deposition. Then in a second phase ($t_d \leq t \leq t_{cc}$), heating of the droplets starts, while the gas cools down. After some time, the droplets reach their equilibrium temperature T_{cc} , while the combustion reactions, activated by the hot gas temperature, start to release heat, resulting in a fast increase of the gas temperature and a second temperature peak at $0.4ms$, corresponding to the creation of a first flame kernel.

This preliminary unsteady DNS confirms the scenario as postulated in the I-crit-LES sequencing and for the case under study. To further confirm the hypothesis introduced in I-crit-LES, other conditions were tested.

As illustrated on Fig. 5.9, if during the spark, the gas temperature does not rise enough, the gas may be cooled too strongly by heat diffusion, and the fuel evaporation becomes too small: reactions can not start and ignition fails (dashed-dotted lines in Fig. 5.9). A series of ignition simulations were performed for the parametric study of the droplet size d_l and of the

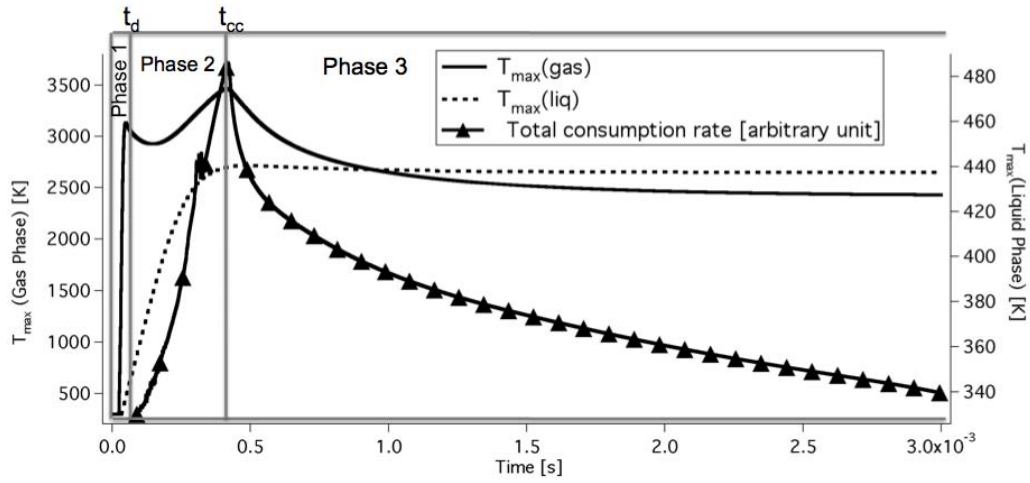


Figure 5.8: Ignition of a homogeneous droplet cloud ($E_{dep} = 4.3mJ$).

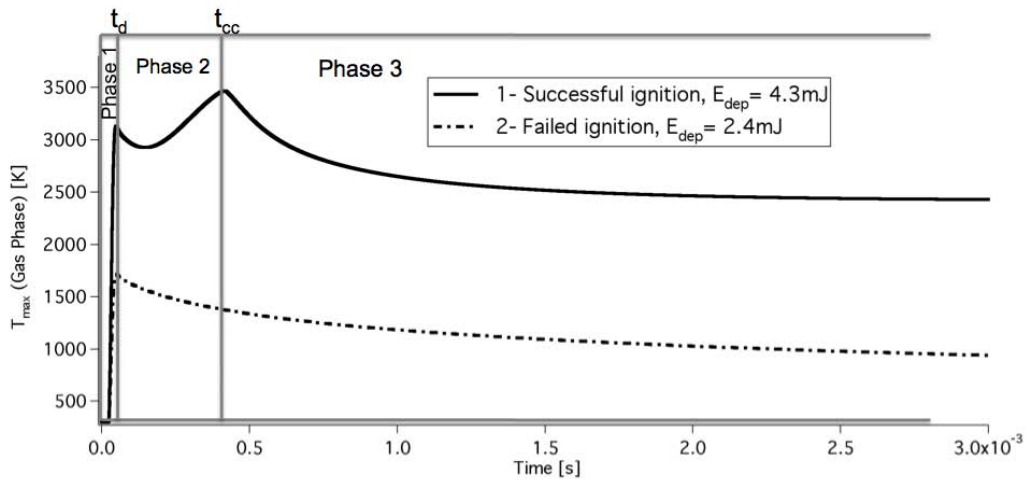


Figure 5.9: Comparison of the temporal evolution of maximum gas temperature between successful (1) and failed (2) ignition.

energy of the spark E_{dep} , keeping all other parameters unchanged. The resulting ignition map is compared to criterion 2 in Fig. 5.10, showing that criterion 2 correctly predicts ignition limits for the presented test cases.

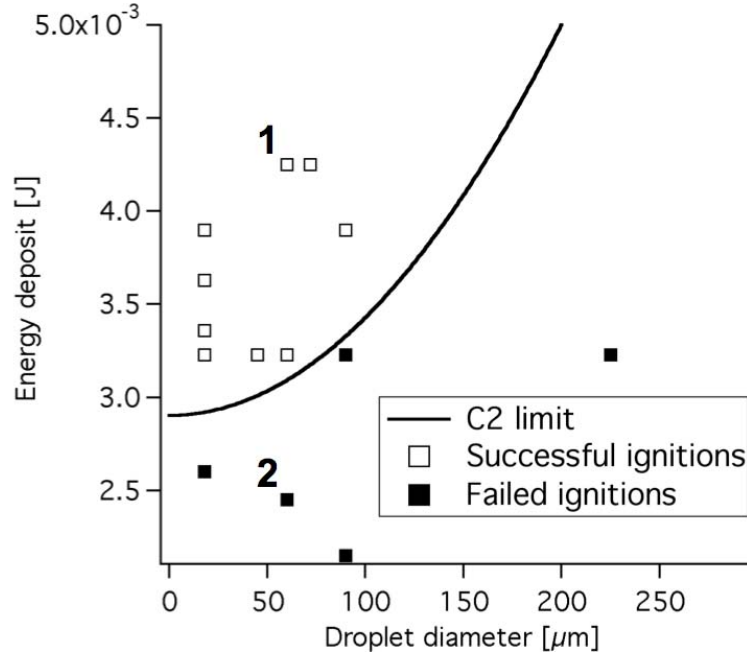


Figure 5.10: Minimal energy as a function of droplet diameter d_l for a stoichiometric mixture. 1 and 2 refer to Fig. 5.9.

5.2.5 The evolution of the I-crit-LES methodology

Recent purely gaseous experiments lead at CORIA within the KIAI project¹, have provided very precise ignition probability maps. Analysing the data and according to experimentator comments, a potential important mechanism in the swirler near field is the flame strength/stress competition which may lead to the extinction of the kernel. To specifically address this mechanism, a new criterion (numbered 6) is computed by first evaluating the stress tensor and then solving for its eigenvalues. The maximum τ_{max} is evaluated using the Tresca formulation:

$$\tau_{max} = \frac{1}{2} |\sigma_{max} - \sigma_{min}| \quad (5.19)$$

where σ_{max} and σ_{min} are respectively the maximum and minimum eigenvalues of the filtered stress tensor. Hence, if we note τ_{limit} the extinction stress limit, criterion 6 is valid if:

$$\frac{1}{2} |\sigma_{max} - \sigma_{min}| < \tau_{limit} \quad (5.20)$$

The limitations of this criterion come from the high difficulty to get an accurate evaluation of τ_{limit} for a wide range of conditions. Indeed, it may depend on the fuel, the equivalence ratio, the pressure and the level of turbulence. An approximation of its value is based on the correlation given by G.L.Pellett *et al.* in [153] for laminar flows, which has been evaluated from

¹Knowledge for Ignition, Acoustics and Instabilities; Seventh framework programme.

a polynomial regression of the available database. Among the fuel used one finds methane, n-heptane or kerosene. In order to deal with turbulence, an ad hoc. coefficient K is added ahead to rescale the correlation:

$$\tau_{limit} = K * 0.10136 * S_l^{1.867} \quad (5.21)$$

where S_l is the local laminar flame speed in cm/s ; K is of the order of 200. Of course a proper study of this coefficient, especially the local turbulence level, would be of interest but has not been done in this work, the main sensitivity of the correlation being contained in the power coefficient of S_l .

The different criteria used in I-crit-LES V2 to model the full ignition of a sector burner, are:

- C1: The fuel distribution must guarantee a flammable mixture.
- C2: The discharge energy must be sufficient to create a first hot gas kernel.
- C3: The local conditions (vaporisation time versus diffusion time) must allow the kernel to increase.
- C4: The flame must not be quenched near walls.
- C5: The flame speed must be larger than the local flow speed to allow the flame to propagate upwards.
- C6: The local stress experienced by the kernel must be low enough to avoid aerodynamic quenching.

5.3 Conclusion

Following the conclusions of part II and according to the previous studies about ignition, a new methodology to evaluate ignition probability has been designed. It uses analytical criteria based on data from non reacting unsteady two-phase flows computed with LES. The list of six criteria is defined according to the phenomena observed through previous simulations (cf. part II). To get analytical formulations for these criteria, several assumptions have been done (locality and independence) and require validations. In the next chapter, a set of configurations with available data of ignition probability is adressed for the validation of I-crit-LES against measurements and limitations are discussed. Note that these configurations have been chosen as representative as possible to get a relevant set of validation for the methodology.

Chapter 6

I-crit-LES: results

In this chapter we present the main configurations that have been used to validate and illustrate the methodology proposed behind I-crit-LES. The first test uses a purely gaseous device, which burns methane. Although I-crit-LES has been designed for two-phase flow configurations, it can easily degenerate to purely gaseous flows. This specific test will underline the need for an additional criterion taking into account strain to recover the ignition probability map. It also emphasises the difficulty of handling history and trajectory effects of the initial flame kernel. The second test is a burner from Cambridge University, for which detailed ignition probability maps have been obtained allowing close comparison [144]. The last configuration tested, the MERCATO bench, has been described earlier (chapter 3). This is a classical configuration used to test two-phase flow ignition with kerosene. The lack of detailed ignition probability map is here clear although campaigns have indicated regions of high probability of ignition from regions of low probability of ignition. Despite needs for improvement, the methodology has also been applied to industrial burners to illustrate its capacity of prediction.

6.1 The KIAI configuration

6.1.1 Description of the burner

The KIAI burner corresponds to an academic methane/air single-burner targeting ignition phenomena as appearing in real gas turbine engines. This configuration has been studied by CORIA providing experimental data for velocity and ignition probability. It corresponds to a swirl experimental burner operating at premixed conditions with a mean equivalence ratio of 0.75 and composed of the following four components, Fig. 6.1. The plenum: its purpose is to smooth down the premixed flow before entering the injection system. The swirler injection system is composed of two admissions, a tube in the center, which is surrounded by a radial swirler. This one consists of 18 radial vanes at a swirl angle of 45° . The combustion chamber has a squared cross section, assuring a symmetric flow field, linked to a convergent exhaust. During the cold flow simulations, temperature is fixed at $T = 298\text{ K}$ and the pressure in the combustion chamber is at ambient pressure $P = 101325\text{ Pa}$. For the ignition, a laser providing 20 mJ to the gas is used. Prior to the application of I-crit-LES, LES of the cold flow is produced.

6.1.2 Validation of the cold LES against measurements (Results from D. Barré).

Boundary conditions in simulations are of characteristic type (NSCBC [169]) for inlets and outlet, respectively defined by imposing the volumetric mass flow rates and the pressure. The wall boundary conditions are defined to match the experimental PIV measurements, by using a wall model on each wall except central injection walls and the crown which surrounds it (where a slip condition was used because of numerical issues at the corners). A Taylor-Galerkin [170] weighted residual central distributions scheme is used for the numerical integration. The Smagorinsky model is used as subgrid scale model. The mesh contains about 4 million cells.

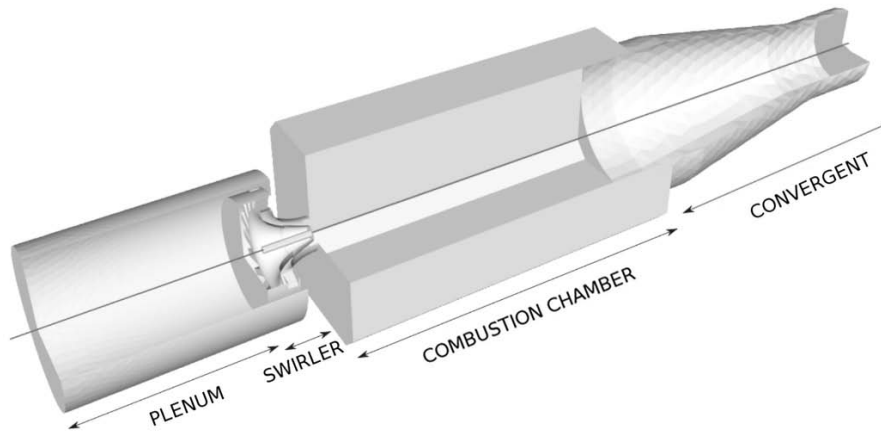


Figure 6.1: Geometry of the KIAI burner.

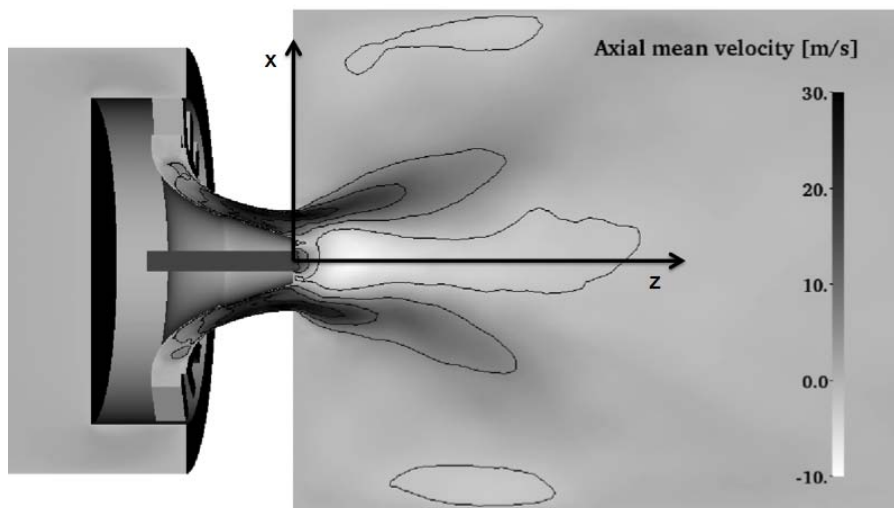
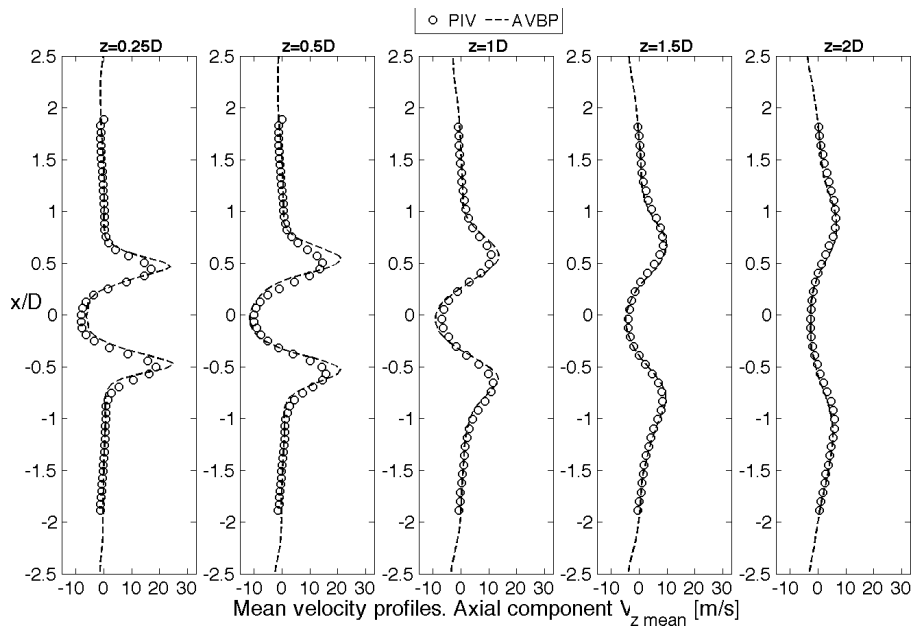


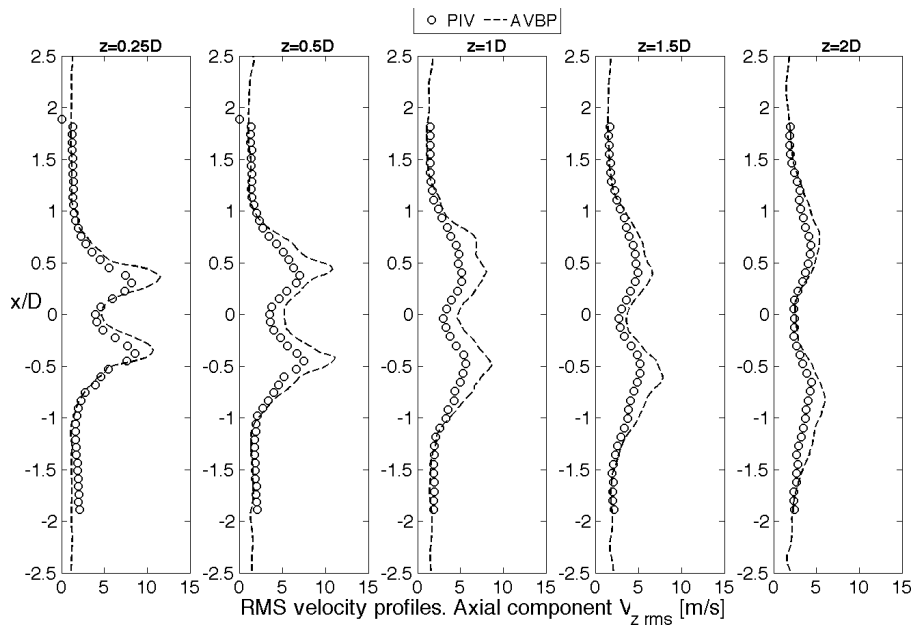
Figure 6.2: Mean axial velocity field in the $x = 0$ plane (black line denotes 0 m/s)

In Fig. 6.2, recirculation zones represented by black isolines are small. The CTRZ is narrow and short, and the CRZ appears only very close to the walls; this could imply difficulties to anchor the flame during the ignition phase if the fluctuation are too small. The comparison between the PIV and the LES velocity profiles is presented in Fig. 6.3 and Fig. 6.4. Figure 6.3 a) shows very good agreement for all abscissa even if the maximum value is slightly overestimated. The RMS (Fig. 6.3 b)) are overestimated by the LES at the jet entry, however the magnitude and the shape are correct.

Figure 6.4, for the tangential component, confirms the preliminary findings. An additional feature is visible on the RMS profile at $z = 0.25D$ for the LES, where an additional pairs of peaks is observed (Fig. 6.4b)). The peaks close to the axis are generated by the shear in the central jet. In the experiments this has been smoothed out earlier and hence not visible at $z = 0.25D$. From these results, the LES of the cold flow is validated and can be used to test



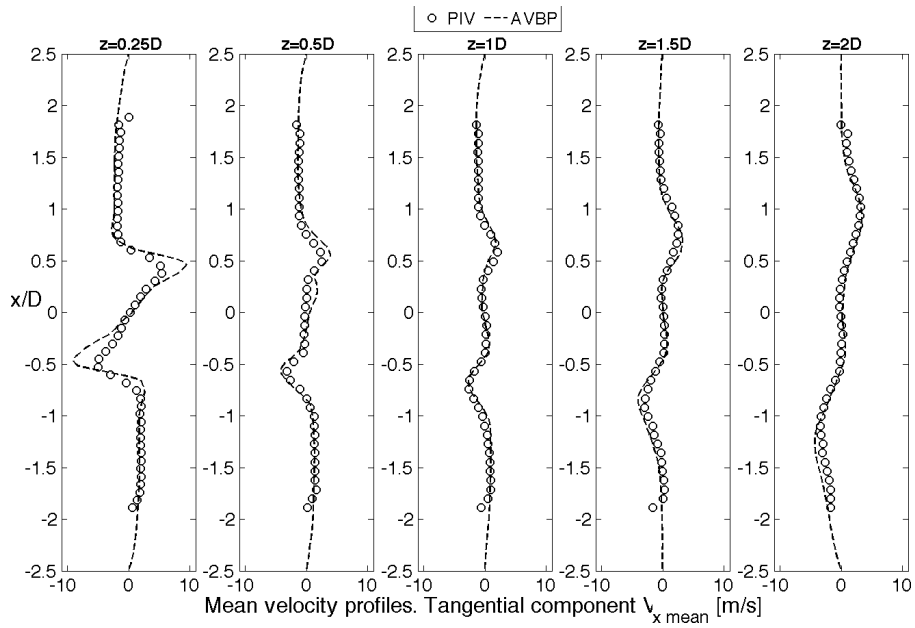
(a) Mean axial velocity



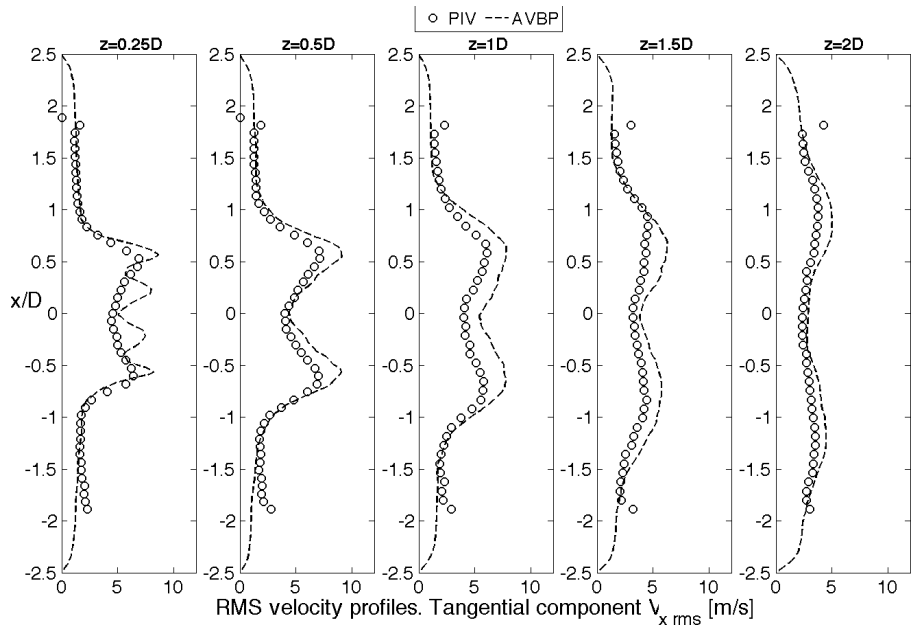
(b) RMS axial velocity

Figure 6.3: Axial velocity profiles of the cold flow

the ability of the methodology I-crit-LES to predict ignition probability of a purely gaseous mixture.



(a) Mean tangential velocity



(b) RMS tangential velocity

Figure 6.4: Tangential velocity profiles of the cold flow

6.1.3 Application of I-crit-LES and confrontations

The I-crit-LES methodology is applied to the KIAI burner and directly confronted to experimental findings obtained from a series of ignition tests. Experimentally 75 positions of the

ignitor were tested, 25 times for each one to get reasonable statistics, cf Fig. 6.5 c). For the prediction of ignition probability by use of I-crit-LES the amount of energy set as input for the model is 20 mJ (note that in the case of a perfectly premixed methane/air flow, the theoretical MIE is very low, less than 1 mJ), an ignition index is built taking 90 instantaneous solutions of a cold flow simulation. A confrontation of the I-crit-LES V1 and V2 (with the additional criterion) estimations are given on Fig. 6.5 a) and b) and directly compared to the experimental findings, Fig. 6.5 c).

In this configuration, the interpretation of I-crit-LES and the respective contributions can be greatly simplified. Indeed, since the flow is perfectly premixed and injected at an equivalence ratio of 0.75, the criterion about flamability limits, C1, is validated everywhere. Second, the fuel being gaseous the criterion which compares evaporation to diffusion, C3, does not make sense. Similarly, with purely gaseous fuel, the MIE is very low and the criterion C2 is validated too. Finally, since there is no jet impact on walls, the low probability area of the flame to be submitted to wall quenching is limited to a very thin layer. As a consequence, the ignition is only driven by aerodynamic considerations, i.e. C5 and C6.

If we look at the predictions of the improved I-crit-LES, Fig. 6.5 b), the triangle shape of the low probability is recovered in terms of level and extension. However, the estimated map still exhibits low probabilities in the high speed regions, i.e. swirled jet expansion. C6 alone, Fig. 6.5 d) seems to define with a very good accuracy the ignition probability map from experiments at the jet exit, Fig. 6.5 c). In the case of a purely gaseous mixture, the limit of the extinction stress plays a major role in the success/failure of ignition compared to the propagation criterion, C5. In addition to these remarks, the difficulty of properly evaluating the flame propagation (C5) is evidenced by the results (not shown here but corresponding to Fig. 6.5 a)). Indeed, C5 tries to predict if the kernel will be convected to the exit or anchor the flame close to the injection. But this effect is highly linked to the size of the recirculation zones, as well as to the geometry or flow history which are difficult to evaluate from local quantities as proposed with I-crit-LES. This case highlights that even if a stable premixed flame is very difficult to extinguish (mainly because flame holes can recover from other parts of the flame still burning), aerodynamic effects such as stretch can prevail in the case of their ignition process.

6.2 The Cambridge burner configuration

6.2.1 Description of the burner

The experimental apparatus consists of a duct (350 mm long) bringing the air through an axial swirler (swirl vanes at 60 degrees with respect to the flow axis) up to the combustion chamber [144]. The connecting section to the combustion chamber is annular of inner diameter of 25 mm and outer diameter of 35 mm . The cylindrical chamber is 70 mm wide and 80 mm long. Pictures of the burner are presented in Fig. 6.6. Because of the compacity of the device, n -heptane has been chosen as fuel. Indeed it evaporates very quickly at atmospheric conditions and hence limits the mass of liquid reaching the end of the combustion chamber. In this case, the mixture experiences evaporation, mixing and burning within the limits of the apparatus, which is of interest.

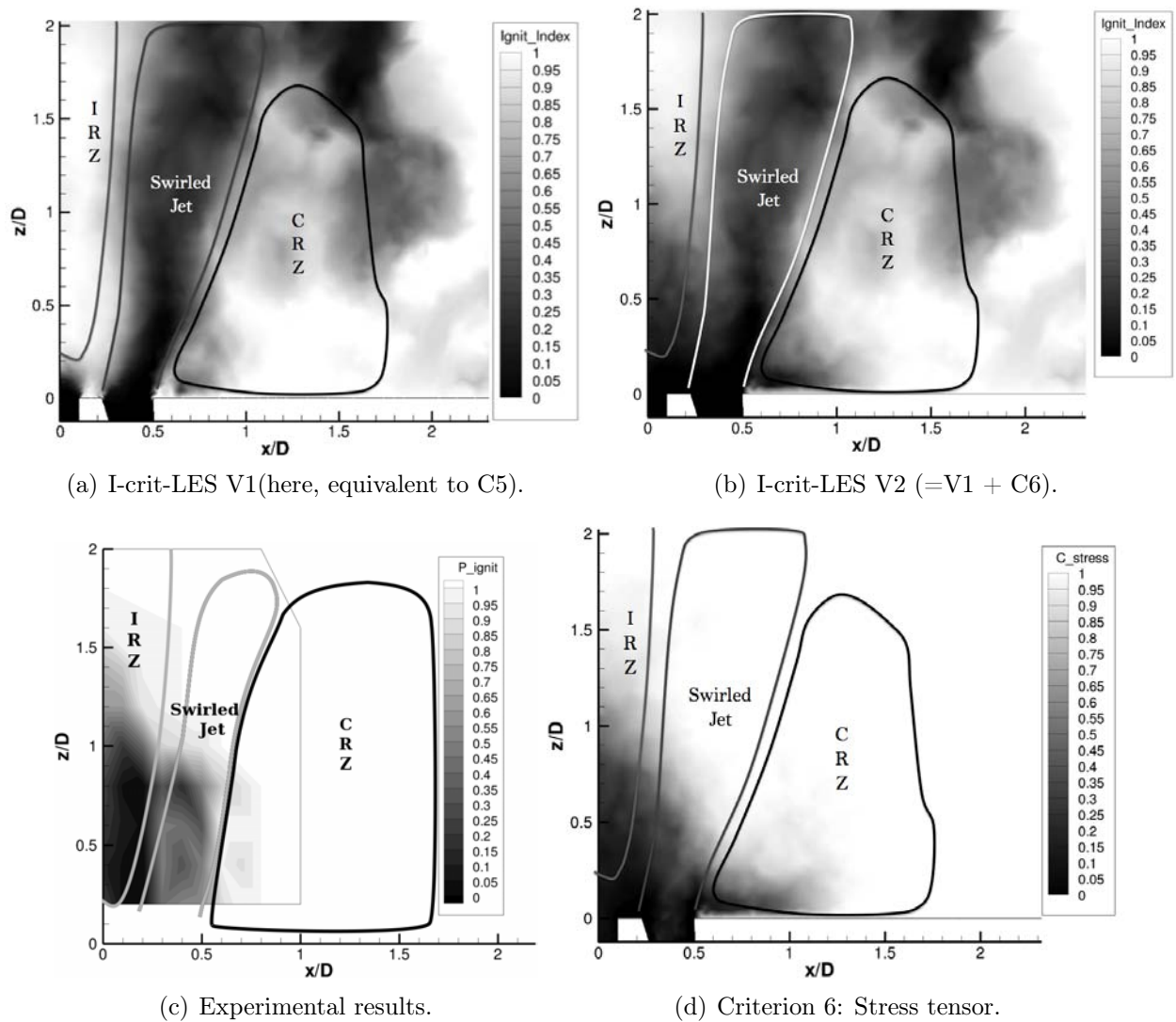


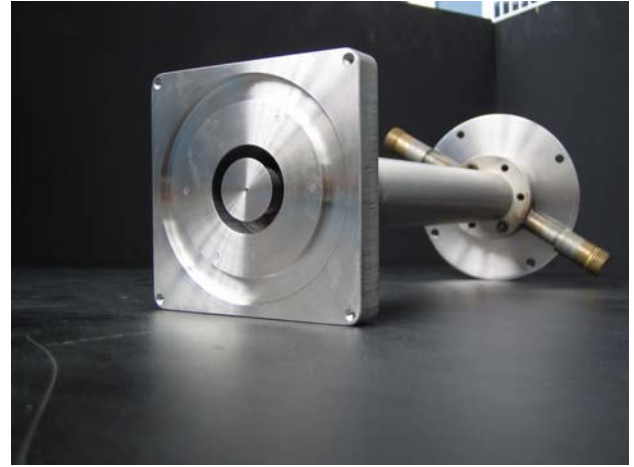
Figure 6.5: Comparison of experimental results with ignition criteria for the ignition operating point on KIAI.

The simulated case $S1$ (see the article of T.Marchione *et al.* [144]) corresponds to n -heptane combustion at a mean equivalence ratio of 0.90 (liquid+gas). Air and fuel are both injected at 300 K and the mean pressure in the chamber is 1 atm. Mass flow rates of air and n -heptane are respectively 0.42 kg/min and 0.025 kg/min .

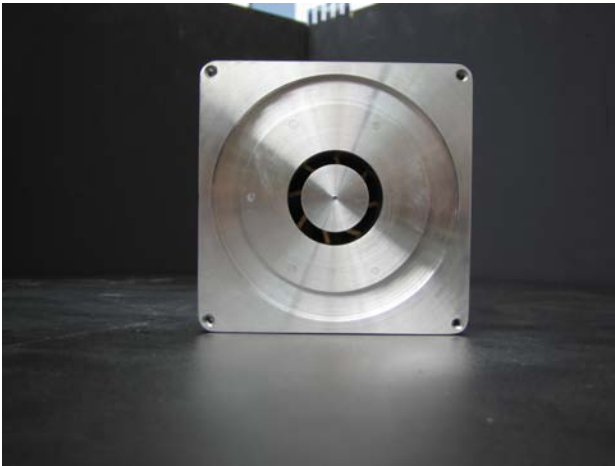
Figure 6.7 presents parts of the geometry which play a major role in the flow topology. Note that the liquid injection has been redrawn to fit the FIM-UR conditions [123] and ease LES: it has been enlarged to have enough cells to discretize the hollow cone and associated gradients of liquid volume fraction α_L . The mesh contains about 3 million cells with a minimal cell size of 0.2 mm close to the liquid injection point (see Fig. 6.7 b).



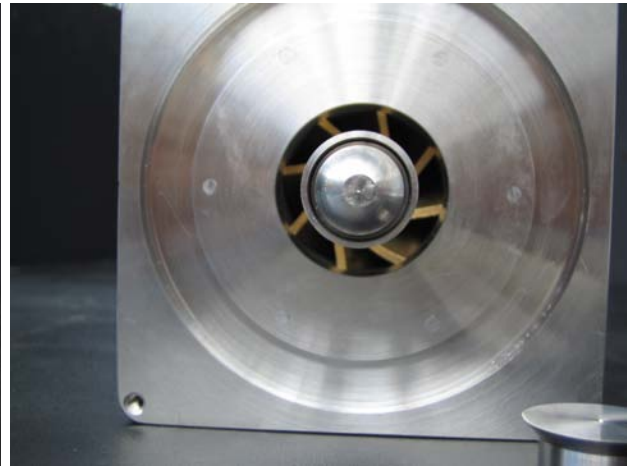
(a) The cylindrical duct bringing the air up to the chamber, the bottom chamber plate and the axial swirler.



(b) The (a) parts mounted.



(c) View of the bottom chamber.



(d) Zoom on the bottom chamber. The swirler is visible through the annular slit.

Figure 6.6: Pictures of the burner (courtesy of Cambridge University, Pr. Mastorakos).

This simulation uses the sub-grid scale model WALE [171] along with no-slip walls. Characteristic boundary conditions NSCBC [169] are used for inlet and outlet sections. A monodisperse Eulerian model has been applied to represent the dispersed phase [121]. The numerical scheme PSI has been used in order to limit the artificial viscosity for the liquid phase [108, 124]. In the experiments, the ignitor is a spark delivering 200 mJ of energy. According to the experimentators, the energy released to the gas is about 60 mJ , which is the value used for I-crit-LES predictions. The size of the energy deposit used by I-crit-LES is the same than the one of the experiments, 2 mm .

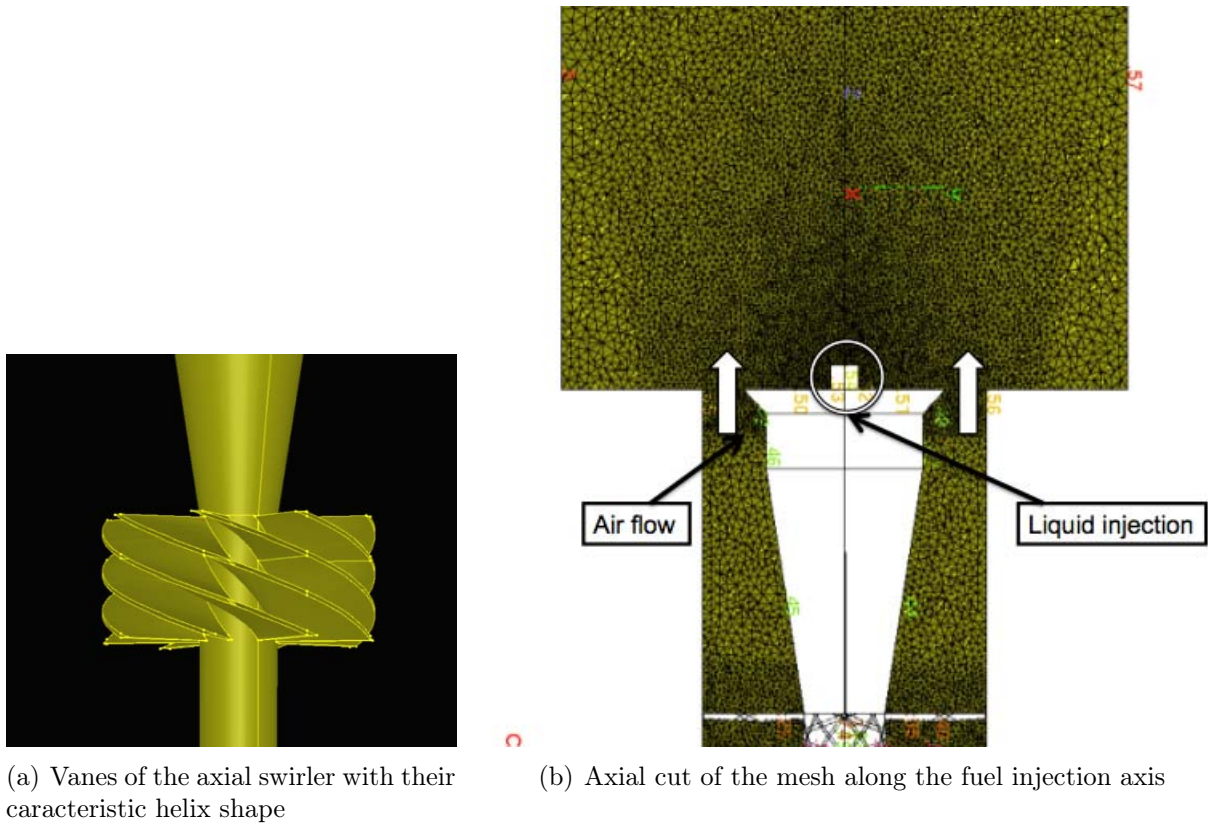


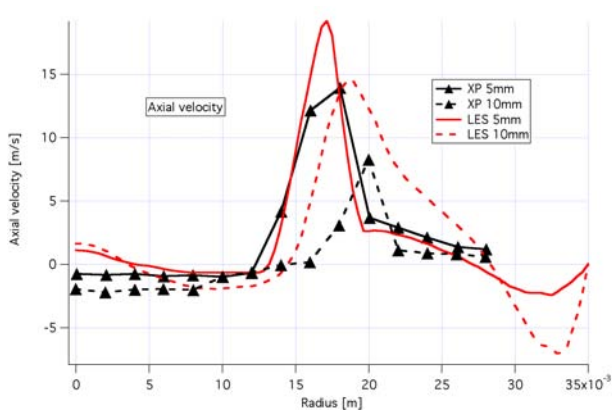
Figure 6.7: Geometry and mesh of the LES

6.2.2 Validation of the cold LES against measurements

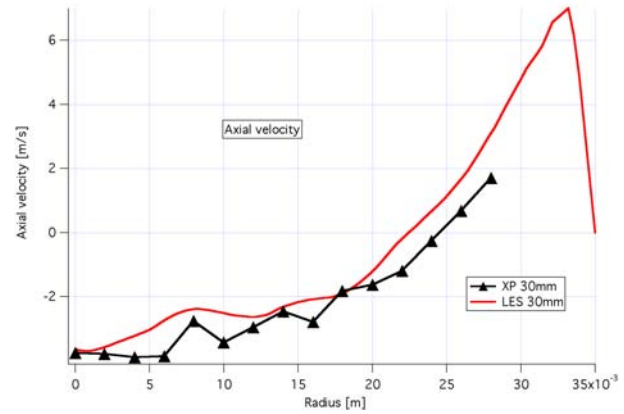
Figure 6.8 presents the velocity profiles of the cold flow with liquid injection. Numerical predictions match quite well experimental findings even if there are some discrepancies for the maximum value for both axial and orthoradial components. In the LES, the peaks are sharper. According to the experimentators, the comparison would benefit of better resolution measurements (2 mm in our case), however the limitations of the LES modeling are clearly part of these discrepancies. Being aware of these limitations, the cold LES is used to extract flow realisations for the I-crit-LES methodology.

6.2.3 Application and results of I-crit-LES V1

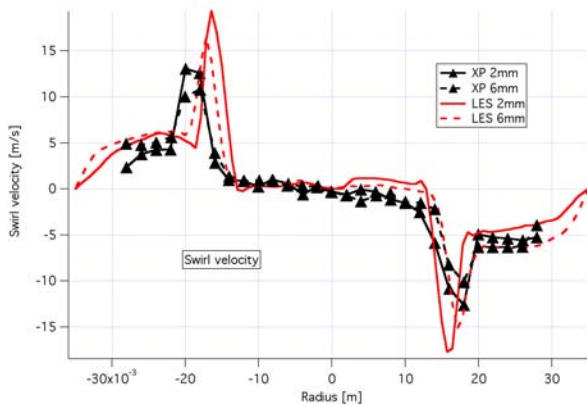
The I-crit-LES model of section 5.2.1 was applied to the bluff body burner from Cambridge and compared to ignition probability maps obtained by [144]. The results are displayed in Fig. 6.9. The poor probability of ignition close to the liquid injection along the axis and for radial positions above 13 mm are recovered. However, the central zone of low probability is larger with I-crit-LES. If we look at the equivalence ratio fields, Fig. 6.10 underlines the high diffusion of the fuel in the transverse direction in the LES. The very high volatility of the *n*-heptane fuel at 300 K and the difficulty of the numerical scheme to handle such strong



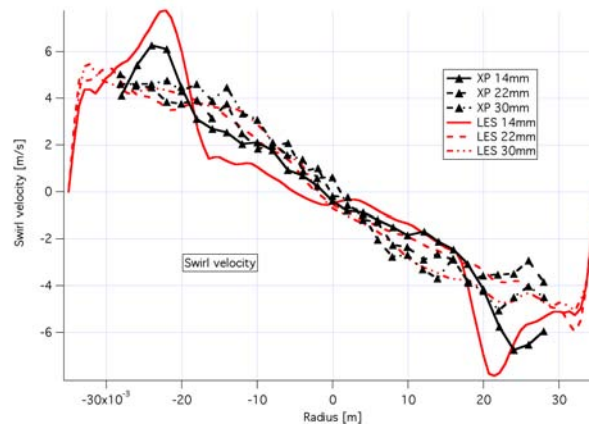
(a) Axial velocity at 5 and 10mm



(b) Axial velocity at 30mm



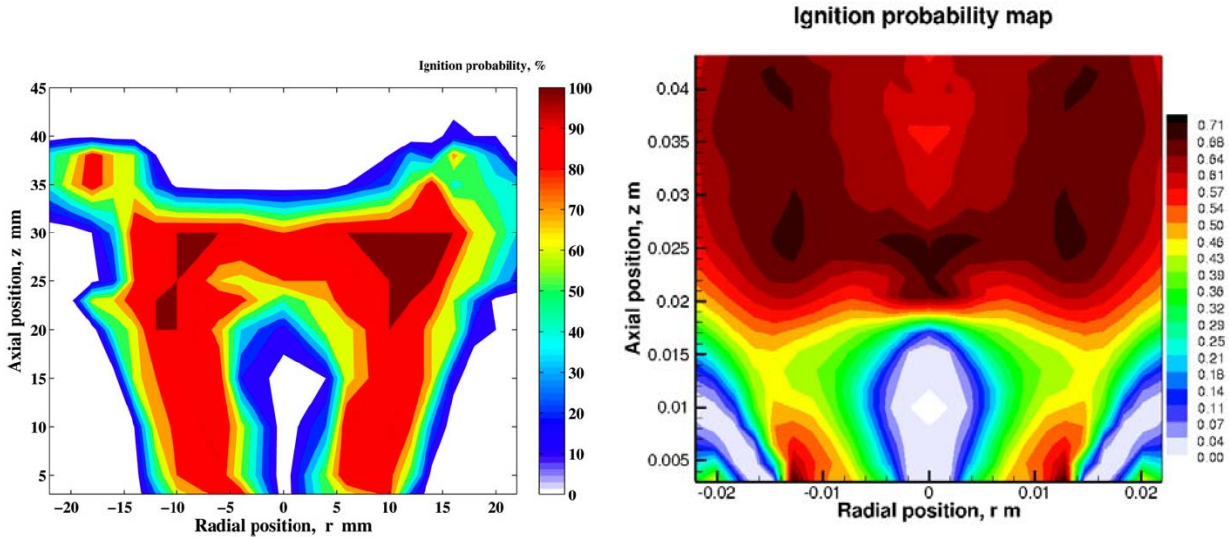
(c) Orthoradial velocity at 5 and 10mm



(d) Orthoradial velocity at 30mm

Figure 6.8: Velocity profiles of the cold flow. Lines represent the LES. Lines + symbols represent the experiments.

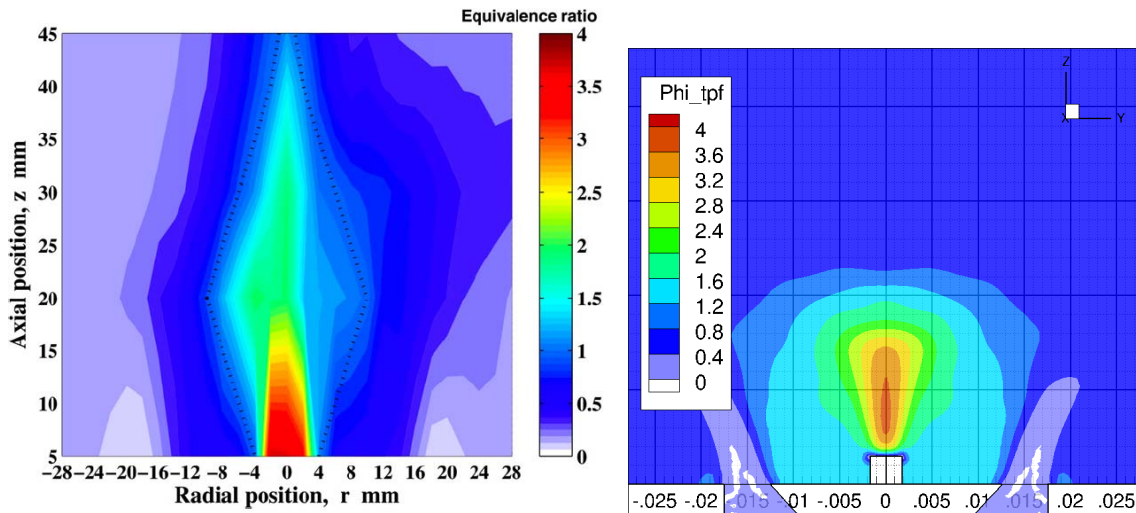
gradients inherent to the Eulerien modelisation of the dispersed phase can explain this excess of diffusion. The net result of this numerical artefact is the change of the chamber carburation and hence the evaluation of the criterion 1 which becomes the most restrictive in this zone. For radial positions above 15 mm, the probability measured is zero up to an axial position of 20 mm. I-crit-LES does not predict such a long zero probability zone. This low probability zone predicted by I-crit-LES is dominated by criterion 5 which is linked to the local axial velocity. Hence, because the velocity profiles compared in section 6.2.2 are similar, the difference comes from an other phenomena not captured by the criteria. For axial positions over 35mm the ignition probability measured in the experiments drops to zero while it keeps very high values with I-crit-LES. According to the auteurs, this is due to high velocities leading to a blow out. The velocity fields being the same between experiments and LES, criterion 5 would capture this. So this is another limit of this version of I-crit-LES which will be improved in the V2 (section 5.2.5).



(a) Experimental measurements (courtesy of Cambridge University, Pr. Mastorakos).

(b) I-crit-LES V1 predictions

Figure 6.9: Ignition probability maps



(a) Experimental measurements (courtesy of Cambridge University, Pr. Mastorakos).

(b) LES results

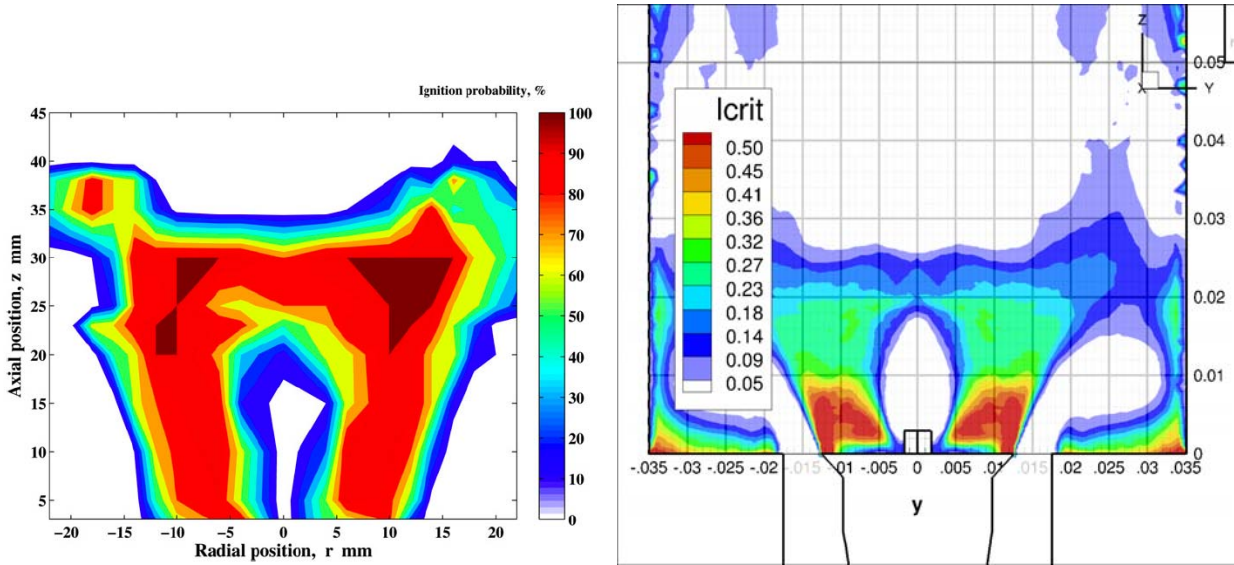
Figure 6.10: Comparison of the carburations XP vs LES

6.2.4 Evolutions of the results with I-crit-LES V2

In Figure 6.9, it has been shown that I-crit-LES fails to catch the suddent drop in ignition probability above an axial position of 35 mm, even if it exhibits a correct behaviour upstream. According to the experimentators, this may be due to a blown out kernel to the exit.

The results obtained with the new version detailed in section 5.2.5 and shown in Fig. 6.11

underline the ability of the new method to capture the probability drop above a certain axial position, here 25 mm . It seems that even if the exact axial position is not fully recovered, the corrections are able to give the right shape of the non-zero probability. This addition also confirms the blow out which has been noticed in the experiments.



(a) Experimental measurements (courtesy of Cambridge University, Pr. Mastorakos).

(b) I-crit-LES V2 predictions

Figure 6.11: Comparison of ignition probability maps

Figure 6.12 presents the two discriminating criteria in this configuration. According to these fields, it appears that the drop of probability position is not due to a convection of the kernel downstream (i.e. $C5 = 0$) but to a ripping of the flame sheet because of a too high strain. Since it is quite challenging to evaluate the correct limiting extinction strain of a flame, more accurate estimates should be tested and could explain the difference in the prediction of the upper axial position of a non-zero probability. Here, the evaluation of criterion 6 could be improved or confirmed in two ways. First, improving the carburation of the chamber, i.e. the equivalence ratio map and second by improving the correlation used to evaluate the extinction limit for the strain.

6.3 The MERCATO configuration

6.3.1 Application and results of I-crit-LES V1

The I-crit-LES model (5.2.1) is now applied to the MERCATO configuration described in chapter 3. Prior to the comparison of true ignition probability (i.e. computed with several snapshots), the first test is to check if I-crit-LES is able to match the success/failure of individual

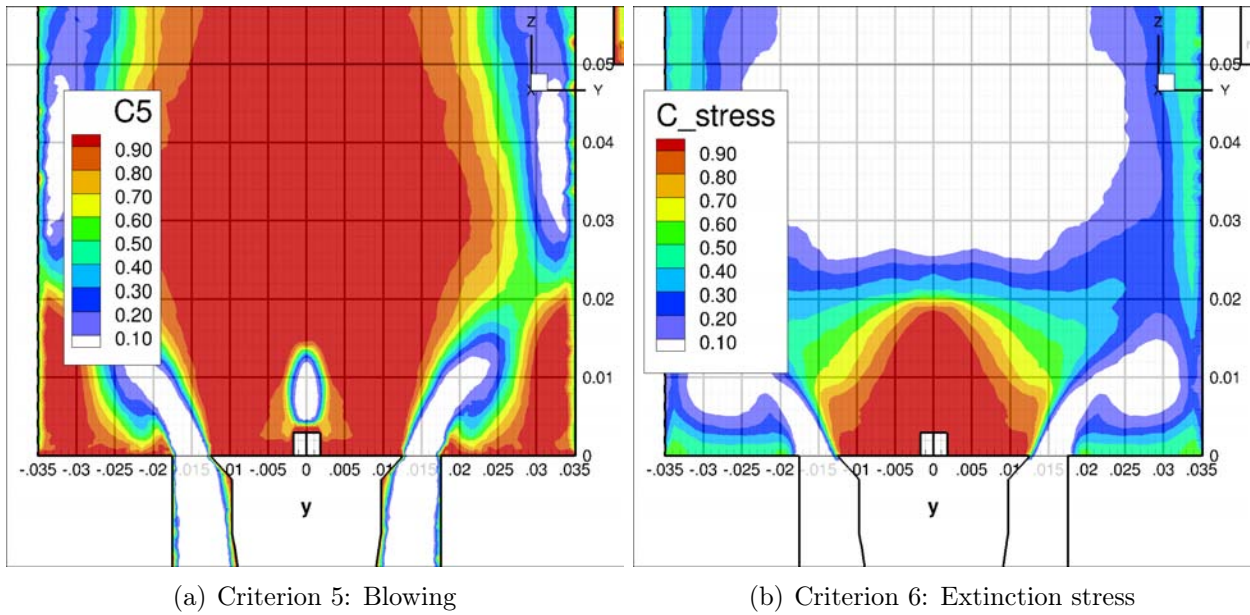


Figure 6.12: Relevant criteria maps on the Cambridge configuration

deterministic ignition sequences as presented in section 4.2 (11 individual tests). For each test, only one LES solution is used (the one at the corresponding t_0), yielding binary values: 0 or 1. The results are shown on Fig. 6.13. The methodology predicts no ignition for $t_0 = 459.75$ ms and 460 ms, almost no ignition for $t_0 = 459.25$ ms and 460.5 ms but with favorable zones for ignition very close to the spark, and ignition for the other instants (especially for $t_0 = 464$ ms). These observations are in very good agreement with the previous ignition sequences performed directly by LES. Like in Fig. 4.4, failure of ignition at time 459.75 ms and 460 ms are predicted as well as the sharp ignition at time 464 ms. I-crit-LES does not predict late ignition phenomena ($t_0 = 459.25$ ms and 460.5 ms), as this involves convection of the kernel (i.e. trajectory computations) which are very expensive and can not be captured simply by analytical models.

The main purpose of this index being to provide statistics about ignition, the strategy is ganged against experimental data. In the experiments [7], several positions of the ignitor were tested (along $z = 26$ mm and $z = 56$ mm). Since a few sparks have been done for each position along the two test lines ¹, an accurate probability cannot be given and only qualitative results are presented from these measurements (never ignite vs may ignite). However, in order to get a quantitative reference, a point, at 56 mm from the bottom chamber and 57 mm from the axis of the burner has been widely measured. The ignition probability was then calculated from the recording of success/failure of ignition. A direct comparison with the present model is thus possible.

¹This is due to difficulties to clean the combustion chamber walls after each tests. Indeed, liquid kerosene flows along the windows and has to be cleaned to get the same conditions for each test.

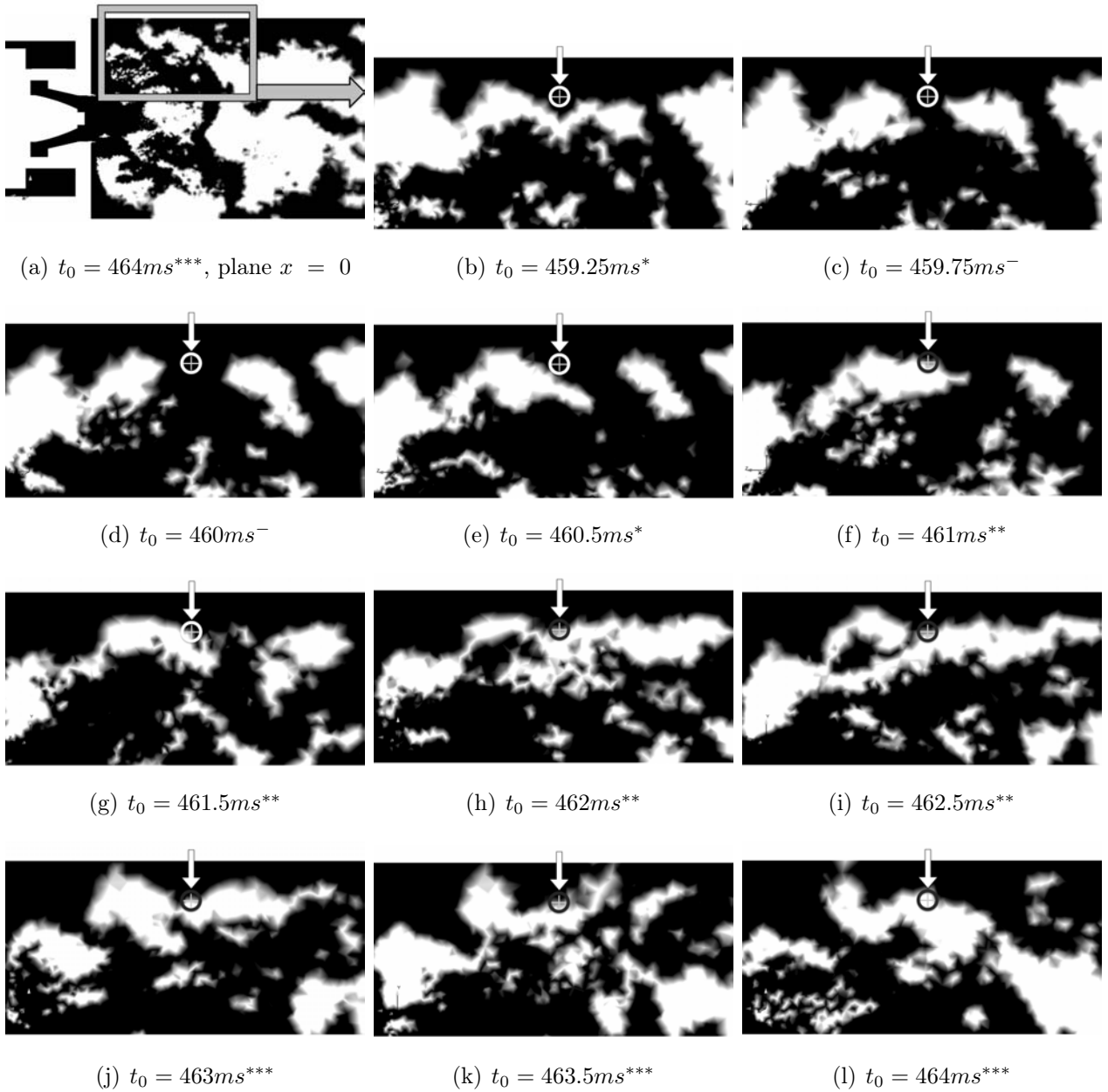
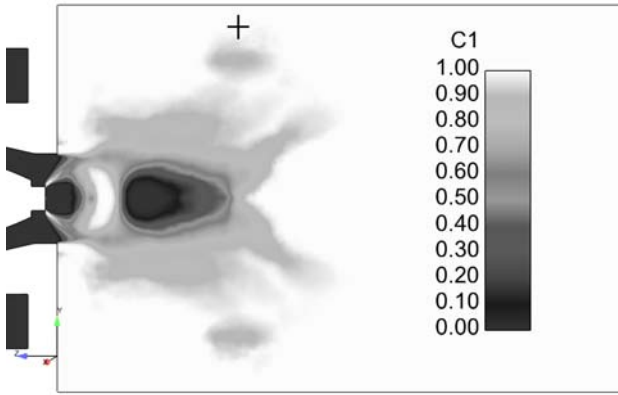
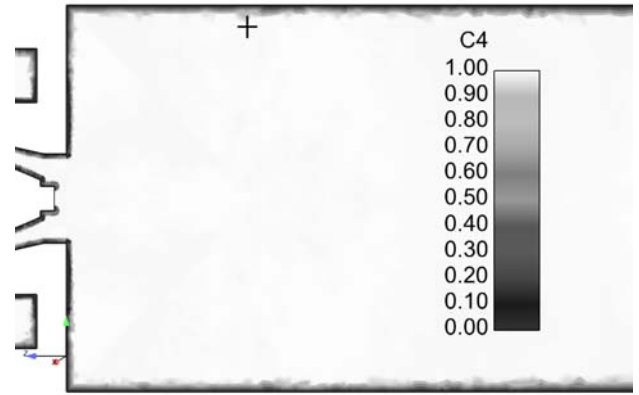


Figure 6.13: I-CRIT-LES applied to single snapshots for the same times as in section 4.2. White: I-CRIT-LES=1 (ignition) ; Black: I-CRIT-LES=0 (no ignition). Reminder of Fig. 4.5: circle denotes spark location. The following superscripts denote sequences that yield $-$: failed ignition ; $*$:late ignition ; $**$: successful ignition ; $***$: sharp ignition.

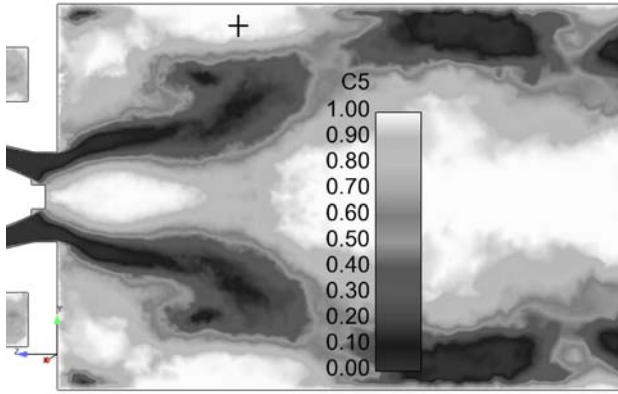
To obtain ignition probabilities, the ignition index is built taking 200 independent instantaneous LES solutions (issued from TTGC simulations) over a total time of 20 ms . The parameters used for I-crit-LES are $E_{dep} = 100 mJ$ (same order than in the experiments) and



(a) Criterion 1: Flamability limits



(b) Criterion 4: Wall quenching



(c) Criterion 5: Blowing

Figure 6.14: Criteria in the $x = 0$ plane (criteria 2 and 3 being valid in the whole combustor are not presented). Black cross: spark location for ignition sequences simulations. $E_{dep} = 100 \text{ mJ}$

$d_k = 8 \text{ mm}$ (this is determined to avoid temperature exceeding 5000 K during the deposit). Figure 6.14 presents the leading criteria of the approach and as obtained when applied to the MERCATO configuration (i.e. not equal to one in the whole chamber). According to the map of α_l (Fig. 4.1 b), the areas of low value for C1 (flammability limits) are located close to the liquid injection (too rich mixture) and in the upstream part of the CTRZ where there is no fuel accumulation. Because of the low velocity oriented toward the walls in the combustion chamber, values of C4 (wall quenching) remain very low confirming that wall quenching is not a main issue in this configuration. The contours of C5 (flame blowing) are almost delimited by those of the recirculation zone, although the borders are smooth in high shear zones where fluctuations are important.

The ignition probability map issued by I-crit-LES (shown in Fig. 6.15) is qualitatively in good agreement with experimental findings, indicated with the black and white arrows in the figure, except in the CTRZ (along $z = 56 \text{ mm}$) where the estimated probability is quite high

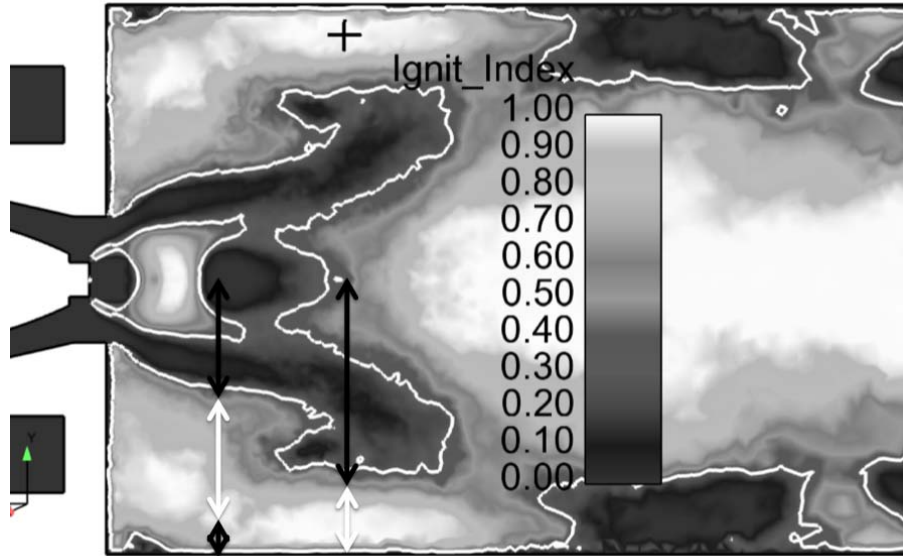


Figure 6.15: Global ignition index in the $x = 0$ plane given by I-crit-LES (V1) for $E_{dep} = 100$ mJ . Dark zones correspond to low ignition probability (white isoline for $P_{ign} = 0.33$). Arrows report experimental tests (white means ignitions have been observed, black means no ignition observed)

(i.e. gray) while no ignition could be obtained experimentally. This is however explained by the fact that the laser ignitor used in the experiment could not be focused at the center of the domain due to the presence of the spray and its diffraction effect on the laser beam ². Now looking at the position of the dark cross (56 mm from the bottom chamber and 57 mm from the axis of the burner, Figs. 6.14 and 6.15), the experiment gives a probability of about 30% (one of the highest for the positions tested) compared to I-crit-LES which gives about 90%. In the following section, the addition of the criterion based on stress, i.e. I-crit-LES V2, is tested to evaluate its potential benefits to some lack of prediction with the original version V1.

6.3.2 Evolutions of the results with I-crit-LES V2

The results of the I-crit-LES V2 approach are displayed on Figs. 6.16 and 6.17. Compared to the original version of the approach, Fig. 6.15, the quantitative estimate (dark cross position) is clearly improved: 40% against 90%.

On Figure 6.16, the relevant criteria of version 2 (5.2.5) are presented for the median axial plane ($x = 0$). Since criteria 4 and 5 are not modified from the initial version the fields remain identical. Criteria 2 and 3 are still not discriminatory. The contribution of C6 (stress limit) is here quite important. Globally it decreases the ignition probability in the whole chamber and appears to be not spatially discriminating, except in very lean areas. As expected, the area

²confirmed by the experiments

where the criterion is zero is the upstream part of the CTRZ where shear is maximum.

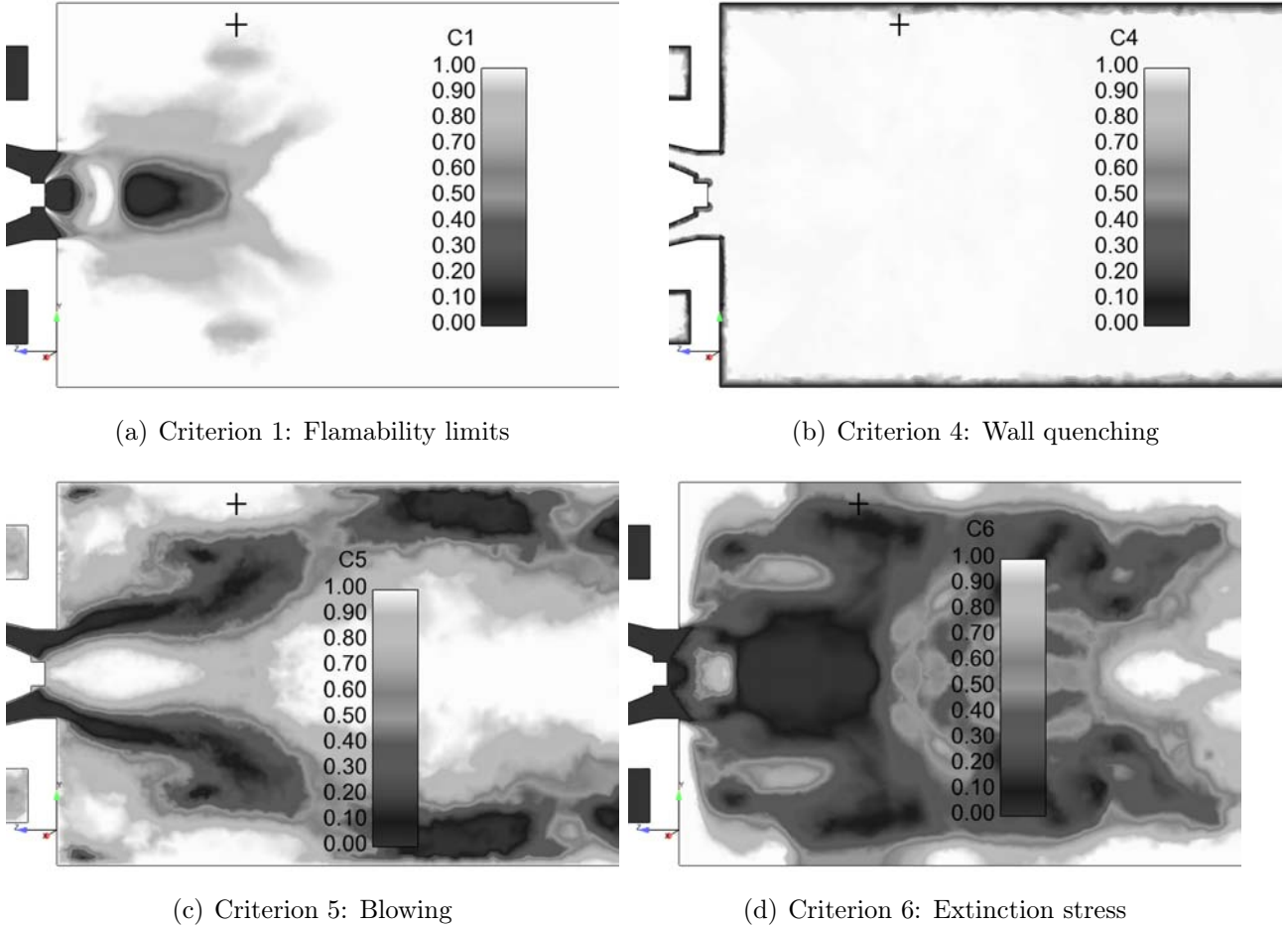


Figure 6.16: Criteria in the $x = 0$ plane. Black cross: spark location for ignition sequences simulations. $E_{dep} = 100 \text{ mJ}$

The addition of C6 (see Fig. 6.17) provides predictions in good agreement with the experimental measurements along with a slight improvement in the region of the liquid injection axis. However, it is difficult to conclude since according to experimentators they cannot focus accurately the laser beam in this region.

In order to better understand the cause of ignition failure, the local limiting criterion is displayed in Fig. 6.18. The values ranging from 1 to 6 for the improved I-crit-LES correspond to the criterion with the lowest probability (over all realisations). The value 7 indicates that all criteria are validated and ignition is highly probable (more than 0.5).

Figure 6.18 provides an identification of the mechanism leading to failed ignition: dark regions correspond to a failure of criterion 1, i.e. flammability limits. The first dark zone is at the fuel injector nozzle, where droplets accumulate because of the recirculation zone just downstream yielding a mixture that is too rich. The second dark zone corresponds to the upstream

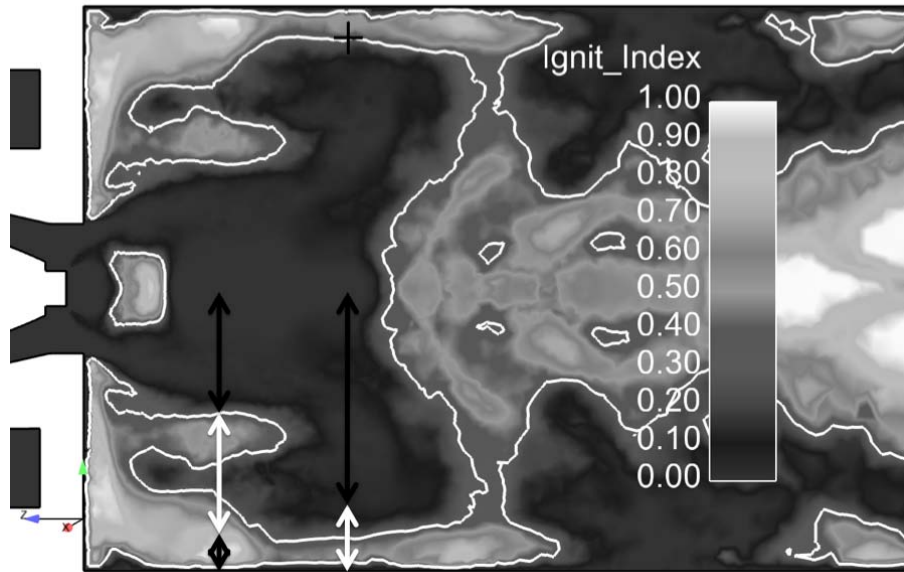


Figure 6.17: Global ignition index in the $x = 0$ plane given by I-crit-LES (V2) for $E_{dep} = 100$ mJ . Dark zones correspond to low ignition probability (white isoline for $P_{ign} = 0.33$). Arrows report experimental tests (white means ignitions have been observed, black means no ignition observed)

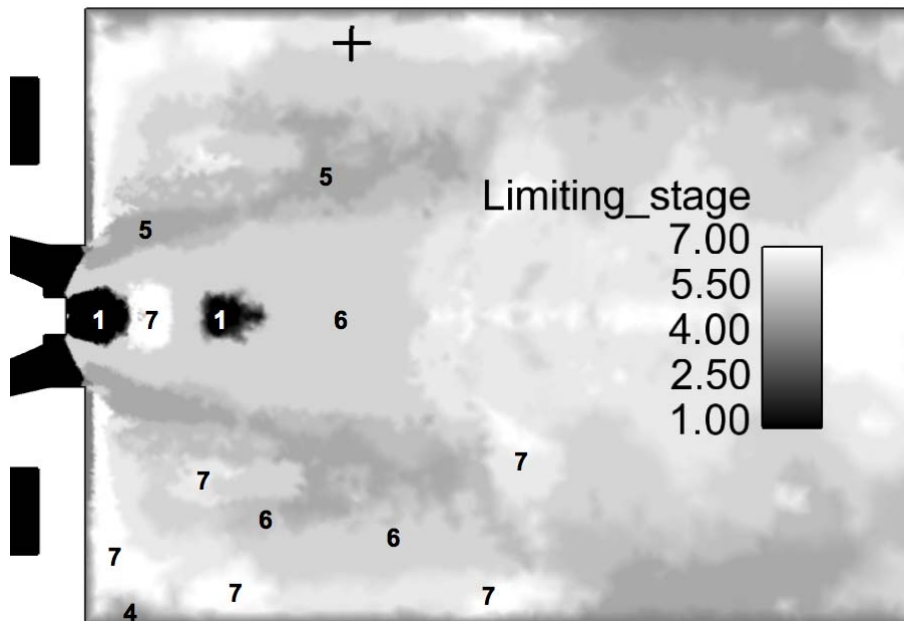


Figure 6.18: Limiting criterion in the $x = 0$ plane. Black cross: spark location for ignition sequences simulations. $E_{dep} = 100$ mJ

part of the CTRZ where there is no fuel accumulation. Criterion 2 is always fulfilled, meaning that the energy deposit is always sufficient in this case. Similarly, the volume of hot gases produced by the initial energy deposit is large enough to sustain combustion and criterion 3 is always fulfilled. Criterion 4 applies only in a thin zone near the wall (as expected). Criterion 5, in light gray, is limiting in zones of strong axial velocity: in the shear zone around the central recirculation where the turbulent flame speed is not sufficient to propagate the flame in the upstream direction. Finally, the velocity gradients inside and around the CTRZ imply restrictions of the ignition probability in these zones. Because of the high shear between the main flow expansion and the CRZ, the effect of criterion 6 is also dominating around the high speed zones.

An alternative use of the ignition index is to determine the Minimum Ignition Energy (MIE) to be provided for successful ignition: this point is reached when criterion 2 becomes the most restrictive. Since the kernel diameter d_k depends on the energy deposited, criterion 3 is also affected and can decrease dramatically in some regions. For this operating point, it was found that a minimal energy of about 20 mJ was necessary to have relatively large area (about few d_k large) of non zero probability to ignite the chamber (the experimental tests were done with an energy from 60 to 212 mJ, its purpose was not to evaluate the MIE) .

6.4 Applications of I-crit-LES to realistic geometries

CONFIDENTIAL INDUSTRY

6.5 Conclusion of part III

The computations of ignition sequences with LES in part II have proven a great potential contribution to the knowledge of the ignition phenomena. However, due to the stochastic characteristic of ignition, only probabilities are practical for industrial applications. Building ignition probability means computing hundreds of LES and brings the CPU cost to unreasonable values.

A new methodology, called I-crit-LES, to evaluate ignition probability has thus been designed. It uses analytical criteria based on data from non reacting unsteady two-phase flows computed with LES. According to the phenomena observed through previous simulations (cf. part II), six criteria are defined to model the full ignition of a sector burner and reads:

- C1: The fuel distribution must guarantee a flammable mixture.
- C2: The discharge energy must be sufficient to create a first hot gas kernel.
- C3: The local conditions (vaporisation time versus diffusion time) must allow the kernel to increase.
- C4: The flame must not be quenched near walls.

- C5: The flame speed must be larger than the local flow speed to allow the flame to propagate upwards.
- C6: The local stress experienced by the kernel must be low enough to avoid aerodynamic quenching.

The methodology I-crit-LES has been applied to various configurations. The purpose is to cover a wide range of conditions to test the limits of the model. The overall results are in good agreement with available experimental data. However, the following limits have been identified and need some improvements:

1. When the proportion of the liquid phase is low (Cambridge burner) or for purely gaseous cases (KIAI burner), the extinction limit by strain seems to play a major role. The main difficulty is to estimate this limit for different fuels (gas or liquid) at different operating conditions. Very few data is available.
2. The evaluation of the criterion are fully local for the moment. However, during its development, the flame kernel may be submitted to relatively large advection and modification of the local conditions. In some regions it may lead to mispredictions like with the KIAI burner.
3. Assuming correct carburation of the chamber, the evaluation of the equivalence ratio is made under the assumption of homogeneous combustion regime, i.e. the liquid is fully evaporated before reaching the flame. The correct estimation of the equivalence ratio actually seen by the flame, especially for rich mixture, is challenging and would improve the quality of the predictions for both C1 (flamability limits) and C6 (extinction strain).

Conclusion and perspectives

The main objective of this thesis is the study of two-phase flow ignition in realistic combustors. The work detailed here is constructed around one main configuration, the MERCATO bench installed at ONERA Fauga-Mauzac. The operating point selected has been experimentally defined to perform ignition sequences as well as some stationary flame LES assessments. The velocity components for both phases has been measured using LDA (gas phase) and PDA (liquid phase). For the non reacting case, the lack of data at the actual operating point has been overcome using autosimilarity correlations giving the correspondence from one operating point to another. For the reacting case, only data measured at the actual operating point are valid and used. Euler-Euler non reacting and reacting LES are performed for the MERCATO configuration and are compared to the experimental data. All this information is capitalized in this work and has been used to assess current two-phase flow LES capabilities.

Two numerical approaches have been applied first to the non-reacting case showing very good agreement with the measurements for both phases. However, some discrepancies between the two numerical strategies have been observed. The difficulty to predict the stagnation point in front of the liquid injection is also clearly underlined. Since the dispersion of the spray is linked to its interaction with the PVC, this difficulty can lead to quite large variations in the carburation of the chamber. Computing correctly the liquid injection seems therefore of primary importance and numerics as well as modeling (cf. P.Sierra PhD (2012)) play a crucial role in that region. In the case of TTGC numerical scheme [125] plus artificial viscosity, the liquid fuel is able to directly reach the CTRZ while with PSI numerical scheme [108] it has to go around before entering in the CTRZ. Such differences yield two reacting different instantaneous flame shapes and potential differences in local combustion regimes. However, mean velocity profiles and flame position remain very similar in terms of mean fields. Further studies of the reacting case show the complexity of the flame, and especially of the flame type (diffusion or premixed). Indeed, depending on the flame part, the fuel feeding the flame does not experience the same level of evaporation and/or mixing. According to these studies, several perspectives to improve the simulations arise:

1. Optimize the numerical strategy: optimize the artificial viscosity sensor for TTGC / find a robust scheme less diffusive than PSI.
2. Improve *RUM* closure models (see E.Masi (2010) or P.Sierra (2012) theses)
3. Improve evaporation models (see P.Sierra (2012) thesis)
4. Improve the spray dispersion using locally polydisperse description (Eulerian [172, 139] or Lagrangian [78, 79])

Statistically stationary flow regimes being validated, the transient phenomena of ignition is studied next. With the use of the ED model [151], numerical energy deposit is performed to mimic forced ignition. It is shown that the ignition process is highly dependent on the initial flow conditions. This implies that at identical mean operating conditions and with identical ignition device, the ignition depends on the spark location and on the spark time. The high variability of the obtained behaviours for 11 distinct transient LES leads to an unreasonable CPU

cost to evaluate ignition of a realistic combustor although of interest to the scientific community.

To predict ignition probability a framework is proposed and exploits non reacting Euler-Euler LES. To do so, the ignition process of one burner is described through several steps. Then these steps are modeled with analytical criteria. Six criteria have been proposed, and the global methodology resulting in the prediction of an ignition probability is called I-crit-LES. The results are first validated against mono dimensionnal DNS. Then the methodology is applied to complex geometries. The purpose is to cover a large range of conditions to test the limits of the model. First, a purely gaseous and perfectly premixed configuration is used (KIAI burner). It allows to evaluate the basis of the modelisation through a gaseous configuration. Second, a configuration with a light liquid fuel is computed (Cambridge burner). One of the challenges of this bench is the stiffness of the fuel because of its strong evaporation at ambient conditions. Then, the main configuration of this work, the MERCATO bench is used as typical academic representation of an aeronautical burner.

The overall results display the potential of such a methodology. Indeed, despite the assumptions made and the limitations of the numerical models presented in the previous parts, good agreement is found with available experimental findings. Since, this represents a first attempt for an application of ignition prediction for the industry, several path for improvement are proposed. Without the additional complexity induced by the liquid phase, it has been noticed that the extinction, or unfavorable conditions, due to strain plays a major role in low liquid laden flows. Hence, a correct estimation of this extinction limit is of primary importance. Then, since the evaluation of the ignition criterion remains local, in some cases it may lead to mispredictions. This evaluation is particularly sensitive in the criteria of convection, C5. Indeed, despite the pertinence of its definition which evaluate if locally the kernel can move upstream to the injector, the history effect may be important through large advection and modification of the local conditions (see A.Neophytou (2010) thesis). Last, the evaluation of the local equivalence ratio should be improved. It can be done at different levels: first, as seen in chapter 3, the models used for the cold LES can influence the carburation of the combustion chamber; second, the equivalence ratio actually seen by the flame, i.e. the combustion regime. This evaluation is challenging, especially for rich mixture and would improve the quality of the prediction for both flammability limits and extinction strain criteria.

Appendix

Appendix A

Acoustic analysis of two swirlers using LES

The work presented in this appendix is part of the european project KIAI ¹, more precisely the work package 5.3.

In comparison with RANS methods, LES shows great improvement concerning CFD unsteady analysis of non reacting flows in industrial injector systems. Studies establish significant comparisons of LES results with experiments [14]. Nonetheless, technological effects such as small geometrical discrepancies on the same injector system have not been tackled until now. Is LES able to predict variations of the acoustic spectrum resulting from small variations of geometry? Two geometries are computed with LES for non reacting flow. Although quite similar, these geometries are chosen to experimentally show up different acoustic behaviours. The experimental measurements are done by ONERA. Comparisons between the two computations will be performed and confronted to measurements.

This appendix is organized as followed: first a brief description of the experimental setup is presented. Second, the two LES are presented, their spectrum are confronted and maps of the acoustic modes are shown. Third, the eigenmodes of the LES acoustic spectrum are identified and compared with the experiments using the acoustic solver AVSP. Fourth, detailed comparison between the LES and experimental spectrum is presented. Then brief study about the influence of the boundary conditions on the results is done.

The studied flow consists in pure air at $T = 300K$ and atmospheric pressure. The mass flow is $25.9g/s$.

A.1 Experimental setup

For both swirlers studied the surrounding geometry is identical, pictures of the experimental device are displayed in Fig. A.1. The air enters through an inlet pipe of section $7.8 \cdot 10^{-3}m^2$ blowing in a cylindrical plenum of section $5.3 \cdot 10^{-2}m^2$ and $380mm$ long. Then a convergent bring the air through the swirler and exits in a confinement tube $120mm$ of diameter and $500mm$ long. At the exit, the air blows in the room as seen in Fig. A.1.

In order to validate the aerodynamic fields provided by LES, velocity profiles are measured using LDA. The position of the measurements without the confinement tube are visible in Fig. A.2. The LDA was not able to get any measurement inside the confinement tube (transparent) due to its thickness. This actual velocity measurements are done $10mm$ after the end of the tube when comparing with LES.

The pressure signal is caught by a microphone in a plane $10mm$ after the end of the confinement tube. Then the temporal signal is directly processed by a spectral analyser B&K type 2032. The output being directly the amplitude of the FFT pressure signal. The details of the recording protocole are presented in Table A.1.

¹Knowledge for Ignition, Acoustics and Instabilities



(a)



(b)

Figure A.1: Views of the experimental device



Figure A.2: View of the LDA system.

Table A.1: Recording protocole

Recorder	B&K type 2032
Measured variable	RMS in Volt
Windowing	Rectangular
Averaging	1000-5000 spectrum
Calibration	dB SPL with $P_{ref} = 20 \cdot 10^{-6}$
Recording frequency	25.6kHz
Recording length	250ms

A.2 LES of the selected swirlers

A.2.1 Geometry and LES meshes

The LES domain is displayed in Fig. A.3. At the exit of this tube, a cylindrical atmosphere has been drawn. Note that the position of the spectrum probe is in a plane orthogonal to the device axis and 10mm after the end of the confinement tube. In LES the probe is located at a radius $r = 75mm$.

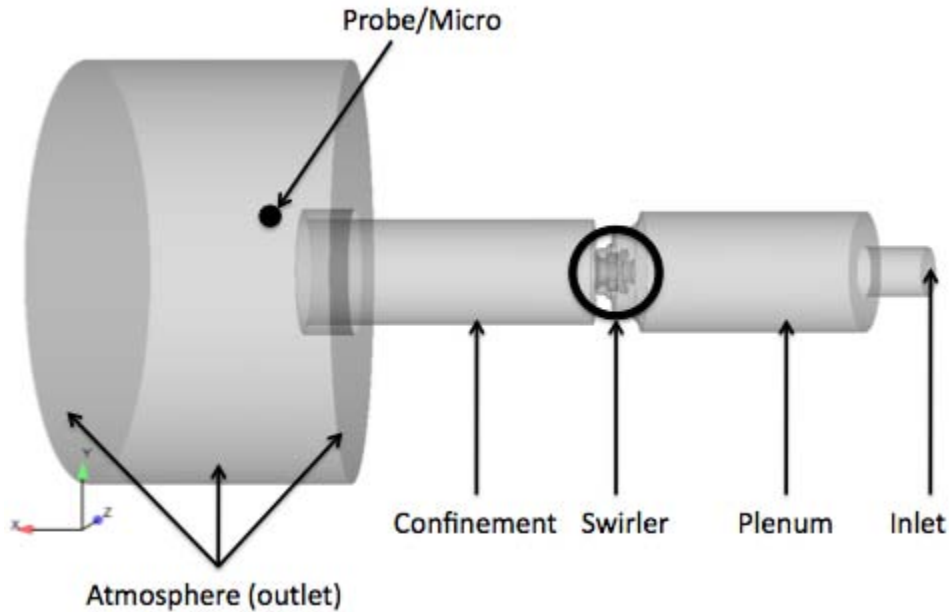
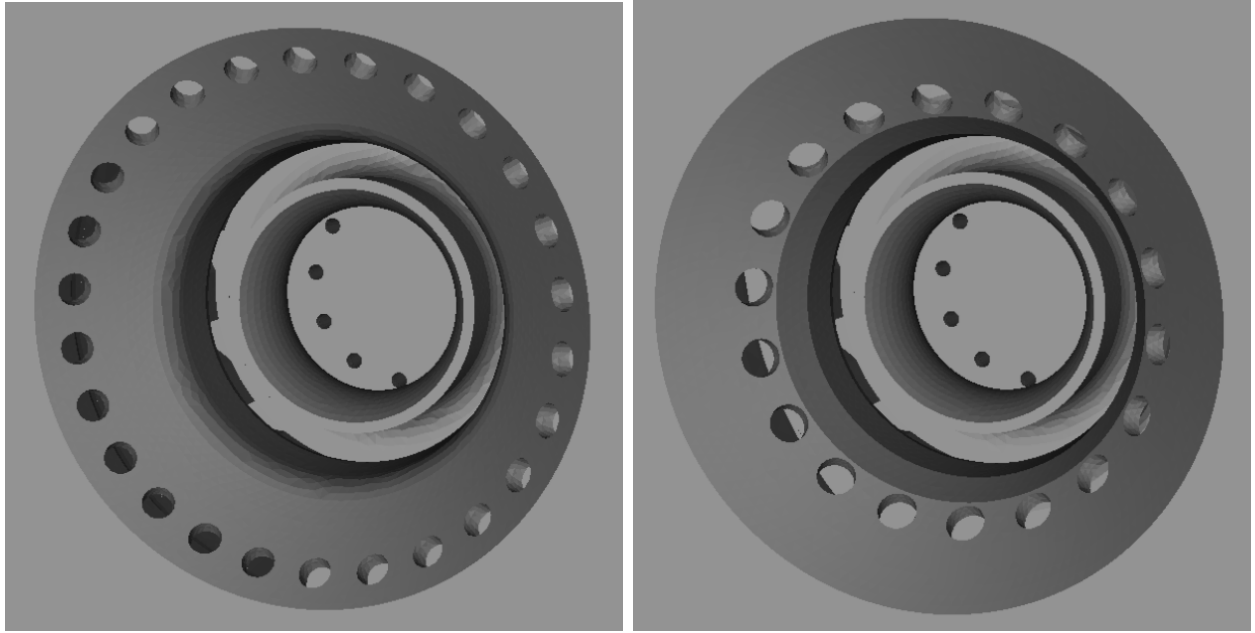


Figure A.3: Geometry of the LES domain

Figure A.4 displays the only difference between the two swirlers. In the geometry A, there are 26 peripheric holes of 2.5mm diameter, the perforation radius being 18mm. In the geometry I, there are less peripheric holes (18) but they are bigger (2.85mm) in order to preserve their total section. Finally the perforation radius is 15mm (closer to the swirler axis).



(a) Swirler A

(b) Swirler I

Figure A.4: Comparative view of the simulated swirlers

The geometry computed by the LES are identical to the swirlers used for the experimental measurements. Because of this, some very small holes (1.5mm of diameter) impose small cells of typical size 0.35mm . The mesh, Fig. A.5, is fully tetraedra and counts about 4.6 millions of cells. The air pathes through the swirler are identified in Fig. A.5: one through axial holes, two through the vanes and one through the peripheric holes.

A.2.2 Numerical parameters

LES use TTGC numerical scheme [125] with the WALE SGS turbulent model [171]. The wall boundary conditions are adherent with adiabatic condition while the inlet and outlet use the NSCBC formalism [169]. To save CPU hours, the equivalent species mixture "air" [173] is used.

A.2.3 Flow topology and validation against measurements

The LES mean statistics presented here are done averaging LES variables for 300ms after statistical convergence. Since, in LES and experiments, the two first moments of aerodynamics provide the results, only configuration A is presented.

Figure A.6 displays the mean and RMS axial velocity fields. The flow exits the inlet channel and does not expend that much inside the plenum, then it hits the back of the swirler. A part of the mass flow goes through the axial holes, the remain mass flow going through the vanes and the peripheric holes. At the swirler exit, as expected ($S = 0.85$) recirculation zones appear, one around the swirler axis so-called CTRZ and the other one in the corner of the wall chamber

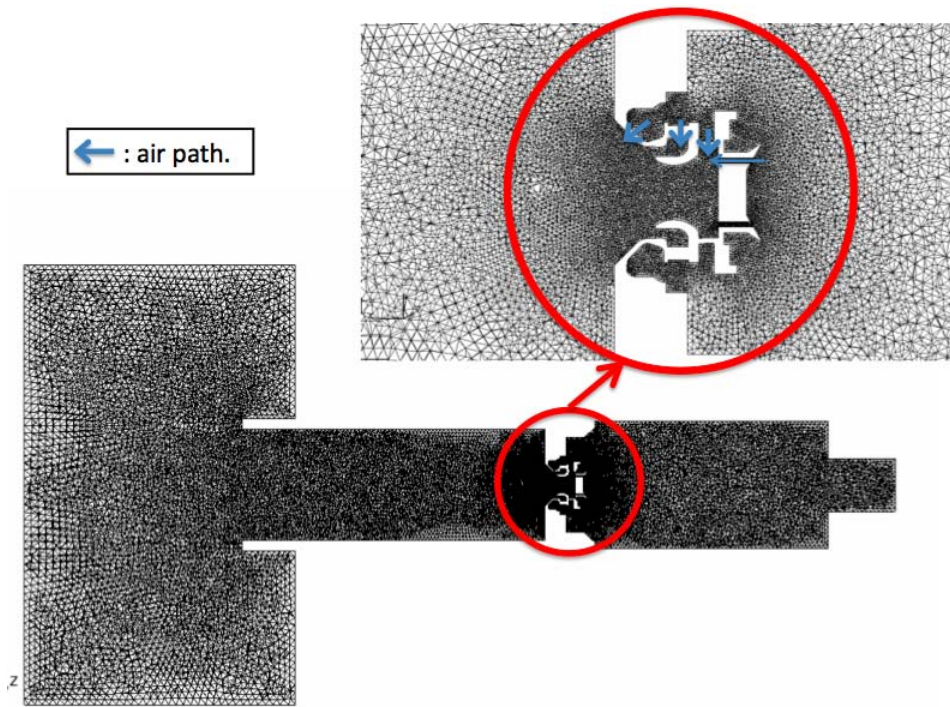


Figure A.5: LES mesh. Axial cut

entrance so-called CRZ, Fig. A.6b). Note that the CTRZ lasts up to the atmosphere, Fig. A.6a). RMS experience high level close to the swirler exit where a PVC takes place, Fig. A.6c-d).

The position of the LDA measurements is displayed in Fig. A.6. Although very low axial velocities encountered at this position, Fig. A.7, LES are in good agreement with the experiments. The variability of the LDA measurements corresponds to the different angular positions.

In order to improve the comparison between LES and the experiments, the length of the CRZ has been measured using "painting" colored by coal, Fig. A.8. The end of the CRZ is identified by the position of a splitting line in the tube. This length is 50mm and matches the LES findings.

The available data being matched with LES, the acoustic spectrum recorded by the probe will be compared in the followings sections.

A.2.4 Acoustics spectrum from LES

The convergence of the flow aerodynamics is obtained after about 100ms . Then, in order to have a spectrum resolution similar to the experiments, the signal is recorded during 300ms and a square windowing is applied for the signal processing. The amplitude spectrum resulting from the two configurations, Fig. A.9, are pretty similar. There are two main peaks around 850Hz and 2400Hz and some secondary peaks around 300Hz , 1350Hz , 2000Hz and 2200Hz .

Using 2000 LES snapshots over 200ms (constant spacing of 0.1ms), for the two configurations the DSP amplitude fields have been processed. The DSP amplitude for the two main

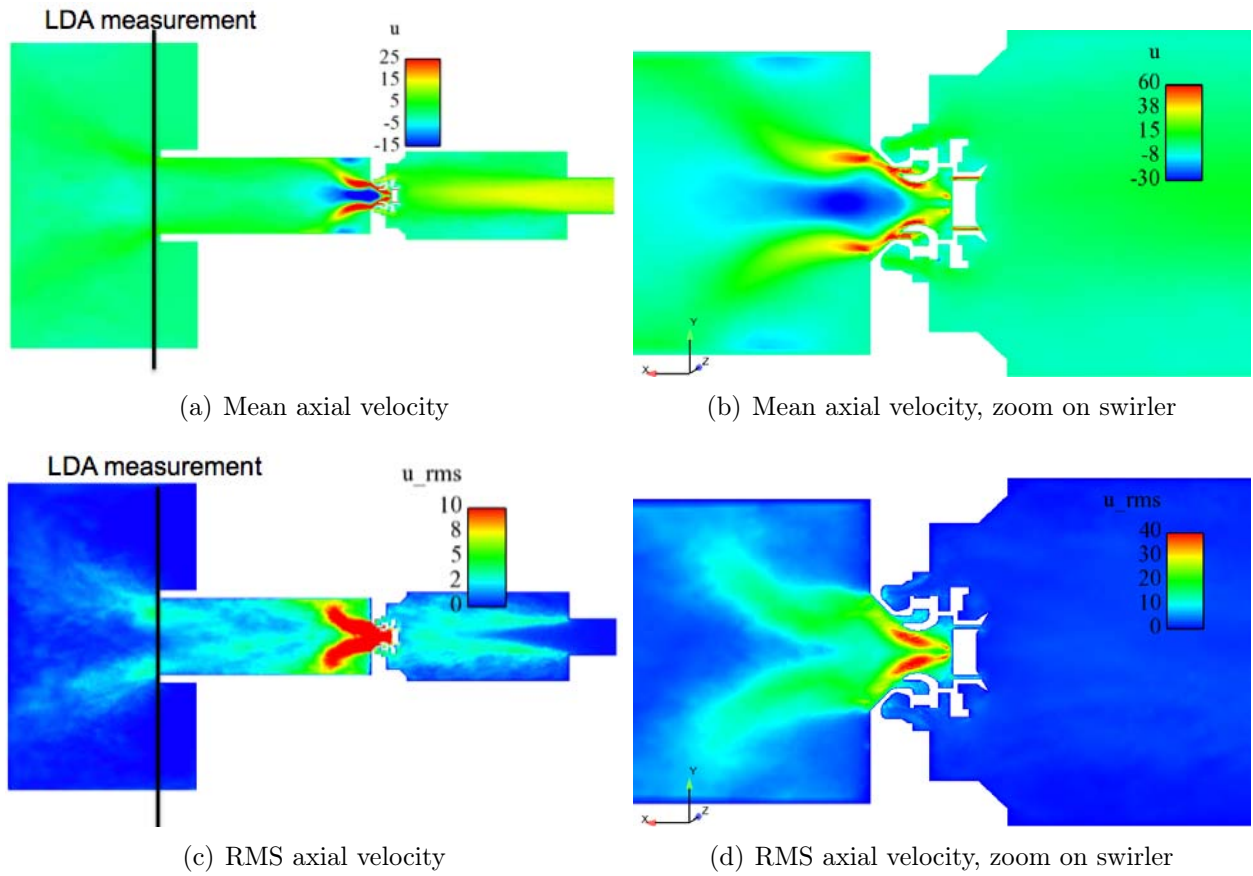


Figure A.6: Axial velocity fields, axial cut

peaks are displayed in Fig. A.10.

As seen in Fig. A.9, the peak located at $850Hz$ has a much lower amplitude in the configuration I than in A (same scales used). The hydrodynamic noise generated by the swirler is more visible on the configuration I. However, the mode in the confinement tube has the same shape for both configurations, corresponding to a longitudinal mode of $3/4$ wave length. For the second peak, there is a small frequency shift between the two configurations: $2350Hz$ for I and $2470Hz$ for A. Their shape are similar and represent a $5/4$ longitudinal wave length mode coupled with the first transverse mode of the confinement tube. One may notice that the confinement tube has a great impact on the resulting spectrum captured by the probe. In order to identify the suspected acoustic origine of the different peaks observed in the spectrum in Fig. A.9, a study of the acoustic eigenmodes of the geometries is done in the next section.

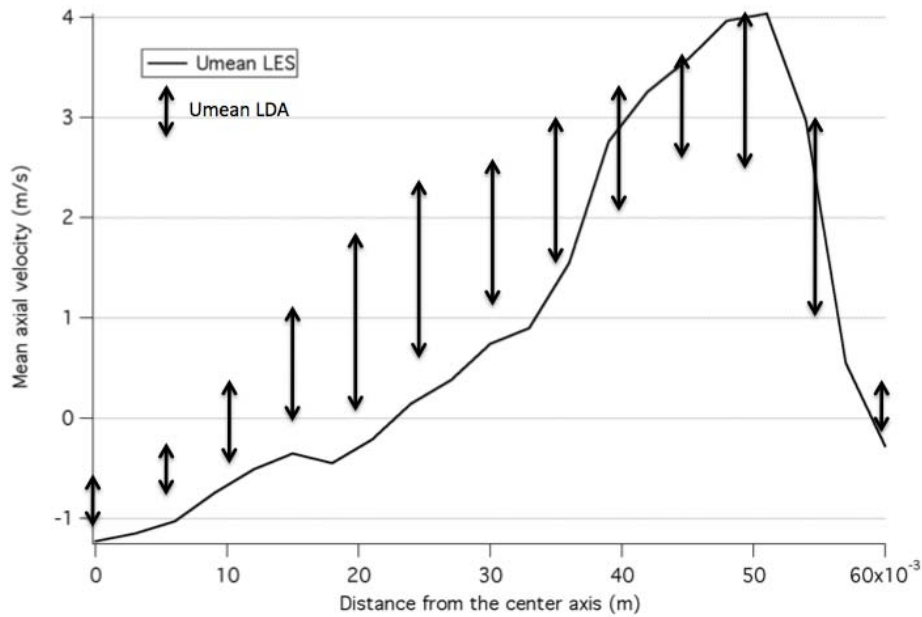


Figure A.7: LDA and LES mean axial velocity profiles.



Figure A.8: Experimental measurement of the CRZ length.

A.3 Identification of the eigenmodes in the LES and experimental spectrum

The acoustic solver AVSP is used to identify the eigenmodes of the two geometries. It solves linearised Euler equations. In our case, the boundary conditions are supposed very simple without any complex acoustic impedance. The geometries and meshes used are identical to LES ones, Fig. A.11. The velocity field used as input for AVSP is an averaged solution obtained with LES.

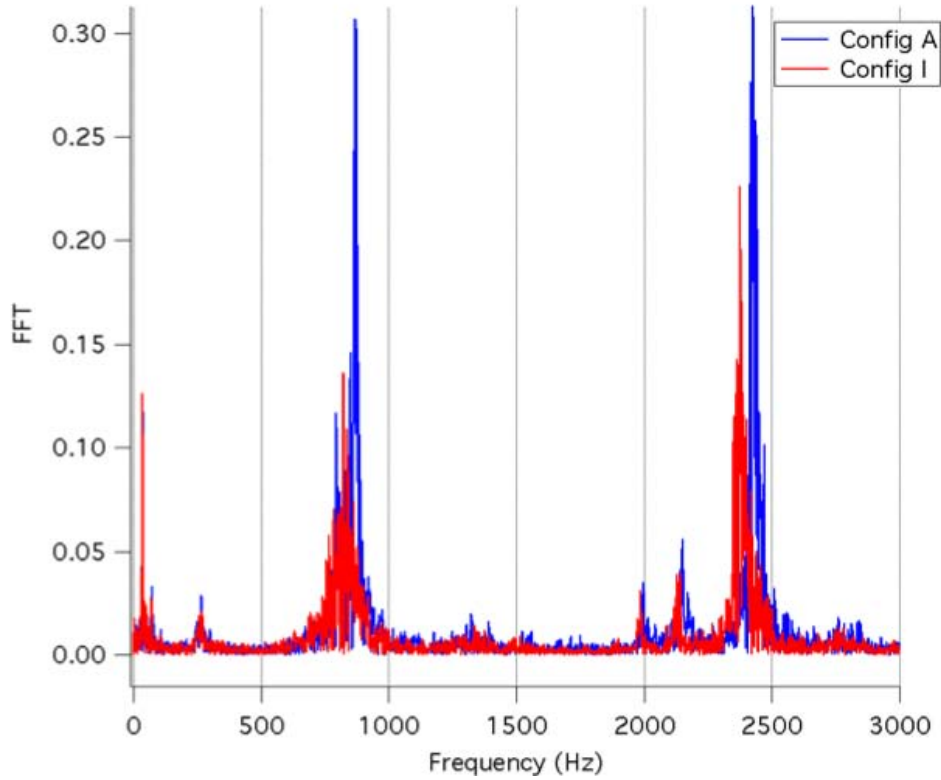


Figure A.9: Amplitude of the FFT of the LES signals (linear scale).

Even if the approximations done in the acoustic code may appear limiting (such as the absence of viscosity for an internal flow), the results presented in Fig. A.12 are in excellent agreement with the LES findings, the frequency shift is only few Hertz. All the peaks observed in LES correspond to an acoustic eigenmode of the confinement tube, their proper shape are displayed in Fig. A.13. For all modes the entrance chamber wall acts as a "ventre" of pressure fluctuation. The influence of the inlet/outlet boundary conditions do not seem influence these modes (slight influence of the constant pressure of the atmosphere for 5th longitudinal quarter wave mode and 5th longitudinal quarter wave mode coupled with the 1st transverse mode). Results and conclusions for configuration I are identical to configuration A.

It is interesting to notice that all the amplified modes, or peaks, in LES are acoustic eigenmodes of the confinement tube. It may be tricky since the confinement tube is the same for both geometries. Furthermore, the purpose of the study is to discriminate the two swirlers from the pressure signal caught by the probe in the atmosphere, Fig. A.3.

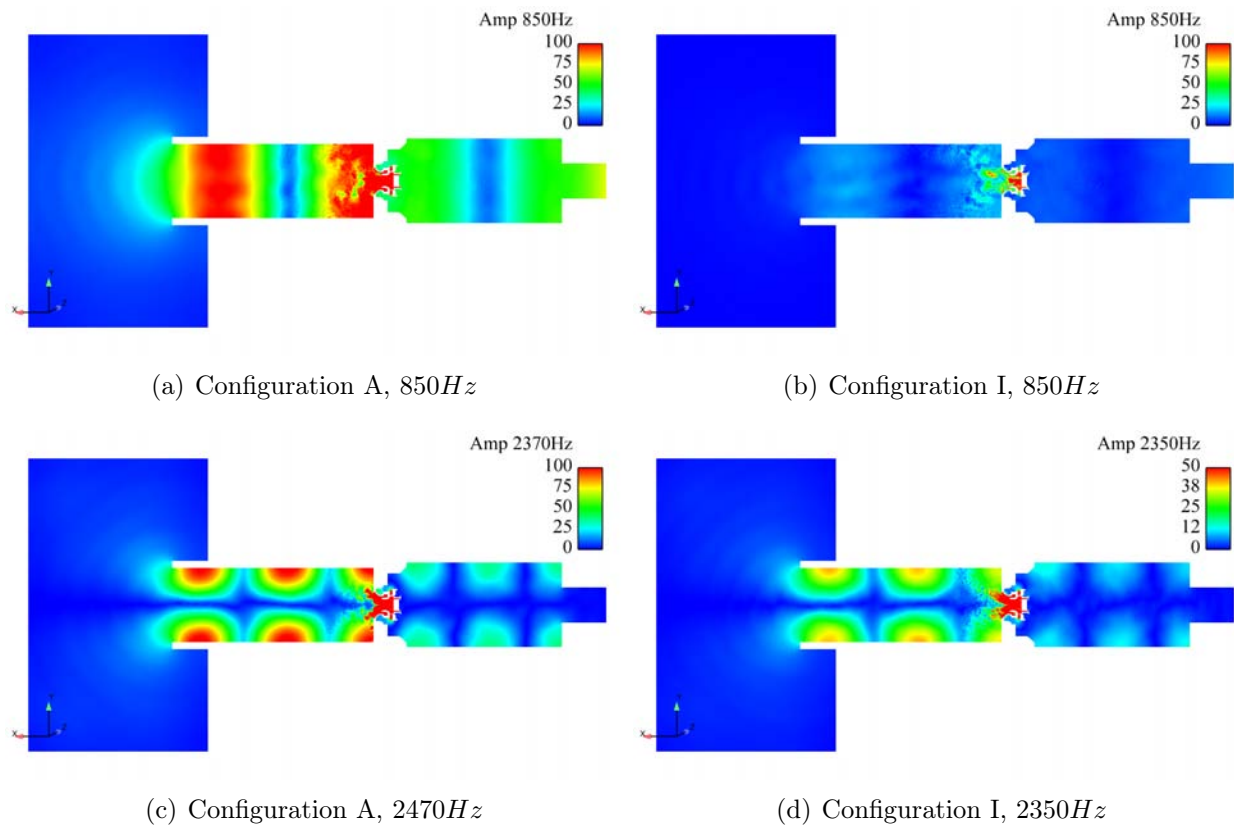


Figure A.10: DSP amplitude fields from LES. Axial cut

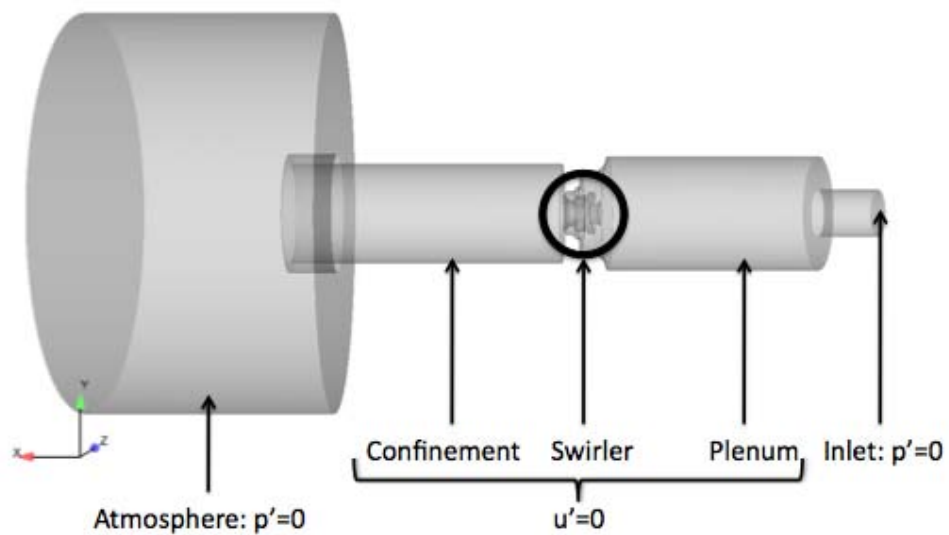


Figure A.11: Geometry and boundary conditions used for the acoustic computations.

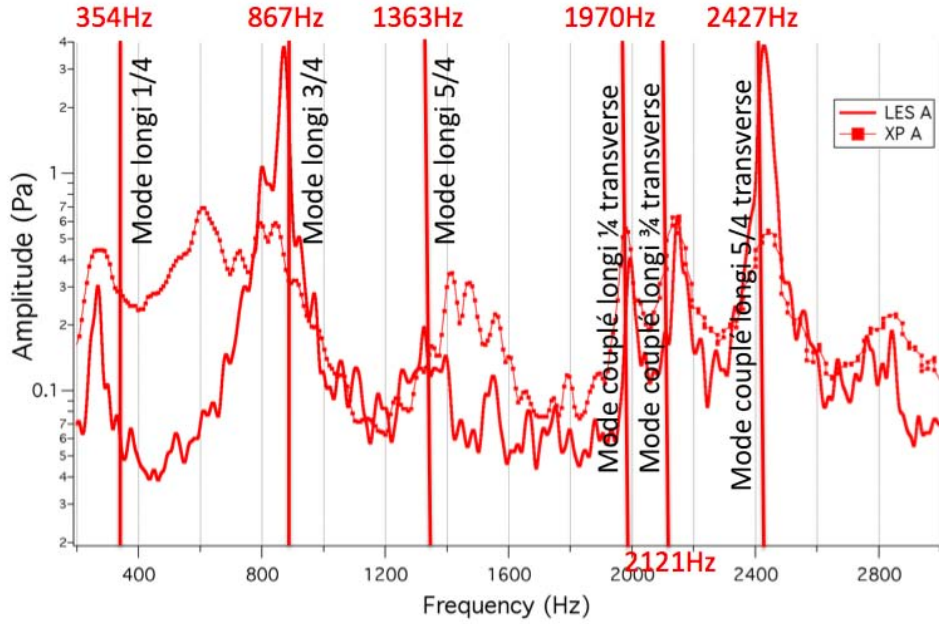


Figure A.12: Identification of the acoustic eigenmodes on the LES and experimental spectrums. Log scale.

A.4 Detailed comparison of the LES and experimental spectrum

Now that the parts of the spectrum due to the acoustic modes of the confinement are identified, i.e. which are identical for the two configurations, the proper comparison of LES with experiment spectrum can be done. For configuration A, Fig. A.14, the LES matches the experiments very well on the majority of the spectrum. However some differences are visible. For the two main peaks, at 850Hz and 2400Hz , the amplitude of the LES is quite different from the experiments: 16dB , but the main difference appears for the range of frequency between 400 and 700Hz where the levels remain almost stable from 300 to 850Hz in the experiments while it drops in LES; the difference being of about 16dB around 500Hz .

For configuration I, Fig. A.15, comments about configuration A are still valid, however the amplitude gap at 850Hz is much smaller ($\approx 8\text{dB}$) while the one at 2400Hz is larger ($\approx 22\text{dB}$). The level differences in the range of frequency between 400 and 700Hz is similar to configuration A.

Independently to the differences observed between LES and the experiments, LES spectrum are very close, Fig. A.16. From LES, only 2 differences can be noticed. A double peak is visible on the LES A spectrum around 850Hz while there is a simple (lower) peak for LES I. The difference in terms of amplitude has been seen previously in Fig. A.10a) and b). The other one is a slight frequency shift of the second main peak around 2400Hz : 2470Hz for configuration A and 2350Hz for configuration I.

Now looking at the experimental curves, Fig. A.16, it appears that the main difference is

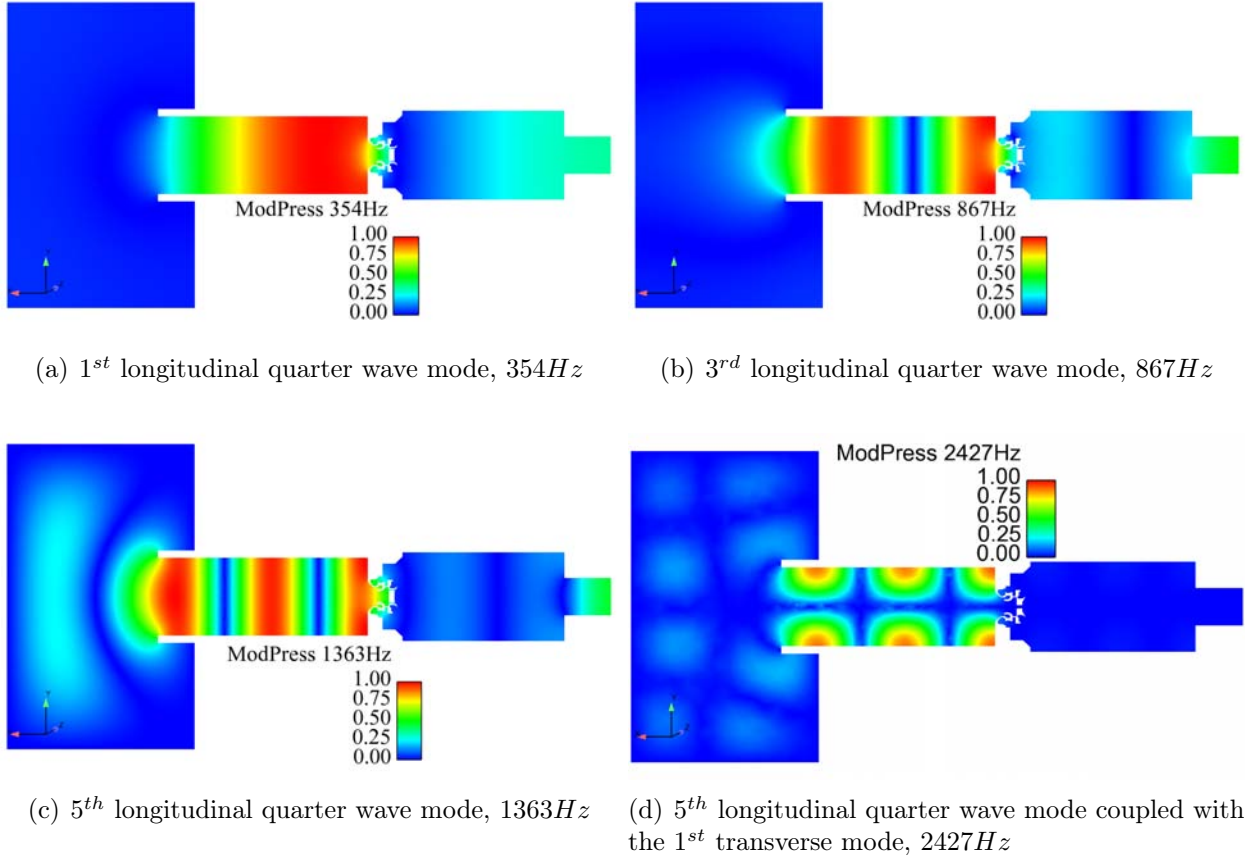


Figure A.13: Amplitude fields of the main acoustic eigenmodes (from acoustic solver AVSP). Axial cut.

located at $600Hz$ where there is a peak for configuration A and a drop for configuration I. This highlights a very different acoustic response of the device at this frequency in the experiments. Unfortunately, this is also within the range of frequency where LES do not match experiments, LES A and I being similar elsewhere.

Because of the relative simplicity of the setup (only air, atmospheric pressure, simple geometry) and of the relatively low frequency range involved (between $400Hz$ and $700Hz$), the problem may come from a bad definition of the boundary conditions in LES. Then, the influence of the boundary conditions on the computed spectrum is evaluated in the next section.

A.5 Influence of the boundary conditions

In the LES of the previous sections, the outlet boundary condition has been supposed perfectly non reflecting. However, since the recording probe is located outside of the confinement tube, i.e. in the atmosphere part of the mesh, if this assumption is not totally true it may impact the real acoustic. Furthermore, the experiments being done in a room without specific acoustic

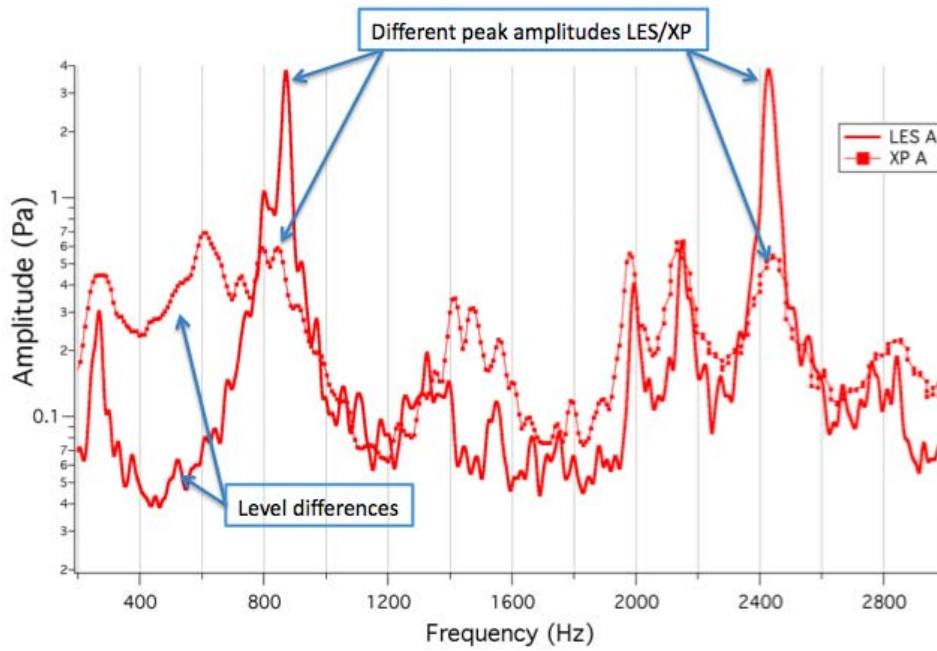


Figure A.14: Configuration A: LES and experimental spectrums. Log scale.

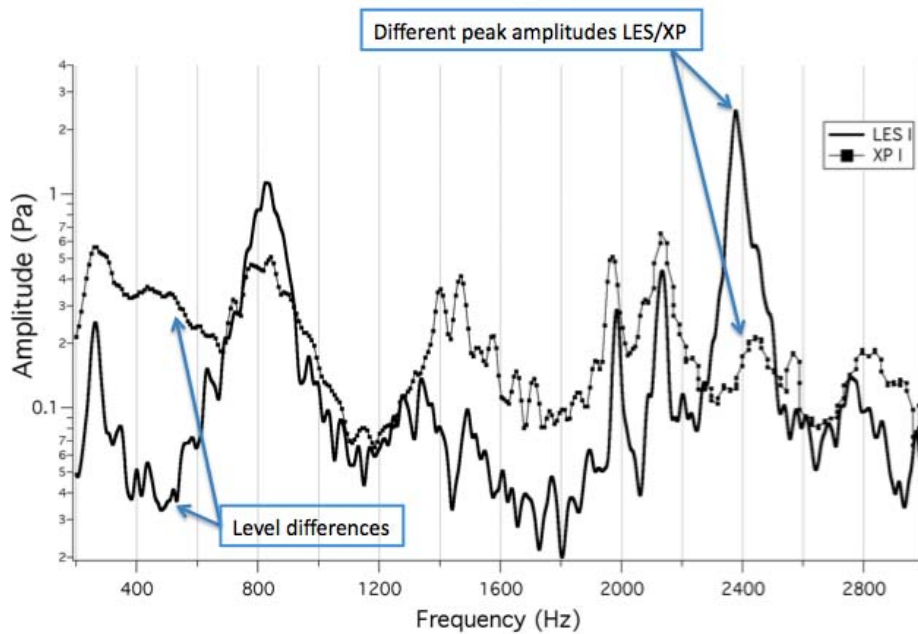


Figure A.15: Configuration I: LES and experimental spectrums. Log scale.

absorbant material, the wall may have reflected a part of the acoustic waves. A first test is to change the outlet boundary condition and to see its impact on the resulting spectrum. The non reflecting outlet boundary condition is replaced by a purely reflecting boundary condition

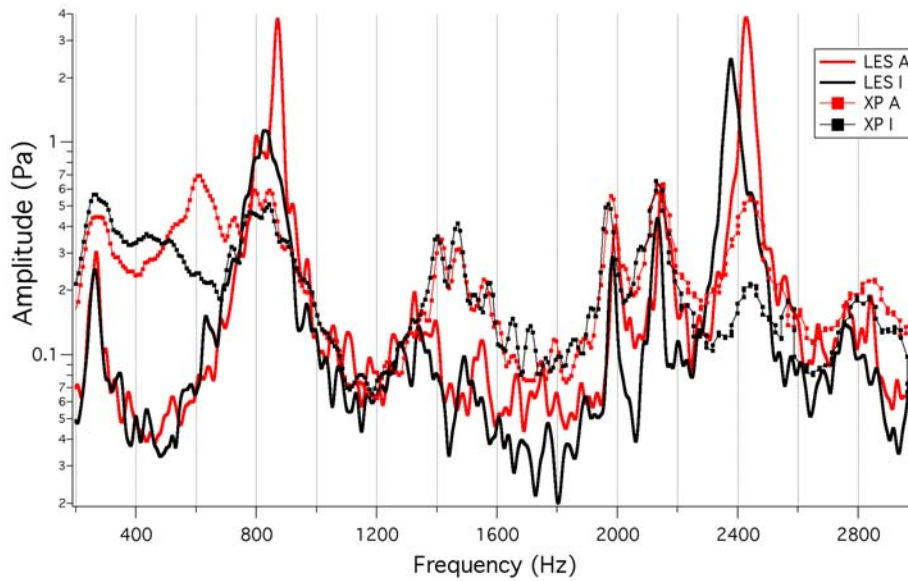


Figure A.16: Comparison of the acoustic spectrum LES and experimental for the two configurations. Log scale.

(a wall), Fig. A.17.

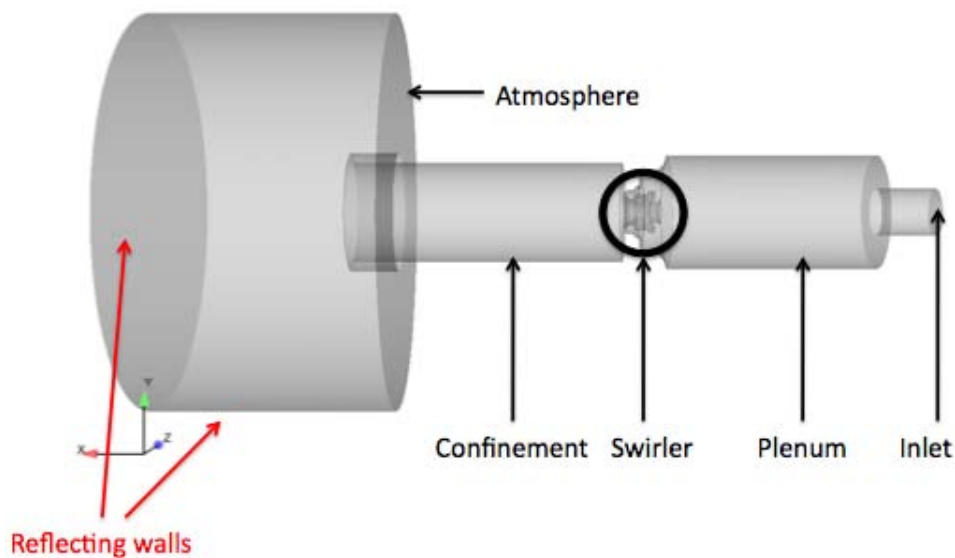


Figure A.17: View of the modified boundary conditions for the reflecting test case.

In spite of the raw characterisation used for the test, the results obtained on LES A are very interesting, Fig. A.18. The reflections on the outlet bring the amplitude of LES to the same level than for the experiments in the frequency range of interest ($400 - 700Hz$). At the same time, the high frequency (HF) noise remains at the same level for frequencies above $1000Hz$. Note that this manipulation also cancelled the high frequency peaks corresponding

to the coupled modes (2000, 2150 and 2400 Hz).

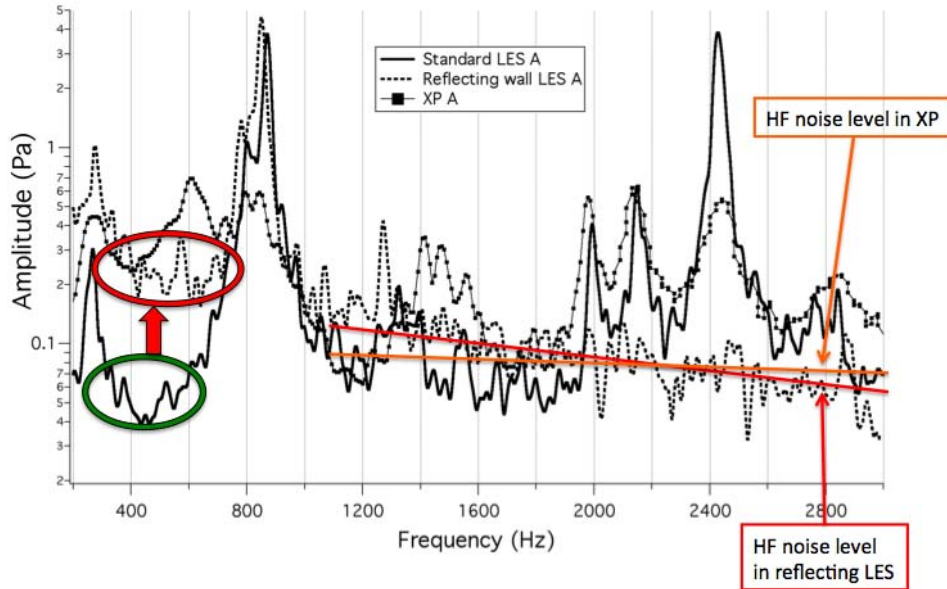


Figure A.18: Comparison of the acoustic spectrum for the configuration A.

This brief study has shown that the low frequencies of the spectrum (below 800 Hz) are highly affected by the outlet acoustic impedance. Since this impedance has not been measured during the experiments, the correct outlet boundary condition can not be defined and the LES comparison of the two swirlers can not be concluded.

However, the study of the acoustic eigenmodes have shown that the spectrum characteristics are dominated by the modes due to the confinement tube. But the purpose of this work was to study the swirlers, thus all invasive component which may altered the spectrum directly issued from the swirler should be avoided. Hence, some additional studies using upstream and downstream infinite acoustically, i.e. with non reflecting boundary conditions, are performed but not concluded yet.

Appendix B

The principles of the FIM-UR methodology

The purpose of this appendix is to give a brief insight on the principles of the FIM-UR (Fuel Injection Method by Upstream Reconstruction) methodology developed by M. Sanjosé in her PhD [123] in collaboration with J.M. Sénoner [174] at CERFACS. The interested reader may report to [123] for the full presentation. The presented methodology proposes an approach to specify the boundary conditions for fuel injection by pressure-swirl atomizer for both EE and EL methods within the same framework.

When LES is performed on a liquid fuel combustion chamber, the main difficulty lies in the lack of information on the spray characteristics. The global parameters of the operating point and the precise geometry of the combustor are specified, but the internal geometry of the atomizer or the characteristic parameters of the atomized spray often remain unknown. In most cases, the only available parameters are the pressure drop or the spray cone angle at a calibrated flow rate (measured sometimes with an other liquid than the fuel) and the liquid flow rate at the considered operating point. The diameter distribution and the velocity field are sometimes measured but only far downstream (about ten to twenty millimeters from the injector nozzle) in the combustion chamber.

The proposed methodology complements this partial information for a simplex type atomizer by using correlations and integral conservation laws. The design parameters of this model simplex atomizer are determined from the specified injection parameters of the real nozzle and empirical correlations.

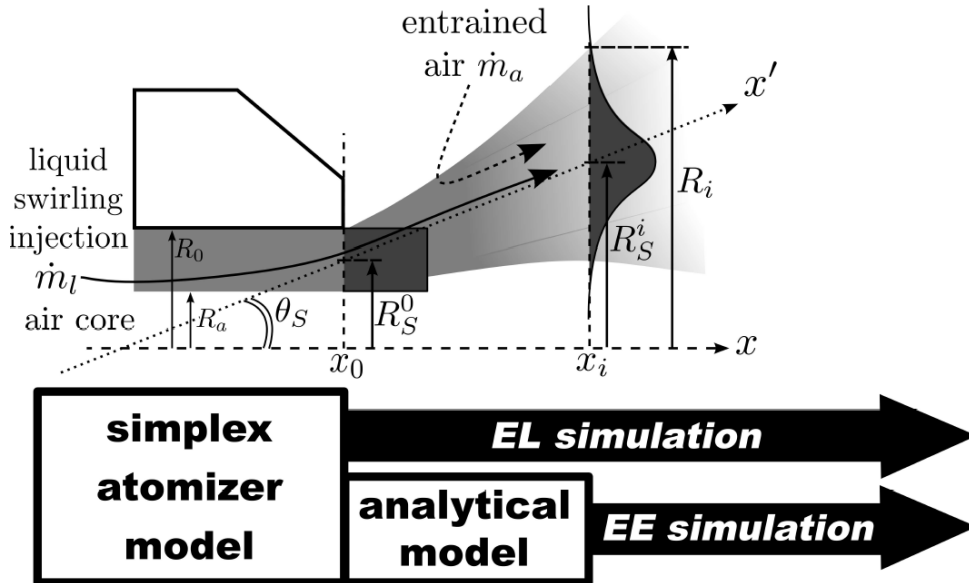


Figure B.1: Definition of parameters and sketch of the methodology FIM-UR

The methodology for EE approach is developed into successive steps, the variables used in the following are displayed in Fig. B.1:

1. First, the design parameters of the model atomizer and the boundary values in the real injection plane $x = x_0$ are determined, Fig. B.2, following the empirical results of Lefebvre

[133].

2. Second, liquid and gas velocity components, as well as the liquid volume fraction profiles on the simulated injection plane $x = x_i$, Fig. B.3, are calculated by writing integral conservation equations for the spray between the planes $x = x_0$ and $x = x_i$. In this approach, the drop diameter is a direct input into the model: it is a characteristic parameter of the atomized spray. Two unclosed terms appear in these integral equations: the mass-flow rate of the air entrained by the spray \dot{m}_a and the momentum loss of the spray $J_{s,l}$.
3. Third, these two unclosed terms \dot{m}_a and $J_{s,l}$ are evaluated at the simulated injection plane $x = x_i$ by using an extension of Cossali's model [134] adapted to hollow cone sprays.

The input parameters to FIM-UR are then of two types:

- **atomizer parameters:** the mass flow-rate of the injected liquid \dot{m}_l , the discharge orifice radius R_0 and the pressure drop coefficient C_D .
- **downstream spray characteristics:** the half spray-angle θ_S , the characteristic diameter of the droplet distribution d after primary and secondary breakups are achieved.

For the EL approach, the model reduces to step **1** to build in the real injection plane $x = x_0$ the velocity and the density profiles of droplets of diameter d . No further analytical model (as in steps **2** and **3**) is required. For the EE approach, at the end of step **3** the outputs of FIM-UR are the velocity and volume fraction profiles of the spray of droplets with mean diameter d in the simulated injection plane $x = x_i$, but also the velocity profiles of the air entrained by the spray.

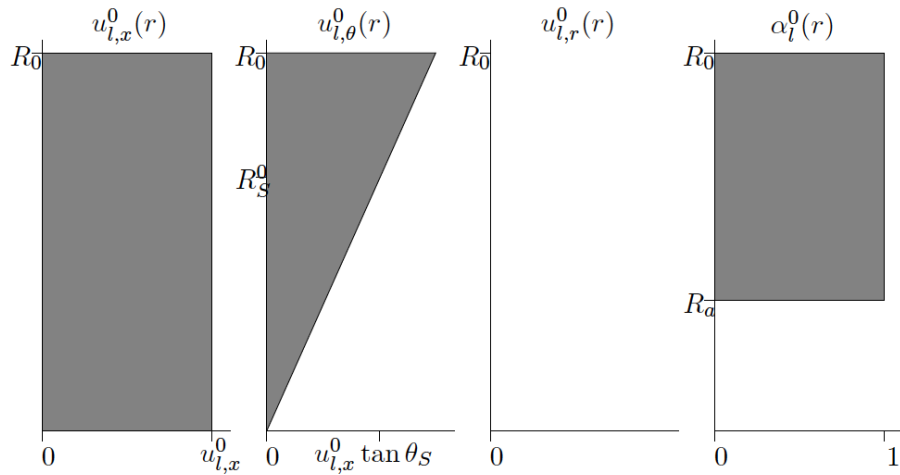


Figure B.2: Liquid variable profiles in the discharge orifice plane $x = x_0$

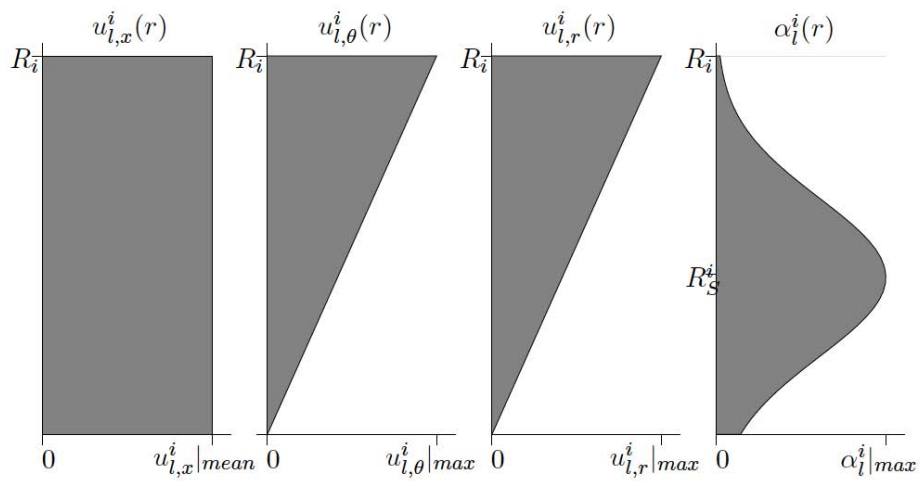


Figure B.3: Liquid variable profiles on the injection plane $x = x_i$

Appendix C

Analytical developments of I-crit-LES criterion 2

The evolution equations for the gas (T) and liquid (T_l) temperatures at the spark location, taking into account heat diffusion, heat transfer between the two phases and a source term S (the spark energy during the deposition phase, see phase 1 in Fig. 5.3 and Fig. 5.8) are:

$$\frac{\partial T}{\partial t} = \frac{\lambda}{\rho C_p} \Delta T + \frac{\Phi}{\rho C_p} + \frac{S}{\rho C_p} \quad (\text{C.1})$$

$$\frac{\partial T_l}{\partial t} = -\frac{\Phi}{\alpha_l \rho_l C_{pl}} \quad (\text{C.2})$$

where λ is the thermal conductivity, ρ the gas density, ρ_l the liquid density and C_p the thermal capacity.

The heat conduction flux Φ between the two phases is defined as:

$$\Phi(T_\zeta) = \alpha_l \lambda Nu \frac{6}{d_l^2} (T_\zeta - T) \quad (\text{C.3})$$

where T_ζ is the droplet surface temperature and is equal to T_l as droplets are supposed to have uniform temperature.

The exact resolution of Eq. C.1 and Eq. C.2 is beyond the scope of this paper but a simple approximation of the gas temperature space shape within the depot can be obtained by replacing the ΔT term in Eq. C.1 by a simplified expression: if the temperature is supposed to follow a parabolic profile (Fig. 5.2) with a maximum value T at $r = 0$ and a temperature T_∞ at $r = d_k/2$, the Laplacien of T can be approximated by:

$$\Delta T = \frac{8n_{dim}(T_\infty - T)}{d_k^2} \quad (\text{C.4})$$

Assuming $Le = 1$ (i.e. $\frac{\lambda}{\rho C_p} = D$), Eq C.1 becomes:

$$\frac{\partial T}{\partial t} = \frac{8n_{dim}D(T_\infty - T)}{d_k^2} + \alpha_l D Nu \frac{6}{d_l^2} (T_l - T) + \frac{S}{\rho C_p} \quad (\text{C.5})$$

Then, introducing: $\tau_{cond} = \frac{d_l^2}{6\alpha_l D Nu}$ and $\tau_{diff} = \frac{d_k^2}{8n_{dim}D}$, Eq C.5 simplifies to:

$$\frac{\partial T}{\partial t} = \frac{1}{\tau_{diff}} (T_\infty - T) + \frac{1}{\tau_{cond}} (T_l - T) + \frac{S}{\rho C_p} \quad (\text{C.6})$$

Similarly, Eq C.2:

$$\frac{\partial T_l}{\partial t} = -A \frac{1}{\tau_{cond}} (T_l - T) \quad (\text{C.7})$$

where $A = \frac{\rho C_p}{\alpha_l \rho_l C_{pl}}$

These equations are valid for the energy deposition (Phase 1 in Fig. 5.3) and the heating phase of the droplets (Phase 2 in Fig. 5.3), before they reach T_{cc} .

- Phase 1: energy deposition ($0 < t \leq t_d$):

$$S = \dot{e}_{dep}(x, t) \quad (\text{C.8})$$

Supposing in this phase that the liquid temperature is constant, equal to $T_{l,0}$, Eq C.6 writes:

$$\frac{\partial T}{\partial t} + \frac{1}{\tau}T = \frac{T_\infty}{\tau_{diff}} + \frac{T_{l,0}}{\tau_{cond}} + \frac{\dot{e}_{dep}(x, t)}{\rho C_p} \quad (\text{C.9})$$

where τ is defined as:

$$\frac{1}{\tau} = \frac{1}{\tau_{diff}} + \frac{1}{\tau_{cond}} \quad (\text{C.10})$$

The solution of Eq C.9 is:

$$T(t) = \left[T_\infty + \int_0^t \left(\frac{T_\infty}{\tau_{diff}} + \frac{T_{l,0}}{\tau_{cond}} + \frac{\dot{e}_{dep}(0, t')}{\rho C_p} \right) e^{\frac{t'}{\tau}} dt' \right] e^{-\frac{t}{\tau}} \quad (\text{C.11})$$

A quantitative analysis of the magnitude of the different terms shows that $\dot{e}_{dep}(0, t')$ is several orders greater than the other two terms which can be neglected. Consequently, at the end of the sparking time (i.e. at $t = t_d$):

$$T(t_d) = T_d = T_\infty + \frac{e_{dep}}{\rho C_p} \quad (\text{C.12})$$

where $e_{dep} = \int \dot{e}_{dep} dt$.

- Phase 2: droplet pre-heating ($t_d < t \leq t_{cc}$):

The second phase lasts from the end of the deposition at t_d , to the time t_{cc} when the temperature of the droplets reaches the saturation value T_{cc} (Fig. 5.3). In this phase, the energy source from spark is null ($S = 0$) and the one from combustion is still negligible. Hence the temperature evolution of the gas phase is:

$$T(t^*) = \left[T_d + \int_0^{t^*} \left(\frac{T_\infty}{\tau_{diff}} + \frac{T_{l,0}}{\tau_{cond}} \right) e^{\frac{t'}{\tau}} dt' \right] e^{-\frac{t^*}{\tau}} \quad (\text{C.13})$$

where $t^* = t - t_d$

Then:

$$\begin{aligned} T(t_{cc}) &= \left[T_d + \int_0^{t_{cc}-t_d} \left(\frac{T_\infty}{\tau_{diff}} + \frac{T_{l,0}}{\tau_{cond}} \right) e^{\frac{t'}{\tau}} dt' \right] e^{-\frac{t_{cc}-t_d}{\tau}} \\ &= T^* + (T_d - T^*) e^{-\frac{t_{cc}-t_d}{\tau}} \end{aligned} \quad (\text{C.14})$$

where $T^* = \tau \left[\frac{T_\infty}{\tau_{diff}} + \frac{T_{l,0}}{\tau_{cond}} \right]$

Now that $T(t_{cc})$ is a function of t_{cc} , this last time has to be determined. Solving Eq. C.7 for $t_d \leq t \leq t_{cc}$, we obtain:

$$T_l(t^*) = \left[T_{l,0} + \int_0^{t^*} \frac{A}{\tau_{cond}} T(t') e^{\frac{A}{\tau_{cond}} t'} dt' \right] e^{-\frac{A}{\tau_{cond}} t^*} \quad (\text{C.15})$$

which leads to:

$$T_{cc} = T_l(t_{cc}) = \left[T_{l,0} + \int_0^{t_{cc}-t_d} \frac{A}{\tau_{cond}} T(t') e^{\frac{A}{\tau_{cond}} t'} dt' \right] e^{-\frac{A}{\tau_{cond}}(t_{cc}-t_d)} \quad (\text{C.16})$$

We suppose in this phase that the gas temperature varies slowly, and in order to integrate Eq. C.16, use $T(t) \approx T_d$. Hence:

$$T_{cc} = \left[T_{l,0} + T_d \left(e^{\frac{A}{\tau_{cond}}(t_{cc}-t_d)} - 1 \right) \right] e^{-\frac{A}{\tau_{cond}}(t_{cc}-t_d)} \quad (\text{C.17})$$

After some rearrangements, one obtains:

$$t_{cc} - t_d = -\frac{\tau_{cond}}{A} \text{Ln} \left(\frac{T_{cc} - T_d}{T_{l,0} - T_d} \right) \quad (\text{C.18})$$

As $T_{cc} - T_{l,0} \ll T_d - T_{l,0}$, a 1st order Taylor expansion gives:

$$t_{cc} - t_d = \frac{\tau_{cond}}{A} \frac{T_{cc} - T_{l,0}}{T_d - T_{l,0}} \quad (\text{C.19})$$

Including expressions in Eqs. C.12 - C.14 and C.19 in the criterion definition Eq. 5.3; and supposing that $T_{l,0}$ and T_∞ are close:

$$T(t_{cc}) \geq T_{ign} \iff T_\infty + \frac{e_{dep}}{\rho C_p} \exp \left(-\frac{\tau_{cond}}{A\tau} \frac{T_{cc} - T_{l,0}}{T_d - T_{l,0}} \right) \geq T_{ign} \quad (\text{C.20})$$

Which leads after another Taylor expansion on the exponential term and some rearrangements to:

$$e_{dep} \geq \rho C_p (T_{ign} - T_\infty) + \rho C_p \frac{\tau_{cond}}{A\tau} (T_{cc} - T_{l,0}) \quad (\text{C.21})$$

Finally, we have:

$$e_{dep} \geq \rho C_p (T_{ign} - T_\infty) + \left(\alpha_l + \frac{4n_{dim}}{3Nu} \frac{d_l^2}{d_k^2} \right) \rho_l C_{p,l} (T_{cc} - T_{l,0}) \quad (\text{C.22})$$

Bibliography

- [1] M. Hilka, D. Veynante, T. Poinso, and M. Baum. Direct simulation of pollutant formation in premixed turbulent $\text{CH}_4/\text{O}_2/\text{N}_2$ flames. Technical report, EM2C, Ecole Centrale de Paris, 1994.
- [2] P. Popp and M. Baum. Heat transfer and pollutant formation mechanisms in insulated combustion chambers. In SAE-952387, editor, *Int. Fuels and Lubricants Meet. and Exposition*, Toronto, 1995.
- [3] F. E. C. Culick. Combustion instabilities in liquid-fueled propulsion systems- an overview. In *AGARD 72B PEP meeting*, 1987.
- [4] M. Cazalens, S. Roux, C. Sensiau, and T. Poinso. Solving combustion instabilities problems for high pressure jet engine cores. *J. Prop. Power* , 24(4), 2008.
- [5] D. R. Ballal and A. H. Lefebvre. The influence of flow parameters on minimum ignition energy and quenching distance. *Proc. Combust. Inst.* , 15:1473–1481, 1974.
- [6] P. Schmitt, T. Poinso, B. Schuermans, and K. P. Geigle. Large-eddy simulation and experimental study of heat transfer, nitric oxide emissions and combustion instability in a swirled turbulent high-pressure burner. *J. Fluid Mech.* , 570:17–46, 2007.
- [7] R. Lecourt. Ignition and extinction results at ambient conditions. Technical report, Timecop Report No. 2.2.1a, 2008.
- [8] C. Beck, R. Koch, and H.J. Bauer. Identification of droplet burning modes in lean, partially prevaporized swirl-stabilized spray flames. *Proc. Combust. Inst.* , 32:in press, 2009.
- [9] P. Domingo, L. Vervisch, S. Payet, and R. Hauguel. DNS of a premixed turbulent V-Flame and LES of a ducted flame using a FSD-PDF subgrid scale closure with FPI-tabulated chemistry. *Combust. Flame* , 143(4):566–586, 2005.
- [10] A. Neophytou, E. Mastorakos, and R.S. Cant. Dns of spark ignition and edge flame propagation in turbulent droplet-laden mixing layers. *Combustion and Flame*, 157(6):1071–1086, 2010.

- [11] K. Mahesh, G. Constantinescu, and P. Moin. A numerical method for large-eddy simulation in complex geometries. *J. Comput. Phys.* , 197(1):215–240, 2004.
- [12] L. Selle, G. Lartigue, T. Poinsot, R. Koch, K.-U. Schildmacher, W. Krebs, B. Prade, P. Kaufmann, and D. Veynante. Compressible large-eddy simulation of turbulent combustion in complex geometry on unstructured meshes. *Combust. Flame* , 137(4):489–505, 2004.
- [13] V. Moureau, G. Lartigue, Y. Sommerer, C. Angelberger, O. Colin, and T. Poinsot. Numerical methods for unsteady compressible multi-component reacting flows on fixed and moving grids. *J. Comput. Phys.* , 202(2):710–736, 2005.
- [14] S. Roux, G. Lartigue, T. Poinsot, U. Meier, and C. Bérat. Studies of mean and unsteady flow in a swirled combustor using experiments, acoustic analysis and large eddy simulations. *Combust. Flame* , 141:40–54, 2005.
- [15] T. Poinsot and D. Veynante. *Theoretical and Numerical Combustion*. R.T. Edwards, 2nd edition, 2005.
- [16] S. V. Apte, K. Mahesh, P. Moin, and J. C. Oefelein. Large-eddy simulation of swirling particle-laden flows in a coaxial-jet combustor. *Int. J. Multiphase Flow* , 29(8):1311–1331, 2003.
- [17] E. Riber, M. García., V. Moureau, H. Pitsch, O. Simonin, and T. Poinsot. Evaluation of numerical strategies for LES of two-phase reacting flows. In *Proc. of the Summer Program* , pages 197–211. Center for Turbulence Research, NASA Ames/Stanford Univ., 2006.
- [18] E. Riber, M. García., V. Moureau, H. Pitsch, O. Simonin, and T. Poinsot. Evaluation of numerical strategies for LES of two-phase reacting flows. *J. Comput. Phys.* , page under review, 2008.
- [19] F. Ham, S. V. Apte, G. Iaccarino, X. Wu, M. Herrmann, G. Constantinescu, K. Mahesh, and P. Moin. Unstructured LES of reacting multiphase flows in realistic gas turbine combustors. In *Annual Research Briefs* , pages 139–160. Center for Turbulence Research, NASA Ames/Stanford Univ., 2003.
- [20] S. Menon and N. Patel. Subgrid modeling for simulation of spray combustion in large scale combustors. *Am. Inst. Aeronaut. Astronaut. J.* , 44(4):709–723, 2006.
- [21] N. Patel and S. Menon. Simulation of spray–turbulence–flame interactions in a lean direct injection combustor. *Combust. Flame* , 153(1-2):228–257, 2008.
- [22] M. Boileau, S. Pascaud, E. Riber, B. Cuenot, L.Y.M. Gicquel, T. Poinsot, and M. Cazalens. Investigation of two-fluid methods for Large Eddy Simulation of spray combustion in Gas Turbines. *Flow, Turb. and Combustion* , 80(3):291–321, 2008.

- [23] M. Boileau, G. Staffelbach, B. Cuenot, T. Poinsot, and C. Bérat. LES of an ignition sequence in a gas turbine engine. *Combust. Flame* , 154(1-2):2–22, 2008.
- [24] R. D. Reitz and F. V. Bracco. Mechanism of atomization of a liquid jet. *Phys. Fluids* , 25(10):1730–1742, 1982.
- [25] A.D. Gosman and D. Clerides. Diesel spray modelling: a review. In *Proceedings of the International Conference on Liquid Atomization and Spray Systems, Florence, Italy*, pages 9–11, 1998.
- [26] L. P. Bayvel and Z. Orzechowski. *Liquid Atomization*. Combustion (Hemisphere Publishing Corporation). Taylor & Francis, Washington, USA, 1993.
- [27] J. Becker and C. Hassa. Breakup and atomization of a kerosene jet in crossflow at elevated pressure. *Atomization and Sprays* , 12(1-3):49–68, 2002.
- [28] O. Desjardins, V. Moureau, and H. Pitsch. An accurate conservative level set/ghost fluid method for simulating turbulent atomization. *J. Comput. Phys.* , 227:8395–8416, 2008.
- [29] S. V. Apte, K. Mahesh, and T. Lundgren. A Eulerian-Lagrangian model to simulate two-phase/particulate flows. In *Annual Research Briefs* , pages 161–171. Center for Turbulence Research, NASA Ames/Stanford Univ., 2003.
- [30] A. Berlemont, P. Achim, and Z. Chang. Lagrangian approaches for particle collisions: The colliding particle velocity correlation in the multiple particles tracking method and in the stochastic approach. *Phys. Fluids* , 13:2946–2956, 2001.
- [31] N. A. Patankar and D. D. Joseph. Lagrangian numerical simulation of particulate flows. *Int. J. Multiphase Flow* , 24:343–366, 2001.
- [32] O. Simonin, E. Deutsch, and J. P. Minier. Eulerian prediction of the Fluid/Particle correlated motion in turbulent two-phase flows. *App. Sci. Res.*, 51:275–283, 1993.
- [33] K. D. Squires and J. K. Eaton. Lagrangian and eulerian statistics obtained from direct numerical simulations of homogeneous turbulence. *Phys. Fluids A*, 3(1):130–143, 1991.
- [34] G. Gouesbet and A. Berlemont. Eulerian and lagrangian approaches for predicting the behaviour of discrete particles in turbulent flows. *Prog. Energy Comb. Sci.* , 25:133–159, 1999.
- [35] A. Kaufmann. *Vers la simulation des grandes échelles en formulation Euler/Euler des écoulements réactifs diphasiques*. Phd thesis, INP Toulouse, 2004.
- [36] M. García, Y. Sommerer, T. Schønfeld, and T. Poinsot. Evaluation of Euler/Euler and Euler/Lagrange strategies for large eddy simulations of turbulent reacting flows. In *EC-COMAS Thematic Conference on Computational Combustion*, 2005.

- [37] E. Mastorakos. Ignition of turbulent non-premixed flames. *Progress in Energy and Combustion Science*, 35:57–97, 2009.
- [38] A.D. Birch, D.R. Brown, M.G. Dodson, and Thomas JR. Turbulent concentration field of a methane jet. *Journal of Fluid Mechanics*, 1978.
- [39] A.D. Birch, D.R. Brown, M.G. Dodson, and Thomas JR. Studies of flammability in turbulent flows using laser raman spectroscopy. In *Proceedings of the combustion institute*, 1978.
- [40] D. R. Ballal and A. H. Lefebvre. Ignition and flame quenching in flowing gaseous mixtures. *Proc. R. Soc. Lond. A* , 357:163–181, 1977.
- [41] D. R. Ballal and A. H. Lefebvre. Ignition and flame quenching of quiescent fuel mists. *Proc. R. Soc. Lond. A* , 364:277–294, 1978.
- [42] D. R. Ballal and A. H. Lefebvre. Ignition and flame quenching of flowing heterogeneous fuel-air mixtures. *Combust. Flame* , 35:155–168, 1979.
- [43] D. R. Ballal and A. H. Lefebvre. A general model of spark ignition for gaseous and liquid fuel-air mixtures. In The Combustion Institute, editor, *Eighteenth Symposium (International) on Combustion*, pages 1737–1747, 1981.
- [44] E.S. Richardson. *Ignition Modelling for Turbulent Non-Premixed Flows*. PhD thesis, Cambridge University, 2007.
- [45] Alexandre Neophytou. *Spark Ignition and Flame Propagation in Sprays*. PhD thesis, University of Cambridge, 2010.
- [46] S. B. Pope. *Turbulent flows*. Cambridge University Press, 2000.
- [47] F. A. Williams. *Combustion Theory*. Benjamin Cummings, Menlo Park, CA, 1985.
- [48] P. Chassaing. *Mécanique des fluides, Éléments d'un premier parcours*. Cépaduès-Éditions, 2000.
- [49] Patrick Chassaing. *Turbulence en mécanique des fluides, Analyse du phénomène dans une perspective de modélisation à l'usage de l'ingénieur*. Institut National Polytechnique de Toulouse, 2000.
- [50] J. Hirschfelder, C. Curtis, and B. Bird. *Molecular Theory of Gases and Liquids*. John Wiley & Sons, 1954 edition, 1954.
- [51] A. Ern and V. Giovangigli. *Multicomponent Transport Algorithms*. Lecture Notes in Physics. Springer Verlag, Heidelberg, 1994.
- [52] A. Ern and V. Giovangigli. *A General-purpose FORTRAN Library For Multicomponent Transport Property Evaluation*. CERMICS and CMAP, 2001.

- [53] W. Sutherland. The viscosity of gases and molecular force. *Philosophical Magazine*, 5(36):507–531, 1893.
- [54] COSILAB, The Combustion Simulation Laboratory, Version 3.0. *www.SoftPredict.com*, Rotexo GmbH & Co. KG, Haan (Germany), 2009.
- [55] A. Favre. Statistical equations of turbulent gases. In *Problems of hydrodynamics and continuum mechanics*, pages 231–266. SIAM, Philadelphia, 1969.
- [56] K. K. Kuo. *Principles of combustion*. John Wiley & Sons, Inc., Hoboken, New Jersey, 2nd edition, 2005.
- [57] P. Chassaing. *Turbulence en mécanique des fluides, analyse du phénomène en vue de sa modélisation à l’usage de l’ingénieur*. Cépaduès-éditions, Toulouse, France, 2000.
- [58] S. B. Pope. Stochastic lagrangian models of velocity in homogeneous turbulent shear flow. *Phys. Fluids* , 14(5):1696–1702, 2002.
- [59] U. Piomelli and J. R. Chasnov. Large eddy simulations: theory and applications. In H. Hallback, D.S. Henningson, A.V. Johansson, and P.H. Alfredsson, editors, *Turbulence and Transition Modelling*, pages 269 – 336. Kluwer Academic Publishers, 1996.
- [60] J. Ferziger. Large eddy simulation: an introduction and perspective. In O. Métais and J. Ferziger, editors, *New tools in turbulence modelling*, pages 29 – 47. Les Editions de Physique - Springer Verlag, 1997.
- [61] M. Lesieur. Recent approaches in large-eddy simulations of turbulence. In O. Métais and J. Ferziger, editors, *New tools in turbulence modelling*, pages 1 – 28. Les Editions de Physique - Springer Verlag, 1997.
- [62] M. Lesieur and O. Metais. New trends in large-eddy simulations of turbulence. *Ann. Rev. Fluid Mech.* , 28:45 – 82, 1996.
- [63] U. Piomelli. Large-eddy simulation: achievements and challenges. *Prog. Aerospace Sci.* , 35:335–362, 1999.
- [64] P. Sagaut. *Large eddy simulation for incompressible flows*. Springer, 2002.
- [65] C. Meneveau and J. Katz. Scale-invariance and turbulence models for large eddy simulation. *Ann. Rev. Fluid Mech.* , 32:1–32, 2000.
- [66] A. N. Kolmogorov. The local structure of turbulence in incompressible viscous fluid for very large reynolds numbers. *C. R. Acad. Sci. , USSR*, 30:301, 1941.
- [67] J. Smagorinsky. General circulation experiments with the primitive equations: 1. the basic experiment. *Mon. Weather Rev.* , 91:99–164, 1963.

- [68] C. Meneveau and T. Lund. The dynamic smagorinsky model and scale-dependent coefficients in the viscous range of turbulence. *Phys. Fluids* , 9(12):3932–3934, 1997.
- [69] M. Germano, U. Piomelli, P. Moin, and W. Cabot. A dynamic subgrid-scale eddy viscosity model. *Phys. Fluids* , 3(7):1760–1765, 1991.
- [70] P. Sagaut. *Introduction à la simulation des grandes échelles*. Springer, mathématiques & applications edition, 1998.
- [71] F. Nicoud and T. Poinsot. Dns of a channel flow with variable properties. In *Int. Symp. On Turbulence and Shear Flow Phenomena.*, Santa Barbara, Sept 12-15., 1999.
- [72] V. R. Moureau, O. V. Vasilyev, C. Angelberger, and T. J. Poinsot. Commutation errors in Large Eddy Simulations on moving grids: Application to piston engine flows. In *Proc. of the Summer Program* , pages 157–168, Center for Turbulence Research, NASA AMES/Stanford University, USA, 2004.
- [73] G. Erlebacher, M. Y. Hussaini, C. G. Speziale, and T. A. Zang. Toward the large-eddy simulation of compressible turbulent flows. *J. Fluid Mech.* , 238:155–185, 1992.
- [74] P. Moin, K. D. Squires, W. Cabot, and S. Lee. A dynamic subgrid-scale model for compressible turbulence and scalar transport. *Phys. Fluids* , A 3(11):2746–2757, 1991.
- [75] C. G. Speziale, G. Erlebacher, T. A. Zang, and M. Y. Hussaini. The subgrid-scale modeling of compressible turbulence. *Phys. Fluids* , 31(4):940–942, April 1988.
- [76] O. Colin, F. Ducros, D. Veynante, and T. Poinsot. A thickened flame model for large eddy simulations of turbulent premixed combustion. *Phys. Fluids* , 12(7):1843–1863, 2000.
- [77] J.-Ph. L egier, T. Poinsot, and D. Veynante. Dynamically thickened flame LES model for premixed and non-premixed turbulent combustion. In *Proc. of the Summer Program* , pages 157–168. Center for Turbulence Research, NASA Ames/Stanford Univ., 2000.
- [78] K. A. Sallam, C. Aalburg, and G. M. Faeth. Breakup of round nonturbulent liquid jets in gaseous crossflow. *Am. Inst. Aeronaut. Astronaut. J.* , 42(12):2529–2540, 2004.
- [79] K. Lee, C. Aalburg, F.J Diez, G.M Faeth, and K.A. Sallam. Primary breakup of turbulent round liquid jets in uniform crossflows. *Am. Inst. Aeronaut. Astronaut. J.* , 45(8):1907–1916, 2007.
- [80] K. D. Squires and J. K. Eaton. Particle response and turbulence modification in isotropic turbulence. *Phys. Fluids A*, 2(7):1191–1203, 1990.
- [81] M. Boivin, O. Simonin, and K. D. Squires. Direct numerical simulation of turbulence modulation by particles in isotropic turbulence. *J. Fluid Mech.* , 375:235–263, 1998.

- [82] O. Vermorel, B. Bédard, O. Simonin, and T. Poinsot. Numerical study and modelling of turbulence modulation in a particle laden slab flow. *J. Turb.* , 4, 025, 2003.
- [83] M. Boivin, O. Simonin, and K. D. Squires. On the prediction of gas-solid flows with two-way coupling using large eddy simulation. *Phys. Fluids* , 12(8):2080–2090, 2000.
- [84] R. Pandya and F. Mashayek. Two-fluid large-eddy simulation approach for particle-laden turbulent flows. *Int. J. Heat and Mass Transfer* , 45:4753–4759, 2002.
- [85] F. Mashayek and R. Pandya. Analytical description of particle/droplet-laden turbulent flows. *Prog. Energy Comb. Sci.* , 29:329–378, 2003.
- [86] M. Sakiz and O. Simonin. Continuum modelling and lagrangian simulation of the turbulent transport of particle kinetic stresses in a vertical gas-solid channel flow. In *Third Int. Conf. Multiphase Flow* , Lyon, France, 1998.
- [87] J. Pozorski and J. P. Minier. On the lagrangian turbulent dispersion models based on the langevin equation. *Int. J. Multiphase Flow* , 24(6):913–945, 1998.
- [88] D. G. MacManus and J. A. Eaton. Flow physics of discrete boundary layer suction - measurements and predictions. *J. Fluid Mech.* , 417:47–75, 2000.
- [89] K. D. Squires and J. K. Eaton. Effect of selective modification of turbulence on two-equation models for particle-laden turbulent flows. *Transactions of the ASME*, 116:778–784, 1994.
- [90] P. K. Yeung and S. B. Pope. An algorithm for tracking fluid particles in numerical simulations of homogeneous turbulence. *J. Comput. Phys.* , 79:373–416, 1988.
- [91] J. Bonet and J. Periare. An alternating digital tree (ADT) algorithm for 3D geometric searching and intersection problems. *Int. J. Numer. Meth. Eng.* , 31(1):1–17, 1991.
- [92] A. Haselbacher, F. M. Najjar, and J. P. Ferry. An efficient and robust particle-localization algorithm for unstructured grids. *J. Comput. Phys.* , 225(2):2198–2213, 2007.
- [93] P. Diniz, S. Plimpton, B. Hendrickson, and R. Leland. Parallel algorithms for dynamically partitioning unstructured grids. *SIAM Proceedings Series 195*, SIAM, Philadelphia:627–632, 1995.
- [94] R. Löhner. Robust Vectorised Search Algorithms for Interpolation on Unstructured Grids. *J. Comput. Phys.* , 118(2):380–387, 1995.
- [95] E. Loth. Numerical approaches for motion of dispersed particles, droplets and bubbles. *Prog. Energy Comb. Sci.* , 26:161–223, 2000.
- [96] P. Moin. Large eddy simulation of multi-phase turbulent flows in realistic combustors. *Prog. Comput. Fluid Dynamics* , 4:237–240, 2004.

- [97] F. Jaegle. *LES of two-phase flow in aero-engines*. PhD thesis, Université de Toulouse - Ecole doctorale MEGeP, CERFACS - CFD Team, Toulouse, December 2009.
- [98] J. M. Senoner, M. Sanjosé, T. Lederlin, F. Jaegle, E. Riber, B. Cuenot, L. Gicquel, H. Pitsch, and T. Poinso. Evaluation of numerical strategies for LES of two-phase reacting flows. In *2nd colloque INCA*, Rouen, France, 2008. CORIA.
- [99] R. D. Williams. Performance of dynamic load balancing algorithms for unstructured mesh calculations. *Concurrency: Practice, and Experience*, 3(5):451–481, 1991.
- [100] J. Ferry and E. Balachandar. A fast eulerian method for disperse two-phase flow. *Int. J. Multiphase Flow*, 27:1199–1226, 2001.
- [101] W. A. Sirignano. *Fluid dynamics and transport of droplets and sprays*. Cambridge University Press, 1999.
- [102] P. Février and O. Simonin. Statistical and continuum modelling of turbulent reactive particulate flows. part 2: Application of a two-phase second-moment transport model for prediction of turbulent gas-particle flows. In *Theoretical and Experimental Modeling of Particulate Flows, Lecture Series 2000-06, von Karman Institute for Fluid Dynamics, Rhode Saint Genese (Belgium)*, 2000.
- [103] P. Février, O. Simonin, and K. Squires. Partitioning of particle velocities in gas-solid turbulent flows into a continuous field and a spatially uncorrelated random distribution: Theoretical formalism and numerical study. *J. Fluid Mech.*, 533:1–46, 2005.
- [104] O. Simonin. Combustion and turbulence in two phase flows. Lecture Series 1996-02, Von Karman Institute fo Fluid Dynamics, 1996.
- [105] J. O. Hirschfelder, C. F. Curtiss, and R. B. Bird. *Molecular theory of gases and liquids*. John Wiley & Sons, New York, 1969.
- [106] M. Boileau. *Simulation aux grandes échelles de l'allumage diphasique des foyers aéronautiques*. Phd thesis, INP Toulouse, 2007.
- [107] E. Riber. *Développement de la méthode de simulation aux grandes échelles pour les écoulements diphasiques turbulents*. Phd thesis, INP Toulouse, 2007.
- [108] N. Lamarque. *Schémas numériques et conditions limites pour la simulation aux grandes échelles de la combustion diphasique dans les foyers d'hélicoptère*. Phd thesis, INP Toulouse, 2007.
- [109] S. De Chaisemartin. *Modèles Eulériens et Simulation Numérique de la dispersion turbulente de brouillards qui s'évaporent*. PhD thesis, Ecole Centrale de Paris, Chatenay-Malabry, France, 2009.

- [110] R.O. Fox, F. Laurent, and M. Massot. Numerical simulation of spray coalescence in an eulerian framework: Direct quadrature method of moments and multi-fluid method. *J. Comput. Phys.* , 227:058–3088, March 2008.
- [111] R. Clift, J. R. Grace, and M. E. Weber. *Bubbles, Drops, and Particles*. Academic Press, 1978.
- [112] G. L. Hubbard, V. E. Denny, and A. F. Mills. Droplet evaporation: effects of transient and variable properties. *Int. J. Heat and Mass Transfer* , 18:1003–1008, 1975.
- [113] O. Simonin. Gaz particules. Cours d’options, Ecole Nationale Supérieure d’Electrotechnique, d’Electronique, d’Informatique, d’Hydraulique et des Télécommunications., 2002.
- [114] A. Kaufmann and M. Moreau. A spectral projection method for analysis of autocorrelation functions and projection errors in discrete particle simulation. *Int. J. Numer. Meth. Fluids* , 58(7):709–725, 2008.
- [115] E. Masi, B. Bédard, M. Moreau, and O. Simonin. Euler-euler large-eddy simulation approach for non isothermal particle-laden turbulent jet. In *8th Int. Sym. on Numerical Methods for Multiphase Flow*, number 55143 in ASME-FEDSM, Jacksonville, Florida, USA, August 2008.
- [116] M. Moreau. *Modélisation numérique directe et des grandes échelles des écoulements turbulents gaz-particules dans le formalisme eulérien mésoscopique*. Phd thesis, INP Toulouse, 2006.
- [117] M. Moreau, O. Simonin, and B. Bédard. Development of gas-particle euler-euler les approach: A priori analysis of particle sub-grid models in homogeneous isotropic turbulence. *Flow, Turb. and Combustion* , available online, 2009.
- [118] A. Yoshizawa and K. Horiuti. A statistically-derived subgrid-scale kinetic energy model for the large-eddy simulation of turbulent flows. *J. Phys. Soc. Japan*, 54(8):2834–2839, 1985.
- [119] D. Lathouwers and J. Bellan. Modeling of dense gas-solid reactive mixtures applied to biomass pyrolysis in a fluidized bed. *Int. J. Multiphase Flow* , 27(12):2155–2187, 2001.
- [120] R. Lecourt. Injection system two-phase flow characterization (lda-pda). Technical report, Timecop Report No. 2.2.1c, 2009.
- [121] J.M. Senoner, M. Sanjosé, T. Lederlin, F. Jaegle, M. García, E. Riber, B. Cuenot, L. Gicquel, H. Pitsch, and T. Poinsot. Evaluation of numerical strategies for two-phase reacting flows. *C. R. Acad. Sci. Mécanique*, 337(6-7):528–538, 2009.
- [122] R. Lecourt. Data reduction of the lda/pda measurements of the timecop set-up in mercato test bench. Technical report, ONERA, 2010.

- [123] M. Sanjosé. *Evaluation de la méthode Euler-Euler pour la simulation numérique aux grandes échelles des chambres à carburant liquide*. PhD thesis, INPT, 2009.
- [124] A. Roux. *Simulation aux grandes échelles d'un statoréacteur*. PhD thesis, Université de Toulouse - Ecole doctorale MEGeP, CERFACS - CFD Team, Toulouse, July 2009.
- [125] O. Colin and M. Rudgyard. Development of high-order taylor-galerkin schemes for unsteady calculations. *J. Comput. Phys.* , 162(2):338–371, 2000.
- [126] A. Jameson, W. Schmidt, and E. Turkel. Numerical solution of the euler equations by finite volume methods using runge-kutta time stepping schemes. In AIAA paper 81-1259, editor, *14th Fluid and Plasma Dynamic Conference*, Palo Alto, 1981.
- [127] J. P. Boris and D. L. Book. Flux-corrected transport iii. minimal-error fct algorithms. *J. Comput. Phys.* , 20:397–432, 1976.
- [128] G. Patnaik, R. H. Guirguis, J. P. Boris, and E. S. Oran. A barely implicit correction for flux-corrected transport. Technical Report D.C., NRL 5855, Naval Research Laboratory, Washington, 1986.
- [129] T. J. R. Hughes, A. A. Oberai, and L. Mazzei. Large eddy simulation of turbulent channel flows by the variational multiscale method. *Phys. Fluids* , 13(6):1784–1799, 2001.
- [130] B. Koobus and C. Farhat. A variational multiscale method for the large eddy simulation of compressible turbulent flows on unstructured meshes - application to vortex shedding. *Comput. Methods Appl. Mech. Eng.* , 193:1367–1383, 2004.
- [131] C. Farhat, A. Rajasekharan, and B. Koobus. A dynamic variational multiscale method for large eddy simulations on unstructured meshes. *Comput. Methods Appl. Mech. Eng.* , 195(13-16):1667–1691, 2006.
- [132] J. Luche, M. Reuillon, J-C. Boettner, and M. Cathonnet. Reduction of large detailed kinetic mechanisms: application to kerosene / air combustion. *Combust. Sci. Tech.* , 176:1935–1963, 2004.
- [133] A. H. Lefebvre. *Atomization and Sprays*. Combustion (Hemisphere Publishing Corporation). Taylor & Francis, 1989.
- [134] G.E. Cossali. An integral model for gas entrainment into full cone sprays. *J. Fluid Mech.* , 439:353–366, 2001.
- [135] O. Lucca-Negro and T. O'Doherty. Vortex breakdown: a review. *Prog. Energy Comb. Sci.* , 27:431–481, 2001.
- [136] D. B. Spalding. The combustion of liquid fuels. In *4th Symp. (Int.) on Combustion*, pages 847–864. The Combustion Institute, Pittsburgh, 1953.

- [137] N. Syred. A review of oscillation mechanisms and the role of the precessing vortex core in swirl combustion systems. *Prog. Energy Comb. Sci.* , 32(2):93–161, 2006.
- [138] M. Massot and Ph. Villedieu. Modélisation multi-fluide eulérienne pour la simulation de brouillards denses polydispersés. *C. R. Acad. Sci. Problèmes mathématiques de la mécanique*, 332(9):869–874, 2001.
- [139] S. de Chaisemartin, L. Fréret, D. Kah, F. Laurent, R. O. Fox, J. Réveillon, and M. Massot. Turbulent combustion of polydisperse evaporating sprays with droplets crossing: Eulerian modeling and validation in the infinite Knudsen limit. In *Proc. of the Summer Program* . Center for Turbulence Research, NASA Ames/Stanford Univ., 2008.
- [140] B. Franzelli, E. Riber, M. Sanjosé, and T. Poinso. A two-step chemical scheme for Large-Eddy Simulation of kerosene-air flames. *Combust. Flame* , 157(7):1364–1373, 2010.
- [141] W. Meier, X.R. Duan, and P. Weigand. Investigations of swirl flames in a gas turbine model combustor: I. flow field, structures, temperature, and species distributions. *Combust. Flame* , 144(1-2):225–236, January 2006.
- [142] S.F Ahmed and E. Mastorakos. Spark ignition of lifted turbulent jet flames. *Combust. Flame* , 146:215–231, 2006.
- [143] S. F. Ahmed, R. Balachandran, T. Marchione, and E. Mastorakos. Spark ignition of turbulent nonpremixed bluff-body flames. *Combust. Flame* , 151:366–385, 2007.
- [144] T. Marchione, S. F. Ahmed, and E. Mastorakos. Ignition of turbulent swirling n-heptane spray flames using single and multiple sparks. *Combustion and Flame*, 156:166–180, 2008.
- [145] P. Boudier, S. Henriot, T. Poinso, and T. Baritaud. A model for turbulent flame ignition and propagation in spark ignition engines. In The Combustion Institute, editor, *Twenty-Fourth Symposium (International) on Combustion*, pages 503–510, 1992.
- [146] T. Kravchik and E. Sher. Numerical modeling of spark ignition and flame initiation in a quiescent methane-air mixture. *Combust. Flame* , 99:635–643, 1994.
- [147] T. M. Sloane. Energy requirements for spherical ignitions in methane-air mixtures at different equivalence ratios. *Combust. Sci. Tech.* , 73:351–365, 1990.
- [148] N. García-Rosa. *Phénomènes d’allumage d’un foyer de turbomachine en conditions de haute altitude*. PhD thesis, Université de Toulouse - Ecole doctorale : Mécanique, Energétique, Génie civil, Procédés, Toulouse, France, July 2008.
- [149] T.X. Phuoc and F.P. White. Laser induced spark ignition of ch₄/air mixtures. *Combust. Flame* , 119:203–216, 1999.
- [150] T.X. Phuoc and F.P. White. An optical and spectroscopic study of laser-induced sparks to determine available ignition energy. *Proc. Combust. Inst.* , 29:1621 – 1628, 2002.

- [151] G. Lacaze, E. Richardson, and T. J. Poinso. Large eddy simulation of spark ignition in a turbulent methane jet. *Combust. Flame*, 156(6):1993–2009, 2009.
- [152] G. Lacaze, B. Cuenot, T. J. Poinso, and M. Oschwald. Large eddy simulation of laser ignition and compressible reacting flow in a rocket-like configuration. *Combust. Flame*, 156(6):1166–1180, 2009.
- [153] AIAA 2007-5664, editor. *Opposed Jet Burner Extinction Limits: Simple Mixed Hydrocarbon Scramjet Fuel vs Air*. 43rd AIAA/ASME/SAE/ASEE Joint Propulsion Conference And Exhibit, 2007.
- [154] Akindele OO, D. Bradley, Mak PW, and McMahan M. Spark ignition of turbulent gases. *Combustion and Flame*, 1982.
- [155] V. Subramanian, P. Domingo, and L. Vervisch. Large eddy simulation of forced ignition of an annular bluff-body burner. *Combustion and Flame*, 157:579–601, 2010.
- [156] M. Champion, B. Deshaies, and G. G. Joulin. Relative influences of convective and diffusive transports during spherical flame initiation. *Combust. Flame*, 74:161–170, 1988.
- [157] F. Dabireau, B. Cuenot, O. Vermorel, and T. Poinso. Interaction of h₂/o₂ flames with inert walls. *Combust. Flame*, 135(1-2):123–133, 2003.
- [158] R. G. Abdel-Gayed, D. Bradley, M. N. Hamid, and M. Lawes. Lewis number effects on turbulent burning velocity. *Proc. Combust. Inst.*, 20:505–512, 1984.
- [159] O. Gulder. Turbulent premixed flame propagation models for different combustion regimes. In *23rd Symp. (Int.) on Comb.*, pages 743–835, Orleans, 1990. The Combustion Institute, Pittsburgh.
- [160] R. Maly and M. Vogel. Initiation and propagation of flame fronts in lean ch₄-air mixtures by the threemodes of the ignition spark. In *17th Symp. (Int.) on Combustion*, pages 821–831. The Combustion Institute, Pittsburgh, 1978.
- [161] M. Kono, K. Hatori, and K. Inuma. Investigation of ignition ability of composite sparks in flowing mixtures. In *20th Symp. (Int.) on Combustion*, pages 133–140. The Combustion Institute, Pittsburgh, 1984.
- [162] M. Thielle, S. Selle, U. Riedel, J. Warnatz, and U. Maas. Numerical simulation of spark ignition including ionization. In The Combustion Institute, editor, *Twenty-Eighth Symposium (International) on Combustion*, pages 1177–1185, 2000.
- [163] R. Teets and J. Sell. Calorimetry of ignition sparks. *SAE transactions*, 97:371–383, 1988.
- [164] C.K. Law. *Combustion physics*. Cambridge University Press, 2006.

- [165] W. M. Huang, S. R. Vosen, and R. Greif. Heat transfer during laminar flame quenching, effect of fuels. In *21st Symp. (Int.) on Combustion*, pages 1853–1860. The Combustion Institute, Pittsburgh, 1986.
- [166] S. R. Vosen, R. Greif, and C. K. Westbrook. Unsteady heat transfer during laminar flame quenching. In *20th Symp. (Int.) on Combustion*, pages 76–83. The Combustion Institute, Pittsburgh, 1984.
- [167] A. Delataillade, F. Dabireau, B. Cuenot, and T. Poinsot. Flame/wall interaction and maximum heat wall fluxes in diffusion burners. *Proc. Combust. Inst.* , 29:775–780, 2002.
- [168] J. Luche. *Elaboration of reduced kinetic models of combustion. Application to a kerosene mechanism*. PhD thesis, LCSR Orleans, 2003.
- [169] T. Poinsot and S. Lele. Boundary conditions for direct simulations of compressible viscous flows. *J. Comput. Phys.* , 101(1):104–129, 1992.
- [170] O. Colin and M. Rudgyard. Development of high-order taylor-galerkin schemes for les. *Journal of Computational Physics*, 162(2):338–371, 2000.
- [171] F. Ducros, F. Nicoud, and T. Poinsot. Wall-adapating local eddy-viscosity models for simulations in complex geometries. In *ICFD*, pages 293–300. Baines M. J., 1998.
- [172] A. Vié, L. Martinez, S. Jay, A. Benkenida, and B. Cuenot. Validation of the eulerian mesoscopic approach in particle-charged homogeneous isotropic decaying turbulence in the scope of large eddy simulation of fuel spray. In *ICLASS Proceedings*, number 090, Colorado, USA, July 2009.
- [173] CERFACS. *AVBP Handbook - http://cerfacs.fr/~avbp/AVBP_V5.X/HANDBOOK*. CERFACS, 2009.
- [174] J. M. Senoner, M. Sanjosé, T. Lederlin, F. Jaegle, M. García, E. Riber, B. Cuenot, L. Gicquel, H. Pitsch, and T. Poinsot. Eulerian and lagrangian large-eddy simulations of an evaporating two-phase flow. *C. R. Acad. Sci.* , 337(6-7):458–468, June-July 2009.